Investigation of precipitation and its retrieval using ground-based remote sensing techniques

Inaugural dissertation
of the Faculty of Science,
University of Bern

presented by

Wenyue Wang

from China

Supervisors of the doctoral thesis: PD. Dr. Klemens Hocke
Institute of Applied Physics

Prof. Dr. Christoph Raible
Climate and Environmental Physics

Investigation of precipitation and its retrieval using ground-based remote sensing techniques

Inaugural dissertation
of the Faculty of Science,
University of Bern

presented by

Wenyue Wang

from China

Supervisors of the doctoral thesis: PD. Dr. Klemens Hocke
Institute of Applied Physics

Prof. Dr. Christoph Raible
Climate and Environmental Physics

Accepted by the Faculty of Science.

The Dean:

Bern, 25 September 2024   Prof. Dr. Jean-Louis Reymond

For women, who aspire to be scientists!

SUMMARY

Precipitation plays an irreplaceable role in many aspects of the climate system, including the global water cycle, climate change, and weather prediction. However, the current mainstream technologies for obtaining precipitation information have its inherent limitations. The potential of ground-based microwave radiometers for rain parameter retrieval is complementary to these techniques. The main aim of my thesis is thus to optimally estimate precipitation for microwave radiometers and further apply these retrieval methods to monitor precipitation systems in synergy with other remote sensing or in situ techniques.

This thesis is divided in three parts. Part i summarizes the formation process and categorization of precipitation in Chapter 1. The virga phenomenon, the inter-relations of aerosols, clouds, and precipitation, and the precursors of rainfall are also introduced.

Part ii covers the principles of radiative transfer and tropospheric microwave radiometers in Chapter 2 and presents the datasets used and the methodology for rain rate retrieval and data analysis in Chapter 3.

Part iii comprises six of my studies that have been published or submitted to peer-reviewed journals. Firstly, based on the physical characteristics of raindrops in the atmosphere that affect microwave radiation signals, I detected rainfall with high accuracy and high time resolution from rain-contaminated microwave radiometer data using Gradient Boosted Decision Tree (GBDT) algorithms in Chapter 4. The rain type classification from micro rain radar (MRR) is used as the target labels to train this model. Secondly, I investigated an optical depth based physical method in Chapter 5 and developed two machine learning based methods in Chapter 6, to retrieve rain rates from the tropospheric microwave radiometers. By comparing with rain rates measured by rain gauges or MRR, all these methods perform excellently. Then, I assessed the performance of indoor and outdoor microwave radiometers for brightness temperature and atmospheric water measurements, and explored the source of deviation in brightness temperature using GBDT by comparing the importance of various factors on the biases in Chapter 7. The innovative device setting of the indoor microwave radiometer effectively avoids the water film on the radome due to rain. Finally, as applications for rain estimation, I investigated the characteristics of atmospheric parameters observed from ground-based microwave radiometer and weather station using a superposed epoch analysis method before, during, and after rain events over the Swiss Plateau, deducing the temporal evolution of rain events and iden-

tifying possible rainfall precursors in Chapter 8. Moreover, I monitored the inter-relations between various factors, such as aerosols, clouds, and meteorological variables, and precipitation systems using ground-based remote sensing and in situ instruments in Granada including a microwave radiometer, ceilometer, cloud radar, nephelometer, and weather station in Chapter 9. I analyzed the potential reasons for the predominant rain type, the main rain intensity class, and the occurrence of the virga phenomenon over southern Spain.

CONTENTS

LIST OF ACRONYMS

ACL   Active Cold Load

AE   Ångström exponent

AGORA   Andalusian Global ObseRvatory of the Atmosphere

ECMWF   European Center for Medium-Range Weather Forecasts

ExWi   Exakte Wissenschaften

FIs   Forecast Indexs

FMCW   Frequency Modulated Continuous Wave

GBDT   Gradient Boosted Decision Tree

GCOS   Global Climate Observing System

G2   Generation 2

HATPRO Humidity And Temperature PROfilers

H_2O Water vapor

IAP   Institute of Applied Physics

IISTA-CEAMA   Andalusian Institute for Earth System Research

ILW   Integrated Liquid Water

IR   Infrared

IWV   Integrated Water Vapor

LightGBM Light Gradient-Boosting Machine

LN_2 Liquid Nitrogen

LTE   Local Thermodynamic Equilibrium

MDI   Mean Decrease Impurity

METEK   Meteorologische Messtechnik GmbH

MeteoSwiss Swiss Federal Office of Meteorology and Climatology

MRR   Micro Rain Radar

NWP   Numerical Weather Prediction

N_2 Nitrogen

OCCR   Oeschger Centre for Climate Change Research

O_2 Oxygen

O_3 Ozone

VIL   Vertically Integrated Liquid

RCS   Range Corrected Signal

RF   Random Forest

RPG   Radiometer Physics GmbH

TROWARA TROpospheric WAter RAdiometer

UGR   Granada urban station

SEA   Superposed Epoch Analysis

SVM   Support Vector Machine

Part I

METEOROLOGICAL BACKGROUND

This part offers an overview of precipitation, covering its formation and various types. It also explores the interrelations between aerosols, clouds, and rainfall, along with the precursors of rain.

1 PRECIPITATION

Water continuously cycles between the Earth and the troposphere, as shown in Figure 1.1. The total amount of water in the cycle remains roughly constant, but the spatio-temporal distribution and the phases of water in the various processes of evaporation, condensation, precipitation, and runoff is constantly changing. Liquid water or solid ice and snow on the Earth's surface can transit into the atmosphere through evaporation or sublimation, forming water vapor, the primary atmospheric water form. Water vapor in the atmosphere condenses to form clouds and is eventually released as precipitation (Bengtsson, 2010).
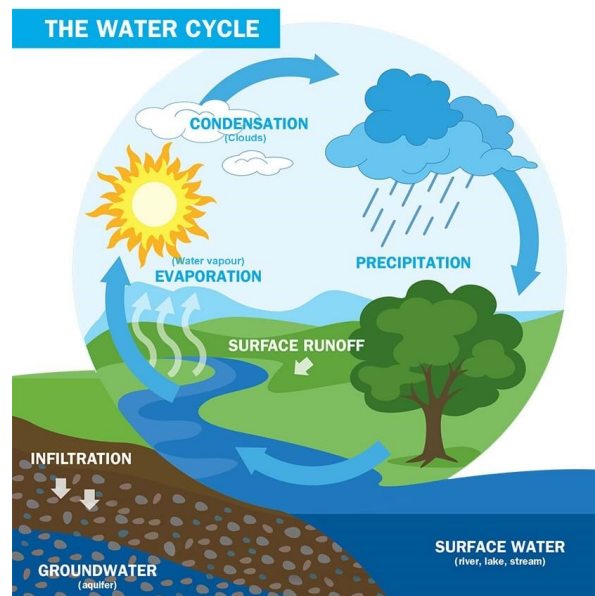
Figure 1.1: Atmospheric water cycle diagram.
https://www.teachengineering.org/curricularunits/view/cub_water_cycle_unit

Precipitation forms in the atmosphere and falls back to the ground. Its formation involves complex meteorological processes, including advection of humid air, vertical winds, adiabatic cooling and condensation of water vapor on aerosols and ice crystals. The subsequent growth of cloud droplets and ice crystals to raindrops, snowflakes or other hydrometers depends on microphysical processes, atmospheric composition, thermodynamics and dy-

namics. Various meteorological conditions and formation mechanisms give rise to diverse types of rainfall, such as frontal rain, convective rain, and orographic rain. Although meteorologists have made significant progress in rainfall research, accurate rainfall predictions remain a formidable challenge.

This chapter offers a general introduction to the topic of this thesis, namely precipitation in the troposphere. In Section 1.1, the processes responsible for precipitation formation are presented, namely, collision-coalescence and the ice crystal process. Different types of precipitation and the virga phenomenon are detailed in Section 1.2 and Section 1.3, respectively. Section 1.4 explores the intricate connections between aerosols, clouds, and rainfall, while Section 1.5 introduces the concept of rainfall precursors. Geographical and climatic characteristics of the two regions under study (Swiss Plateau and Andalusia) are provided in Section 1.6.

1.1 PRECIPITATION PROCESSES

Precipitation primarily occurs through two processes: collision-coalescence and ice crystal process (Wegener–Bergeron–Findeisen process). The two processes are distinguished by cloud temperature. Warm clouds, with temperatures above 0°C, are composed of liquid droplets and hence the collision-coalescence process is effective. Cold clouds, with temperatures below 0°C, prevail in middle and high latitudes, and here the ice crystal process is effective (Ritter, 2017).

Cloud droplets are small, with an average diameter of around 0.02 mm, making them approximately 100 times smaller than typical raindrops (Ahrens and Henson, 2019b). Figure 1.2a shows the process of the cloud droplet collision and coalescence to form the raindrop, where t_0 to t_n represent various moments in time. The cloud droplet at t_0 moves upwards due to the updraft. The droplet at t_1 collides and captures smaller droplets along its path to grow larger. As droplet at t_2 reaches a certain altitude, a balance between the cloud's updraft and the droplet's gravity is established, allowing the droplet to remain suspended in the air. The droplet at t_3 slowly falls as it grows larger. The falling droplet at t_4 captures larger cloud droplets, leading to further growth. As the droplet moves through the cloud at t_5, it transforms into a sizable raindrop. These raindrops fall rapidly, contributing to warm convective cumulus cloud showers.

Figure 1.2b shows the ice crystal process of stratiform precipitation. Cloud droplets, due to their small size, can remain in liquid form even at very low temperatures (as low as -40°C), called supercooled droplets. Cold clouds contain supercooled droplets and ice crystals. The saturated vapor pressure above water is higher than that above ice. This saturated vapor pressure gradient causes the water molecules of droplets to transfer to the ice crystals,

providing a continuous water source for the rapid growth of ice crystals. As the gravity of the ice crystal becomes stronger than the updraft, it begins to fall. In warmer cloud layers, the collision of ice crystals with supercooled droplets leads to the incorporation of droplets into the ice, forming graupel. As graupel falls, it can break into smaller pieces and develop into new graupel. In cooler cloud layers, delicate ice crystals collide with other crystals and break into tiny ice pellets that come into contact with supercooled droplets and freeze them. In both cases, numerous ice crystals merge to create snowflakes through aggregation. The snowflake melts while passing through the melting layer (0°C) before reaching the ground, transforming into raindrops (Ahrens and Henson, 2019b).
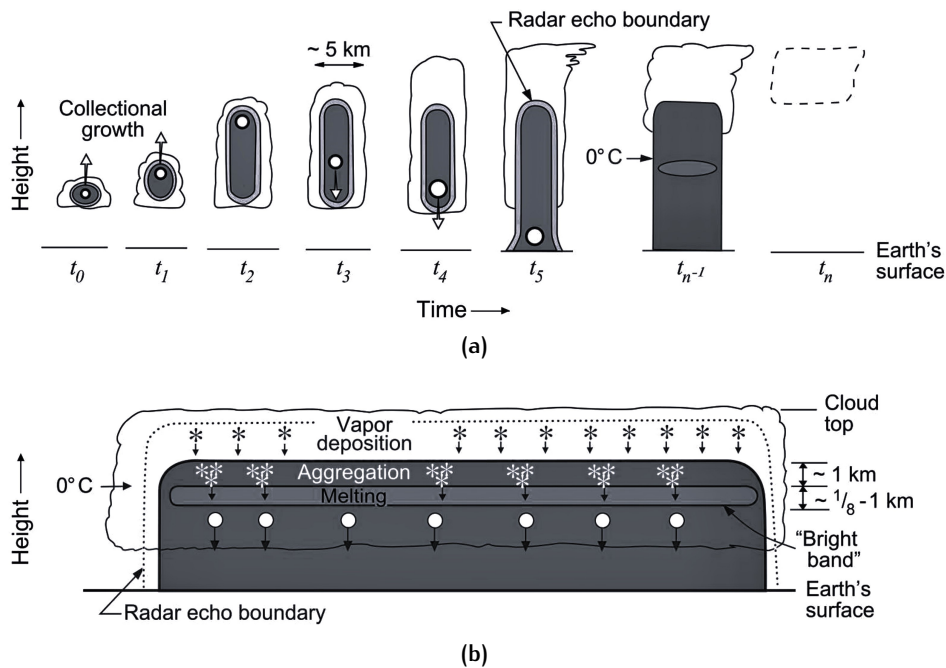
Figure 1.2: Diagrams of **(a)** collision-coalescence process of convective precipitation and **(b)** ice crystal process of stratiform precipitation.

— Houze Jr. (2014)

1.2 CATEGORIZATION OF PRECIPITATION

Precipitation is typically categorized into three types based on their formation mechanisms: frontal rain, convective rain, and orographic rain. Frontal rain occurs at the boundary of cold and warm air masses, where warm air is lifted up by cold air to form clouds and precipitation. This type of rain is typically steady, uniform, and of moderate intensity. Convective rain is when the ground heats up and and the humid air rises to form a convection cell that leads to altocumulus or thunderstorm clouds and precipitation. This type of rain usually covers relatively small areas and is relatively intense. La-

tent heat release due to condensation of water vapor amplifies the vertical updraft and the size of the convection cell. Orographic rainfall is when moist air is forced up by terrain obstacles such as mountains. Adiabatic cooling of the rising humid air leads to formation of clouds and precipitation. In nature, the multiple factors influencing precipitation are often interconnected, so that resulting rain is not always easily categorized into a single type. In all cases, the occurrence of vertical winds and the adiabatic cooling of rising moist air are essential for the formation of precipitation. In addition, atmospheric instability due to surface heating, enhanced atmospheric humidity and latent heat release of moist air generates convective rain.

1.2.1 Frontal rain

Frontal rain refers to the precipitation phenomenon caused when cold fronts, warm fronts or other fronts appear. A front is a cold front when cooler air passes by and replaces warmer air. Cold air retreats and is overlayed by warm air, forming a warm front (Ahrens and Henson, 2019a).

1.2.1.1 *Cold front*

Cold air shovels under the warm air like a snowplow, forcing the warm air to rise as if it were snow being plowed. The cold front causes rising of warm and moist air with subsequent generation of clouds and precipitation. Stratiform clouds (nimbostratus) become the predominant cloud type. Due to their slower movement, cold fronts often lead to extensive cloud coverage in the area behind them. The leading edge of a front is steep because friction slows the airflow near the ground. An active band of thunderstorms ahead of the front can produce heavy rain with gusty winds. Cooler air follows behind the front, and rainfall ends as pressure rises.

1.2.1.2 *Warm front*

Less dense warm air rises and overrides the denser cold air, creating clouds and precipitation ahead of the front. Over time, the clouds become thicker, going from altostratus to nimbostratus. The warm front separating the warm and cold air masses has a far gentler slope than a typical cold front. Weather changes near fronts are noticeable, yet much milder compared to cold fronts, exhibiting gradual transitions rather than abrupt shifts. Under stable weather conditions with relatively dry upper warm air, only mid-to-high clouds will develop, and no precipitation will take place. Heavy showers can occur when the warm air is both humid and unstable, often accompanied by thunderstorms within the clouds, some of which are elevated storms (Ahrens and Henson, 2019a).

1.2.2 Convective rain

The sun's radiant energy heats the Earth's surface. Water evaporates into water vapor. The shallow air near the ground is hotter and less dense than the surrounding air, while the cooler, denser air descends. This movement causes the warmer air mass to rise, forming a convection cell which is further amplified by latent heat release by condensation of water vapor. Convection cells can range from a few kilometers in vertical height (e.g., cumulus humilis clouds) to over a dozen kilometers (e.g., cumulonimbus capillatus). As the moist, warm air rises, it cools and condenses at higher altitudes, forming clouds composed of tiny water droplets and producing rain. Rainfall occurs through the collision-coalescence of droplets, as shown in Figure 1.2a. This type of rainfall is typically characterized by a relatively small aerial coverage and intermittent occurrence. Strong vertical convection motion leads to the formation of deep convection, which gives rise to towering cumulonimbus clouds capable of causing heavy rainfall and thunderstorms (Marshall and Schott, 1999).

1.2.3 Orographic rain

Moist air is blocked by mountains and forced to rise. Adiabatic cooling of the rising air mass leads to the formation of cloud and orographic rain. The intensity of orographic rain hinges on several factors, including the amount of lifted water vapor, the steepness and elevation of the mountain, and temperature difference with the ground. When water vapor condenses, latent heat is released, heating the air parcel and causing it to rise further. Thus, a moist air parcel can reach higher altitudes than a dry one. The major part of the precipitation takes place on the windward side, whereas the leeward side is dry, and lenticular clouds sometimes appear in the updraft area of the leeward wave. Although orographic rain can be a vital source of river flow, it can also pose issues such as mudslides and landslides (Guernsey, 1987).

1.3 VIRGA

Virga refers to rain, ice, or snow that transforms into water vapor before it reaches the ground. According to the American Meteorological Society's glossary of meteorology, virga is defined as "Wisps or streaks of water or ice particles falling out of a cloud but vaporizing before reaching the Earth's surface as precipitation." The shape of virga often appears hook-like, with streaks descending nearly vertically from the source of precipitation but transitioning to an almost horizontal orientation at their lower ends (AMS, 2015). Figure 1.3 shows an example of virga above Granada. This distinctive shape is a result of strong vertical wind shear, while the evaporation-induced shrinking of the

droplets also contributes to their reduced falling speed. This phenomenon can be attributed to the increase in temperature heating as the precipitation particles near the ground. In regions where the ice crystal process predominates, particularly in high latitudes, these crystals melt into rain droplets and then evaporate. In the case of snow virga, the snowflakes undergo direct sublimation (Beynon and Hocke, 2022; Jullien et al., 2020).

A wet downburst inside virga cloud may transition into a dry downburst below the cloud (Beynon and Hocke, 2022). The cooling effect from the evaporation of rain droplets or the melting of snowflakes generates downbursts (Srivastava, 1987), posing a risk to low-flying aircraft. Virga can also trigger droughts and inaccurate weather forecasts, and have a negative impact on agricultural irrigation.

1.4 AEROSOLS, CLOUDS, AND RAINFALL

The interrelationships between aerosols, clouds, and climate are pivotal in shaping weather and climate change. Aerosols influence cloud formation and affect the frequency and intensity of rain events. Conversely, rainfall has the capacity to remove aerosols from the atmosphere.

Aerosols from natural sources (e.g., Saharan dust, salt from ocean spray) or anthropogenic emission (e.g., motor vehicle exhaust) lead to the presence of a significant number of aerosol particles in the air. The aerosols act as condensation nuclei, increasing the condensation of water vapor and forming cloud droplets. The latent heat released by this process triggers the air to rise. More water droplets are transported upward, promoting the vertical growth of clouds. As the cloud height increases, it forms deep convection. The process of collision-coalescence of water droplets, which often originate high in clouds, increases the intensity of rain events (Rosenfeld, 2006).

Regions impacted by aerosol pollution can also experience decreased rainfall and even drought conditions. For shallow clouds with limited moisture content, an accumulation of condensation nuclei results in the formation of numerous tiny droplets that remain suspended in the air, delaying their transformation into raindrops (Rosenfeld et al., 2008). Additionally, aerosols create a stable layer in the atmosphere that hinders convection, thereby suppressing precipitation (Dave et al., 2017). Both, aerosols and clouds, have a strong influence on atmospheric radiative transfer and the vertical structure of the atmosphere (Zhu et al., 2023).

Precipitation aids in depositing aerosol particles to the ground due to the numerous condensation nuclei (aerosols) contained within raindrops (Cugerone et al., 2018). It is crucial to recognize that not all aerosols can be effectively removed. Wet removal efficiency depends largely on particle size (Ohata et

al., 2016). Certain tiny aerosol particles resist adsorption and persist in the atmosphere.

1.5 RAINFALL PRECURSORS

Rainfall precursors are the signs of weather, atmosphere, and meteorological phenomena (e.g. virga) that precede the onset of rain. For example, Table 1 shows the variations in weather factors before the frontal rain in the Northern Hemisphere. These precursors may exhibit regional and seasonal variations. The prediction of rainfall in the next 0-6 hours based on various observations is referred to as the precipitation nowcasting. It can issue timely weather warnings for severe rain events like thunderstorms, formulate emergency response strategies, and enhance public safety. Being able to provide precursors in the short period before rainfall will improve the accuracy of nowcasting and also play a vital role as model input. Accurate rainfall prediction necessitates the comprehensive consideration of multiple parameters (Wang and Hocke, 2022). The convection and transport of water vapor are closely related to rainfall. Before rain, moist air accumulates in the atmosphere and the Integrated Water Vapor (IWV) increases. Changes in meteorological parameters also show the instability of the atmosphere before rain. Moreover, ground-based microwave radiometers show potential in weather forecasting. Cimini et al. (2015) indicated that the Forecast Indexs (FIs) commonly used in operational meteorology derived from a commercial microwave radiometer correlate well with those calculated from radiosonde values. The continuous monitoring of the troposphere with a high temporal resolution by ground-based microwave radiometers is invaluable for nowcasting.

WEATHER FACTOR	COLD FRONT	WARM FRONT
Winds	South or southwest	South or southwest
Temperature	Falling	Slowly warming
Pressure	Falling steadily	Usually falling
Clouds	Increasing cirrostratus and cirrus	Cirrostratus, cirrus, altostratus, nimbostratus, stratus, and fog
Dew point	High	Steady rise

Table 1: Prior to frontal rain in the Northern Hemisphere (Ahrens and Henson, 2019a)

1.6 STUDY AREA

For this thesis, I analyzed ground-based observations from two regions: Bern and Granada. Granada was selected because my research stay at the University of Granada in 2022 provided access to instruments and data from the Andalusian Global ObseRvatory of the Atmosphere (AGORA).

Bern is situated at the center of the Swiss Plateau, with the Gurten and the Bantiger being its two closest mountains. Bern has a maritime climate with an annual mean precipitation of approximately 1059 mm (MeteoSwiss, 2014). Brandsma and Buishand (1997) suggests that the region is characterized by pre-frontal or post-frontal showers and thunderstorms during the summer months (from June to August), resulting in the highest total rainfall. Winter in Bern is characterized by primarily frontal rain influenced by uphill or leeward effects, resulting in a notably drier season.

Granada, situated in southern of Spain, is encompassed by the Sierra Nevada, Sierra de Huétor, and Sierra de Almijara mountain ranges. Granada has a Mediterranean climate characterized by hot and arid summers, while winters are mild and relatively humid. July registers as the hottest month, with an average maximum temperature of 34.2°C (AEMET, 2012). Rainfall predominantly takes place from October to May. Granada is affected by local and European anthropogenic pollution as well as North African Saharan dust, causing its complex precipitation (Wang et al., 2024).

(a)

(b)

Figure 1.3: Virga appears in the sky over **(a)** city of Granada and **(b)** the University of Granada urban station (UGR) on the afternoon of January 11, 2023.
https://twitter.com/GFAT_ugr/status/1613186058665201666?s=20

Part II

INSTRUMENTATION AND METHODOLOGY

This part introduces radiative transfer and the principles of ground-based microwave radiometry, outlines the datasets employed for the study of atmospheric water and precipitation including the basic meteorological parameters. The new retrieval of the rain rate from radiometer data is explained in detail. Data analysis methods such as machine learning and composite analysis are described.

2 | RADIATIVE TRANSFER AND MICROWAVE RADIOMETRY

Solar radiation is the primary energy source for the Earth, undergoing processes of atmospheric absorption, scattering, and transmission before reaching the Earth's surface. Part of it is absorbed by the surface and converted into heat energy, while the remaining part is reflected back to the atmosphere and space. Absorption of radiation energy at various wavelengths by gases, clouds, and particles in the atmosphere contributes to an increase in atmospheric temperature. Greenhouse gases (e.g. water vapor and carbon dioxide) redirect the heat energy radiated from the Earth back towards the surface, while a portion of the heat is released into space. The Earth maintains the radiation budget in the above-described way, and Figure 2.1 shows the radiative transfer process (Zhang, 2019).

The radiative transfer equation is essential to comprehending the transport and distribution of solar radiation in the atmosphere and on the Earth's surface. To fully grasp this equation (Section 2.1.3), it is necessary to first introduce blackbody radiation and its related laws in Section 2.1.1, as well as the interaction, emission, and scattering of microwave radiation across various frequency bands in the presence of atmospheric particles in Section 2.1.2. I focus on microwave radiation since most of the instruments in my thesis receive and/or transmit microwave radiation. A tropospheric microwave radiometer captures and analyzes microwave radiation signals from the atmosphere to characterize tropospheric parameters. I describe the principles of the radiometer measurement process (Section 2.2).

2.1 RADIATION PRINCIPLES

2.1.1 Blackbody radiation

Microwave radiometers are receivers designed for measuring thermally emitted electromagnetic radiation. To grasp the fundamental principle of microwave radiometers, it is essential to introduce the concept of of blackbody radiation. A blackbody is an idealized body that absorbs all incident radiation without any reflection or transmission, while it is also a complete emitter that is solely dependent on its temperature (Planck, 1914). When in thermal
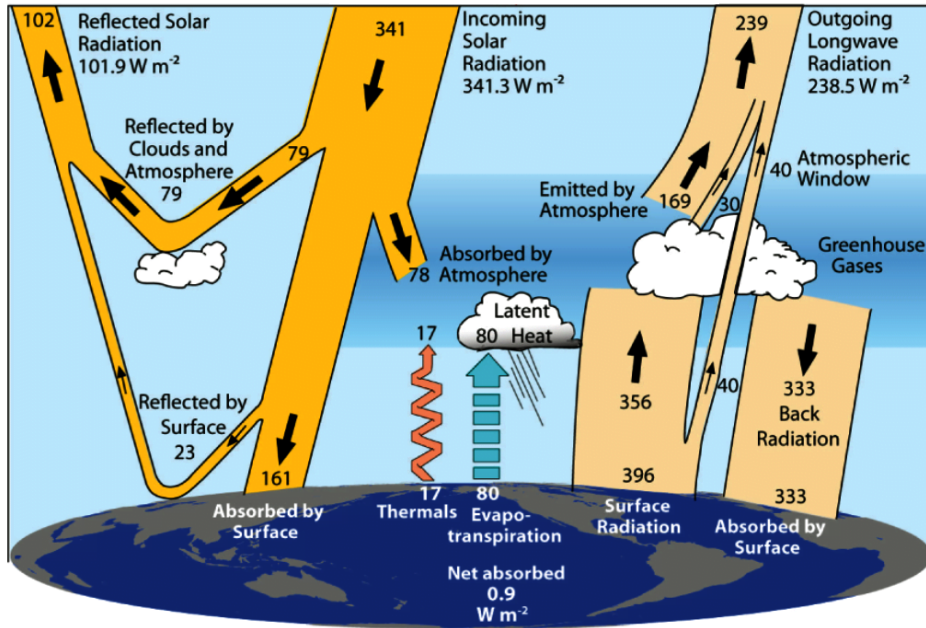
Figure 2.1: Schematic diagram of global annual average radiation budget from March 2000 to May 2004 (W m^{-2}). Arrows indicate energy flow.
— Trenberth et al. (2009)

equilibrium, meaning at a constant temperature, a blackbody has an emissivity of 1.

2.1.1.1 *Planck's law*

Planck's law describes the intensity of electromagnetic radiation emitted by a blackbody at temperature in thermal equilibrium, when the blackbody is in equilibrium with the radiation field (Planck, 1914). Planck's law has several forms depending on the correspondence between spectral variable such as wavelength λ, frequency ν, and wavenumber $\tilde{\nu}$. As a function of temperature and wavelength, the spectral radiance is

$$B_\lambda(T) = \frac{2hc^2}{\lambda^5} \frac{1}{e^{\frac{hc}{\lambda kT}} - 1} \tag{1}$$

where $c = 2.998 \times 10^8$ m s^{-1} is the speed of light. $h = 6.626 \times 10^{-34}$ J Hz^{-1} is the Planck constant, and $k = 1.381 \times 10^{-23}$ J K^{-1} is the Boltzmann constant. T is the absolute temperature of blackbody in Kelvin. B_λ is the energy radiated at unit wavelength λ intervals from unit area and unit solid angle.

Figure 2.2 shows the Planck curve for blackbodies at various temperatures. The higher the temperature of a blackbody is, the more radiation it emits at each frequency. When short wavelengths (i.e., $\nu = \frac{c}{\lambda} \to \infty$), Planck's law approaches Wien's approximation, while long wavelengths (i.e., $\nu \to 0$), Planck's law approaches Rayleigh–Jeans law.
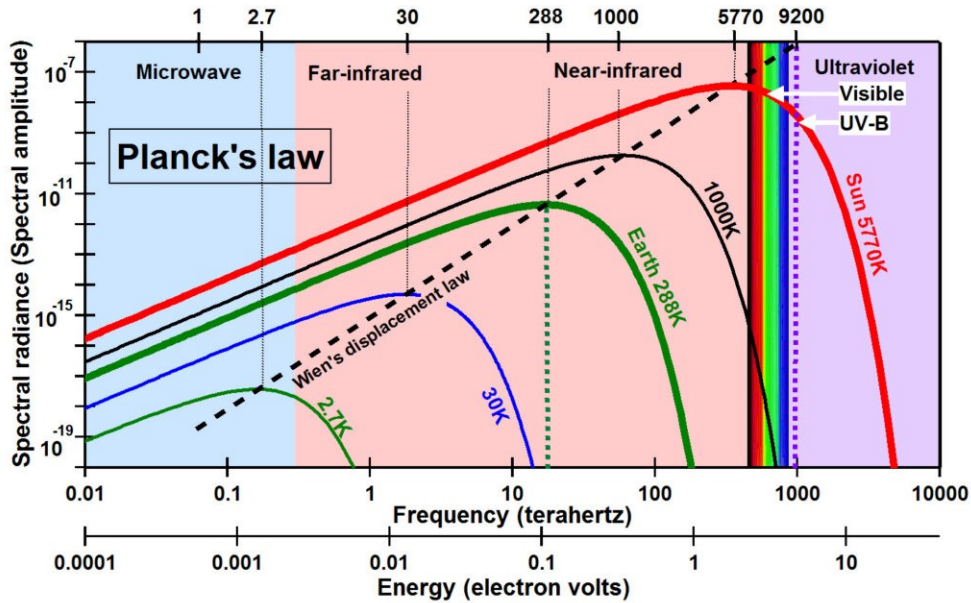
Figure 2.2: Spectral radiance of a blackbody as a function of frequency. The solid red and green lines represent the blackbody temperatures at 5770 K and 288 K for the spectral radiation of the Sun and Earth surface. The dashed line is the frequency of peak spectral radiation of a blackbody calculated by Wien's displacement law. Background colors indicate spectra in different frequency ranges.

— Peter L. Ward. All Rights Reserved

https://ozonedepletiontheory.info/ImagePages/plancks-law-frequency1/

2.1.1.2 *Wien's displacement law*

Wien's displacement law describes the peak wavelength or frequency in the radiation curve of a blackbody as a function of temperature (Wien, 1894). This displacement is directly connected to Planck's law and expresses the common observation in quantitative form that the peak wavelengths of spectral radiation shift towards higher values as the temperature decreases (Ma et al., 2009). The peak at wavelength λ_{peak} is given by

$$\lambda_{peak} = \frac{b}{T} \tag{2}$$

where T is the absolute temperature of blackbody in Kelvin. $b = 2.898 \times 10^{-3}$mK is the Wien's displacement constant.

As Figure 2.2 shows, the sun can be described as a remarkably effective blackbody, exhibiting a temperature of around 5770 K, which aligns with Wien's law and indicates the peak emission within the visible region of the spectrum. The Earth's surface can be roughly regarded as a blackbody at a temperature of 280 K, whereby the maximum spectral radiation occurs in the thermal infrared region of the spectrum.

2.1.1.3 *Stefan–Boltzmann law*

Stefan–Boltzmann law describes the total energy radiated by the surface of a blackbody as a function of its temperature (Boltzmann, 1884; Stefan, 1879), i.e. the blackbody radiant emittance or radiant flux $F(T)$. T is the absolute temperature of blackbody in Kelvin.

$$F(T) = \int_0^{\infty} B_\lambda(T) d\lambda = \sigma T^4 \tag{3}$$

where σ is the Stefan–Boltzmann constant and is derived from Planck constant h, Boltzmann constant k, and speed of light in the vacuum c.

$$\sigma = \frac{2\pi^5 k^4}{15c^2 h^3} \approx 5.67 \times 10^{-8} Wm^{-2}K^{-4} \tag{4}$$

The stefan-Boltzmann law quantifies the energy emitted by the Sun at a specific temperature, allowing for the determination of the Sun's temperature based on the energy received by the Earth per square meter. Additionally, this law predicts the amount of heat radiated by the Earth into space.

2.1.1.4 *Rayleigh–Jeans law*

Rayleigh-Jeans law is a large wavelength approximation of Planck's radiation law for the blackbody radiation. In the large wavelength limit for $\lambda \gg \frac{hc}{kT}$, the first-order expansion of Taylor polynomial is $e^{\frac{hc}{\lambda kT}} \approx 1 + \frac{hc}{\lambda kT}$. Rayleigh–Jeans law is given by

$$B_\lambda(T) = \frac{2ckT}{\lambda^4} \tag{5}$$

In the microwave range (0.3 GHz to 300 GHz frequency range), the large wavelength limit is fulfilled so that a linear relationship between radiance $B(T)$ and T according to equation 5 exists. Due to its ability to circumvent the complexities of Planck's law and simplify calculations, the Rayleigh-Jeans law finds widespread application in microwave radiometry.

2.1.1.5 *Brightness temperature*

Given the spectral radiance, the (Planck-equivalent) brightness temperature T_b of a blackbody emitting this radiation can be calculated. The expression of T_b is deduced from the Rayleigh–Jeans law

$$T_b = \frac{B_\lambda \lambda^4}{2ck} \tag{6}$$

2.1.2 Radiation and interactions

Radiation propagates through a medium, such as air, and undergoes interactions with particles, such as raindrops, which consist of various dielectric materials. Figure 2.3 illustrates the interactions. Absorption involves the transfer

of energy from the radiation to particles, while scattering alters the direction of the radiation beam without changing its energy or frequency. The combination of absorption and scattering are referred to as extinction. Further details regarding absorption and scattering are described in the following section. The radiation emitted by the particles is called emission and is given by Planck's and Kirchhoff's laws.
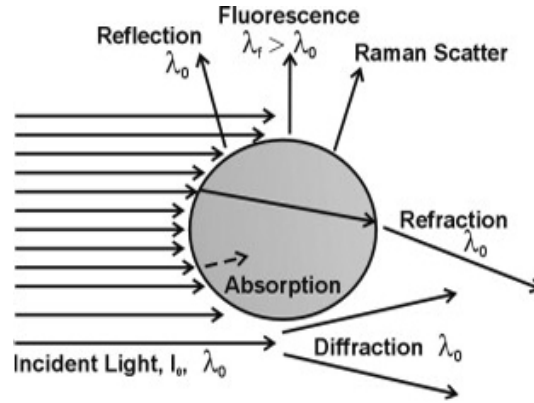

Figure 2.3: Diagram of potential optical interactions between radiation and particles. Scattering represents the effects of reflection, refraction, and diffraction for small particles, while fluorescence and Raman radiation are excluded from the discussion.

— Redmond et al. (2010)

2.1.2.1 Kirchhoff's law

Kirchhoff's law of thermal radiation states that in thermodynamic equilibrium, the emitted and absorbed radiation are equal at a given temperature and wavelength (Kirchhoff, 1978). The absorptivity is equal to the emissivity

$$\varepsilon_\lambda = \alpha_\lambda \tag{7}$$

where ε is the emissivity, and α is the absorptivity. λ is the wavelength. This formula represents the general form of Kirchhoff's law, applicable not only within a medium but also at interfaces between different media. Violation of this law results in deviations from local thermal equilibrium, leading to the medium becoming either colder or warmer.

In remote sensing radiation observation, based on the Local Thermodynamic Equilibrium (LTE), the radiation emission of the actual body can be expressed as

$$B_\lambda(T_b) = \varepsilon_\lambda \cdot B_\lambda(T) \tag{8}$$

where $B_\lambda(T_b)$ represents the radiance emitted by a body with a temperature of T_b, and $B_\lambda(T)$ represents the radiance of a blackbody with the same temperature T of the body.

2.1.2.2 *Atmospheric absorption*

As radiation passes through the atmosphere, it undergoes absorption by atmospheric particles, resulting in energy attenuation. The degree of attenuation is influenced by the internal structure and shape of the particles. Water vapor (H_2O) and Oxygen (O_2) in the atmosphere strongly absorb microwave radiation, while the contributions of other gases to gas absorption lines are negligible due to their low concentrations or a lack of microwave absorption lines (e.g. nitrogen) (Grody, 1976).

Microwave radiation is absorbed differently by various compositions of the atmosphere such as water vapor, oxygen, clouds, and precipitation. Specific frequencies correspond to significant absorption peaks for certain compositions, allowing for effective detection of these parameters when these frequencies are selected. Figure 2.4 shows the variation of atmospheric transmittance with frequency in the microwave band. It can be seen that the water vapor absorption line causes obvious atmospheric attenuation at 22.235 GHz, which can be used to detect the water vapor content in the atmosphere. H_2O exhibits a weak pressure-induced broadening absorption line at 22.235 GHz and a strong absorption line at 183 GHz (Cimini et al., 2009; Kummerow, 2020). The 31.4 GHz frequency has a low total atmospheric absorption (absorption by water vapor and oxygen), a relatively clean atmospheric window, corresponding to the window between the resonant water vapor lines. The absorption at 31.4 GHz is mainly due to liquid water. The absorption lines enable the calculation of the absorption and emission coefficients of these gases at specific frequencies. The oxygen molecule has a magnetic dipole moment resulting from the collective spin of its two unpaired electrons in the electronic ground state. The variation in electron spin orientation with respect to molecular rotation gives rise to a prominent magnetic dipole transition band at 60 GHz and a single transition at 118.75 GHz (Li, 2019). Collisions between Nitrogen (N_2) molecules contribute to enhanced atmospheric absorption. In the stratosphere, Ozone (O_3) absorption plays a significant role in atmospheric attenuation (Klein and Gasiewski, 2000; Zhang, 2019).

The chemical and physical properties of liquid water are very complex and are greatly affected by hydrogen bonds (Han et al., 2023). Microwaves are electromagnetic waves with frequencies ranging from 300 MHz to 300 GHz. When microwaves pass through water droplets, the electric dipole moments of water molecules inside a droplet are redirected to rotate along the direction of the electric field, and microwave radiation is absorbed. As a result, water molecules absorb microwaves more significantly while overcoming the effects of hydrogen bonds, leading to high dielectric loss in the microwave frequency band. According to Kirchhoff's theory, raindrops exhibit strong microwave radiation, which is introduced in detail in Section 3.2.1.2.
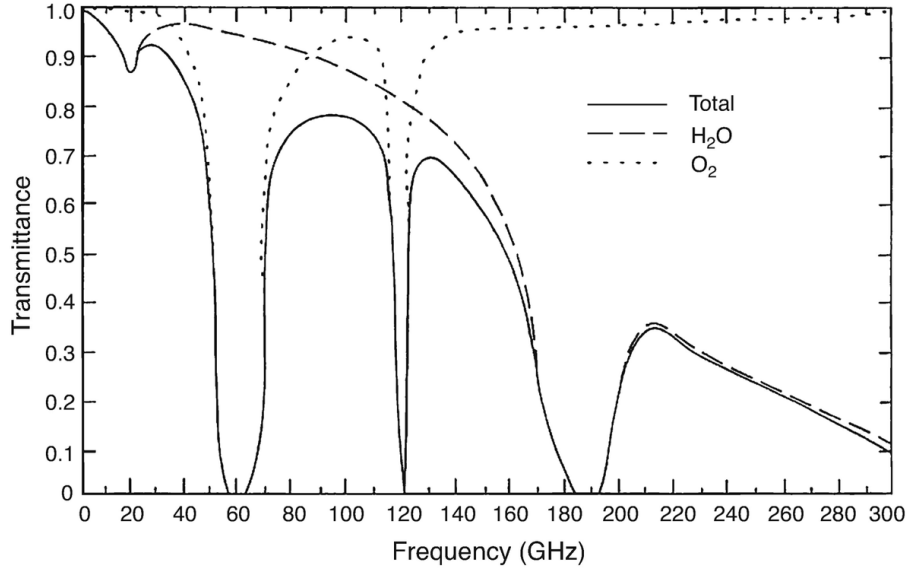
Figure 2.4: Vertical atmospheric transmittance (total, H2O and O2) of standard atmosphere as a function of frequency.

— Kummerow (2020)

2.1.2.3 *Scattering*

In clear skies, microwave radiative transmission is primarily affected by the absorption and emission of atmospheric gases. However, when hydrometeors (e.g., cloud and rain droplets) are present, they interact with radiation through scattering. Typically, particles in the atmosphere can be considered incoherent and the contribution of a single particle can be extrapolated to multiple particles. For atmospheric ice crystals and water droplets, they are assumed to be spherical in shape (Zhang, 2019). The significance of particle scattering depends on the specific scattering regimes involved, as shown in Figure 2.5. The scattering characteristics of particles are determined by the dimensionless size parameter χ, representing the ratio of the particle perimeter to the radiation wavelength (Muinonen et al., 2011).

$$\chi = \frac{2\pi r}{\lambda} \tag{9}$$

where r is the particle radius. As shown in Figure 2.5, when particle sizes are much smaller than the wavelength ($2\pi r \ll \lambda$), the scattering by particles is small compared to the absorption, and the multiple-scattering plays a minor role. Particles smaller than the radiation wavelength undergo Rayleigh scattering ($\chi < 1$) (Moosmüller and Arnott, 2009). For particle sizes comparable to the radiation wavelength ($\chi \geqslant 1$), the Mie theory is utilized. When particle size becomes significantly larger ($\chi \gg 1$) compared to the wavelength, the light can be described by rays, and geometric optics can be applied to compute the scattering (Leuenberger, 2009).

2.1.2.4 *Absorption and scattering by clouds and precipitation*

Essentially, the interaction between microwaves and cloud and rain particles is completely different from the interaction with other gases like oxygen and water vapor. Hydrometeors both absorb and scatter microwaves, and this absorption and scattering is related to the physical parameters of the particles, such as size, shape, and dielectric constant. When the raindrop sizes are much larger than the wavelength, the interaction between the particle and the electromagnetic wave is mainly scattering, otherwise it is mainly absorption.

For the microwave frequency band (1-300 GHz, 1 mm-1 cm), Figure 2.5 shows that scattering behavior varies depending on the size and composition of particles present in the atmosphere. Air molecules (below 1 nm), fog (below 10 µm), and haze (2.5 µm) exhibit negligible scattering. Cloud droplets (5-50 µm), ice crystals (10-100 µm), and light raindrops (about 100 µm) undergo Rayleigh scattering. Raindrops (0.1-3 mm) can exhibit either Rayleigh scattering or Mie scattering, depending on the frequency. Hailstones (about 1 cm) follow Mie scattering principles (Zhang, 2019).
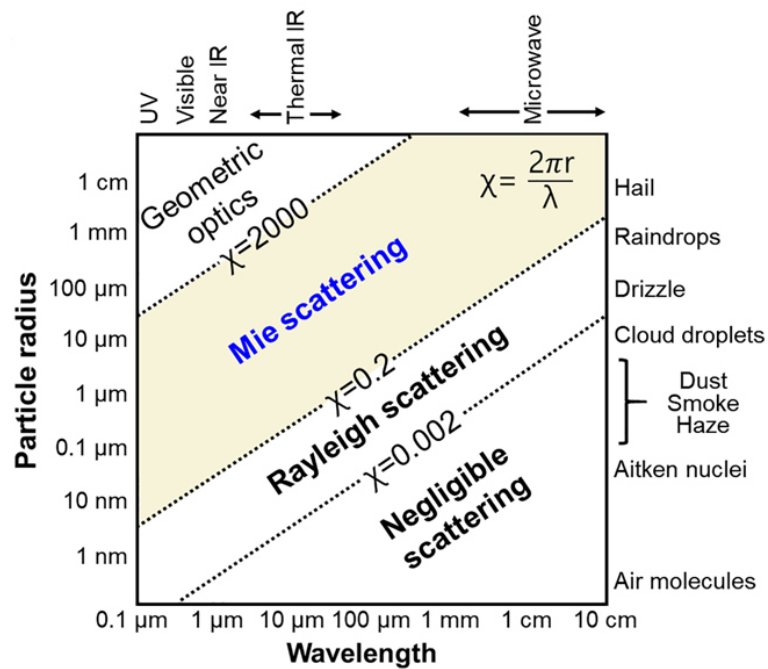

Figure 2.5: Scattering regimes and size parameter χ as a function of radiation wavelength and atmospheric particles radius. The dashed line is the transition value of the scattering regimes.

— Cho et al. (2021)

Cross section and Mie theory

Absorption and scattering cross sections (σ_{abs} and σ_{sca}) represent the pro-

portion of energy that is absorbed and scattered after an incident electromagnetic wave interacts with a particle.

$$\sigma_{abs} = \frac{W_{abs}}{I_i} \tag{10}$$

$$\sigma_{sca} = \frac{W_{sca}}{I_i} \tag{11}$$

and the extinction cross section is defined as

$$\sigma_{ext} = \sigma_{abs} + \sigma_{sca} \tag{12}$$

where W_{abs} and W_{sca} are the absorbed and scattered power. I_i is the incident irradiance.

The Mie extinction and scattering efficiencies (Q_{ext} and Q_{sca}) can be written as

$$Q_{ext} = \frac{\sigma_{ext}}{\sigma_{geom}} = \frac{2}{\chi^2} \sum_{n=1}^{\infty} (2n + 1)\Re(a_n + b_n) \tag{13}$$

$$Q_{sca} = \frac{\sigma_{sca}}{\sigma_{geom}} = \frac{2}{\chi^2} \sum_{n=1}^{\infty} (2n + 1)(|a_n|^2 + |b_n|^2) \tag{14}$$

and

$$Q_{abs} = Q_{ext} - Q_{sca} \tag{15}$$

where $\sigma_{geom} = \pi r^2$ is the geometrical cross section of an imaginary sphere particle with radius r. χ is the size parameter. a_n and b_n are Mie coefficients, which are calculated by the spherical Bessel function (Bohren and Huffman, 1998). $\Re$ represents the real part.

Rayleigh scattering

Rayleigh scattering occurs when particles are much smaller than the wavelength of the incident electromagnetic wave (Bohren and Huffman, 1998; Rayleigh, 1871). The Rayleigh absorption and scattering efficiencies (Q_{abs} and Q_{sca}) are given by

$$Q_{abs} = -4\chi \Im\left(\frac{m^2 - 1}{m^2 + 2}\right) \propto \frac{1}{\lambda} \tag{16}$$

$$Q_{sca} = \frac{8}{3}\chi^4 \left|\frac{m^2 - 1}{m^2 + 2}\right|^2 \propto \frac{1}{\lambda^4} \tag{17}$$

and

$$Q_{ext} = Q_{abs} + Q_{sca} \tag{18}$$

where m is the complex refractive index. $\Im$ represents the imaginary part.

Ice scatters microwave radiation but does not absorb it. The extent of absorption and scattering in ice and water depends on their size relative to the microwave frequency. At 22-31 GHz, the scattering effect of ice is negligible, making ice almost transparent to microwave radiation. This characteristic is useful for estimating rain rates (Li, 2019).

2.1.3 Radiative transfer

2.1.3.1 *Optical depth and formal radiative transfer equation*

In radiation transmission, the total attenuation caused by medium absorption and scattering per unit cross-sectional area is called *optical depth*, which is a dimensionless quantity (Mätzler and Melsheime, 2006). The optical depth τ at frequency ν along the path between two points s_0 and s_1 is defined by

$$\tau_\nu := \int_{s_0}^{s_1} \kappa_\nu \rho \, ds \tag{19}$$

which can also be written as $d\tau_\nu = -\kappa_\nu \rho \, ds$. κ_ν is the opacity or absorption coefficient, and ρ is the mass density.

The radiation intensity I increases by dI as it propagates through a thickness of ds. The formal radiative transfer equation considering only absorbing (and non-emitting) media is

$$\frac{dI_\nu}{\kappa_\nu \rho \, ds} = -I_\nu \tag{20}$$

Given the incident radiation at position s_0, denoted as I_{ν,s_0}, then the radiation intensity at position s_1 can be determined by integrating the Equation 20, where $s_0 < s_1$.

$$I_{\nu,s_1} = I_{\nu,s_0} \cdot e^{-\tau_\nu} \tag{21}$$

Radiation enhancement is caused by medium emitting and multiple scattering into the observation direction. The source function J is added to Equation 20 to characterize it and replace $-d\tau_\nu$ with $\kappa_\nu \rho \, ds$. The complete *formal radiative transfer equation* is

$$-\frac{dI_\nu}{d\tau_\nu} = -I_\nu + J_\nu \tag{22}$$

Multiplying both sides of Equation 22 by $e^{-\tau}$ and integrating it from $\tau_\nu = 0$ to τ_ν gives

$$I_{\nu,\tau_\nu} = I_{\nu,0} \cdot e^{-\tau_\nu} + \int_0^{\tau_\nu} J_{\nu,\tau} \cdot e^{-\tau} d\tau \tag{23}$$

In the Rayleigh–Jeans approximation, the radiance I_ν replaced by the brightness temperature T_b, and Equation 23 becomes

$$T_{b,\tau_\nu} = T_{b,0} \cdot e^{-\tau_\nu} + \int_0^{\tau_\nu} T_\tau \cdot e^{-\tau} d\tau \tag{24}$$

where $T_{b,0}$ is the input. If the temperature T_τ of the emitting medium layer is constant, the expression for T_{b,τ_ν} after integration is

$$T_{b,\tau_\nu} = T_{b,0} \cdot e^{-\tau_\nu} + T_m \cdot (1 - e^{-\tau_\nu}) \tag{25}$$

where T_m is the temperature of homogeneous layer, called effective mean temperature.

2.1.3.2 *Effective mean temperature*

Equation 25 is very practical even though usually the temperature of the layer is not constant. The effective mean temperature can be calculated such that Equation 25 is valid (Dicke et al., 1946; Mätzler and Melsheime, 2006).

$$T_m = \frac{\int_0^{\tau_\nu} T_\tau \cdot e^{-\tau} d\tau}{1 - e^{-\tau_\nu}} \tag{26}$$

where a frequent assumption is that T_τ follows a temperature profile linear distribution with increasing or decreasing optical depth τ.

$$T_\tau = T_c + T_d \tau \tag{27}$$

where T_c is the cosmic-microwave background brightness temperature (approximately to 2.73 K). T_d is the temperature gradient. Equation 27 is inserted into Equation 26 to get

$$T_m = T_c + T_d \left[1 - \frac{\tau_\nu \cdot e^{-\tau_\nu}}{1 - e^{-\tau_\nu}} \right] \tag{28}$$

For the solution of T_m, there are two cases: $T_m \to T_c + 0.5 T_d \tau_\nu$ for an optically thin layer ($\tau_\nu \ll 1$), and $T_m(\tau = 1) \to T_c + T_d$ for an optically thick layer ($\tau_\nu \gg 1$).

2.2 GROUND-BASED MICROWAVE RADIOMETER

Ground-based microwave radiometers are passive microwave remote sensing instruments used for measuring the power of the thermal noise emitted by bodies at a physical temperature greater than 0 K (Emery and Camps, 2017). They have become popular across various fields due to their highly sensitive receivers that can operate in all weather conditions, day and night (Hocke et al., 2017). Radiometers require low maintenance and are often equipped with multiple channels. Passive microwave remote sensing is widely recognized as the most precise method for continuous measurements of integrated water vapor, integrated liquid water, and temperature profiles in the troposphere over land. This capability plays a vital role in the evaluation and near real time data supply for future high-resolution Numerical Weather Prediction (NWP) models.

Microwave radiometers receive radiation and expresses it as the brightness temperature. In the microwave range, several atmospheric gases display absorption signatures as shown in Figure 2.4. At the 183 GHz water vapor line or oxygen absorption bands, where the atmospheric optical depth is large, the detected radiation originates from the vicinity of the radiometer. In case of weaker lines which are optically thin, the radiometer captures radiation from more distant regions. For example, the weak 22 GHz H_2O line can be used for measuring water vapor in the stratosphere and mesosphere using a ground-based microwave radiometer (Deuber et al., 2004).

2.2.1 Calibration techniques

A microwave radiometer measures the output voltage to determine the brightness temperature (Wu et al., 2010). Calibration establishes an equation between the radiometer output voltage and the antenna or sky temperature. This process involves observing the output voltage from hot and cold targets with known brightness temperatures (Tien et al., 2007). The common calibration methods include liquid nitrogen calibration and tipping curve calibration, which I performed for the two radiometers at the University of Bern. Regular calibrations of the radiometers are required in order to obtain accurate and reliable observations.

2.2.1.1 *Liquid Nitrogen (LN2) calibration*

The nonlinear expression of radiometer detector voltage V and spectral radiation B_ν is:

$$V = G \cdot B_\nu^\alpha \tag{29}$$

where G is the system gain, and α the non-linearity parameter. The spectral radiance B_ν of the calibration load is obtained directly from the known

temperature according to Planck's law (Equation 1). The total system noise temperature T_{sys} is the sum of receiver noise temperature T_R and antenna temperature T_A (Maschwitz et al., 2013).

$$T_{sys} = T_R + T_A \tag{30}$$

Figure 2.6a shows the external liquid nitrogen calibration technique, which can determine the unknown variables G, T_{sys}, and α (Küchler et al., 2016). The noise temperature T_{noise} is injected/added separately by noise diode at the hot temperature T_{hot} of the internal ambient target and the cold temperature T_{cold} of the LN2 cryogenic load, so that four equations are established to solve the above four unknowns (G, T_{sys}, α, and T_n).
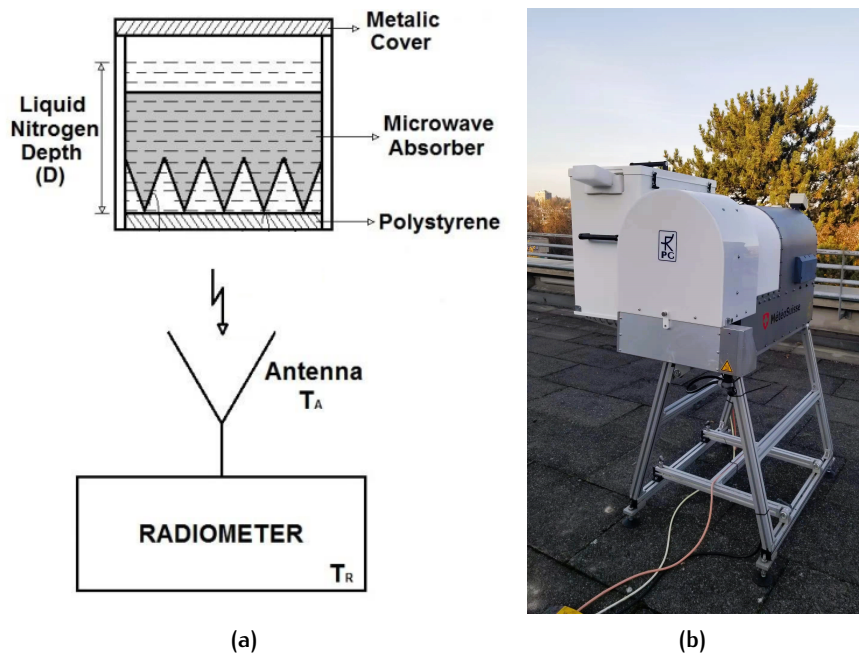
Figure 2.6: **(a)** External liquid nitrogen cold load for the radiometer. The conical blackbody is immersed within a non-absorbing polystyrene container. **(b)** Liquid nitrogen calibration for Humidity And Temperature PROfilers (HATPRO).

— Miacci et al. (2015)

2.2.1.2 *Tipping curve calibration*

The radiometer comprises two calibration reference targets: a hot target and a cold target with known temperatures T_{hot} and T_{cold}, respectively. The antenna brightness temperature has a linear relationship with the radiometer output voltage (Han and Westwater, 2000; Tien et al., 2007), which can be written as

$$T_{sky} = \frac{V_{sky} - V_{hot}}{V_{hot} - V_{cold}} (T_{hot} - T_{cold}) + T_{hot} \tag{31}$$

where V_{sky}, V_{hot}, and V_{cold} are radiometer detector voltages detected from the radiation sources of the sky, hot target, and cold target, respectively. T_{sky} is the sky brightness temperature.

The tipping curve calibration uses sky measurements taken at various elevation angles to determine the optical depth of the horizontally stratified atmosphere (Wu et al., 2010). Zenith optical depth over zenith angle θ is derived from Equation 25:

$$\tau_{v,zen}(\theta) = -\mu \cdot \ln\left(\frac{T_m - T_{sky}(\theta)}{T_m - T_c}\right) \tag{32}$$

where μ is the cosine of θ. T_m is the effective mean temperature (Equation 26). The zenith optical depth $\tau_{v,zen}$ can be determined as the slope of a linear function, represented by the equation $y = \tau_{v,zen} \cdot x$, where $x = 1/\mu = 1/\cos\theta$ and $y = -\ln\left((T_m - T_{sky}(\theta))/(T_m - T_c)\right)$. By performing a linear regression analysis on the observation point pairs from various directions of the radiometer, $\tau_{v,zen}$ can be solved.

2.2.2 Tropospheric radiometers

TROpospheric WAter RAdiometer (TROWARA) and HATPRO are ground-based passive microwave radiometers used for measuring atmospheric water in the troposphere. TROWARA, developed and operated by the Institute of Applied Physics (IAP) at the University of Bern, has been in operation since November 1994 in Bern, Switzerland. Numerous studies have compared it with GPS, field instruments, and reanalysis data, consistently demonstrating its superior ability to retrieve atmospheric water, particularly IWV (Cossu et al., 2015; Hocke et al., 2011; Wang et al., 2021). The HATPRO, a commercial radiometer manufactured by Radiometer Physics GmbH (RPG), finds wide application in weather monitoring and forecasting networks globally (Rose et al., 2005).

2.2.2.1 *TROpospheric WAter RAdiometer (TROWARA)*

The TROWARA radiometer operates with a time resolution of 7 seconds and measures brightness temperatures at three microwave frequency channels. Two channels are at frequencies of 21.385 GHz (bandwidth=100 MHz) and 31.5 GHz (bandwidth=200 MHz), while the third channel, added in November 2007, operates at 22.235 GHz (bandwidth=400 MHz). The antenna beams of TROWARA have a half-power beam width of 4° for all frequencies. TROWARA conducts sky observations with an elevation angle of 40°. Additionally, TROWARA includes an infrared channel at 9.5–11.5 μm.

In November 2002, TROWARA was relocated from an outdoor setting to an indoor laboratory with a controlled temperature (Morland, 2002). The antenna captures atmospheric radiation through a microwave-transparent window, while the overhang design of the wall effectively prevents rainwater from

entering. The windows get wet only in the rare case of strong southeasterly winds of rainy season. Operating indoors, TROWARA has successfully avoided measurement contamination caused by wet antennas, allowing accurate measurements even in rainy weather (Wang et al., 2023). Peter and Kämpfer (1992) provides a description of the original design and construction of TROWARA. In 2004, the cooled cold load was replaced with the Active Cold Load (ACL), featuring two ferrite switches each frequency to alternate between the antenna, ACL, and the matching waveguide termination serving as the hot load (Morland, 2007). TROWARA conducts manual tipping curve calibration using the clear sky brightness temperature at various antenna elevation angles ranging from 20° to 45° as the cold load. The brightness temperature measurements of TROWARA are stable, requiring only a manual tipping curve calibration every six months. Optionally, larger elevation angles up to the zenith angle can be reached by means of a mirror outside of the laboratory. The developed radiometer model accurately estimates the antenna temperature by measuring the reflection and transmission coefficients of all radiometer components, and enables automatic internal calibration at 7 seconds (Hocke et al., 2019; Morland, 2002; Wang et al., 2023).

2.2.2.2 *Humidity And Temperature PROfilers (HATPRO)*

The HATPRO Generation 2 (G2) is a ground-based dual polarization radiometer that offers a remarkable time resolution of 1-2 seconds. The radiometer is equipped with seven microwave channels in the water vapor band (K-band) spanning from 22.24 to 31.4 GHz, allowing for measurements of atmospheric water vapor and cloud liquid water content in the troposphere. For this band, the user can select the bandwidth, ranging from 0.1 to 2 GHz, and the half-power beamwidth of the antenna beam is 3.5°. The other seven channels are in the oxygen band (V-band), ranging from 51 to 58 GHz, designed to characterize atmospheric temperature. The HATPRO is equipped with an GPS system and a weather sensor that accurately measures weather parameters including surface temperature, pressure, and relative humidity. This thesis utilizes two HATPRO instruments: one conducting sky observations in Bern at a 40° elevation angle, and another performing zenith and profile observations in Granada, Spain. The HATPRO in Granada has an additional infrared radiometer. Rose et al. (2005) described the HATPRO instrument in detail.

The HATPRO operates in outdoor conditions, with its receiver functioning within a temperature range of -30°C to 40°C. The HATPRO antenna receives atmospheric radiation through a microwave radome, which is designed with hydrophobic material and radial blowers to prevent or minimize water film during and after rainfall. The HATPRO incorporates a rain sensor to detect rain, and the speed of the blowers is automatically controlled based on software-defined humidity thresholds (RPG, 2014; Wang et al., 2023).

The absolute calibration of the HATPRO uses a liquid nitrogen cooled load

attached to the outside of the radiometer box, as shown in Figure 2.6b. The ambient load is a pyramidal absorber material made of carbon loaded foam with very low thermal capacity, serving as the hot load (Rose et al., 2005). A built-in noise diode in each receiver of the HATPRO replaces the liquid nitrogen cold load, enabling automatic internal calibration. HATPRO G2 offers the option of tipping curve calibration for high transparency channels.

3 | DATA AND METHODOLOGY

Obtaining accurate precipitation information is challenging due to the inherent limitations of precipitation monitoring technologies. Rain gauges are sparsely distributed and susceptible to environmental influences such as wind (Marzano et al., 2010, 2006); weather radars are costly and prone to measurement errors due to instrument calibration, ground clutter, and beam blocking (Villarini and Krajewski, 2010); satellite microwave radiation measurements have low spatial and temporal resolution and uncertainty about land precipitation (Marzano et al., 2002). Ground-based microwave radiometers can operate effectively in rainy conditions and detect rain signals against a cold, homogeneous sky background (Wang et al., 2021). They can complement rain gauges and radars in monitoring rainfall and provide tools to validate spaceborne radiometer rainfall estimates. An effective way to improve the accuracy of rainfall quantification is to integrate all these data sources (radiometers, rain gauges, and radars) into a synergistic scheme for high temporal resolution precipitation monitoring (Marzano et al., 2006).

This thesis draws on long-term datasets from two sites, each of which employs a variety of ground-based remote sensing and in situ techniques to measure tropospheric water vapor, clouds, precipitation, and aerosols. One site operates various meteorological instruments on the roof of the Exakte Wissenschaften (ExWi) building at the University of Bern, where I focus on the two tropospheric microwave radiometers TROWARA and HATPRO, a Micro Rain Radar (MRR), and a weather station. The other site is the AGORA observatory in Granada, equipped with a ground-based microwave radiometer HATPRO, a ceilometer, a cloud radar, a nephelometer, and a weather station, as shown in Figure 1.3b. The latest Atmospheric Reanalysis ERA5 data from the European Center for Medium-Range Weather Forecasts (ECMWF) was also used to compare radiometer-estimated rain rates. ERA5 assimilates rain rate information from surface radar observations and rain gauges into climate or weather models to reconstruct the most accurate estimate of precipitation (Hersbach et al., 2018). Section 3.1 provides a detailed description of the instrument measurements.

For the methodology, TROWARA and HATPRO use physical and quadratic regression methods to retrieve IWV and Integrated Liquid Water (ILW), respectively. I developed and applied an optical depth-based physical method and two machine learning methods, including Random Forest (RF) and Gradient Boosted Decision Tree (GBDT), to retrieve the rain rate from microwave

radiometer measurements. I also employed GBDT to detect rainfall from rain-contaminated microwave radiometer data and investigate the source of the brightness temperature deviation between TROWARA and HATPRO. The Superposed Epoch Analysis (SEA) method is used to study the evolution of atmospheric parameters during rain events. Section 3.2 explains the retrieval and data analysis methods involved. Special attention is given to the new retrievals of the rain rate from radiometer data.

3.1 DATASETS

3.1.1 Remote sensing datasets

3.1.1.1 *Microwave radiometers*

The technical specifications of TROWARA and HATPRO were presented in the previous chapter Section 2.2. The two tropospheric microwave radiometers provide information on water vapor, liquid water, and rainfall. TROWARA utilizes an optical depth-based physical retrieval algorithm to accurately estimate IWV, ILW, and high-quality rain rates (Mätzler and Morland, 2009). During the thesis, I further refined and validated the rain rate retrieval for the TROWARA radiometer by using data from the years 2005 to 2019 (Wang et al., 2021). HATPRO G2 employs the quadratic regression algorithm in its manufacturer-provided software to retrieve IWV and ILW. I applied the rain rate retrieval developed for TROWARA to the HATPRO data set.

3.1.1.2 *Ceilometer*

The Jenoptik CHM15k ceilometer in Granada, which is part of the E-PROFILE project (European networks of wind and aerosols profiles, `https://e-prof ile.eu/`), provides information on vertical distribution and concentration of aerosol, cloud layers, and rainfall (Alexander and Protat, 2018; Ceccaldi et al., 2013; Guyot et al., 2022). The ceilometer measures atmospheric backscatter profiles with a time resolution of 15 seconds. It operates a Nd:YAG narrow-beam microchip laser at 1064 nm, with a pulse energy of 8.4 μJ and a pulse repetition rate of 5-7 kHz. The field of view receiver is 0.45 mrad, and the laser beam divergence is less than 0.3 mrad. The ceilometer has an altitude range of 15-15000 m and a vertical resolution of 15 m. Full optical overlap occurs at 1500 m above the ceilometer, and the manufacturer's overlap function allows for achieving 90% overlap between 555 and 885 m above ground level. The calculation of the Range Corrected Signal (RCS) for the CHM15k is described by Cazorla et al. (2017).

3.1.1.3 *Cloud radar*

The 94 GHz Doppler cloud radar in Granada, manufactured by RPG, measures vertical reflectivity profiles with a time resolution of 3-4 seconds. The target classification for this instrument data is available on the ACTRIS-Cloudnet website (Hogan and O'Connor, 2004; Illingworth et al., 2007, `https://cloudn et.fmi.fi/`). The cloud radar operates at a wavelength of 3.19 mm which enables the measurement of aerosols, cloud droplets and raindrops with high sensitivity. It is zenith-pointing, covering an altitude range of 50-12000 m with a vertical resolution of 30 m. The radar system incorporates precise absolute calibration and a reliable rain protection mechanism. Reliable operation and low maintenance are achieved using a low transmit power of 1.5 W (Myagkov and Rose, 2016).

3.1.1.4 *Micro rain radar*

The MRR, manufactured by Meteorologische Messtechnik GmbH (METEK) (METEK, 2009), has been located 2 m from TROWARA since March 2007. This compact Frequency Modulated Continuous Wave (FMCW) Doppler radar operates at 24.23 GHz and captures data with a 10-second time resolution. The MRR measures the Doppler frequency shift between the transmitted and received signals, which relates to the falling velocity of the hydrometeors, allowing their diameter to be inferred. It has a vertical measurement range of 100 to 3,100 m with a resolution of 100 m, a 3 dB beamwidth of 1.5°, and a modulation bandwidth range of 0.5 to 15 MHz. Garcia-Benadi et al. (2020) developed a model that processes the spectral raw data of the MRR to classify precipitation types into five categories: snow, drizzle, rain, hail, and mixed. The mixed types include wet snow, a mixture of dry snow and rain, or graupel. The classification utilizes a decision tree that considers the empirical relationship between hydrometeor fall velocity and equivalent radar reflectivity, as well as the size and particle properties of various hydrometeors, along with the presence or absence of bright bands. The model also calculated the rain rate (R_{MRR}) by integrating the droplet diameter.

$$R_{MRR} = \frac{\pi}{6} \int_0^\infty N(D)D^3 v(D) dD \tag{33}$$

where $N(D)$ represents the drop size distribution corrected for attenuation for a raindrop of diameter D, indicating the number of drops per unit volume per diameter. $v(D)$ represents the corrected terminal falling velocity. Beynon (2022) compared rainfall recorded by the MRR with that from the ExWi rain gauge and found the MRR operated reliably from 2008 to 2010.

3.1.2 In situ datasets

3.1.2.1 *Nephelometer*

The TSI Model 3563 integrating nephelometer in Granada provides information about aerosols by measuring the light scattering coefficient and Ångström exponent (AE) of aerosol particles at wavelengths of 450, 550, and 700 nm under dry conditions with a time resolution of 1 minute (Titos et al., 2012). The wide-angle integral of the nephelometer covers an angular range of 7 to 170°, while the backscatter measurement focuses on the range of 90 to 170°. The instrument undergoes regular routine maintenance and calibration, involving the use of CO_2 and filtered air. Non-idealities caused by truncation errors and non-Lambertian lighting were corrected (Anderson and Ogren, 1998), and the scattering coefficient has an uncertainty of approximately 7% (Heintzenberg et al., 2006). Further details on data preprocessing and processing can be found in the work by Pandolfi et al. (2018).

Scattering coefficients reflect the concentration of aerosol mass or volume, while AE estimates the average size of primary aerosols in dry conditions. AE>2 suggests the dominance of fine particles, while AE<1 indicates the dominance of coarse particles.

3.1.2.2 *Weather stations*

The ExWi automatic weather station in Bern, located near the TROWARA on the ExWi building, records surface air temperature, pressure, relative humidity, and precipitation monitored by a Vaisala Weather Transmitter WXT520. In this station wind speed was measured by a Vaisala Wind Sensor WS425. The weather station supplements TROWARA retrieval algorithms by providing these meteorological parameters with a time resolution of 10 minutes. The WXT520 rain sensor with a precision of 0.1 mm was utilized until September 2012, and this station also had a tipping bucket rain gauge with a precision of 0.2 mm until September 2016. In August 2017, the Vaisala Weather Transmitter was replaced by the WXT-536 model, which offers a precipitation precision of 0.01 mm. The rain sensor is very sensitive to snow. Additionally, the Zimmerwald Observatory near Bern uses a Vaisala automatic weather station with a rain sensor of 0.2 mm precision (Wang et al., 2021).

The UGR automatic weather station in Granada records surface air temperature and relative humidity monitored by a Vaisala HMP60 probe , and pressure monitored by a Vaisala PTB110 barometer. In this station wind speed was measured by an anemometer model 05103, manufactured by Campbell Scientific (Arruda Moreira et al., 2022). The time resolution of these parameters measurements is 1 minute. The rain sensor at the station delivers precipitation data from 2020 to 2022 with a precision of 0.1 mm, and another rain sensor operated on the roof from 2010 to 2022 with a precision of 0.2 mm.

Comparisons between the two rain sensors demonstrate consistent results for the overlapping period of 2020 to 2022.

3.2 METHODOLOGY

3.2.1 Retrieval methods for radiometers

3.2.1.1 *IWV and ILW retrieval*

TROWARA

TROWARA retrieval derives optical depth at two frequencies ($\nu = 21.385$ GHz and 31.5 GHz) to estimate the IWV and ILW respectively. Assuming a plane-parallel and non-scattering atmosphere, zenith optical depth $\tau_{\nu,zen}$ is derived from Equation 25:

$$\tau_{\nu,zen} = -\mu \cdot \ln \left(\frac{T_{m,\nu} - T_{b,\nu}}{T_{m,\nu} - T_c} \right) \tag{34}$$

where μ is the cosine of zenith angle which is 50 degrees for TROWARA. $T_{b,\nu}$ is the brightness temperature measured by TROWARA, and T_c is the brightness temperature of the cosmic microwave background. $T_{m,\nu}$ represents the effective mean temperature in the troposphere. The calculation of $T_{m,\nu}$ involves a linear equation with surface temperature T_s, relative humidity RH_s, and pressure P_s observed by ExWi weather station as variables, which is also dependent on the frequency and location.

$$T_{m,\nu} = A_{0,\nu} + A_{1,\nu} \cdot T_s + A_{2,\nu} \cdot RH_s + A_{3,\nu} \cdot P_s \tag{35}$$

where the coefficients $A_i, i = 0, 1, 2, 3$ are determined by radiosonde data based on the Rosenkranz radiation model (Mätzler and Morland, 2009; Rosenkranz, 1998).

Microwave radiation from ice and dry snow is negligible due to their small dielectric losses (Mätzler and Morland, 2014). Equation 34 can thus be expressed as a linear combination for the clear sky, water vapor, liquid water, and rain (Leuenberger, 2009).

$$\tau_{\nu,zen} = (a_\nu + b_\nu \cdot IWV + c_\nu \cdot ILW) + \tau_{\nu,rain,zen} \tag{36}$$

$$\tau_{\nu,rain,zen} = c_\nu \cdot G_{\nu,Mie} \cdot VIL \tag{37}$$

where the coefficients a_ν and b_ν are determined statistically by simultaneous measurements of radiosondes and refined during clear sky periods (Mätzler

and Morland, 2009). The coefficient c_v is the Rayleigh mass absorption coefficient of cloud water and is determined by a dielectric model of water (Ellison, 2007; Mätzler and Morland, 2014). $\tau_{v,rain,zen}$ is the zenith optical depth of rain layer. $G_{v,Mie}$ is the Mie gain of raindrops (Wang et al., 2021). Vertically Integrated Liquid (VIL) contains only rainwater. IWV and ILW retrieval equations can be derived by joint computation of Equation 36 at 21.385 (subscript 21) and 31.5 (subscript 31) GHz during no rainfall ($G_{v,Mie} = 0$). The selection of these two frequency channels is due to the absorption and scattering properties of water vapor and cloud droplets (Section 2.1.2).

$$IWV = \frac{\tau_{21,zen} - a_{21} - \gamma(\tau_{31,zen} - a_{31})}{b_{21}(1 - \beta\gamma)} \tag{38}$$

$$ILW = \frac{\tau_{31,zen} - a_{31} - \beta(\tau_{21,zen} - a_{21})}{c_{31}(1 - \beta\gamma)} \tag{39}$$

where $\beta = b_{31}/b_{21} < 0.5$, and $\gamma = c_{21}/c_{31} \cong 0.5$.

Two criteria are employed to detect cloud-free periods: the standard deviation of ILW and the Infrared (IR) brightness temperature. A threshold σ_{max} for the standard deviation of retrieved ILW values σ_{ILW} during the analysis period is used to identify ILW ≈ 0, which increases slightly with the mean daily air temperature T_s.

$$\sigma_{ILW} < \sigma_{max} = 0.0011 + 0.000012 \cdot \overline{T_s} \tag{40}$$

where the units of σ_{max} and T_s are mm and °C respectively.

In the case of fog interference in the lower troposphere in winter, IR brightness temperature T_b^{IR} is lower than the most likely cloud-free brightness temperature $T_{b,cloudfree}^{IR}$ based on IWV empirical fitting.

$$T_b^{IR} < T_{b,cloudfree}^{IR} = 192 + 3 \cdot IWV - 0.032 \cdot IWV^2 \tag{41}$$

where the units of $T_{b,cloudfree}^{IR}$ and IWV are K and mm respectively.

Assume a cloud-free case where at least one of these two criteria is satisfied, then calculate β and IWV from Equations 39 and 38.

$$\beta = \frac{\tau_{31,zen} - a_{31}}{\tau_{21,zen} - a_{21}} \tag{42}$$

$$IWV = \frac{\tau_{21,zen} - a_{21}}{b_{21}} \tag{43}$$

The coefficient b_{21} is fairly constant and can be calculated using a linear equation.

$$b_{21} = B_0 + B_1\tau_{21,zen} + B_2 \cdot \tau_{21,zen} + B_3 \cdot T_s + B_4 \cdot D_{wv} \tag{44}$$

where the coefficients $B_i, i = 0, 1, 2, 3, 4$ are determined statistically by radiosonde data (Mätzler and Morland, 2009). D_{wv} is the surface water vapor density.

HATPRO

The HATPRO software provided by RPG manufacturer retrieves IWV and ILW for HATPRO G2 (RPG, 2014). The retrieval method is a quadratic regression (QR) which is expressed as

$$
\begin{aligned}
Out = & \delta + \sum_{sensors} ML_s \cdot M_s + \sum_{sensors} MQ_s \cdot M_s^2 \\
& + \sum_{freq} TL_\nu \cdot T_{b,\nu} + \sum_{freq} TQ_\nu \cdot T_{b,\nu}^2
\end{aligned}
\tag{45}
$$

where Out is the output parameter (IWV or ILW). δ is the offset. M_s is the sth meteorological parameter (temperature, pressure, relative humidity) from the weather sensor. ML_s and MQ_s are the linear primary and quadratic coefficient of M_s respectively. $T_{b,\nu}$ is the brightness temperature observed by HATPRO at the νth microwave frequency. TL_ν and TQ_ν are the linear primary and quadratic coefficient of $T_{b,\nu}$ respectively (RPG, 2014). These coefficients were obtained from long-term datasets of radiosondes. This retrieval method is limited to be useful in the atmospheric conditions involved in these training datasets (Rose et al., 2005).

3.2.1.2 *Physical retrieval of rain rate*

The HATPRO software lacks the retrieval of the rain rate. An optical depth-based physical method to estimate the rain rate was introduced by Mätzler and Morland (2014). In my thesis, I refined and tested this method using a large dataset of TROWARA observations together with rain gauge measurements and ERA5. After validating the rain rate retrieval for TROWARA, I applied this method to the HATPRO measurements. In the following, I provide a detailed description of the rain rate retrieval method. An ILW threshold value ILW_{rain} is utilized as a criterion to detect rain, usually ranging between 0.1 and 0.6 mm. Rain is assumed to be present if the following condition is satisfied.

$$
ILW > ILW_{rain}
\tag{46}
$$

Even imprecise values are effective in identifying rain, as the increase in Mie emission causes a significant rise in ILW values when the diameter of droplet in the atmosphere exceeds 0.3 mm which is already the size of a raindrop. I selected 0.4 mm and 0.6 mm as thresholds ILW_{rain} to detect rain for TROWARA and HATPRO, respectively. The threshold for HATPRO is a bit higher because the retrieval algorithm of HATPRO overestimates ILW. Even in a clear sky without clouds, the ILW of HATPRO is greater than 0 (Wang et al.,

2023).

For the frequencies used, the absorption of raindrops in the atmosphere is much higher than the scattering. Raindrops lead to a strong increase in the observed brightness temperature because the radiation emitted by the Earth's surface is scattered by the backward hemisphere of the raindrops. Their sum gives the effective absorption coefficient for rain in Equation 37.

$$c_v \cdot G_{Mie,v} = Q_{abs,rain} + Q_{sca,rain} \cdot \frac{1 - <\cos\theta>}{2} \tag{47}$$

where $Q_{abs,rain}$ (Equation 15 and 16) is the rain absorption coefficient, and $Q_{sca,rain} \cdot \frac{1 - <\cos\theta>}{2}$ is the scattering coefficient $Q_{sca,rain}$ (Equation 14 and 17) in the backward hemisphere.

The VIL associated with rain rate R_v can be illustrated as follows.

$$VIL = R_v \cdot \frac{H_{rain}}{v} \tag{48}$$

where H_{rain} is the height from the melting layer to the ground, which is calculated by the ratio of the difference between the surface temperature (T_s) and the melting layer temperature ($T_{ML} = 273.15K$) to the temperature gradient with altitude ($\Gamma = \frac{dT}{dH}$). v is the velocity at which the raindrops fall.

The relationship between rain rate R_v and rain zenith optical depth $\tau_{v,rain,zen}$ is deduced by Equations 37 and 48.

$$R_v = \frac{\tau_{v,rain,zen}}{g_{v,rain} \cdot H_{rain}} \tag{49}$$

where $g_{v,rain} = c_v \cdot G_{Mie,v}/v$ is the specific and effective rain absorption coefficient. Since $g_{v,rain}$ is almost independent of rain rate and very weakly dependent on temperature, a constant value is assumed for a given frequency. At 21 GHz and 31 GHz, the values of $g_{v,rain}$ is set to 0.0165 h/mm/km and 0.0345 h/mm/km, respectively, which guarantees 20% accuracy (Mätzler and Morland, 2014). $\tau_{v,rain,zen}$ is determined iteratively by the radiative transfer equation.

$$\tau_{v,rain,zen}^{(k+1)} = -\mu \cdot \ln\left(\frac{T_{m,v,rain}(\tau_{v,rain,zen}^{(k)}) - T_{b,v,rain}}{T_{m,v,rain}(\tau_{v,rain,zen}^{(k)}) - T_{b,v,rainfree}}\right) \tag{50}$$

where $\tau_{v,rain,zen}^{(k+1)}$ is the rain zenith optical depth at the kth iteration. $T_{b,v,rain}$ is the brightness temperature measured by ground-based microwave radiometer during rain. $T_{b,v,rainfree}$ is the brightness temperature without rain, that is, the atmospheric water contains only water vapor and clouds. $T_{m,v,rain}$ is the effective mean temperature during rain. $T_{b,v,rainfree}$ and $T_{m,v,rain}$ give:

$$T_{b,v,rainfree} = T_c \cdot e^{-\tau_{v,rainfree,zen}/\mu} + T_{m,v}\left(1 - e^{-\tau_{v,rainfree,zen}/\mu}\right) \tag{51}$$

$$T_{m,v,rain}(\tau_{v,rain,zen}) = \frac{\int_{0}^{\tau_{v,rain,zen}/\mu} T(\tau) \cdot e^{-\tau} d\tau}{1 - e^{-\tau_{v,rain,zen}/\mu}} \cong T_s - \frac{1}{2}(T_s - T_{ML}) \cdot e^{-0.19 \cdot \tau_{v,rain,zen}/\mu}$$

(52)

where $\tau_{v,rainfree,zen}$ is the zenith optical depth without rain. Microwave radiometers are unable to measure it during rainfall, so it is estimated through temporal interpolation of measurements obtained during intermittent periods with no rain. Equation 50 basically converges after two iterations.

3.2.2 Machine learning methods

3.2.2.1 *Gradient Boosted Decision Trees (GBDT)*

GBDT is a powerful machine learning method known for its high generalization ability and robustness. GBDT fits the residual of previous base learners using the negative gradient of the loss function, gradually reducing the residual at each round to achieve accurate predictions (Hu et al., 2021). It is an ensemble learning method for building strong learners by combining decision trees. Algorithm 1 shows the regression procedure of GBDT. It generates a forest with M regression trees based on a dataset D, where N is the number of training samples, J is the number of leaf terminal node of trees, $1(\cdot)$ is an indicator function, it is 1 if the argument (e.g. $x \in R_{mj}$) is true, otherwise zero. γ is the transcendental parameter.

GBDT has the capability to select features that contribute more to the prediction in each iteration and output feature importance scores (Zhang et al., 2022). The calculation of GBDT feature selection was proposed by Breiman et al. (1984). The basic idea is to gauge the importance of a feature n by tallying how frequently it is selected on average. During the splitting process of the regression tree, if the input feature is chosen more often as the splitting feature, it is considered more important. This frequency is then generalized to relative influences I_n of the individual inputs x_n, and the average frequency of feature selection is computed across all regression trees (Friedman, 2001).

$$\hat{I}_n^2(T) = \sum_{t=1}^{J-1} \hat{i}_j^2 1(v_j = n)$$

(53)

where v_j is the splitting variable associated with nonterminal split node j for a decision tree T. $\hat{i}_t^2$ is the empirical improvement in the square of loss reduction due to splits.

Assuming that every tree is a binary tree, Equation 53 can be generalized

---

Algorithmus 1 : Gradient Boosting Decision Tree

Input : Training dataset
$D = \{(x_1, y_1), (x_2, y_2), \cdots, (x_N, y_N)\}, x_n \in X \subseteq \mathbf{R}^n, y_n \in Y \subseteq \mathbf{R};$
Loss function $L(y, f(x));$

Output : GBDT model $f_M(x);$

1 Initialize $f_0(x) = \arg\min\limits_{\gamma} \sum_{n=1}^{N} L(y_n, \gamma);$

2 **for** $m \in [1, M]$ **do**

3   **for** $n \in [1, N]$ **do**

4   Compute residual: $r_{mn} = -\left[\frac{\partial L(y_n, f(x_n))}{\partial f(x_n)}\right]_{f(x) = f_{m-1}(x)};$

5   **end**

6   Fit a regression tree with (x_i, r_{mn}) to obtain a leaf node set of the mth tree: $R_{mj}, j \in [1, J];$

7   **for** $j \in [1, J]$ **do**

8   Minimized loss function:
        $\gamma_{mj} = \arg\min\limits_{\gamma} \sum_{x_n \in R_{mj}} L(y_n, f_{m-1}(x_n) + \gamma);$

9   **end**

10   Update prediction: $f_m(x) = f_{m-1}(x) + \sum_{j=1}^{J} \gamma_{mj} 1(x \in R_{mj});$

11 **end**

12 Get the final GBDT function:
$\hat{f}(x) = f_M(x) = \sum_{m=1}^{M} \sum_{j=1}^{J} \gamma_{mj} 1(x \in R_{mj});$

13 **return** $f_M(x);$

---

by averaging it over a collection of decision trees $\{T_m\}_1^M$ obtained through boosting.

$$\hat{I}_n^2 = \frac{1}{M} \sum_{m=1}^{M} \hat{I}_n^2(T_m) \tag{54}$$

3.2.2.2 *Random Forest (RF)*

RF, proposed by Breiman (2001), is a machine learning algorithm in the bagging category of ensemble methods. It excels in regression tasks and is widely used in precipitation studies due to its robust performance (Zhang et al., 2021). RF incorporates two important randomness settings: it samples the original dataset using the bootstrap method and randomly selects a subset of features, from which the best ones are chosen. In a random forest, each node is split using the best value among a randomly chosen subset of predictors at that node (Liaw, Wiener, et al., 2002). The final model averages the predictions from all decision trees. Hastie et al. (2009) demonstrated the process of the RF algorithm.

Evaluating feature importance is crucial in RF as it aids in selecting features that improve model performance and generalization. In RF, each tree is built

---

Algorithmus 2 : Random Forest

Input : Training dataset
$$D = \{(x_1, y_1), (x_2, y_2), \cdots, (x_N, y_N)\}, x_n \in X \subseteq \mathbf{R}^n, y_n \in Y \subseteq \mathbf{R};$$
Output : Output the ensemble of trees $\{T_m\}_1^M$;

1 Initialize an empty forest F;

2 **for** $m \in [1, M]$ **do**

3   a. Draw a bootstrap sample D_m from D;

4   b. Grow a random-forest tree T_m using the bootstrapped data by recursively repeating the following steps for each terminal node until the minimum node size is reached:

5   **for** $n \in [1, N]$ **do**

6   i. Select n variables at random from the N variables;

7   ii. Pick the best variable or split-point among the n;

8   iii. Split the node into two daughter nodes;

9   **end**

10 **end**

11 Get the final RF function:

12 $\hat{f}(x) = f_M(x) = \frac{1}{M} \sum_{m=1}^{M} T_m(x);$

13 **return** $f_M(x);$

---

by recursively selecting the best splitting features and calculating the Mean Decrease Impurity (MDI) from these splits. A feature's importance is determined by summing its impurity reductions at each split across all trees and then averaging these sums to compute the importance score of the feature (Louppe et al., 2013).

3.2.3 Superposed epoch analysis (SEA)

Superposed epoch analysis (SEA) (Chree, 1913), also referred to as composite analysis method, is simple and one of the most powerful widely used statistical analysis techniques (Walton and Murphy, 2022). Python also releases packages that perform SEA. Studies have utilized SEA for a range of evolutionary characteristics of meteorological or climatic phenomena that are challenging to observe as a whole or events occurring over an extended period. To identify the evolution of time series of atmospheric variables affected by rain events, SEA is an effective option. SEA can be divided into two phases: pre-epoch and post-epoch. An epoch can be a specific point in time or a discrete event in time, such as a rain event. Before and after the occurrence of an epoch is a long continuous uniformly sampled time series, such as atmospheric variables observations (Rao et al., 2019). These events are assumed to result in the characteristics of a continuous time series. These two phases for each epoch are combined and put into a set of equally spaced bins, the

number of bins N being the same as the number of events. A statistic is determined, such as mean, for all binned data (Rong et al., 2020).

$$V(x) = \frac{1}{N} \sum_{epoch=1}^{N} V_{x,epoch} \tag{55}$$

where V is the observation of atmospheric variables. x is the time between $-a$ and b. If conducting a 2D SEA, the data is organized into bins in the second dimension before computing the statistics for each bin. To form the superposed epoch analysis of rain events, the criteria are:

- the onset time of rainfall is set as epoch time 0. The occurrence/duration time of a rain event is set as t. 1 hour before rainfall is set as -1, 1 hour during rainfall is set as $+1$, and 1 hour after rainfall is set as $t + 1$.

- ILW=0.4 and ILW=0.6 determine the start and end time of rain detection by TROWARA and HATPRO respectively (Cossu et al., 2015; Löhnert and Crewell, 2003; Mätzler and Morland, 2009; Wang et al., 2023).

- If no rainfall occurs during a hours before the epoch 0 and during b hours after the time t, then this rain event is selected.

Part III

RESULTS AND DISCUSSION

This part presents six studies that have either been published or submitted to peer-reviewed journals. These studies focus on rainfall retrieval, tropospheric radiometers, and precipitation over the Swiss Plateau and Mediterranean climates affected by Saharan dust.

4 RAIN DETECTION BY MICROWAVE RADIOMETER

4.1 SUMMARY OF THE STUDY

Measurements of brightness temperature and retrieval of atmospheric parameters (e.g. water vapour and clouds) from ground-based microwave radiometers are valid under most weather conditions, but are no longer applicable during rainfall. Microwave radiometer data can be contaminated because the radiation signal is affected by raindrops in the atmosphere. Several physical and statistical methods have been presented in recent years that specifically use rain-contaminated microwave radiometer data for rain rate retrieval (Marzano et al., 2005a; Marzano et al., 2005b; Wang et al., 2021), but the premise is that rain-free and rain-contaminated data have been identified. An effective rain detection model can directly detect rain-contaminated data, eliminating the dependence on rain gauges, and can serve as rain flags for co-located remote sensing instruments facing similar challenges.

The article presented in this chapter proposed a GBDT-based rain detection method for microwave radiometer measurements. Using rain detected by MRR as target variable, my method considered various precipitation patterns contained in different seasons and demonstrates strong generalization ability. It can detect rain-contaminated microwave radiometer time series data with high time resolution (10 seconds), effectively overcoming the time dependence of rain occurrence. The rain detection capability is competitive, achieving 98.4% accuracy, 97% precision, 99.9% recall, and a 98.4% F1 score.

The following article was submitted to Journal of Hydrology in July 2024.

4.2 PUBLICATION

FULL CITATION

Wang Wenyue, Wenzhi Fan, and Klemens Hocke. "Rain detection for rain-contaminated ground-based microwave radiometer data using physics-informed machine learning method." In: *Journal of Hydrology*, in review.

Rain Detection for Rain-Contaminated Ground-Based Microwave Radiometer Data Using Physics-Informed Machine Learning Method

Wenyue Wang[a,b,*], Wenzhi Fan[c] and Klemens Hocke[a,b]

[a]*Institute of Applied Physics, University of Bern, 3012, Bern, Switzerland*

[b]*Oeschger Centre for Climate Change Research, University of Bern, 3012, Bern, Switzerland*

[c]*School of Earth and Space Sciences, Peking University, 100084, Beijing, China*

ARTICLE INFO

ABSTRACT

Because the radiation signal is strongly influenced by emission and scattering from rain, microwave radiometer data suffer from rain contamination. The traditional method of using rain gauges to detect rain for microwave radiometers has limitations. For example, it can only detect rain that reaches the ground and is ineffective for raindrops suspended in the atmosphere that can still contaminate remote sensing data. This article presents a rain detection method for microwave radiometer measurements, based on Gradient Boosted Decision Trees (GBDT). First, the characteristic that the increase in microwave radiometer brightness temperature when raindrops are present in the atmosphere, along with the seasonal dependency of rainfall patterns, is combined with meteorological variables to form feature vectors. Then, the GBDT is employed to classify data into rain-free and rain-contaminated categories. Microwave radiometer (MWR) measurements and simultaneous Micro Rain Radar (MRR) target classification collected from the Swiss Plateau in 2008 are utilized to train the model, which is subsequently tested using two testing schemes: ten-fold cross-validation technique and time series test sets. Compared with the detection accuracy of the integrated liquid water (ILW) threshold method (73.6% and 68.3%) in both testing schemes, our GBDT-based method achieved superior accuracy, recording approximately 100% and 98.4%, respectively. The proposed method exhibits strong generalization capabilities, allowing it to directly detect rain contamination in time series data and effectively overcome the time dependence of rainfall occurrence. In addition, compared with the ILW threshold method, the GBDT-based method considers various rainfall patterns contained in various seasons. Features selected for this method enable its direct application to other tropospheric microwave radiometer systems.

1. Introduction

Ground-based microwave radiometers have been developed as widely used atmospheric remote sensors because of their continuous, all-weather observations both day and night (Hocke, Bernet, Hagen, Murk, Renker and Mätzler, 2019). On the other hand, microwave radiometers are especially crucial for cross-validation of satellite observations, thanks to their high temporal resolution and precise retrieval capabilities for atmospheric parameters (Sauvageat, Hocke, Maillard Barras, Hou, Errera, Haefele and Murk, 2023). Various methods have been proposed to retrieve water vapor, cloud liquid water, temperature, ozone, and wind from brightness temperatures (T_B) measured by microwave radiometers (Wang, Hocke and Mätzler, 2021; Sauvageat, Maillard Barras, Hocke, Haefele and Murk, 2022; Krochin, Navas-Guzmán, Kuhl, Murk and Stober, 2022). Although these methods are effective under most weather conditions, they are no longer suitable during rainfall, as the radiation signal is affected by strong emission and scattering from raindrops in the atmosphere, and water films form on radiometers' radome (Wang, Murk, Sauvageat, Fan, Dätwyler, Hervo, Haefele and Hocke, 2023). This leads to a degradation in the data quality of atmospheric T_B and these

parameters retrieval. No algorithms have yet been developed to mitigate the effects of rain. Therefore, microwave radiometer data contaminated by rainfall should be detected and excluded. Several physical and statistical methods have been presented in recent years that specifically use rain-contaminated microwave radiometer data for rain rate retrieval (Marzano, Cimini and Ware, 2005b; Marzano, Cimini, Ciotti and Ware, 2005a; Wang et al., 2021; Marzano, Fionda and Ciotti, 2006), but the premise is that rain-free and rain-contaminated data have been identified. Traditionally, rain gauges, rain sensors, or rain detector, with a time resolution typically ranging from 1 to 10 minutes, serve as rain flags for detecting rainfall and quantifying the amount of precipitation reaching the ground. Löhnert and Crewell (2003) indicated that Integrated Liquid Water (ILW) can serve as a threshold for detecting rain-contaminated microwave radiometer data. In their study of atmospheric water parameters, Cossu, Hocke, Martynov, Martius and Mätzler (2015) utilized an ILW threshold greater than 0.4 mm for rain detection on the tropospheric microwave radiometer TROWARA. The ILW threshold method is straightforward, but precise ILW retrieval is essential, and the threshold value can only be determined empirically. The accuracy of ILW threshold method in detecting rain-contaminated data has also not been previously analyzed. Hence, it is imperative

*Corresponding author

✉ wenyue.wang@unibe.ch (W. Wang); wenzhi.fan@pku.edu.cn (W. Fan); klemens.hocke@unibe.ch (K. Hocke)

ORCID(s): 0000-0002-8251-2514 (W. Wang); 0000-0003-2178-9920 (K. Hocke)

to propose a novel detection method for tropospheric microwave radiometers that is accurate and adaptable to various measurement setups. In addition, an effective rain detection model allows for direct detection of rain-contaminated data, eliminating reliance on rain gauges, and can function as a rain flag for co-located remote sensing instruments facing similar challenges (Chen, Huang, Zhao and Tian, 2020).

Rain detection essentially boils down to a binary classification task, segregating microwave radiometer measurements into two categories: rain-free and rain-contaminated (Chen et al., 2020). The machine learning method Gradient Boosted Decision Trees (GBDT) captures the complex nonlinear relationships of data through the combination of multiple decision trees (Friedman, 2001, 2002). Also, GBDT can efficiently handle large-scale data with mixed feature types and has certain robustness to data with noise and outliers. GBDT is widely used in classification tasks in remote sensing field to solve recognition problems, such as cloud detection from microwave humidity sounder (Liu, Yin, Chu and An, 2020) and diagnosis of precipitation types from surface observations (Zhuang, Lehner and DeGaetano, 2024; Fu, Kan, Liu, Liang, He and Ding, 2023). To the best of our knowledge, this article is the first article on rain detection in rain-contaminated ground-based microwave radiometer data using GBDT. Previous studies, such as the one mentioned in (Ma, Zhang and Lu, 2018), applied GBDT to identify hourly rain areas during the summer using data from the advanced Himawari imager. Another study cited in (Lei, Zhao and Ao, 2022) utilized GBDT for precipitation identification and estimation from multi-source precipitation products, including one reanalysis product and five satellite precipitation products, along with rain gauge observations from 2000 to 2017 over China. However, none of these studies explored the use of GBDT for detecting rain in ground-based microwave radiometer data, marking a novel contribution of this research. In addition, in this article, features take into account various rainfall patterns in various seasons. Note that the method must possess exceptional generalization capabilities, as rainfall is a time-dependent dynamic phenomenon with varying intensity and duration at each time step (Pudashine, Guyot, Petitjean, Pauwels, Uijlenhoet, Seed, Prakash and Walker, 2020).

Here, we apply both the proposed GBDT-based method and the ILW threshold method to detect rain-contaminated data for microwave radiometer. The article is structured as follows. Section II introduces and derives the rain detection method based on GBDT. Section III compares and analyzes the results obtained from the two testing schemes using the proposed technique and the ILW threshold method. Discussion and conclusions are in Section IV and V.

2. GBDT-based rain-contaminated data detection

2.1. Effect of raindrops on radiometric signals

The radiometer used in this article is a ground-based tropospheric microwave radiometer at 21.385, 22.235, and 31.5 GHz operating indoors for monitoring atmospheric water vapor and cloud liquid water. The microwave radiometer functions by receiving signals emitted from microwave radiation in the atmosphere that originate from particles (Battaglia, Simmer, Crewell, Czekala, Emde, Marzano, Mishchenko, Pardo, Prigent et al., 2006), such as raindrops. In other words, radiation traverses through the atmosphere and interacts with raindrops, where absorption refers to the transfer of energy from the radiation to raindrops, whereas scattering alters the direction of the radiation beam without affecting its energy or frequency. The combination of absorption and scattering is called extinction (Q_{ext}). For the microwave frequency band (1-300 GHz), scattering depends on the size and composition of particles present in the atmosphere. Light raindrops (approximately 100 μm) undergo Rayleigh scattering (Bohren and Huffman, 2008; Rayleigh, 1871). Raindrops (0.1-3 mm) can exhibit Rayleigh scattering or Mie scattering (Mishchenko, Yatskiv, Rosenbush and Videen, 2011). Rayleigh absorption and scattering efficiencies (Q_{abs} and Q_{sca}) are given by

$$Q_{abs} = -4\chi\mathfrak{I}\left(\frac{m^2-1}{m^2+2}\right) \propto \frac{1}{\lambda} \tag{1}$$

$$Q_{sca} = \frac{8}{3}\chi^4\left|\frac{m^2-1}{m^2+2}\right|^2 \propto \frac{1}{\lambda^4} \tag{2}$$

and

$$Q_{ext} = Q_{abs} + Q_{sca} \tag{3}$$

where χ is the dimensionless size parameter. m is the complex refractive index. λ is the wavelength. $\mathfrak{I}$ represents the imaginary part. The effect of raindrops on microwave radiation signals is directly related to Q_{abs} and Q_{sca}. Ice primarily scatters microwave radiation without absorbing it, whereas raindrops both absorb and scatter microwave radiation, with absorption being the dominant interaction (Mätzler and Morland, 2014). The extent of absorption and scattering in ice and water is contingent upon their magnitude relative to the microwave frequency. For frequencies ranging from 22 to 31 GHz, the scattering effect of ice is negligible, rendering ice nearly transparent to microwave radiation (Mätzler and Wegmüller, 1987).

Figure 1 shows the effect of precipitation types on the microwave radiometer. Figure 1(b) illustrates a significant increase in brightness temperature (T_B) observed by the microwave radiometer at 21, 22, and 31 GHz during convective rainfall on August 19, 2008 in Figure 1(a). For example, the T_B at 31 GHz rose rapidly from approximately 30 to over 180 K from 14:40 to 15:40 UTC. The convective rain mainly includes rain and drizzle types of precipitation. Furthermore, mixed (rain and snow or graupel) also contaminates microwave radiometer data. As shown in Figure 1(c) and (d), during periods dominated by mixed from 14:30 to 15:10 UTC on March 21, 2008, the T_B exhibits higher values. However, dry snow, composed mainly of ice crystals, has no
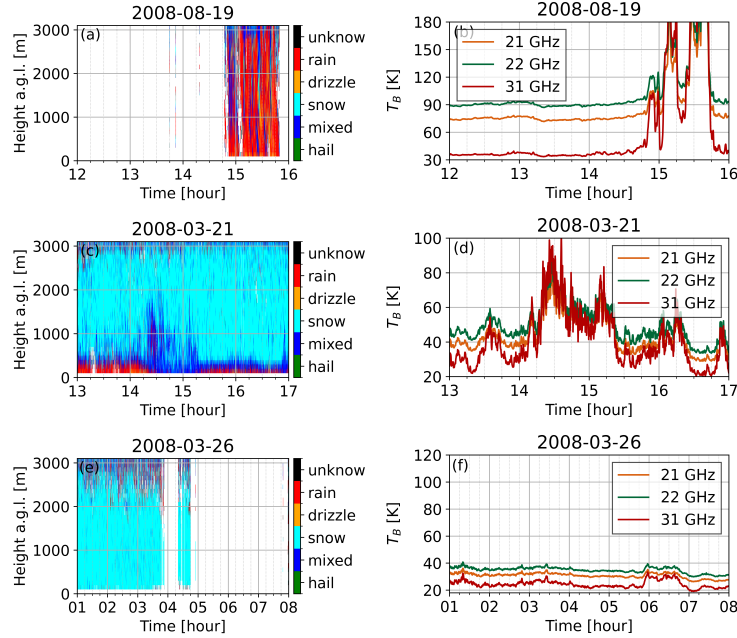
Figure 1: Rain-contaminated microwave radiometer data. The time periods are from 12:00 to 16:00 UTC on August 19, from 13:00 to 17:00 UTC on March 21, and from 1:00 to 8:00 UTC on March 26, 2008, respectively. (a), (c), and (e) Micro Rain Radar (MRR) target classification exist for rain, drizzle, mixed, and snow, respectively. (b), (d), and (f) brightness temperature (T_B) from microwave radiometer TROWARA. Channels at 21.385, 22.235, and 31.5 GHz are orange line, green line, and red line, respectively.

significant impact on T_B from the data presented in Figure 1(e) and (f). It follows that only certain precipitation types, specifically rain, drizzle, and mixed, can affect microwave radiation signals.

2.2. Data sources
2.2.1. Microwave radiometer data

The microwave radiometer data used in this study were provided by the Tropospheric Water Radiometer (TROWARA) (Peter and Kämpfer, 1992), which operates on the roof of the Exakte Wissenschaften (ExWi) building (46.95°N, 7.44°E; alt. 575 m asl) at the University of Bern since November 1994 in Bern, Switzerland. T_B data were collected at a temporal resolution of 7-11 seconds. The corresponding bandwidths of the 21.385 GHz, 22.235 GHz and 31.5 GHz microwave channels are 100 MHz, 400 MHz and 200 MHz respectively. The half-power beamwidth of the antenna beam is 4°. TROWARA is directed towards the southeast of the sky at a zenith angle of 50°. Since November 2002, TROWARA moved from outdoor to an indoor temperature-controlled laboratory and reinstalled (Morland, 2002), where its antenna receives atmospheric radiation through a microwave-transparent window (Morland, 2007). The wall surrounding the window is effectively shielded from rain, ensuring the antenna remains dry and enabling TROWARA to conduct

measurements even on rainy days (Wang et al., 2023). In addition, TROWARA is equipped with a thermal infrared channel operating within the wavelength range of 9.5–11.5 μm to measure infrared cloud base brightness temperature. TROWARA can retrieve accurate integrated water vapour (IWV) and integrated liquid water (ILW) using opacity based physical retrieval algorithm (Mätzler and Morland, 2009). Assuming a plane-parallel atmosphere, the radiative transfer equation for a non-scattering atmosphere is:

$$T_{B,i} = T_C \cdot e^{-\tau_i/\mu} + T_{mean,i} \cdot (1 - e^{-\tau_i/\mu}) \quad (4)$$

where τ_i represents the zenith opacity, μ denotes the cosine of the zenith angle, $T_{B,i}$ stands for the TROWARA brightness temperature at frequency i (e.g., 31.5 GHz), and T_C signifies the brightness temperature of the cosmic microwave background. Furthermore, $T_{mean,i}$ represents the effective mean temperature of the troposphere, which is dependent on frequency (and site). $T_{mean,i}$ can be derived via a linear equation that integrates meteorological parameters (Wang et al., 2021).

The zenith opacity τ_i can be derived from Equation 4:

$$\tau_i = -\mu \cdot \ln \left(\frac{T_{mean,i} - T_{B,i}}{T_{mean,i} - T_C} \right) \quad (5)$$

Equation 5 can alternatively be represented as a linear combination of IWV and ILW, both measured along the zenith direction.

$$\tau_i = a_i + b_i \cdot \text{IWV} + c_i \cdot \text{ILW} \qquad (6)$$

where the coefficients a_i and b_i are air pressure-dependent and can be statistically derived from concurrent radiosonde measurements, further refined during clear-sky periods. The coefficient c_i varies with air temperature and frequency and represents the Rayleigh mass absorption coefficient of cloud water, obtainable from a dielectric model of water (Ellison, 2006).

2.2.2. Meteorological data

The meteorological data used in this study were sourced from a standard weather station situated a few meters away from TROWARA on the roof of ExWi building. The weather station provides weather conditions and supplementary data essential for the rain detection model, including surface air temperature, air pressure, and relative humidity, recorded at a 10-minute time resolution.

2.2.3. Micro rain radar data

The precipitation type classification data used in this study were obtained from the Micro Rain Radar (MRR) manufactured by Meteorologische Messtechnik GmbH (Metek) (METEK, 2009), located two meters away from TROWARA on the roof of the ExWi building since March 2007. The MRR is a compact frequency modulated continuous wave (FMCW) Doppler radar operating at a frequency of 24.23 GHz, pointed towards the zenith direction with a time resolution of 10 seconds. The MRR system can measure vertically over ranges from 100 to 3100 m with a resolution of 100 m. The 3-dB beamwidth is 1.5°, and the modulation bandwidth ranges from 0.5 to 15 MHz. For classification, the model developed by Garcia-Benadi, Bech, Gonzalez, Udina, Codina and Georgis (2020) was employed to process the MRR's spectral raw data, enabling the classification of precipitation types into five categories including snow, drizzle, rain, hail, and mixed. The mixed category includes wet snow, a mixture of dry snow and rain, or graupel. The classification employs a decision tree that incorporates the empirical relationship between hydrometeor fall velocity and equivalent radar reflectivity, as well as the size and particle properties of various hydrometeors and the presence or absence of bright bands. Beynon (2022) compared the rain time recorded by the MRR with the rain gauge and showed that the MRR operated most reliably in 2008, and the data loss caused by the shutdown was negligible, so this article uses the 2008 data to train the model.

2.3. GBDT algorithm for rain detection

Gradient Boosting Decision Trees (GBDT) is one of the best algorithms for fitting actual distributions among traditional machine learning algorithms. It demonstrates strong generalization capabilities and is effective for classification tasks. GBDT binary classification is an ensemble learning algorithm that combines multiple weak learners (trees) to form a strong learner. Each weak learner is a binary decision tree that corrects the residuals caused by all previous trees using iterations, and uses the negative gradient of the loss function to fit a new decision tree model that minimizes the classification error of the previous model (Friedman, 2002). Assume that given the training set to train rain detection model $\{x_1, y_1\} \{x_2, y_2\}, \ldots, \{x_n, y_n\}$ $(x_i \in R^n, y_i \in \{0, 1\})$, where n is the sample size, and i from 1 to n. x_i represents a feature vector of sample i. y_i represents a binary label, which is marked as rain-free (category 0) or rain-contaminated (category 1). The weak classifier $f_m(x)$ is assembled into the final GBDT model $F_M(x)$ through the additive model after the m-th round of iteration.

$$F_M(x) = \sum_{m=1}^{M} f_m(x) \qquad (7)$$

where M is the number of decision trees or weak learners, and m is from 1 to M.

The process of model training is as follows (Liu et al., 2020; Shen and Yong, 2021):

1. Initialize the first learner $F_0(x)$ as prior information in binary classification.

$$F_0(x) = \underset{c}{argmin} \sum_{i=1}^{n} L(y_i, c) \qquad (8)$$

where L is the loss function. c is the optimal constant predictor.

2. Calculate the error residual r_{mi} between each tree and the previous result, that is, the negative gradient of the loss function with respect to the current model $f_{m-1}(x)$.

$$r_{mi} = -\left[\frac{\partial L\left(y_i, f(x_i)\right)}{\partial f\left(x_i\right)}\right]_{f(x)=f_{m-1}(x)} = y_i - \hat{y}_i \quad (9)$$

3. Calculate the optimal fitting value of leaf node $j = 1, 2, \ldots, J$ in each partitioning method to approximate the residual error.

$$c_{mj} = \underset{c}{argmin} \sum_{x_i \in R_{mj}} L(y_i, f_{m-1}(x_i) + c) \quad (10)$$

where R_{mj} represents the set of predicted values of all leaf nodes of the m-th sub-tree.

4. Update the model to adjust to a better fit to the training data by adding newly trained trees.

$$f_m(x) = f_{m-1}(x) + \sum_{j=1}^{J} c_{mj} I\left(x \in R_{mj}\right) \quad (11)$$

where I is a function. If the sample on the node of R_{mj}, then $I = 1$, otherwise $I = 0$.

5. Repeat step 2-4 until the preset number of iterations is reached or the improvement is no longer significant. The strong classifier obtained by the final model $F_M(x)$ can be applied to predict new samples.

The GBDT-based model assesses the importance of features by calculating their average selection frequency *J* in tree branching. This metric is derived by normalizing and averaging how frequently each feature is selected as a branch point across all regression trees. Essentially, the more frequently a feature is chosen, the more important it is considered (Wang et al., 2023; Friedman, 2001).

$$\hat{J}^2 = \frac{1}{M} \sum_{m=1}^{M} \hat{J}^2 (T_m) \tag{12}$$

The importance of a feature within a decision tree T is calculated as follows:

$$\hat{J}^2 (T) = \sum_{t=1}^{N-1} \hat{i}_t^2 1 (v_t) \tag{13}$$

In this context, each tree is assumed to be binary, with N representing the number of terminal nodes and $N − 1$ the number of nonterminal nodes. The variable v_t denotes the feature used for splitting at node t, and i_t^2 quantifies the squared loss reduction resulting from that split. A larger value of i_t^2 signifies a more significant reduction in loss, highlighting the importance of the feature at that node.

The quantitative evaluation of rain detection results is based on metrics such as accuracy, precision, recall, and F1 score, as detailed in Table 1. The samples are divided into two categories: positive (rain-contaminated data) and negative (rain-free). TP (True Positives): the number of positive samples correctly predicted as positive. TN (True Negatives): the number of negative samples correctly predicted as negative. FP (False Positives): the number of negative samples incorrectly predicted as positive. FN (False Negatives): the number of positive samples incorrectly predicted as negative. Accuracy is calculated as the sum of all correct predictions divided by the total number of predictions. Accuracy represents the proportion of correct predictions by the model for the rain-contaminated data and rain-free categories, and it is the most straightforward metric in the case of balancing positive and negative samples. Precision represents the proportion of rain-contaminated data among all samples predicted by the model that are actually rain-contaminated. High precision means that the proportion of mislabeled cases that the model labels as rain-contaminated data is low. Recall is the model's ability to correctly identify actual rain-contaminated data. A high recall means that the model effectively captures rain-contaminated data, that is, fewer missed detection occur. F1 score is a comprehensive reflection of the two metrics of precision and recall.

TROWARA provides three variables: brightness temperature at 31.5 GHz, infrared cloud base brightness temperature, and integrated water vapor. These, along with the three variables air temperature, air pressure, and relative humidity provided by the weather station, are used as feature inputs for the GBDT learning dataset, with rain detection by MRR serving as the label, covering the period from January 1 to December 31, 2008. TROWARA's time resolution is 11

Table 1
Validation metrics with the range and optimum.

Metrics	Equation	Range	Optimum
Accuracy	$\frac{TP+TN}{TP+TN+FP+FN}$	[0,1]	1
Precision	$\frac{TP}{TP+FP}$	[0,1]	1
Recall	$\frac{TP}{TP+FN}$	[0,1]	1
F1 Score	$2 \times \frac{Precision \times Recall}{Precision + Recall}$	[0,1]	1

seconds in 2008. All the data is standardized to a uniform 10-second time resolution using a sample resampling method. The dataset comprises 340,536 samples, balanced at a 1:1 ratio between rain-contaminated and rain-free samples.

3. Experiment and results

3.1. Data preprocessing

To ensure the reliability of MRR data as rainfall labels, data preprocessing should be performed to remove outlier lines. As shown in Figure 2(a), MRR data often contain numerous radial and large-area outlier lines due to interference from the instrument and the environment. Figures 2(b) and (c) provide enlarged views of these outliers. Outliers in the MRR data can lead to misjudgments regarding the presence of raindrops in the troposphere. To address this issue, the data is filtered to include only rain events that last for a minimum of three minutes, effectively removing these outliers. In addition, considering that the melting layer can be very low, only the presence of rain, drizzle, or mixed below 200 m is selected as the positive category. Figure 2(d) shows the MRR target classification after outlier lines removal from Figure 2(a). This study performs the above preprocessing on all rain events in 2008.

Seasonal effects need to be considered when analyzing rainfall-related data. This is because climatic factors, such as temperature fluctuations, pressure systems and ocean currents, along with geographical factors like topography and proximity to bodies of water, can cause rainfall patterns and intensity to vary significantly across various seasons. Bern is situated on the Swiss Plateau. The Swiss Plateau features rolling hills and abundant lakes and rivers. It lies in the transition zone between oceanic and continental climates, resulting in variable and often cloudy weather. Summers are cool due to frequent cloud cover, whereas winters are relatively mild (Wang and Hocke, 2022). Figure 3(a), (b), (c), and (d) show examples of rainfall across various seasons spring, summer, autumn and winter respectively. In the example from April 6, the melting layer was notably low (about 500 m) and less distinct, with mixed also observed after 3:40 UTC. In summer such as July, convective rain occurs frequently. The stratiform rain with a melting layer higher than about 2000 m on October 16. Winter in January is a season of mixed and snow. Therefore, the months from January to December were added to the features of the GBDT model in this article using one-hot encoding (Lucas, 2014).
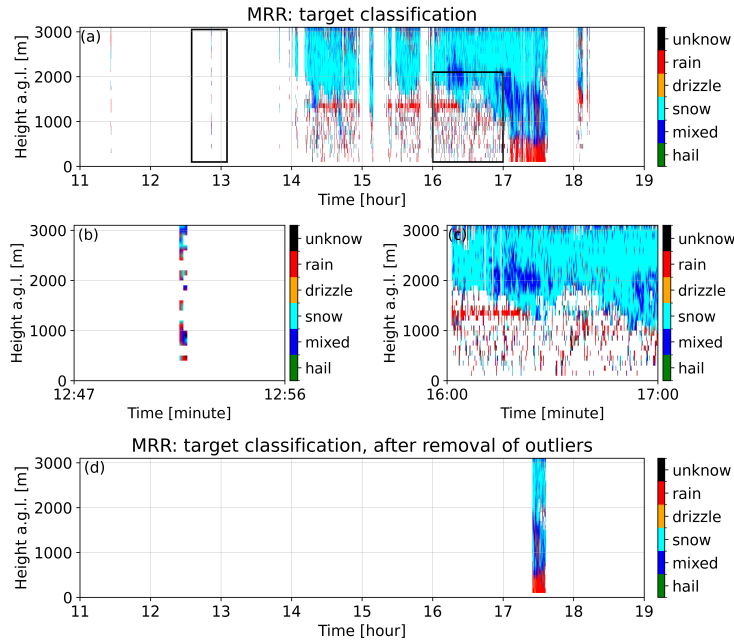
Figure 2: Outlier lines in MRR data. (a) Raw MRR target classification data from 11:00 to 19:00 UTC on January 18, 2008. Part of the outlier lines is outlined in two black box. (b) Zoom in on the left black box to view the outlier lines. (c) Zoom in on the right black box to view large distribution outlier lines. (d) MRR target classification data with outlier lines removed and rainfall duration exceeding 3 minutes.

To comprehensively evaluate the fitting potential and predictive ability of the GBDT-based rain detection model, we adopted two test methods: Testing scheme 1 and Testing scheme 2. Testing scheme 1 employs the ten-fold cross-validation (CV) technique (Rodriguez, Perez and Lozano, 2010). The entire sample is randomly split into 10 equal subsets. One subset is used to test the model, whereas the remaining subsets train it. This process is repeated ten times, with the overall performance of the model evaluated by averaging the outcomes of these ten tests. On the other hand, considering rainfall has a strong dependence on time (Pudashine et al., 2020), as the onset and end of rainfall interact with atmospheric parameters (Wang and Hocke, 2022). Testing scheme 2 is designed that the test set consists of the time series from the last two rainy days of each month, and the remaining data is used to train the model. The ratio of training set and test set sample size for Testing scheme 2 is 9:1.

3.2. Test and validation

Table 2 shows rain detection results of microwave radiometer (MWR) data based on GBDT and ILW threshold method, where the threshold is denoted as ILW_R. Results show that for Testing scheme 1, the GBDT method achieves 100% detection accuracy, precision, recall, and F1 score across all testing samples. Note that it is impossible for 100% of the test samples to be detected correctly. The 100% figure is a rounded from 99.9%. Using the ILW threshold method, the corresponding metrics are 73.6% accuracy, 99.9% precision, 46.9% recall, and 63.8% F1 score. The GBDT method is fully correct for the detection of rain-free and rain-contaminated in Testing scheme 1. The high precision of the ILW threshold method confirms that rain detected by this method is indeed rain, whereas its low recall indicates that many actual rain cases are missed. Figure 4 shows an example of the experimental results of Testing scheme 1. In Figure 4(a), rain detected by MWR based on the GBDT method is completely consistent with rain measured by MRR. In Figure 4(b), rain detected by ILW>0.4 mm is all correct, whereas rain-free detected by ILW≤ 0.4 mm actually includes many rain cases. This example echoes the results in Table 2, indicating that a significant amount of rain goes undetected using ILW threshold method. Results show that for Testing scheme 2, as detailed in Table 2, the GBDT method achieves 98.4% accuracy, 97% precision, 99.9% recall, and 98.4% F1 score across all testing samples. Using the ILW threshold method, the corresponding metrics are 68.3% accuracy, 99.6% precision, 36.7% recall, and 53.6% F1 score. The GBDT method still performs very well when the test set is an unseen time series in Testing scheme 2, although the recall is slightly better than the precision, which indicates
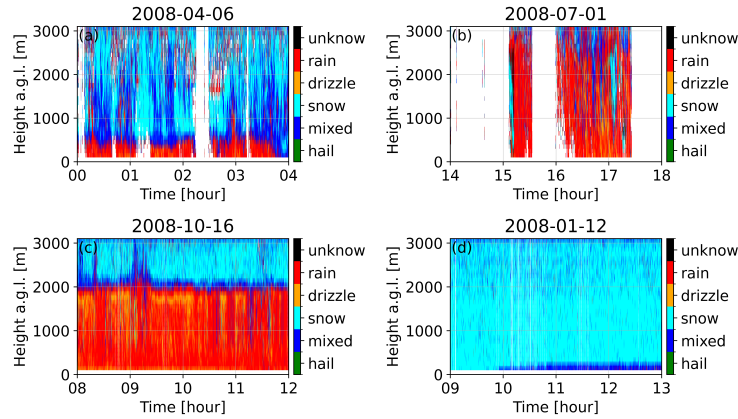
Figure 3: Examples of various rainfall patterns in various seasons. (a) Spring: rain with low melting layer on April 6, 2008. (b) Summer: convective rain on July 1, 2008. (c) Autumn: stratiform rain on October 16, 2008. (d) Winter: mixed (rain and snow or graupel) on January 12, 2008.

Table 2
Rain detection results using GBDT based method and ILW threshold method in two testing schemes.

Method	GBDT				ILW_R (0.4 mm)			
	Accuracy [%]	Precision [%]	Recall [%]	F1 Score [%]	Accuracy [%]	Precision [%]	Recall [%]	F1 Score [%]
Testing scheme 1	100	100	100	100	73.6	99.9	46.9	63.8
Testing scheme 2	98.4	97.0	99.9	98.4	68.3	99.6	36.7	53.6

that there will be a small number of false rain detections, but almost no missed detections. The performance of the ILW threshold method in Testing Scheme 2 is significantly inferior to that in Testing Scheme 1, but the same missed detection with low recall. Figure 5 shows an example of the experimental results of rain detection of Testing scheme 2. Rain event is stratiform rain with a melting layer of around 1000 m from 22:53:10 UTC on January 24 to 04:15:20 UTC on January 25, 2008. In Figure 5(b), rain detected by MWR based on the GBDT method is completely consistent with rainfall measured by MRR except for several time points between 4:13 UTC to 4:15 UTC. In Figure 5(c), rain detected by ILW>0.4 mm is all correct, whereas rain cases below ILW=0.4 mm is missed by the ILW threshold method.

Figure 6 shows rain detection performance in various seasons. As shown in Figure 6(a), rain detection by the MWR based on the GBDT method achieves nearly 100% accuracy, precision, recall, and F1 score in all seasons, with the best performance observed in summer and winter. On the other hand, as shown in Figure 6(b), rain detection by the MWR based on the ILW threshold method achieves an precision close to 100% in all seasons, but other metrics are low. Performance was relatively good in the summer, with these metrics above 68%.

4. Discussion

Due to their low cost and wide geographical coverage, rain gauges are frequently used as target variables for developing machine learning rain detection methods (Chen et al., 2020). The method presented in this article can also consider using rain gauges to detect rain-contaminated data in microwave radiometer measurements. Nonetheless, rain gauges have their limitations, making the Micro Rain Radar (MRR) a more suitable option. First, the rain gauge is an in-situ instrument and can only measure precipitation that falls on the ground, whereas the microwave radiometer is a remote sensing instrument, and rain that does not reach the ground will also affect the radiation signal, such as virga (Beynon, 2022; Beynon and Hocke, 2022; Wang, Hocke, Nania, Cazorla, Titos, Matthey, Alados-Arboledas, Millares and Navas-Guzmán, 2024). Second, microwave radiometers are affected by various forms of liquid precipitation like rain, drizzle, and mixed but not by dry snow, whereas rain gauges measure dry snow, but lack the capability to distinguish between different precipitation types, such as distinguishing rain from dry snow. As a remote sensing instrument, micro rain radar can measure various precipitation types and classify them. Moreover, rain gauges may be affected by wind, evaporate water after rain, and be unable to hold all the rainwater and overflow during heavy rain, resulting in inaccurate measurements. Finally, the time resolution of
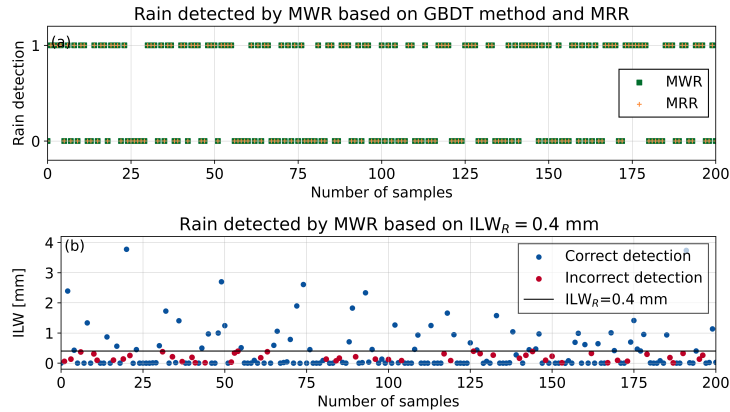
Figure 4: Experimental results of rain and no rain detection for Testing scheme 1. The data are the first 200 samples of the test set in Testing scheme 1. (a) Rain and no rain detected by microwave radiometer (MWR) based on GBDT method and MRR. No rain and rain-contaminated data are marked as 0 and 1. (b) Rain and no rain detected by MWR based on ILW$_R$=0.4 mm. The horizontal black line is the threshold ILW$_R$=0.4 mm. Correct or incorrect detection using ILW$_R$ is represented by blue and red points, respectively.

tropospheric microwave radiometers is as high as 1 to 10 seconds, whereas the common time resolution of rain gauges is 1 to 10 minutes. The 10-second time resolution of the micro rain radar is closer to the 11-second time resolution of the microwave radiometer.

The ILW threshold method commonly adopts an empirical value of ILW$_R$=0.4 mm to exclude rain-contaminated data in TROWARA measurements. To find methods or instrumental observations that effectively assess the reliability of the ILW threshold of 0.4 mm is challenging. A smaller ILW threshold can result in the exclusion of valuable cloud information, whereas raising the threshold risks including data that has been contaminated by rain. Figure 7(a) shows that using ILW$_R$ =0.4 mm successfully covers most rain-free samples, although it does result in the loss of a small number of samples in the range of 0.4 mm to 0.6 mm. Figure 7(b) demonstrates that an ILW threshold of 0.4 mm fails to detect rain accurately. For example, from 21:30:50 UTC to 23:04:50 UTC on February 1, 2008, there was rainfall that the ILW threshold method did not register. This oversight highlights the need to employ more sophisticated techniques, such as the GBDT method, to more effectively detect rain-contaminated data.

By selecting or constructing features that distinctly capture the physical characteristics pertinent to rain detection, this makes the GBDT model of this article a physics-informed machine learning that is interpretable and has strong predictive capabilities. Figure 8 shows the variable importance of features included in GBDT method for rain detection. The first two important features are brightness temperature at 31.4 GHz ($T_{B,31}$) and infrared cloud base brightness temperature ($T_{B,IR}$). The frequency 31.4 GHz is more sensitive to microwaves from atmospheric liquid water (Hocke, Navas-Guzmán, Moreira, Bernet and Mätzler,

2017). $T_{B,IR}$ can obtain cloud dynamics and then infer possible rain events by monitoring the temperature changes at the cloud base (Wang and Hocke, 2022). The third to sixth important features are, respectively, air pressure (P), integrated water vapor (IWV), relative humidity (RH), and air temperature (T). These variables evolve according to various rainfall types before, during, and after rain (Wang and Hocke, 2022; Wang et al., 2024). Furthermore, these feature variables were chosen so that the method can also be directly applied to other tropospheric microwave radiometers. For example, the Humidity and Temperature Profiler (HATPRO) radiometer, widely used in global weather monitoring and forecasting networks, includes the 31.4 GHz microwave channel and additional weather sensors, often complemented by an infrared radiometer.

We also applied the machine learning method Support Vector Machine (SVM) to detect rain-contamination in microwave radiometer data (Cortes and Vapnik, 1995). Results show that for Testing scheme 2, the detection accuracy, precision, recall, and F1 score across of all testing samples are 88.1%, 81%, 99.5%, and 89.3%, respectively. In general, the performance of the SVM method is slightly inferior to the GBDT method when using microwave radiometer time series data for rain detection. Potential reasons may stem from inherent characteristics of these two models. The SVM method tends to be less effective than the GBDT method in handling complex non-linear datasets. Although neither GBDT nor SVM are explicitly designed for time series data, GBDT often exhibits superior adaptability, likely due to its ability to automatically interact features and its robustness against overfitting in large datasets.
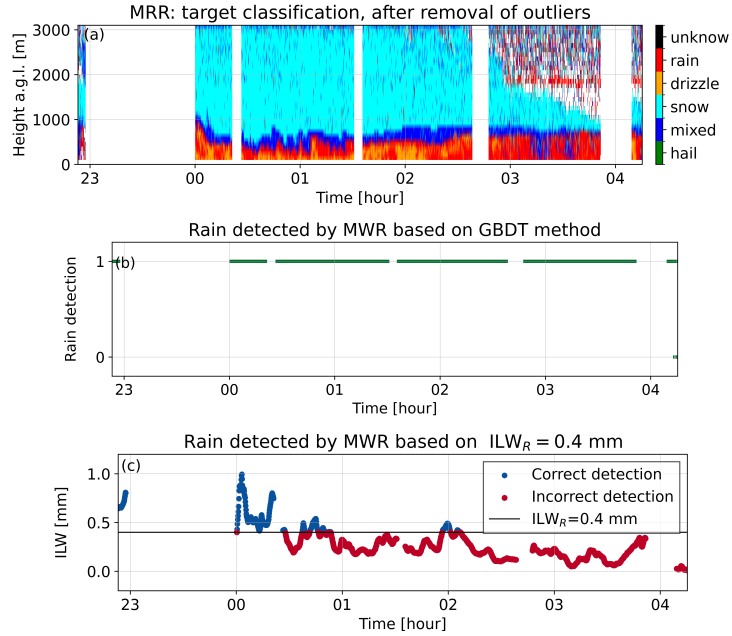
Figure 5: Experimental results of rain detection for Testing scheme 2. The data is all rain times in the January test set (22:53:10 UTC on January 24 to 04:15:20 UTC on January 25, 2008) of Testing scheme 2. (a) MRR target classification data with outlier lines removed and rainfall duration exceeding 3 minutes. (b) Rain detected by MWR based on GBDT method. No rain and rain-contaminated data are marked as 0 and 1. (c) Rain detected by MWR based on ILW_R=0.4 mm. The horizontal black line is the threshold ILW_R=0.4 mm. Correct or incorrect detection using ILW_R is represented by blue and red points, respectively.
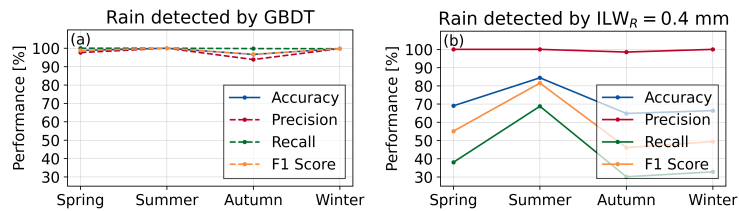
Figure 6: Detection performance in four seasons. (a) Detection performance using GBDT method. Metrics accuracy, precision, recall and f1 score are blue straight line, red dashed line, green dashed line, and orange dashed line respectively. (b) Detection performance using ILW threshold method. The threshold is ILW_R=0.4 mm. Metrics accuracy, precision, recall and f1 score are blue straight line, red straight line, green straight line, and orange straight line respectively.
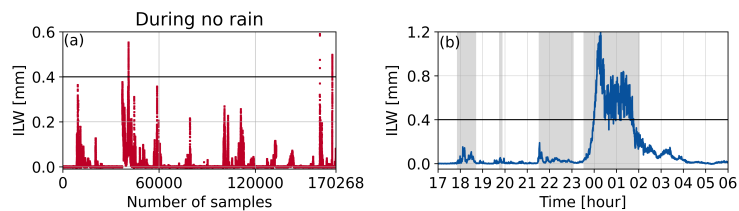
Figure 7: (a) ILW in all samples during no rain. (b) ILW from 17:00 UTC on February 1 to 6:00 UTC on February 2, 2008. The horizontal black line is the threshold ILW_R=0.4 mm. Gray shades represent MRR-detected rainfall.
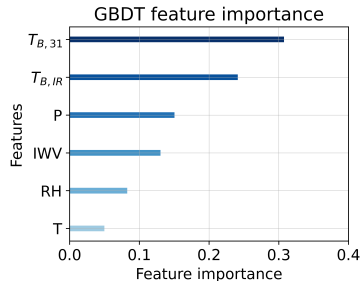
Figure 8: Variable importance of features included in GBDT method for rain detection.

5. Conclusions

This article presents a GBDT-based rain detection method by accurately classifying microwave radiometer data into rain-free and rain-contaminated categories. By understanding the precipitation types (rain, drizzle, and mixed) that affect microwave radiometer brightness temperatures, precipitation events contaminating microwave radiometer data can first be accurately captured from the MRR target classification. After data preprocessing removes outliers, one-hot encoding of months is then performed to consider that various seasons contain various rainfall patterns. Finally, these characteristics, along with meteorological parameters, are selected as feature variables to train the GBDT classification model for rain detection.

The method was validated using two testing schemes on the Swiss Plateau in 2008: ten-fold cross-validation technique and time series test sets. The simultaneous target classification data collected by the MRR is used as actual rainfall data to determine whether the microwave radiometer data is contaminated by raindrops in the atmosphere. The results show that this method, compared to ILW threshold method, achieves high detection accuracy in both testing schemes. Specifically, while the ILW threshold method reached accuracy of 73.6% and 68.3% for the two schemes respectively, the GBDT method achieved 100% and 98.4%. This proves that the GBDT method exhibits strong generalization capabilities and is effective even on time series test sets. This is particularly advantageous given the time-dependent nature of rainfall occurrences. Moreover, the method presented in this article accounts for different rainfall patterns that vary across seasons, such as stratiform rain with various melt layer heights and convective rain. The GBDT method selects feature vectors based on the physical relationships between rainfall and variables. The choice of these features also enables the application of this method to other tropospheric microwave radiometers. In contrast, the ILW threshold method shows significant missing detection in identifying rain-contaminated data. The rain detection method of this article is anticipated to be useful for identifying water films on radomes caused by rainfall for outdoor tropospheric microwave radiometers and important for other remote sensing instruments, such as Fourier transform infrared (FTIR) spectrometers.

CRediT authorship contribution statement

Declaration of Competing Interest

The authors declare that they have no known competing financial interests or personal relationships that could have appeared to influence the work reported in this paper.

Data availability

Data will be made available on request.

Acknowledgments

References

Battaglia, A., Simmer, C., Crewell, S., Czekala, H., Emde, C., Marzano, F., Mishchenko, M., Pardo, J., Prigent, C., et al., 2006. Emission and scattering by clouds and precipitation. Thermal microwave radiation: Applications for remote sensing, edited by: Mätzler, C , 101–233.

Beynon, R., 2022. Observations of virga precipitation with a micro rain radar. Master's Thesis, Physik-Institut, Universität Zürich, Zürich, Switzerland .

Beynon, R., Hocke, K., 2022. Snow virga above the swiss plateau observed by a micro rain radar. Remote Sensing 14. doi:10.3390/rs14040890.

Bohren, C.F., Huffman, D.R., 2008. Absorption and scattering of light by small particles. John Wiley & Sons.

Chen, X., Huang, W., Zhao, C., Tian, Y., 2020. Rain detection from x-band marine radar images: A support vector machine-based approach. IEEE Transactions on Geoscience and Remote Sensing 58, 2115–2123. doi:10.1109/TGRS.2019.2953143.

Cortes, C., Vapnik, V., 1995. Support-vector networks. Machine learning 20, 273–297.

Cossu, F., Hocke, K., Martynov, A., Martius, O., Mätzler, C., 2015. Atmospheric water parameters measured by a ground-based microwave radiometer and compared with the wrf model. Atmospheric Science Letters 16, 465–472. doi:10.1002/asl.583.

Ellison, W., 2006. Freshwater and sea water. thermal microwave radiation: Applications for remote sensing 52, 431–455.

Friedman, J.H., 2001. Greedy function approximation: a gradient boosting machine. Annals of statistics , 1189–1232.

Friedman, J.H., 2002. Stochastic gradient boosting. Computational statistics & data analysis 38, 367–378.

Fu, X., Kan, G., Liu, R., Liang, K., He, X., Ding, L., 2023. Research on rain pattern classification based on machine learning: A case study in pi river basin. Water 15. doi:10.3390/w15081570.

Garcia-Benadi, A., Bech, J., Gonzalez, S., Udina, M., Codina, B., Georgis, J.F., 2020. Precipitation type classification of micro rain radar data using an improved doppler spectral processing methodology. Remote Sensing 12. doi:10.3390/rs12244113.

Hocke, K., Bernet, L., Hagen, J., Murk, A., Renker, M., Mätzler, C., 2019. Diurnal cycle of short-term fluctuations of integrated water vapour above switzerland. Atmospheric Chemistry and Physics 19, 12083–12090. doi:10.5194/acp-19-12083-2019.

Hocke, K., Navas-Guzmán, F., Moreira, L., Bernet, L., Mätzler, C., 2017. Oscillations in atmospheric water above switzerland. Atmospheric Chemistry and Physics 17, 12121–12131. doi:10.5194/acp-17-12121-2017.

Krochin, W., Navas-Guzmán, F., Kuhl, D., Murk, A., Stober, G., 2022. Continuous temperature soundings at the stratosphere and lower mesosphere with a ground-based radiometer considering the zeeman effect. Atmospheric Measurement Techniques 15, 2231–2249. doi:10.5194/amt-15-2231-2022.

Lei, H., Zhao, H., Ao, T., 2022. A two-step merging strategy for incorporating multi-source precipitation products and gauge observations using machine learning classification and regression over china. Hydrology and Earth System Sciences 26, 2969–2995. doi:10.5194/hess-26-2969-2022.

Liu, S., Yin, Y., Chu, Z., An, S., 2020. Cdl: A cloud detection algorithm over land for mwhs-2 based on the gradient boosting decision tree. IEEE Journal of Selected Topics in Applied Earth Observations and Remote Sensing 13, 4542–4549. doi:10.1109/JSTARS.2020.3014136.

Lucas, A., 2014. Ising formulations of many np problems. Frontiers in physics 2, 74887.

Löhnert, U., Crewell, S., 2003. Accuracy of cloud liquid water path from ground-based microwave radiometry 1. dependency on cloud model statistics. Radio Science 38. doi:10.1029/2002RS002654.

Ma, L., Zhang, G., Lu, E., 2018. Using the gradient boosting decision tree to improve the delineation of hourly rain areas during the summer from advanced himawari imager data. Journal of Hydrometeorology 19, 761 − 776. doi:10.1175/JHM-D-17-0109.1.

Marzano, F., Cimini, D., Ciotti, P., Ware, R., 2005a. Modeling and measurement of rainfall by ground-based multispectral microwave radiometry. IEEE Transactions on Geoscience and Remote Sensing 43, 1000–1011. doi:10.1109/TGRS.2004.839595.

Marzano, F.S., Cimini, D., Ware, R., 2005b. Monitoring of rainfall by ground-based passive microwave systems: models, measurements and applications. Advances in Geosciences 2, 259–265. doi:10.5194/adgeo-2-259-2005.

Marzano, F.S., Fionda, E., Ciotti, P., 2006. Neural-network approach to ground-based passive microwave estimation of precipitation intensity and extinction. Journal of Hydrology 328, 121–131. URL: https://www.sciencedirect.com/science/article/pii/S0022169405006438, doi:10.1016/j.jhydrol.2005.11.042.

Mätzler, C., Morland, J., 2009. Refined physical retrieval of integrated water vapor and cloud liquid for microwave radiometer data. IEEE Transactions on Geoscience and Remote Sensing 47, 1585–1594. doi:10.1109/TGRS.2008.2006984.

Mätzler, C., Morland, J., 2014. Advances in surface-based radiometry of atmospheric water. IAP Research Report 2008-02-MW; Institute of Applied Physics, University of Bern: Bern, Switzerland .

Mätzler, C., Wegmüller, U., 1987. Dielectric properties of freshwater ice at microwave frequencies. Journal of Physics D: Applied Physics 20, 1623. doi:10.1088/0022-3727/20/12/013.

METEK, 2009. Mrr physical basics valid for mrr service version 5.2.1.0. METEK: Elmshorn, Germany .

Mishchenko, M.I., Yatskiv, Y.S., Rosenbush, V.K., Videen, G., 2011. Polarimetric detection, characterization and remote sensing. Springer.

Morland, J., 2002. Trowara-tropospheric water vapour radiometer: Radiometer review and new calibration model. IAP Research Report 2008-02-MW; Institute of Applied Physics, University of Bern: Bern, Switzerland .

Morland, J., 2007. Trowara-rain flag development and stability of instrument and calibration. IAP Research Report 2008-02-MW; Institute of Applied Physics, University of Bern: Bern, Switzerland .

Peter, R., Kämpfer, N., 1992. Radiometric determination of water vapor and liquid water and its validation with other techniques. Journal of Geophysical Research: Atmospheres 97, 18173–18183. doi:10.1029/92JD01717.

Pudashine, J., Guyot, A., Petitjean, F., Pauwels, V.R.N., Uijlenhoet, R., Seed, A., Prakash, M., Walker, J.P., 2020. Deep learning for an improved prediction of rainfall retrievals from commercial microwave links. Water Resources Research 56, e2019WR026255. doi:10.1029/2019WR026255.

Rayleigh, L., 1871. On the light from the sky, its polarization and colour. Phil Mag 41, 274.

Rodriguez, J.D., Perez, A., Lozano, J.A., 2010. Sensitivity analysis of k-fold cross validation in prediction error estimation. IEEE Transactions on Pattern Analysis and Machine Intelligence 32, 569–575. doi:10.1109/TPAMI.2009.187.

Sauvageat, E., Hocke, K., Maillard Barras, E., Hou, S., Errera, Q., Haefele, A., Murk, A., 2023. Microwave radiometer observations of the ozone diurnal cycle and its short-term variability over switzerland. Atmospheric Chemistry and Physics 23, 7321–7345. doi:10.5194/acp-23-7321-2023.

Sauvageat, E., Maillard Barras, E., Hocke, K., Haefele, A., Murk, A., 2022. Harmonized retrieval of middle atmospheric ozone from two microwave radiometers in switzerland. Atmospheric Measurement Techniques 15, 6395–6417. doi:10.5194/amt-15-6395-2022.

Shen, Z., Yong, B., 2021. Downscaling the gpm-based satellite precipitation retrievals using gradient boosting decision tree approach over mainland china. Journal of Hydrology 602, 126803. doi:10.1016/j.jhydrol.2021.126803.

Wang, W., Hocke, K., 2022. Atmospheric effects and precursors of rainfall over the swiss plateau. Remote Sensing 14. doi:10.3390/rs14122938.

Wang, W., Hocke, K., Mätzler, C., 2021. Physical retrieval of rain rate from ground-based microwave radiometry. Remote Sensing 13. doi:10.3390/rs13112217.

Wang, W., Hocke, K., Nania, L., Cazorla, A., Titos, G., Matthey, R., Alados-Arboledas, L., Millares, A., Navas-Guzmán, F., 2024. Interrelations of precipitation, aerosols, and clouds over andalusia, southern spain, revealed by the andalusian global observatory of the atmosphere (agora). Atmospheric Chemistry and Physics 24, 1571–1585. doi:10.5194/acp-24-1571-2024.

Wang, W., Murk, A., Sauvageat, E., Fan, W., Dätwyler, C., Hervo, M., Haefele, A., Hocke, K., 2023. An indoor microwave radiometer for measurement of tropospheric water. IEEE Transactions on Geoscience and Remote Sensing 61, 1–13. doi:10.1109/TGRS.2023.3261067.

Zhuang, H.R., Lehner, F., DeGaetano, A.T., 2024. Improved diagnosis of precipitation type with lightgbm machine learning. Journal of Applied Meteorology and Climatology 63, 437 − 453. doi:10.1175/JAMC-D-23-0117.1.

5

PHYSICAL RETRIEVAL OF RAIN RATES

5.1 SUMMARY OF THE STUDY

Physical algorithms are reasonable, interpretable, and estimate atmospheric parameters with high accuracy by analyzing atmospheric physical mechanisms. However, very few studies have applied physical algorithms to ground-based microwave radiometers for retrieving rain rates. The article presented in this chapter described and validated a novel physical rain rate retrieval method for ground-based microwave radiometer. The method iteratively adjusts the rain effective temperature using the radiative transfer equation to determine rain optical depth and then estimates rainfall based on the relationship between rain rate and rain optical depth. Compared to two nearby rain gauges and ERA5 reanalysis data, the rain rate retrieved at the 31 GHz channel closely matches actual situation.

The study contributed to the Global Climate Observing System (GCOS) Project "Operational Monitoring of the Rain Rate by Ground-based Microwave Radiometry in Switzerland". For other work packages of the GCOS project, I have also completed the following tasks:

- I improved the physical rain rate retrieval algorithm of TROWARA , making it capable of processing the HATPRO dataset in Payerne. However, HATPRO rain rate estimates show an unacceptable positive bias compared to Payerne rain gauge measurements, possibly due to the water film on the HATPRO radome during rain. Further research on this issue is presented in Chapter 7.

- I processed the available data from the HATPRO radiometers in Schaffhausen and Grenchen. As expected, the outdoor HATPRO radiometers in these locations appear to overestimate rain rates, similar to the HATPRO in Payerne.

- I built the STARTWAVE database website for near real-time operational processing of TROWARA rain rates. It is publicly accessible on the Internet (`https://startwave.mw.iap.unibe.ch/`). The website displays daily cumulative rain, monthly and annual rain rate averages in Bern, and provides downloadable long-term time series of TROWARA rain rates in Bern from November 2002 to the present, HATPRO rain rates in Payerne from September 2009 to February 2021, HATPRO rain rates

in Schaffhausen from March 2010 to May 2012, HATPRO rain rates in Grenchen from July 2020 to July 2021.

The GCOS Steering Committee raised the question of whether rain rates measured by ground-based microwave radiometers can replace the existing network of rain gauges. The answer is that achieving this is difficult because running a dense network of microwave radiometers is expensive and time-consuming. Accurate rain rate measurements for tropospheric microwave radiometers remain challenging, but the algorithm could be advantageous for cross-validating precipitation obtained from atmospheric models and satellite observations (Hocke, 2022).

The following article was peer-reviewed and published in Remote Sensing in June 2021.

5.2 PUBLICATION

FULL CITATION

Wang Wenyue, Klemens Hocke, and Christian Mätzler (2021). "Physical retrieval of rain rate from ground-based microwave radiometry." In: *Remote Sensing* 13.11, pp. 2217. https://doi.org/10.3390/rs13112217.

remote sensing

MDPI

Article

Physical Retrieval of Rain Rate from Ground-Based Microwave Radiometry

Wenyue Wang [1,2,*], Klemens Hocke [1,2] and Christian Mätzler [1,2]

[1] Institute of Applied Physics, University of Bern, CH-3012 Bern, Switzerland; klemens.hocke@iap.unibe.ch (K.H.); christian.matzler@iap.unibe.ch (C.M.)
[2] Oeschger Centre for Climate Change Research, University of Bern, CH-3012 Bern, Switzerland
* Correspondence: wenyue.wang@iap.unibe.ch

Abstract: Because of its clear physical meaning, physical methods are more often used for space-borne microwave radiometers to retrieve the rain rate, but they are rarely used for ground-based microwave radiometers that are very sensitive to rainfall. In this article, an opacity physical retrieval method is implemented to retrieve the rain rate (denoted as Opa-RR) using ground-based microwave radiometer data (21.4 and 31.5 GHz) of the tropospheric water radiometer (TROWARA) at Bern, Switzerland from 2005 to 2019. The Opa-RR firstly establishes a direct connection between the rain rate and the enhanced atmospheric opacity during rain, then iteratively adjusts the rain effective temperature to determine the rain opacity, based on the radiative transfer equation, and finally estimates the rain rate. These estimations are compared with the available simultaneous rain rate derived from rain gauge data and reanalysis data (ERA5). The results and the intercomparison demonstrate that during moderate rains and at the 31 GHz channel, the Opa-RR method was close to the actual situation and capable of the rain rate estimation. In addition, the Opa-RR method can well derive the changes in cumulative rain over time (day, month, and year), and the monthly rain rate estimation is superior, with the rain gauge validated R^2 and the root-mean-square error value of 0.77 and 22.46 mm/month, respectively. Compared with ERA5, Opa-RR at 31GHz achieves a competitive performance.

Keywords: rain rate; opacity; physical algorithm; ground-based microwave radiometer; long-term monitoring; precipitation; rain gauge; ERA5

1. Introduction

The rain rate is a key meteorological parameter used to measure the amount of rainfall over time, and its level is closely tied to human life. Low rain rates are not sufficient to irrigate crops. High rain rates may cause flash floods, soil erosion, and urban waterlogging. Accurate rain rate information is essential for climate change models, water resources management, and assimilation into numerical weather prediction (NWP) models to improve rainfall forecasts [1,2].

To monitor rainfall, the rain gauge was developed to measure rainfall at sparsely distributed points, and it is the most commonly used instrument for comparing and verifying land rain rates derived from space-borne and ground-based microwave radiometers. The weather radar, on the other hand, can provide the three-dimensional (3D) image of rain in addition to the rain rate over a given location, but the accuracy is limited by a strong dependence on the drop-size distribution, ground clutter, instrument calibration, and beam blockage. Even though space-borne microwave radiometers have been successfully applied to rain-rate retrieval on a global scale and proved that microwave radiometry is fairly accurate, at least over the ocean, its disadvantages include low spatial resolution and temporal coverage; large uncertainties are found over land due to its heterogeneity and reduced contrast with regard to the rain signal [3]. The ground-based radiometry is suitable for operation under rainy conditions, and for the purpose of retrieving simultaneously water

vapor, liquid water path [4,5], and rain [6]. Its main advantage is the large atmospheric signal by atmospheric emitters, and especially for rain, against a cold and homogeneous sky background [7].

The rain-rate retrievals of microwave radiometers can be divided into (1) statistical algorithms, (2) physical-statistical algorithms, and (3) physical algorithms. Statistical algorithms do not need to resort to complex radiation transmission models, so their calculation speed is high and as a consequence their timeliness. Won et al. [8] used two simple statistical algorithms, linear and logarithmic regression, to estimate the rain rate, and they analyzed the relationship between brightness temperature and rain rate. Using historical radiosonde data for training, Xu et al. [9] investigated the influence of the off-zenith neural network method on the rain rate measurement of microwave radiometers. However, statistical algorithms not only rely excessively on the number and representativeness of measured samples, but also lack a physical explanation for the retrieval process. To overcome these limitations, the physical-statistical algorithm is proposed to estimate the rain rate. For example, Marzano et al. [3] conducted a statistical analysis of the relationship between brightness temperature and rain rate on land, based on the numerical simulation data set of the radiative transfer model, using ordinary multiple regression and a variance-constrained regression algorithm.

The physical algorithm, compared with the above two algorithms, is more reasonable and can get a higher estimated accuracy of atmospheric parameters, because it can analyze from the perspective of atmospheric physical mechanisms and gain an in-depth understanding of the retrieval process. However, few studies used this algorithm for ground-based microwave radiometers. For example, Marzano et al. [7] performed detailed radiometric simulations to derive the rain rate from measurements of ground-based passive microwave systems.

In 2008, Mätzler and Morland [10] suggested a new physical method of the rain rate estimation for a ground-based microwave radiometer and showed that the atmospheric opacity at 31 GHz is closely related to the rain rate. However, this method only tested a few rain events, and whether it can estimate the rain rate in the long-term is not yet clear. The TROpospheric WAter RAdiometer (TROWARA) is a ground-based microwave radiometer that has provided long-term high-quality data of the atmospheric opacity (optical depth) every 6 s in Bern, Switzerland since 2005 [11]. Therefore, the objective of this article is to use the rain zenith opacity derived from TROWARA for the long-term rain rate using the new physical retrieval method and to perform operational processing and archiving of the rain rate estimated by the TROWARA radiometer. For comparison, the correlation between the rain rate from TROWARA and the rain rate measured by the rain gauges was determined for the assessment of the performance of the rain rate retrieval. Later, the rain rates of ECMWF Reanalysis v5 (ERA5) were compared with those of the rain gauges.

2. Data Set

2.1. Ground-Based Microwave Radiometer Data

The ground-based microwave radiometer, TROWARA, started working on the roof of the Physics and Mathematics (ExWi) Building of the University of Bern in 1994. The frequencies of the TROWARA microwave channel are 21.4 GHz (band width = 100 MHz) and 31.5 GHz (band width = 200 MHz), and the thermal infrared radiometer (IR) channel is at λ = 9.6–11.5 μm. The antenna coil of TROWARA at the full width of half-power is 4° and observes the atmosphere in the southeast direction at an elevation angle of 40°. TROWARA was designed for retrieving the integrated water vapor (IWV) and integrated liquid water (ILW) of cloud droplets, and it provides a practically uninterrupted time series with a time resolution of 6 s in almost all-weather during day and night.

The radiative transfer equation in the Rayleigh-Jeans approximation is:

$$T_{B,i} = T_C \cdot e^{-\tau_i/\mu} + T_{\text{mean},i} \cdot \left(1 - e^{-\tau_i/\mu}\right) \tag{1}$$

where i represents the frequency channel (e.g., 21 GHz). $T_{B,i}$ is the radiant brightness temperature observed by the radiometer, and $T_C = 2.7\ K$ is the cosmic background temperature. τ_i is the zenith opacity. μ is the cosine of the zenith angle θ, i.e., $\mu = \cos\theta$. $T_{\text{mean},i}$ is the effective mean temperature of the atmosphere [12,13].

The zenith opacity can be solved by Equation (1).

$$\tau_i = -\mu \cdot ln\left(\frac{T_{\text{mean},i} - T_{B,i}}{T_{\text{mean},i} - T_C} \right) \tag{2}$$

In fact, the microwave radiation measured by TROWARA during rain is strongly enhanced by the microwave emission from raindrops ($d > 0.2$ mm) [11]. Thus, it is raining when ILW exceeds a threshold value of about 0.4 mm. In times of rain, the retrieval of ILW of cloud droplets is not possible. Instead, TROWARA will provide the rain rate [10]. The retrieval of ILW uses a refined physical algorithm based on the zenith opacity for ground-based microwave radiometers [14].

$$\text{ILW} = \frac{\tau_{31} - a_{31} - \beta \cdot (\tau_{21} - a_{21})}{c_{21} \cdot (1 - \beta \cdot \gamma)} \tag{3}$$

where a_i ($i = 21$ and 31) is the absorption of the dry atmosphere. $\beta = b_{31}/b_{21}$, and the coefficient b_i is the specific absorption by water vapor. $\gamma = c_{31}/c_{21}$, and the coefficient c_i is the specific absorption of cloud liquid water in the Rayleigh approximation. It is computed from the dielectric constant of liquid water [15].

The initial construction and retrieval principles of TROWARA were given in Peter and Kämpfer [16]. To estimate the antenna temperature well, a new radiometer model was established, which uses continuous internal calibration and external tipping calibration a few times each year [17]. In November 2002, the instrument was moved to an indoor laboratory to observe the sky, and the antenna received the atmospheric microwave radiation through a transparent window. The indoor operation of TROWARA prevents the antenna from being exposed to rain [18]. In 2004, the new refined physical scripts [14] were used to retrieve IWV and ILW, and TROWARA has continuously performed measurements in Bern since then [11]. Therefore, to maintain the consistency of measurements and not be affected by previous outdoor observations, we presume that the data after 2005 are well-suited for the rain-rate estimation.

2.2. Meteorological Data

A standard weather station is located on the ExWi building together with TROWARA and is known as the ExWi weather station. Another weather station is an automatic Vaisala weather station at the Zimmerwald Observatory near Bern, called Zimmerwald weather station. The weather data are composed of surface air temperature (T_S, K), the surface relative humidity (RH$_S$, %), the surface atmospheric pressure (P_S, hPa), rain rate, and other parameters measured by the ExWi and Zimmerwald weather stations with a time resolution of 10 min. Registered users can access the data for free from the STudies in Atmospheric Radiative Transfer and WAter Vapor Effects (STARTWAVE) database (http://www.iapmw.unibe.ch/research/projects/STARTWAVE/, accessed on 3 June 2021).

Under non-rainfall conditions, the effective mean temperature $T_{\text{mean},i}$ is estimated from the linear combination:

$$T_{\text{mean},i} = A_{0,i} + A_{1,i} \cdot T_S + A_{2,i} \cdot \text{RH}_S + A_{3,i} \cdot P_S \tag{4}$$

where the coefficients $A_{n,i}$ ($n = 0, 1, 2, 3$) were statistically obtained by radiosonde measurements using the Rosenkranz [19] radiative model and making corrections through clear sky observations. The information of $T_{\text{mean},i}$ is mainly derived from T_S. The parameters RH$_S$ and P_S are used to consider the statistical characteristics of atmospheric anomalies, such as detecting the atmosphere above the boundary layer.

2.3. Rain-Rate Measurements

The rain gauge at ExWi weather station is a tipping bucket rain gauge with a resolution of 0.2 mm, and its time resolution is 10 min. The maximum rain rate value that it can observe is 50 mm/10 min. The tipping bucket rain gauge guides the rain in the receiving funnel into two small bucket collectors. When a certain amount of rain (0.2 mm) accumulates in one bucket, the weight of the water tips it and empties it. Then another bucket moves under the funnel to collect the rain. The advantage of the tipping bucket rain gauge is that it can easily identify rainfall intensity (light, moderate, heavy, or violent). Observers can count the number of rain gauge marks within a set time period (10 min) to determine the rain intensity.

However, the accuracy of tipping bucket rain gauges is usually not as good as that of standard rain gauges. For example, it is possible that the bucket will not tip over until the rain stops, and it may take one or two drops of rain to tip the bucket when the next rain starts. On the other hand, the tipping bucket rain gauge tends to underestimate the rain rate [20,21], because it loses rain every time it tips [22].

The rain gauge at the Zimmerwald weather station has the same resolution as the ExWi rain gauge (0.2 mm). In addition, an optical rain sensor with a resolution of 0.1 mm at the ExWi weather station is another ground-based rain rate observation, and its time resolution is 10 min.

2.4. ERA5 Reanalysis Data

ERA5 reanalysis is an atmospheric reanalysis product recently released by the European Centre for Medium-Range Weather Forecasts (ECMWF) with a time resolution of 1 h and a horizontal resolution of 30 km grid spacing [23]. ERA5 has been providing rain rate data on the global land surface since 1950 and has assimilated rain rate information from ground radar measurements since 2009. ERA5 used approximately 24 million observations every day by the end of 2018. Users can access rain rates for free from the Climate Data Store (CDS) website (https://cds.climate.copernicus.eu, accessed on 3 June 2021).

ERA5 uses the all-sky method instead of the clear sky method to assimilate a large number of satellite channels that are sensitive to humidity. ERA5 not only provides new information in rainy areas, but also solves the problem of abnormal precipitation caused by the radiation assimilation technology on rainy days [24]. ERA5 also contains the bias correction of assimilated data and benefits from model physics and core dynamics developed over the years. In addition, the large-scale precipitation program of ERA5 has been upgraded, including the improvement of the prognostic variables of rainfall and snowfall, and many optimizations in the microphysical parameterization, especially for warm rain processes [25].

However, previous research suggested that ERA5 reanalysis may overestimate the rain rate. For example, Xu et al. [26] indicated that ERA5 typically has an overestimation of the spring rain rate in the Assiniboine River Basin. Nogueira's [27] process-based analysis shows that ERA5 tends to overestimate precipitation and reveals positive bias (1 mm/day) in most tropical oceans, as well as the Himalayas and Andes. Amjad et al. [28] evaluated the rain rate of ERA5 under the complex terrain and climate change in Turkey and found that ERA5 has a wet bias (0.5 mm/day) and consistently overestimates the rain rate in all relatively wetter and slope levels. Moreover, ERA5 is not so reliable to distinguish between rainy and non-rainy days (at least for Bern). Its original precipitation data show that there is rain for 93% of the days from 2005 to 2019, which is unreasonable and will lead to overestimation. However, our study avoids much of the overestimation of ERA5 because the rain events we use are simultaneously available in all data sets. This ensures that there will not be a situation where ERA5 detects rain on a certain day, while TROWARA and rain gauges cannot detect it.

3. Methods

3.1. Physical Retrieval Method Opa-RR for Rain-Rate Estimation

3.1.1. Effective Zenith Opacity and Specific Rain Absorption

Figure 1 shows the change in the total zenith opacity over time during a 6-day rain event in 2019. The total zenith opacity is the sum of the rain zenith opacity $\tau_{R,i}$ and the non-rain zenith opacity $\tau_{0,i}$, and their calculations are described in the next subsection. As it can be observed from Figure 1, the total zenith opacity increases significantly when the rain gauge detects rain. Moreover, the more accumulated rain in a short time (moderate and heavy rain), the more the change of the total zenith opacity. Assuming the height of the rain layer is known, this indicates that the zenith opacity is an excellent proxy for rain rate.
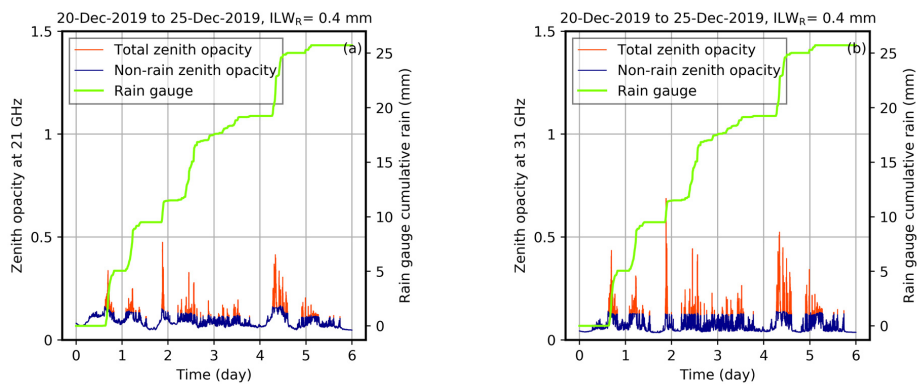
Figure 1. An example of the total zenith opacity (red), the non-rain zenith opacity (blue), and the ExWi rain gauge cumulative rain (green) versus time from 20 December 2019 to 25 December 2019. (**a**)The total zenith opacity measured by TROWARA at 21 GHz. (**b**) The total zenith opacity measured by TROWARA at 31 GHz.

The radiative transfer equation of the rainy atmosphere usually includes the treatment of radiation scattered by raindrops. Here we avoid considering the interaction of radiation with raindrops. We still apply Equation (2) for the computation of an effective zenith opacity τ_i for ground-based radiometry. Scattering is included in a simplified way. During the rainfall period, the zenith opacity is be expressed as:

$$\tau_i = (a_i + b_i \cdot \text{IWV} + c_i \cdot \text{ILW}) + \tau_{R,i}$$
$$\tau_{R,i} = c_i \cdot G_{M,i} \cdot \text{IRL} \tag{5}$$

The content in the bracket of Equation (5) is the zenith opacity without rain, where the coefficients a_i, b_i, and c_i are the same as in Equation (3). The contribution of $\tau_{R,i}$ is caused by the column of precipitation. $G_{M,i}$ is the Mie gain of raindrops, which can reach 10 at 21 GHz and 7 at 31 GHz [29], IRL is the integrated rain liquid, which is related to the rain rate R_i as shown below:

$$\text{IRL} = R_i \cdot H_R / v \tag{6}$$

where H_R is the height of the rain column, and we assume a homogeneous rain column. H_R is calculated by the temperature lapse rate $\Gamma = dT/dH$, the surface temperature T_S, and the temperature of melting layer $T_{\text{ML}} = 273.15\ K$, i.e., $H_R = (T_S - T_{\text{ML}})/\Gamma$. The temperature lapse rate Γ depends on weather conditions and is generally more than 4 K/km but less than 8 K/km [30]. v is the vertical fall velocity of rain.

Since the dielectric loss of ice is very small, the absorption of dry snow above the rain layer can be ignored. Furthermore, we ignore the influence of wet snow in the melting layer and consider the rain column, only.

For the frequencies used, the absorption coefficient of the rainy atmosphere is clearly larger than the scattering coefficient as shown by simulations using Mie theory for spherical raindrops [29]. This means that only single scattering may have an influence. In our geometry, the forward-scattered radiation is from the cold sky and thus can be ignored. However, the radiation emitted by the earth's surface can be scattered by raindrops in the backward hemisphere and received by the radiometer. The earth's surface has high emissivity. Its temperature is close to the rain temperature. This scattering of raindrops is simulated by enhanced emission of the raindrops, using an effective absorption coefficient given by the sum.

$$c_i \cdot G_{M,i} = \gamma_{a,R} + \gamma_{s,R} \cdot \frac{1 - <\cos\theta>}{2} \tag{7}$$

where $\gamma_{a,R}$ is the true absorption coefficient, while $\gamma_{s,R} \cdot \frac{1-<\cos\theta>}{2}$ is the fraction of the scattering coefficient $\gamma_{s,R}$ that causes scattering in the backward hemisphere, and $<\cos\theta>$ is the mean cosine of the scattering angle.

From Equations (5) and (6), the rain opacity can be written as:

$$\tau_{R,i} = g_{R,i} \cdot H_R \cdot R_i \tag{8}$$

where $g_{R,i} = c_i \cdot G_{M,i}/v$ is the specific and effective rain-absorption coefficient at frequency i. Computations of $g_{R,i}$ with Mie theory for different drop-size distributions and for a parameterized fall velocity [31] showed that the coefficient is almost constant, and nearly independent of rain rate. In addition, the temperature dependence is weak, so we assume constant values at a given frequency. At 21 GHz and at 31 GHz, the value of $g_{R,i}$ is set to 0.0165 h/mm/km and 0.0345 h/mm/km, respectively, which ensures an accuracy of 20% [10].

3.1.2. Rain Zenith Opacity from TROWARA

Radiation changes with rainfall, which leads to the atmospheric effective temperature to rise, while at the same time the low zenith opacity changes to a high zenith opacity. The variability of the atmosphere caused by rain makes it difficult to directly obtain precise formulas for radiative transfer problems of the rain layer. Based on Equation (5), the rain layer includes contributions from the non-rainfall atmosphere and contributions from rainfall. Therefore, an approximate but still accurate method is to assume that the additional contribution of rainfall to the atmosphere is an additional layer on the non-rainfall atmosphere, which can decouple the rainfall effect from the rest of the atmosphere. Figure 2b shows the radiative transfer model of this additional layer, which is the same as that of the non-rainfall period (Figure 2a). First, ILW is compared with the threshold value ILW_R and assume that $ILW \leq ILW_R$ means the non-rainfall period, and $ILW > ILW_R$ means the rainfall period. Next, Figure 2b shows the rain radiant brightness temperature $T_{B,R,i}$ observed by the ground-based radiometer TROWARA is derived from:

(1) The non-rainfall brightness temperature $T_{B,0,i}$. As shown in Figure 2, $T_{B,0,i}$ is the background temperature during the rainfall period and is calculated from the radiative transfer equation as:

$$T_{B,0,i} = T_C \cdot e^{-\tau_{0,i}/\mu} + T_{\text{mean},i} \left(1 - e^{-\tau_{0,i}/\mu} \right) \tag{9}$$

where $\tau_{0,i}/\mu$ is the non-rainfall slant-path opacity.

(2) The rain effective mean temperature $T_{\text{mean},R,i}$ [31].

$$T_{\text{mean},R,i} = \frac{\int_0^{\tau_{R,i}/\mu} T(\tau) \cdot e^{-\tau} \, d(\tau)}{1 - e^{-\tau_{R,i}/\mu}} \tag{10}$$

where τ is the slant-path opacity. $T(\tau)$ can be described by a linear temperature profile $T(\tau) = T_S - \Gamma \cdot h$. We assume that the constant extinction coefficient $\gamma_{e,R,i}$ in the homoge-

neous vertical rain column ranges from $h = 0$ to $h = H_R = \tau \cdot \mu / \gamma_{e,R,i}$ and no extinction above [32]. Insertion in Equation (10) gives:

$$T_{\text{mean},R,i}(\tau_{R,i}) = T_S - \Gamma \cdot \frac{\mu}{\gamma_{e,R,i}} \left[1 - \frac{\tau_{R,i}/\mu \cdot e^{-\tau_{R,i}/\mu}}{1 - e^{-\tau_{R,i}/\mu}} \right] \qquad (11)$$

From the function $f(x) = \frac{2\,[1 - e^{-x}(1 + x)]}{x \cdot (1 - e^{-x})} \cong e^{-0.19\,x}$ and replacing $\Gamma \cdot H_R$ with $T_S - T_{\text{ML}}$, we can write:

$$T_{\text{mean},R,i}(\tau_{R,i}) = T_S - \Gamma \cdot H_R \cdot \frac{f(\tau_{R,i}/\mu)}{2} \cong T_S - \frac{1}{2}\,(T_S - T_{\text{ML}}) \cdot e^{(-\,0.19\,\tau_{R,i}/\mu)} \qquad (12)$$
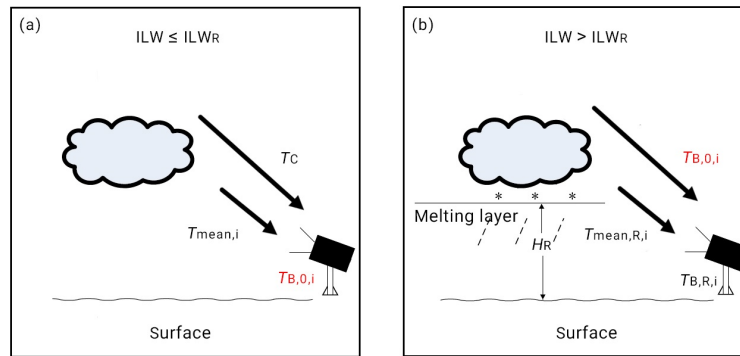
Figure 2. Radiative transfer process of the ground-based microwave radiometer. (**a**) The radiative transfer process during the non-rainfall period. (**b**) The radiative transfer process of the assumed additional layer during the rainfall period.

However, during rain, the zenith opacity $\tau_{0,i}$ of the atmosphere without rain cannot be measured. It has to be estimated by temporal interpolation of measurements obtained during rain-free periods. Furthermore, the determination of the effective mean temperature $T_{\text{mean},i}$ (Equation (4)) is delicate. This will cause the rain zenith opacity $\tau_{R,i}$ to be inaccurate. The initial estimated value of the rain zenith opacity is $\tau_{R,0,i} = \tau_i - \tau_{0,i}$, where the zenith opacity τ_i is also not very accurate as well because it is calculated based on $T_{\text{mean},i}$. Because of complications of the inversion problem, physical algorithms which attempt to directly invert the optimal atmospheric parameters typically rely on the iterative adjustment of the radiative transfer model [33]. Therefore, we iteratively determine the rain zenith opacity $\tau_{R,i}$.

$$\tau_{R,i}^{(k+1)} = -\mu \cdot ln\left(\frac{T_{\text{mean},R,i}\left(\tau_{R,i}^{(k)}\right) - T_{B,R,i}}{T_{\text{mean},R,i}\left(\tau_{R,i}^{(k)}\right) - T_{B,0,i}} \right) \qquad (13)$$

where $\tau_{R,i}^{(k+1)}$ is the (*k*+1)th iteration value of the rain zenith opacity. $\tau_{R,0,i}$ is used as the input value of the iteration, i.e., $\tau_{R,i}^{(0)} = \tau_{R,0,i}$. According to Equation (13), the initial estimate of the rain zenith opacity is gradually improved in an iterative manner. The basis for the improvement is to correct the rain zenith opacity using the difference between the rain effective mean temperature estimated in the *k*th iteration and the actual observed brightness temperature. It was found that the results basically converge after two iterations. However, this iteration distributes the error in the form of a natural logarithm, which does not take into account the actual situation and will amplify the error. Moreover, the correction value generated by the iteration is mainly positive, which is likely to cause the overestimation of the light rain.

3.2. Data Processing

Bern (46.95°N, 7.45°E) is the study area of this article. The TROWARA instrument (46.95°N, 7.44°E; Alt. 575 m asl) together with the ExWi weather station is located near the center of Bern. The ExWi optical rain sensor was discontinued in September 2012, so it is only used for short-term rain rate comparisons. The Zimmerwald weather station (46.88°N, 7.47°E; Alt. 907 m asl) is located about 8.4 km southeast of TROWARA, and its position happens to be in the direction that TROWARA is pointing. The curve of the accumulated rain obtained by the Zimmerwald rain gauge is too smooth and difficult to clearly describe the details of the rainfall, so it is only used for long-term rain rate comparisons. In the process of estimating and comparing the rain rate, the unit of all data is unified as mm/h. TROWARA estimated the long-term series of the rain rate from 1 January 2005 to 31 December 2019 for 15 years. The following is the selection process for the precipitation data:

- Step1: rain-day events detected by TROWARA;
- Step2: rain-day events detected by the rain gauge (ExWi or Zimmerwald rain gauge);
- Step3: simultaneous and available rain-day events at Step 1 and Step 2;
- Step4: the data of TROWARA, the rain gauge, and ERA5 all follow rain-day events of Step 3.

Table 1 shows the number of rain-day events for different daily rainfall intensities [34]. After removing outliers that more than 3 standard deviations (σ), the total number of rain-day events compared with the ExWi rain gauge from 2005 to 2018 is 1748, of which the light rain and moderate rain account for about 94%; the total number of rain-day events compared with the Zimmerwald rain gauge from 2008 to 2019 is 1529, of which the light rain and moderate rain account for about 97%. Because the time periods of the two rain gauges are different, and each rain gauge corresponds to different data missing, the above steps are repeated for the ExWi rain gauge and the Zimmerwald rain gauge, respectively. This means that the day-rain events of each rain gauge are not at exactly the same time.

Table 1. The classification of daily rainfall intensity and the corresponding number of rain-day events.

Rainfall Intensity	Rain Accumulation in a Day (mm)	Number of Rain-Day Events	
		ExWi	Zimmerwald
Light rain	$R < 5$	1030	963
Moderate rain	$5 \leq R < 20$	610	515
Heavy rain	$20 \leq R < 50$	105	51
Violent rain	$R \geq 50$	3	0

In this work we assume a constant temperature lapse rate Γ of 6 K/km. This is the typical value for saturated-adiabatic temperature profiles and has proved that the estimated rain rate using this value is in good agreement with the ground rain sensor in many cases. The presence of raindrops is very likely when the ILW value exceeds 0.4 mm [14,35], so this study uses 0.4 mm as the rain threshold value ILW_R. It should be noted that ILW_R is usually between 0.1 mm and 0.6 mm, but the choice of the value of ILW_R is not a big deal for the detection of rainfall intervals. This is because the emission enhanced by the Mie effects leads to a very strong increase in ILW value when the drop size (diameter) increases to more than 0.3 mm [36].

The evaluation statistics are used to assess the robustness of the Opa-RR physical algorithm, including the coefficient of determination (R^2), the root-mean-square error (RMSE), the bias, the intercept, and the slope. The daily rain rate is the accumulated precipitation per day in mm/day; the monthly rain rate is the accumulated precipitation per month in mm/month; the annual rain rate is the accumulated precipitation per year in mm/year. We archive these estimated rain rate data in the STARTWAVE database.

4. Results

4.1. Daily Rain-Rate Estimation

Figure 3 shows six rain events that each lasted less than one day representing heavy (Figure 3a,d), moderate (Figure 3b,e), and light rain (Figure 3c,f), respectively, and the stratiform rain events (Figure 3g) with the rain rate less than 10 m/h that lasted for 8 days. As it can be observed from Figure 3, in these rain events, the cumulative rain curve of Opa-RR at 21 GHz is higher than that of at 31 GHz. From the beginning and end of the rain period, the changing trends of estimated value curves and observed value curves over time are the same. For example, Figure 3d shows a heavy rain event on 31 May 2007. There was no rain before 3:20 UT, and the value of accumulated rain was 0, then it drizzled for a few minutes when the zenith opacity changed slightly. The zenith opacity reached a very high value at 16:40 UT, and the cumulative rain increased rapidly. After 30 min, the cumulative rain curves showed a certain slope change over time, and the rain decreased slightly. The accumulated rain climbed above 35 mm in a time interval of 7 h. In addition, as shown in Figure 3g, there are mainly light rain events from the third day to the fifth day, and the other times are moderate rain or heavy rain events. The correlation between the estimated moderate and heavy rain and observed values is better than that in light rain. Opa-RR at 21 GHz is more related to the ExWi optical rain sensor, and Opa-RR at 31 GHz is more consistent with the ExWi rain gauge.

Figure 4 shows the verification scatter plots of the daily rain rate estimated by Opa-RR, and the comparison between ERA5 and rain gauges. As can be observed from Figure 4, the Opa-RR estimate of the 31 GHz channel achieves slightly better performance than the 21 GHz channel, compared with the ExWi rain gauge (the Zimmerwald rain gauge), with R^2 and RMSE verifications are 0.44 (0.41) and 6.58 (5.63) mm/day, respectively. R^2 and RMSE verifications of the Opa-RR estimation at 21 GHz are 0.43 (0.39) and 7.83 (6.75) mm/day, respectively. This is not surprising because the sensor at 31 GHz is less sensitive to water vapor than at 21 GHz [12].
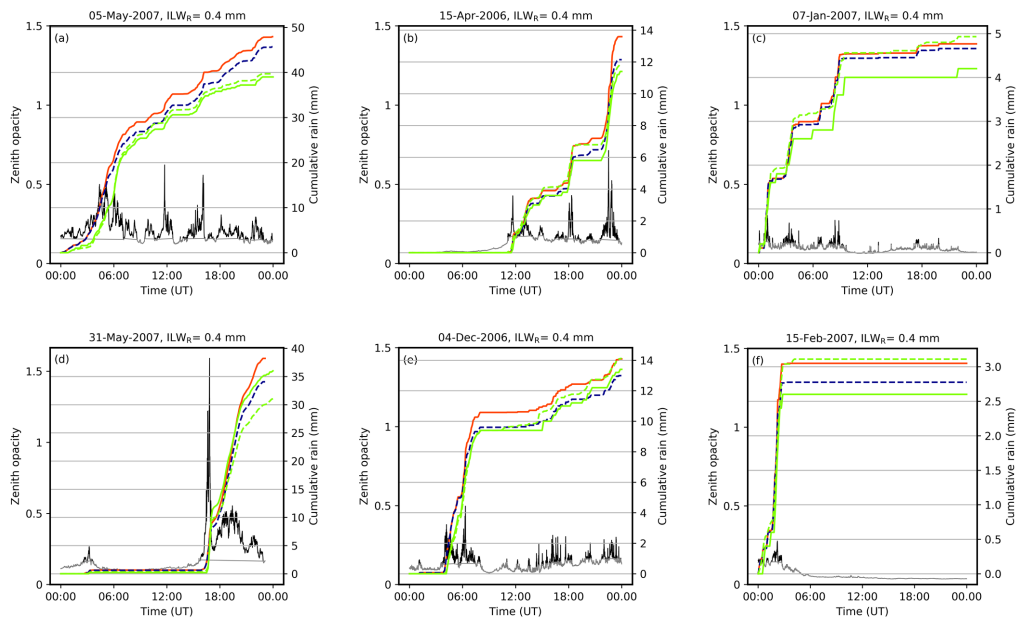
Figure 3. *Cont.*
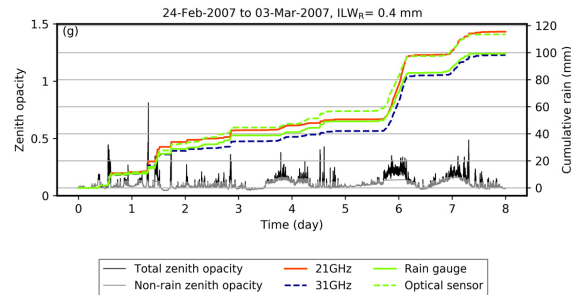
Figure 3. Examples of cumulative rain versus time for Opa-RR at 21 GHz (solid red), at 31 GHz (dashed blue), the ExWi rain gauge (solid green), the ExWi optical rain sensor (dashed green). The black and grey lines are the total zenith opacity and the non-rain zenith opacity, respectively. (**a**) heavy rain on 05 May 2007; (**b**) moderate rain on 15 April 2006; (**c**) light rain on 7 January 2007; (**d**) heavy rain on 31 May 2007; (**e**) moderate rain on 4 December 2006; (**f**) light rain on 15 February 2007; (**g**) 8-day stratiform rain from 24 February 2007 to 3 March 2007.
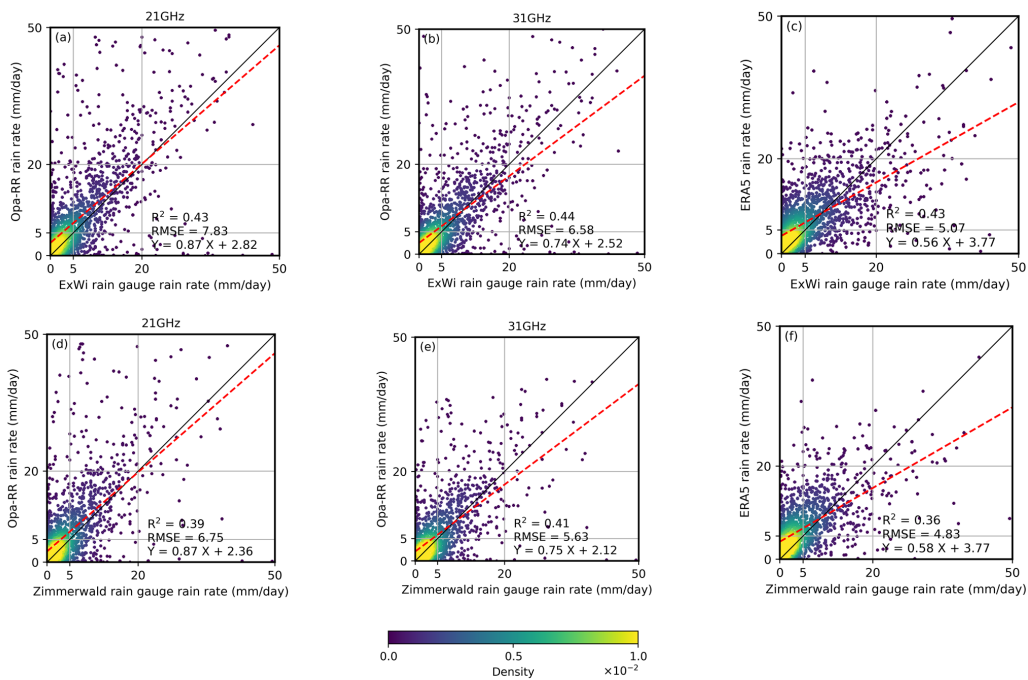
Figure 4. Scatter plots of daily rain rates estimated by Opa-RR and provided by ERA5 versus measured by the ExWi rain gauge over the period 2005 to 2018 (**a**–**c**) and the Zimmerwald rain gauge over the period 2008 to 2019 (**d**–**f**) in Bern. The solid black line shows the $x = y$ line, and the red dashed line shows the linear regression fit line. The color shows the density of the data distribution calculated by Gaussian kernels.

Another finding worth noting in Figure 4 is that the daily rain rate using Opa-RR is significantly lower than rain gauges when rain rates are between 20 mm/day and 50 mm/day (heavy rain), since the linear regression fit line is located below the $x = y$ line. Table 2 gives the biases of daily rain rates for different daily rainfall intensities, except for the 21 GHz channel, the daily rain rate bias of heavy rains estimated by Opa-RR is all

negative. This means that the proposed Opa-RR physical algorithm tends to underestimate during heavy rains, which affects Opa-RR's performance in estimating the daily rain rate to a certain extent. The main reason for the heavy rain underestimation may be that (1) due to its small scale and spatial complexity, heavy rain has an extreme variability of precipitation in a short period of time, and it is usually difficult to accurately capture. Decreasing the threshold ILW_R increases the estimated amount of rain, but it will also extend the rainfall period. Note that it is more effective to adapt the temperature lapse rate. (2) During heavy rains, the brightness temperature tends to be saturated at higher frequencies such as the 31 GHz channel [3,37–39], thus underestimating rain. (3) The model requires that the rain fill in the antenna's field of view is fairly homogeneous, this means the rain zenith opacity will lead to underestimation if there is any inhomogeneity [10].

Table 2. Bias statistics of the daily rain rate for different daily rainfall intensity, Opa-RR$_{21}$ and Opa-RR$_{31}$ represent the daily rain rate estimated by Opa-RR at 21 GHz and 31 GHz of TROWARA, respectively.

Daily Rain Rate	Bias (mm/Day)			
	Light Rain	Moderate Rain	Heavy Rain	Total
Opa-RR$_{21}$ vs. ExWi rain gauge	2.12	2.30	0.31	1.96
Opa-RR$_{31}$ vs. ExWi rain gauge	1.69	0.61	−4.19	0.89
ERA5 vs. ExWi rain gauge	2.64	0.04	−8.78	0.98
Opa-RR$_{21}$ vs. Zimmerwald rain gauge	1.74	1.99	−2.46	1.69
Opa-RR$_{31}$ vs. Zimmerwald rain gauge	1.35	0.48	−6.07	0.81
ERA5 vs. Zimmerwald rain gauge	2.72	0.56	−9.82	1.57

In moderate rain (5 mm/day to 20 mm/day), Figure 4 shows that the daily rain rate estimated by Opa-RR at 31GHz works well, and the linear regression fit line almost coincides with the $x = y$ line. Their biases are all less than 0.61 mm/day (Table 2). However, during light rains, the daily rain rate using Opa-RR is higher than the rain gauges, since the mean value curve in the range of 0 mm/day to 5 mm/day is located above the $x = y$ line. The bias of light rains is all positive (Table 2). The possible explanations for the light rain overestimation include (1) the tipping bucket rain gauge underestimated light rain due to the limitations of the instrument's working principle. (2) Virga is precipitation that evaporates or sublimates before it reaches the ground, which is a likely explanation for the discrepancy during light rain. In addition, the total biases between Opa-RR estimation at 31 GHz and rain gauges show a small bias on the daily scale.

It can be seen that the daily rain rate estimated by Opa-RR shows a better correlation with the rain gauges than that of ERA5, especially at 31 GHz. Except for the RMSE, Opa-RR estimations show a significant advantage over ERA5 for all verification factors (R^2, the bias, the intercept, and the slope). The slope of the linear fitting line of ERA5 scattered points is only about 0.58 at most. Moreover, the correlation between ERA5 and rain gauges is weaker and unstable, because the comparison results between ERA5 and different rain gauges report a larger drop (from 0.43 to 0.36 for R^2) than Opa-RR.

4.2. Monthly Rain-Rate Estimation

Figure 5 shows the verification scatter plots of the monthly rain rate estimated by Opa-RR, and the comparison between ERA5 and rain gauges. As can be observed from Figure 5, the Opa-RR estimate of the 31 GHz channel achieves slightly better performance than the 21 GHz channel, compared with the ExWi rain gauge (the Zimmerwald rain gauge), with R^2 and RMSE verifications are 0.73 (0.77) and 29.33 (22.46) mm/month, respectively. R^2 and RMSE verifications of the Opa-RR estimation at 21 GHz are 0.72 (0.75) and 34.70 (26.79) mm/month, respectively. The monthly estimate of Opa-RR is slightly overestimated because all the biases are positive. It can be seen that, except for R^2 and RMSE compared with ExWi rain gauge, Opa-RR at 31 GHz estimation shows some advantages over ERA5 for all verification factors (R^2, RMSE, the bias, the intercept, and the slope) compared with rain gauges.
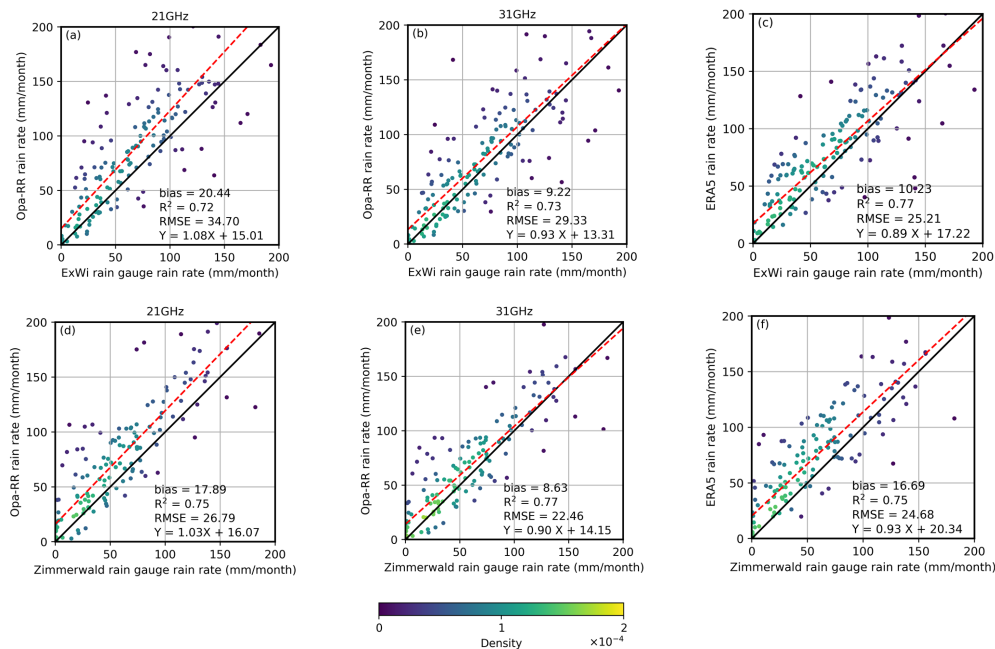
Figure 5. Same as in Figure 4, but with regard to the monthly rain rate in Bern.

Figure 6 shows the monthly time series comparison of rain rates estimated by Opa-RR, measured by the rain gauges, and provided by ERA5 reanalysis in Bern. As it can be observed from Figure 6, the Opa-RR estimation is very close to the observations, and we see a similar fluctuation trend, except for the overestimated rain in July 2007, May and November 2009, June 2015. The observation data of the rain gauge indicated that some extreme rainstorms occurred in these months, with the rain rate greater than 50 mm/10 min. In addition, the monthly rain rate estimated by Opa-RR can well detect that Bern has more rainfall in summer and less rainfall in winter [40]. For example, during the winter of 2010/2011 (December through February), the ExWi (Zimmerwald) rain gauge reported 137.20 (118.20) mm of precipitation, as well as Opa-RR at 21 GHz and 31 GHz estimated 161.47 (163.19) and 144.75 (146.35) mm of precipitation, respectively. During the summer of 2011 (June through August), the ExWi (Zimmerwald) rain gauge reported 273.60 (277.80) mm of precipitation, as well as Opa-RR at 21 GHz and 31 GHz estimated 333.56 (334.97) and 300.25 (301.70) mm of precipitation, respectively. Furthermore, there is a large amount of missing data. For example, the cumulative rain reaches around 300 mm in July 2014 in Figure 6a, while in Figure 6b this value is 0 mm. It is also obvious that the missing data exist in 2008 and 2017 in Figure 6a and from 2016 to 2019 in Figure 6b. However, although Figure 6a,b use rain gauges at different locations and not exactly the same rain events, their monthly rain rate trends for many years are almost the same, such as from 2009 to 2013. The behavior of ERA5 and Opa-RR is almost similar, slightly overestimating the cumulative rain for most months. However, the difference is that ERA5 is underestimated in some months with more precipitation, such as from May to July 2007 in Figure 6a and July 2009 in both Figure 6a,b.
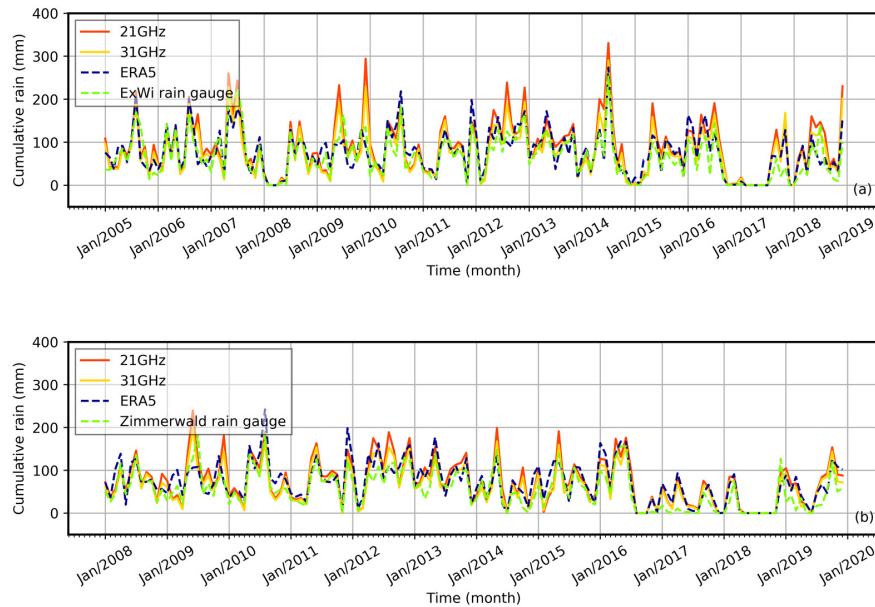
Figure 6. Monthly time series of the rain rate for Opa-RR at 21 GHz (solid red), at 31 GHz (solid yellow), rain gauges (dashed green), and ERA5 (dashed blue) in Bern. It is assigned as 0 for months without rain or when data are missing. (**a**) comparison with the ExWi rain gauge; (**b**) comparison with the Zimmerwald rain gauge.

4.3. Annual Rain-Rate Estimation

Figure 7 shows the annual time series comparison of rain rates estimated by Opa-RR, measured by the rain gauges, and provided by ERA5 reanalysis in Bern. As it can be observed from Figure 7, the curve of annual rain rate estimated by Opa-RR and the situ observations show a similar temporal variation and trend. For example, in Figure 7a, these four curves all show the lowest annual rainfall in 2008 and 2017, and in 2012 they are relatively high. Furthermore, the Opa-RR estimation has a good correlation with the rain gauges. From 2005 to 2014 in Figure 7a and from 2008 to 2016 in Figure 7b, the curve of Opa-RR at 31 GHz almost coincides with the rain gauge, but at 21 GHz has an overestimation. From 2015 to 2018 in Figure 7a and in 2017 and 2019 in Figure 7b, compared with the rain gauge, the performance of Opa-RR in estimating annual rain rates is not outstanding. This may be because the tipping bucket rain gauge underestimated annual rain rates or had instrumental errors. The behavior of Opa-RR and ERA5 is almost similar with slight overestimation in comparison with in situ observations, while Opa-RR at 31GHz achieves a better agreement than ERA5 in 2009 and 2010.
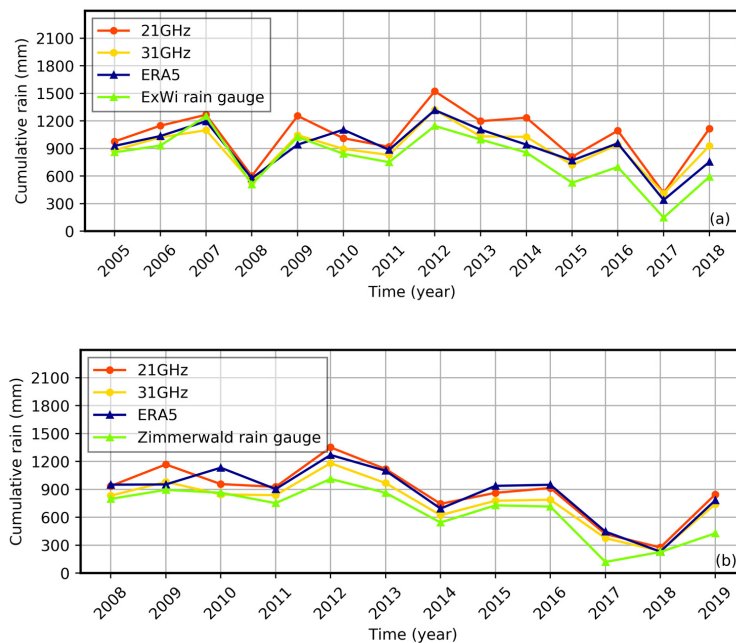
Figure 7. Same as in Figure 6, but with regard to the annual time series of the rain rate in Bern.

5. Conclusions

Benefitting from a new physical retrieval method, based on the ground-based microwave radiometer, this article used the rain zenith opacity derived from TROWARA to estimate the rain rate in Bern over a long-time interval from 2005 to 2019. The assumption of homogeneous radiation beam filling established the relationship between rainfall rate and zenith opacity. To calculate the rain zenith opacity, this retrieval method constructed an additional layer through the non-rainy radiative transfer model to describe the contribution of rain to radiation. The rain-rate estimation was tested by the time series of accumulated rain (day, month, year), and the performance of this method in different rain intensities (light, medium, and heavy) was evaluated. Compared with the measurements from the ExWi rain gauge and Zimmerwald rain gauge, there is fairly good agreement between estimations and observations. Compared with ERA5, it is found that the rain rate estimated by Opa-RR at 31GHz obtains slightly better results, especially the daily rain rates (Figure 4 and Table 2).

Using zenith opacity to directly estimate the rain rate performs well in detecting daily moderate rain. However, heavy rain is underestimated, which might be due to its spatial complexity, the brightness temperature saturation at high frequencies, and the difficulty of the antenna beam to be absolutely homogeneous. Light rain is overestimated, probably because the temperature lapse rate will be affected by the weather, and the iteration for the zenith opacity is the positive correction. Moreover, ground-based radiation measurements at 21.4 and 31.5 GHz were used for experimental testing of retrieval algorithms and proved that the microwave frequency of 31 GHz has superior rain rate retrieval capabilities due to its lower sensitivity to water vapor. At the monthly timescale, Opa-RR 31 GHz precipitation estimates are very close to the Zimmerwald rain gauge, a high R^2 value reaches 0.77 and a low RMSE value is 22.46 mm/month. The figures for the daily rain rate are slightly lower, but they are stable no matter which of these two rain gauges are compared, the R^2 value is 0.39 to 0.44, and the RMSE value is 5.63 to 7.83 mm/day.

Ground-based microwave estimation of rain rate with high temporal resolution and high sensitivity to ground rainfall has the potential to provide important support for fine rainfall forecasting and disaster risk reduction. The high temporal resolution of ground-based microwave radiometry is expected to reveal short-term processes of convective rainfall events and atmospheric phenomena, such as virga, which are not accessible by rain gauges. Furthermore, ground-based microwave radiometry is a new, independent data source for rain rate measurement. This article is important not only for understanding the physical mechanism of rain rate inversion and analyzing the variation of rainfall accumulation over time, but also for enriching the research of ground-based microwave radiometry for atmospheric environment remote sensing and promoting the further development of the rain-rate estimation research.

References

1. Orlandi, A.; Ortolani, A.; Meneguzzo, F.; Levizzani, V.; Torricella, F.; Turk, F.J. Rainfall assimilation in RAMS by means of the Kuo parameterisation inversion: Method and preliminary results. *J. Hydrol.* **2004**, *288*, 20–35. [CrossRef]
2. Wang, J.; Xu, Y.; Yang, L.; Wang, Q.; Yuan, J.; Wang, Y. Data assimilation of high-resolution satellite rainfall product improves rainfall simulation associated with landfalling tropical cyclones in the Yangtze river Delta. *Remote Sens.* **2020**, *12*, 276. [CrossRef]
3. Marzano, F.S.; Fionda, E.; Ciotti, P.; Martellucci, A. Ground-based multifrequency microwave radiometry for rainfall remote sensing. *IEEE Trans. Geosci. Remote Sens.* **2002**, *40*, 742–759. [CrossRef]
4. Cadeddu, M.P.; Ghate, V.P.; Mech, M. Ground-based observations of cloud and drizzle liquid water path in stratocumulus clouds. *Atmos. Meas. Tech.* **2020**, *13*, 1485–1499. [CrossRef]
5. Cadeddu, M.P.; Marchand, R.; Orlandi, E.; Turner, D.D.; Mech, M. Microwave passive ground-based retrievals of cloud and rain liquid water path in drizzling clouds: Challenges and possibilities. *IEEE Trans. Geosci. Remote Sens.* **2017**, *55*, 6468–6481. [CrossRef]
6. Battaglia, A.; Saavedra, P.; Rose, T.; Simmer, C. Characterization of precipitating clouds by ground-based measurements with the triple-frequency polarized microwave radiometer ADMIRARI. *J. Appl. Meteorol. Climatol.* **2010**, *49*, 394–414. [CrossRef]
7. Marzano, F.S.; Cimini, D.; Ware, R. Monitoring of rainfall by ground-based passive microwave systems: Models, measurements and applications. *Adv. Geosci.* **2005**, *2*, 259–265. [CrossRef]
8. Won, H.Y.; Kim, Y.-H.; Lee, H.-S. An application of brightness temperature received from a ground-based microwave radiometer to estimation of precipitation occurrences and rainfall Intensity. *Asia-Pac. J. Atmos. Sci.* **2009**, *45*, 55–69.
9. Xu, G.; Ware, R.; Zhang, W.; Feng, G.; Liao, K.; Liu, Y. Effect of off-zenith observations on reducing the impact of precipitation on ground-based microwave radiometer measurement accuracy. *Atmos. Res.* **2014**, *140–141*, 85–94. [CrossRef]
10. Mätzler, C.; Morland, J. *Advances in Surface-Based Radiometry of Atmospheric Water*; IAP Research Report 2008-02-MW; Institut für Angewandte Physik, Universität Bern: Bern, Switzerland, 2014.
11. Hocke, K.; Navas-Guzmán, F.; Moreira, L.; Bernet, L.; Mätzler, C. Diurnal cycle in atmospheric water over switzerland. *Remote Sens.* **2017**, *9*, 909. [CrossRef]
12. Hocke, K.; Bernet, L.A.L.; Hagen, J.; Murk, A.; Renker, M.; Mätzler, C. Diurnal cycle of short-term fluctuations of integrated water vapour above Switzerland. *Atmos. Chem. Phys.* **2019**, *19*, 12083–12090. [CrossRef]

13. Ingold, T.; Peter, R.; Kämpfer, N. Weighted mean tropospheric temperature and transmittance determination at millimeter-wave frequencies for ground-based applications. *Radio Sci.* **1998**, *33*, 905–918. [CrossRef]
14. Mätzler, C.; Morland, J. Refined physical retrieval of integrated water vapor and cloud liquid for microwave radiometer data. *IEEE Trans. Geosci. Remote Sens.* **2009**, *47*, 1585–1594. [CrossRef]
15. Ellison, W. Dielectric properties of natural media. In *Thermal Microwave Radiation: Applications for Remote Sensing*; Mätzler, C., Ed.; IET Electromagnetic Waves Series: London, UK, 2006; Volume 52, pp. 431–454.
16. Peter, R.; Kämpfer, N. Radiometric determination of water vapor and liquid water and its validation with other techniques. *J. Geophys. Res. Atmos.* **1992**, *97*, 18173–18183. [CrossRef]
17. Morland, J. *TROWARA–Tropospheric Water Vapour Radiometer: Radiometer Review and New Calibration Model*; IAP Research Report 2002-15; Institut für Angewandte Physik, Universität Bern: Bern, Switzerland, 2002.
18. Marzano, F.S.; Cimini, D.; Ciotti, P.; Ware, R. Modeling and measurement of rainfall by ground-based multispectral microwave radiometry. *IEEE Trans. Geosci. Remote Sens.* **2005**, *43*, 1000–1011. [CrossRef]
19. Rosenkranz, P.W. Water vapor microwave continuum absorption: A comparison of measurements and models. *Radio Sci.* **1998**, *33*, 919–928. [CrossRef]
20. Hwang, S.H.; Kim, K.B.; Han, D. Comparison of methods to estimate areal means of short duration rainfalls in small catchments, using rain gauge and radar data. *J. Hydrol.* **2020**, *588*, 125084. [CrossRef]
21. Yilmaz, K.K.; Hogue, T.S.; Hsu, K.-L.; Sorooshian, S.; Gupta, H.V.; Wagener, T. Intercomparison of rain gauge, radar, and satellite-based precipitation estimates with emphasis on hydrologic forecasting. *J. Hydrometeorol.* **2005**, *6*, 497–517. [CrossRef]
22. Donald Ahrens, C.; Henson, R. *Meteorology Today: An Introduction to Weather, Climate and the Environment*, 9th ed.; Cengage Learning: Belmont, CA, USA, 2009; pp. 164–181.
23. Zscheischler, J.; Naveau, P.; Martius, O.; Engelke, S.; Raible, C.C. Evaluating the dependence structure of compound precipitation and wind speed extremes. *Earth Syst. Dynam.* **2021**, *12*, 1–16. [CrossRef]
24. Hersbach, H.; De Rosnay, P.; Bell, B.; Schepers, D.; Simmons, A.; Soci, C.; Abdalla, S.; Balmaseda, A.; Balsamo, G.; Bechtold, P.; et al. *Operational Global Reanalysis: Progress, Future Directions and Synergies with NWP, ERA Report Series 27*; European Centre for Medium RangeWeather Forecasts: Reading, UK, 2018. [CrossRef]
25. Hersbach, H.; Bell, B.; Berrisford, P.; Horányi, A.; Sabater, J.M.; Nicolas, J.; Radu, R.; Schepers, D.; Simmons, A.; Soci, C. Global reanalysis: Goodbye ERA-Interim, hello ERA5. *ECMWF Newsl.* **2019**, *159*, 17–24. [CrossRef]
26. Xu, X.; Frey, S.K.; Boluwade, A.; Erler, A.R.; Khader, O.; Lapen, D.R.; Sudicky, E. Evaluation of variability among different precipitation products in the Northern Great Plains. *J. Hydrol. Reg. Stud.* **2019**, *24*, 100608. [CrossRef]
27. Nogueira, M. Inter-comparison of ERA-5, ERA-interim and GPCP rainfall over the last 40 years: Process-based analysis of systematic and random differences. *J. Hydrol.* **2020**, *583*, 124632. [CrossRef]
28. Amjad, M.; Yilmaz, M.T.; Yucel, I.; Yilmaz, K.K. Performance evaluation of satellite- and model-based precipitation products over varying climate and complex topography. *J. Hydrol.* **2020**, *584*, 124707. [CrossRef]
29. Mätzler, C.; Martin, L. *Effects of Rain on Propagation, Absorption and Scattering of Microwave Radiation Based on the Dielectric Model of Liebe*; IAP Research Report 2002-10-MW; Institut für Angewandte Physik, Universität Bern: Bern, Switzerland, 2002.
30. Leuenberger, A. Precipitation Measurements with Microwave Sensors. Master's Thesis, Philosophisch-Naturwissenschaftliche Fakultät, Universität Bern, Bern, Switzerland, 2009.
31. Mätzler, C.; Melsheimer, C. Radiative transfer and microwave radiometry. In *Thermal Microwave Radiation: Applications for Remote Sensing*; Mätzler, C., Ed.; IET Electromagnetic Waves Series: London, UK, 2006; Volume 52, pp. 1–23.
32. Mätzler, C. Ground-based observations of atmospheric radiation at 5, 10, 21, 35, and 94 GHz. *Radio Sci.* **1992**, *27*, 403–415. [CrossRef]
33. Petty, G.W. Physical retrievals of over-ocean rain rate from multichannel microwave imagery. Part I: Theoretical characteristics of normalized polarization and scattering indices. *Meteorl. Atmos. Phys.* **1994**, *54*, 79–99. [CrossRef]
34. Latupapua, H.; Latupapua, A.I.; Wahab, A.; Alaydrus, M. Wireless sensor network design for earthquake's and landslide's early warnings. *Indones. J. Electr. Eng. Comput. Sci.* **2018**, *11*, 437–445. [CrossRef]
35. Mätzler, C. *Drop-Size Distributions and Mie Computations for Rain*; IAP Research Report 2002-16-MW; Institut für Angewandte Physik, Universität Bern: Bern, Switzerland, 2002.
36. Cossu, F.; Hocke, K.; Martynov, A.; Martius, O.; Mätzler, C. Atmospheric water parameters measured by a ground-based microwave radiometer and compared with the WRF model. *Atmos. Sci. Lett.* **2015**, *16*, 465–472. [CrossRef]
37. Marzano, F.S.; Fionda, E.; Ciotti, P. Neural-network approach to ground-based passive microwave estimation of precipitation intensity and extinction. *J. Hydrol.* **2006**, *328*, 121–131. [CrossRef]
38. Battaglia, A.; Saavedra, P.; Simmer, C.; Rose, T. Rain observations by a multifrequency dual-polarized radiometer. *IEEE Geosci. Remote. Sens. Lett.* **2009**, *6*, 354–358. [CrossRef]
39. Zhang, W.; Xu, G.; Xi, B.; Ren, J.; Wan, X.; Zhou, L.; Cui, C.; Wu, D. Comparative study of cloud liquid water and rain liquid water obtained from microwave radiometer and micro rain radar observations over central China during the monsoon. *J. Geophys. Res. Atmos.* **2020**, *125*, e2020JD032456. [CrossRef]
40. *Climate Normals Bern/Zollikofen (Reference Period. 1981−2010)*; Zurich-Airport; Swiss Federal Office of Metreology and Climatology, MeteoSwiss: Zurich, Switzerland, 2014.

6 | MACHINE LEARNING RAIN RATE RETRIEVAL

6.1 SUMMARY OF THE STUDY

Considering the complex nonlinear relationship between precipitation and atmospheric variables, machine learning techniques were applied to the study of microwave radiometer precipitation estimation. Raindrops significantly affect microwave signals, not only causing extinction and emission but also inducing various scattering phenomena. Based on these physical characteristics I developed two novel machine learning-based rain rate retrieval algorithms, RF and GBDT, with high temporal resolution for a ground-based microwave radiometer over Swiss Plateau. The rain rates measured by MRR was used as target variable for the algorithms. Compared with other machine learning algorithms, Light Gradient-Boosting Machine (LightGBM) and Support Vector Machine (SVM), the rain rate retrieval I studied is highly competitive in terms of accuracy ($R^2 > 0.95$) and model training efficiency. The methods and results are described in the article presented in this chapter.

The following article was submitted to Journal of Hydrology in June 2024.

6.2 PUBLICATION

FULL CITATION

Wang Wenyue, Wenzhi Fan, and Klemens Hocke. "Precipitation retrievals for ground-based microwave radiometer using physics-informed machine learning methods." In: *Journal of Hydrology*, in review.

Precipitation Retrievals for Ground-Based Microwave Radiometer Using Physics-Informed Machine Learning Methods

Wenyue Wang[a,b,*], Wenzhi Fan[c] and Klemens Hocke[a,b]

[a]Institute of Applied Physics, University of Bern, 3012, Bern, Switzerland

[b]Oeschger Centre for Climate Change Research, University of Bern, 3012, Bern, Switzerland

[c]School of Earth and Space Sciences, Peking University, 100084, Beijing, China

ARTICLE INFO

ABSTRACT

Precipitation is complex due to its significant temporal and spatial variability, and current mainstream precipitation estimation techniques have their inherent limitations. The complementary role of ground-based microwave radiometer in precipitation monitoring to these technologies is gaining increasing attention. Based on the physical characteristics of microwave radiation signals affected by raindrops in the atmosphere, this study presented two novel machine learning based rain rate retrieval algorithms, random forest (RF) and gradient boosting decision tree (GBDT), for a ground-based microwave radiometer (MWR) over Swiss Plateau from 2008 to 2010. Both methods are trained using the rain rate observed by the remote sensing technology micro rain radar (MRR) as the target variable, and consider meteorological parameters in the feature input. For data preprocessing of the retrieval methods, outliers and noise in the MRR rain rate are removed. Cross-validation results show that both RF-based and GBDT-based methods achieve superior precipitation estimation performance, with R^2 values of 0.96 and 0.95 and mean square error of 0.01 mm/h and 0.02 mm/h, respectively. Comparing light gradient-boosting machine (LightGBM) and support vector machine (SVM) algorithms, rain rate retrieval based on RF and GBDT are highly competitive in terms of accuracy and model training timeliness, respectively. This study offers an accurate and reliable method for high temporal resolution (10 seconds) precipitation estimation from MWR under complex terrain conditions, and it also has the potential for application in other regions and with other tropospheric microwave radiometers.

1. Introduction

Precipitation is a key element in assessing and predicting climate change (Kundzewicz, 2008). With global warming, rising temperatures cause the atmosphere to hold more water vapor. The Clausius-Clapeyron equation indicates that atmospheric water vapor content will rise by 7% for every 1-degree Celsius increase in temperature (Held and Soden, 2006). The events and intensity of precipitation, especially extreme rainfall events, are therefore likely to increase, leading to more frequent natural disasters such as floods and landslides (Hong, Adler, Negri and Huffman, 2007). Global warming also affects the hydrological cycle, altering the distribution of precipitation, which results in reduced rainfall and increased drought in some areas (Kundzewicz, 2008; Allen and Ingram, 2002). Effective disaster prevention and mitigation strategies depend largely on accurate estimates of precipitation (Netzel, Heldt and Denecke, 2021). The variability of precipitation distribution in space and time complicates retrieval, as all techniques show their potential and limitations (Marzano, Fionda and Ciotti, 2006).

Rain gauges, which are low-cost and easy to maintain, measure precipitation at fixed points and are sparsely distributed to form a network that provides large-area precipitation information through interpolation (Marzano, Cimini

and Montopoli, 2010). Rain gauges collect data with minute-level temporal resolution, but errors often occur due to wind effects, evaporation and spillage. Weather radar, another important technology for precipitation monitoring, is often used for nowcasting the future location and intensity of various types of precipitation such as rain, snow, hail, and other hydrometeors, as they provide near real-time data with high resolution and cover a wide geographical area (Rombeek, Leinonen and Hamann, 2024). Processing radar data is challenging and requires complex algorithms and models due to factors such as instrument calibration, ground clutter and anomalous propagation, beam blockage, and range degradation, all of which can significantly impact precipitation estimates (Villarini and Krajewski, 2010). The installation and maintenance of an entire radar system typically involve substantial costs. Over the past three decades, satellite technology has rapidly advanced, enabling the capture of global spatial distributions of precipitation using primarily microwave radiation, infrared, and precipitation radar (Liu, Yang, Shao, Wang, Liu, Tang, Xue and Bai, 2022; Wang, Tang, Xiong, Ma and Zhu, 2021a). A wide array of satellite precipitation products have been put into use such as the Tropical Rainfall Measuring Mission (TRMM), the Climate Prediction Center morphing technique (CMORPH), and Precipitation Estimation from Remotely Sensed Information using Artificial Neural Networks (PERSIANN). Satellite products suffer from poor spatial resolution (e.g., 0.1° or less) and low temporal resolution (Shen and Yong, 2021). In addition, the accuracy of satellite precipitation estimates is influenced by altitude and precipitation intensity.

*Corresponding author

✉ wenyue.wang@unibe.ch (W. Wang); wenzhi.fan@pku.edu.cn (W. Fan); klemens.hocke@unibe.ch (K. Hocke)

ORCID(s): 0000-0002-8251-2514 (W. Wang); 0000-0003-2178-9920 (K. Hocke)

Ground-based microwave radiometers have been applied for widespread use in the estimation of atmospheric integrated water vapor content, integrated cloud liquid water, temperature and relative humidity profiles due to their ability to provide continuous day and night, all-weather observations (Hocke, Bernet, Hagen, Murk, Renker and Mätzler, 2019; Hocke, Navas-Guzmán, Moreira, Bernet and Mätzler, 2017; Wang, Murk, Sauvageat, Fan, Dätwyler, Hervo, Haefele and Hocke, 2023; Yu, Xu, Jin, Ma, Liu and Gong, 2022). The accurate retrieval of these atmospheric variables by microwave radiometers is of great significance for monitoring changing trends of atmospheric parameters to assess the impact of global warming. Microwave radiometers are capable of capturing emitted and scattered radiation signals from raindrops in the atmosphere and hold potential for retrieval of rain rates (Wang et al., 2023; Mätzler and Morland, 2014). Microwave radiometer may offer unparalleled advantages over the above-mentioned techniques for precipitation estimation (Marzano, Fionda, Ciotti and Martellucci, 2002; Marzano et al., 2006, 2010; Wang, Hocke and Mätzler, 2021b). Compared to rain gauges, microwave radiometers can estimate regional cumulative rainfall with a high temporal resolution of 1 to 10 seconds. In addition, tropospheric microwave radiometers are remote sensing sensors that can detect rain that does not reach the ground, such as Virga. Compared to weather radar, microwave radiometers are not only relatively low-cost and easier to maintain, but they can also be portable sensors such as the commercial microwave radiometer Humidity And Temperature PROfiler radiometer (HATPRO) manufactured by Radiometer Physics GmbH (RPG) (Rose, Crewell, Löhnert and Simmer, 2005). Compared to satellite products, microwave radiometers enable more precise hydrological monitoring in local regions and can also facilitate large-area surveillance through a network of multiple ground stations (Cimini, Hewison, Martin, Güldner, Gaffard and Marzano, 2006). All these superior characteristics of microwave radiometers are frequently utilized to cross-validate and correct satellite observations (Sauvageat, Hocke, Maillard Barras, Hou, Errera, Haefele and Murk, 2023). Due to the inability of single technologies such as radiometers, radars, and rain gauges to estimate precipitation with high accuracy, the development of synergistic schemes that combine data from these instruments has gained widespread attention.

Precipitation estimation for ground-based microwave radiometers mainly uses statistical and physical algorithms (Wang et al., 2021b). Statistical algorithms are computationally efficient as they do not require complex radiative transfer models, but their accuracy heavily depends on the quantity and representativeness of the measurement samples (Won, Kim and Lee, 2009; Xu, Ware, Zhang, Feng, Liao and Liu, 2014). Physical algorithms can be analyzed from the perspective of atmospheric physical mechanisms to provide physical explanations for the retrieval process (Marzano, Cimini and Ware, 2005b). Considering the complex non-linear relationship between precipitation and variables from microwave radiometers and meteorology, machine learning

technology is applied to precipitation estimation research. Marzano et al. (2006) proposed a precipitation retrieval method based on an artificial neural network (ANN) feedforward algorithm for a ground-based microwave radiometer, but the target variable used was the surface rain rate measured by a rain gauge, rather than the MRR. Random Forest (RF) and Gradient Boosting Decision Tree (GBDT) are both ensemble learning methods known for their strong performance in handling regression tasks (Breiman, 2001, 1996; Friedman, 2001, 2002). RF improves the overall prediction accuracy and stability by combining the outcomes of multiple decision trees. The training speed is relatively fast, it also has a high tolerance for outliers and noise, and it has strong resistance to overfitting. By gradually building a decision tree model and iteratively correcting residuals of the previous model, GBDT has the ability to automatically select features during training and captures non-linear relationships within the data during training. Therefore, using RF and GBDT for precipitation estimation from ground-based microwave radiometers shows promising potential.

Here, we apply both the RF- and GBDT-based method to retrieve rain rates with high time resolution and accuracy for the ground-based microwave radiometer. The article is structured as follows. Section 2 introduces study area and data sets. Section 3 derives the rain rate retrieval method based on RF and GBDT. Section 4 compares and analyzes the results obtained from the two methods. Discussion and conclusions are in Section 5 and 6.

2. Study area and data sets

2.1. Study area

The Swiss Plateau, locates north of the Alps, stretches from Lake Geneva on the French border in the west to Lake Constance on the German-Austrian border in the east, with the Jura Mountains to the northwest. Characterized by rolling hills, numerous lakes and rivers, and an average altitude of 580 meters, it covers about one-third of Switzerland's area but is home to two-thirds of its population. According to the Köppen climate classification scheme, the plateau lies in a transition zone between the oceanic (Cfb) and continental (Dfb) climates, featuring changeable and often cloudy weather. Summers are cool due to cloud cover, while winters are relatively mild, with freezing temperatures typically occurring from December to early March (Wang and Hocke, 2022).

The ground-based microwave radiometer TRopospheric WAter RAdiometer (TROWARA) used in this study is located in Bern (46.95°N, 7.44°E, 575 m a.s.l.) on the Swiss Plateau. The area experiences its highest rainfall in the summer, averaging about 10 mm daily, typically from prefrontal or post-frontal showers and thunderstorms. Winter features are mainly frontal rainfall due to uphill or leeward winds, marking it as a relatively dry season with an average daily rainfall of nearly 6 mm (Brandsma and Buishand, 1997). This article primarily focuses on precipitation types including rain, drizzle, and mixed (rain and snow or graupel), and only stratiform rain is considered. This limitation is

caused by the properties of microwave radiometers (MWR) and Micro rain radar (MRR). Microwave radiation signals are not affected by dry snow (ice crystals) (Mätzler and Morland, 2014). In the case of non-stratiform convective rainfall, strong updrafts and downdrafts may lead to erroneous interpretation of fall velocity measured by MRR (Leuenberger, 2009).

2.2. Data sets
2.2.1. MWR data

Ground-based microwave radiometer data include brightness temperatures (T_B) at 21.385, 22.235, and 31.5 GHz, integrated water vapor (IWV), integrated liquid water (ILW), and infrared cloud base brightness temperature ($T_{B,IR}$) as six feature variables for the retrieval model in this article. The data are collected by the Tropospheric Water Radiometer (TROWARA) located on the roof of the Exakte Wissenschaften (ExWi) building at the University of Bern since November 1994. TROWARA is equipped with a thermal infrared channel operating in the 9.5–11.5 μm wavelength range and has been functioning in an indoor constant-temperature laboratory since November 2002 (Morland, 2002, 2007). Its antenna, which receives atmospheric radiation through a microwave-transparent window facing southeast at a 50° zenith angle, is designed to effectively prevent rain interference, ensuring reliable measurements even on rainy days. The time resolution for T_B is 7-11 seconds, and the bandwidths for the 21.385 GHz, 22.235 GHz, and 31.5 GHz microwave channels are 100 MHz, 400 MHz, and 200 MHz, respectively, with an antenna beam half-power beamwidth of 4° (Wang et al., 2023).

The radiative transfer equation in a plane-parallel atmosphere for a non-scattering atmosphere can be expressed as:

$$T_{B,i} = T_C \cdot e^{-\tau_i/\mu} + T_{mean,i} \cdot (1 - e^{-\tau_i/\mu}) \tag{1}$$

where τ_i is the opacity in zenith direction. Here, $\mu = \cos\theta$, with θ being the zenith angle of the TROWARA observation. $T_{B,i}$ is the brightness temperature measured by TROWARA at frequency i (e.g., 31.5 GHz), and T_C is the cosmic microwave background brightness temperature. $T_{mean,i}$ represents the tropospheric effective mean temperature calculated by a linear relationship based on temperature, pressure, and relative humidity, varying by frequency and site location (Wang et al., 2021b).

After deriving Equation 1, the zenith opacity τ_i can be expressed as:

$$\tau_i = -\mu \cdot \ln\left(\frac{T_{mean,i} - T_{B,i}}{T_{mean,i} - T_C}\right) \tag{2}$$

The zenith opacity τ_i can also be expressed as a linear combination of IWV and ILW along the zenith directions.

$$\tau_i = a_i + b_i \cdot \text{IWV} + c_i \cdot \text{ILW} \tag{3}$$

where the coefficients a_i and b_i vary with air pressure and are statistically derived from concurrent radiosonde measurements, with further refinement during clear-sky periods.

The coefficient c_i depends on air temperature and frequency and represents the Rayleigh mass absorption coefficient of cloud water. It can be derived from a dielectric model of water (Ellison, 2006).

By incorporating different frequencies (21.385 and 31.5 GHz) into Equation 3 and combining them, IWV and ILW can be retrieved as:

$$\text{IWV} = \frac{\tau_{21} - a_{21} - \gamma(\tau_{31} - a_{31})}{b_{21}(1 - \beta\gamma)} \tag{4}$$

$$\text{ILW} = \frac{\tau_{31} - a_{31} - \beta(\tau_{21} - a_{21})}{c_{31}(1 - \beta\gamma)} \tag{5}$$

where $\beta = b_{31}/b_{21} < 0.5$ and $\gamma = c_{21}/c_{31} \cong 0.5$. Mätzler and Morland (2009) described the retrieval process in detail.

2.2.2. Meteorological data

Meteorological data include air temperature, air pressure, and relative humidity as three feature variables for the retrieval model in this article. The data are collected by the ExWi weather station located a few meters away from TROWARA with a time resolution of 10 minutes (Wang et al., 2021b). The ExWi weather station uses a tipping bucket rain gauge with a measurement resolution of 0.2 mm to measure rainfall that reaches the ground. Although this type of gauge can easily identify rainfall intensity class (light, moderate, and heavy), it cannot classify precipitation types and is generally less accurate than standard rain gauges. For example, the bucket may not tip until the rain event has ended, yet a mere drop or two can cause it to tip at the onset of the next rainfall (Ahrens, 2015; Yilmaz, Hogue, lin Hsu, Sorooshian, Gupta and Wagener, 2005).

2.2.3. MRR data

Rain rate at the second bin height (200 m a.g.l.) of micro rain radar data is used as the target variable for the retrieval model in this article. The data are collected by a ground-based Micro Rain Radar (MRR) manufactured by Meteorologische Messtechnik GmbH (Metek) (METEK, 2009) located 2 m away from TROWARA since March 2007. The MRR, a compact Frequency Modulated Continuous Wave (FMCW) Doppler radar operating at 24.23 GHz, captures data with a 10-second time resolution. It can measure vertically from 100 to 3100 meters along the zenith direction with a 100-meter height resolution. The radar has a 3dB beamwidth of 1.5° and a modulation bandwidth ranging from 0.5 to 15 MHz. Garcia-Benadi, Bech, Gonzalez, Udina, Codina and Georgis (2020) developed a model that processes the MRR's spectral raw data to calculate rain rates (RR) by integrating over the drop size.

$$\text{RR} = \frac{\pi}{6} \int_0^\infty N(D) D^3 v(D) dD \tag{6}$$

where $N(D)$ is the drop size distribution with attenuation correction for a rain drop of diameter D, indicating the

number of drops per unit volume per diameter. $v(D)$ is the corrected terminal falling velocity. Beynon (2022) compared rainfall occurrences recorded by the MRR with those from the rain gauge and found that the MRR provided stable operation from 2008 to 2010, so this article uses data from January 1, 2008, to December 31, 2010, to train the rain rate retrieval model.

2.3. Data preprocessing

MRR measures raindrop size distributions in the atmosphere by changing the phase or frequency between the transmitted radar signals and the received backscattered signals (Maddikera, Kotamraju, Kavya and Gande, 2022). However, radar waves reflected by other atmospheric particles can be confused with raindrop signals, leading to misidentification and the creation of data outliers. The radar instrument system itself can also generate a certain amount of noise. To use accurate rain rates from the MRR as labels for the machine learning retrieval model, outliers and noise should first be removed from the data.

Figure1(a) shows the MRR target classification. Precipitation types are mainly divided into rain, drizzle, snow, mixed, and hail. Figure1(b) shows the rain rate from MRR. This is a stratiform rain with a melting layer around 900 m. By comparison with Figure1(a), it can be found that the rain rate measured by MRR mainly includes rain types: rain and drizzle. The two windows in Figure1(b) contain a large number of outliers. In addition to the outliers, the right window also captures a rain event lasting about 2 minutes. Stratiform rain is characterized by wide coverage, uniform intensity, and long duration, while this short rainfall event may be caused by local air movement and is therefore not considered. This paper uses the method of selecting only rain events lasting more than 5 minutes to preprocess rain rate outliers. Figure 1(c) shows the rain rate after removing outliers.

After removing outliers, the rain rate data is denoised using the median filtering method, as illustrated in Figure 2. To effectively eliminate noise while preserving the characteristics of rainfall rate changes, the filter window size is set to 9, corresponding to a duration of 90 seconds. The rain rate is measured at the second bin height rather than the first because data at 100 meters is excessively noisy. In addition, meteorological and microwave radiometer data are filtered using a window size of 7. Comparisons with rain gauge data confirm that this filtering approach is reasonable. Note that the rain gauge has a delay of about 10 minutes after the rain stops compared to the radar. The time and measurement resolution of the rain gauge may limit its response speed during the final phase of low rainfall (Qiao, Li, Fu, Tian, Bi, Zhou, Committee et al., 2012; Zhang, Wu, Zhang, Zhang, Xiao, Wang, Zhou, Song and Peng, 2021).

Table 1 shows that the rain intensity of MRR is divided into 3 grades according to meteorological standards (Qiao et al., 2012; Zhang et al., 2021), and the number of samples under these rain intensities. Light rain is the main rain

Table 1
Classification of rain intensity for samples in training set.

Intensity	Range	Number of samples
Light rain	(0 mm/h, 1.5 mm/h]	217312
Moderate rain	(1.5 mm/h, 7 mm/h]	12633
Heavy rain	>7 mm/h	50

intensity in Bern (Wang et al., 2021b), constituting about 94% of training samples.

3. Methods

3.1. Precipitation observation characteristics of ground-based microwave radiometer

Raindrops significantly affect microwave signals, not only causing extinction and emission but also inducing various scattering phenomena (Marzano et al., 2006). Radiative transfer theory provides a comprehensive theoretical framework for modeling the brightness temperature measured by microwave radiometers due to precipitation (Marzano et al., 2002). Consider a rain layer starting at a bottom height of 0 (surface) and extending to a top height of H. The integral form of zenith opacity τ, or extinction, can be expressed as:

$$\tau_{i,R} = \int_0^H k_{e,i}(z)dz \tag{7}$$

where z is the vertical height from 0 to H, and $k_{e,i}$ is the extinction coefficient. The scattering efficiency and angular scattering of rainfall are measured by the volume albedo w (where $w = k_e/k_s$ and k_s is the scattering coefficient) and the volume phase function p, respectively. They together with τ describe the single scattering properties of rainfall (Marzano et al., 2006). The scattering effect of ice is negligible for frequency observations between 22 and 31 GHz, making snow, which is composed of ice crystals, invisible to the microwave radiometer used in this article (Mätzler and Wegmüller, 1987). Microwave radiometer signals can be primarily affected by precipitation types including rain, drizzle and mixed.

Figure 3 shows the variations in brightness temperature (T_B) over time during the rain event from 11:00 to 21:00 UTC on October 6, 2008. As depicted in Figure 3(a), both the Micro Rain Radar (MRR) and the rain gauge detect precipitation, leading to a significant increase in T_B at frequencies of 21.385, 22.235, and 31.5 GHz, as shown in Figure 3(b). Furthermore, the more intense the rain rate, ranging from light to moderate, the greater the change observed in T_B. This suggests that T_B serves as an excellent proxy of rain rate. Statistical analysis reveals that the correlation coefficients between T_B at 21.385, 22.235, and 31.5 GHz and the MRR-measured rain rate across all samples are 0.61, 0.60, and 0.69, respectively. These high correlation coefficients further support the viability of using T_B as a feature variable in machine learning models for rain rate retrieval.
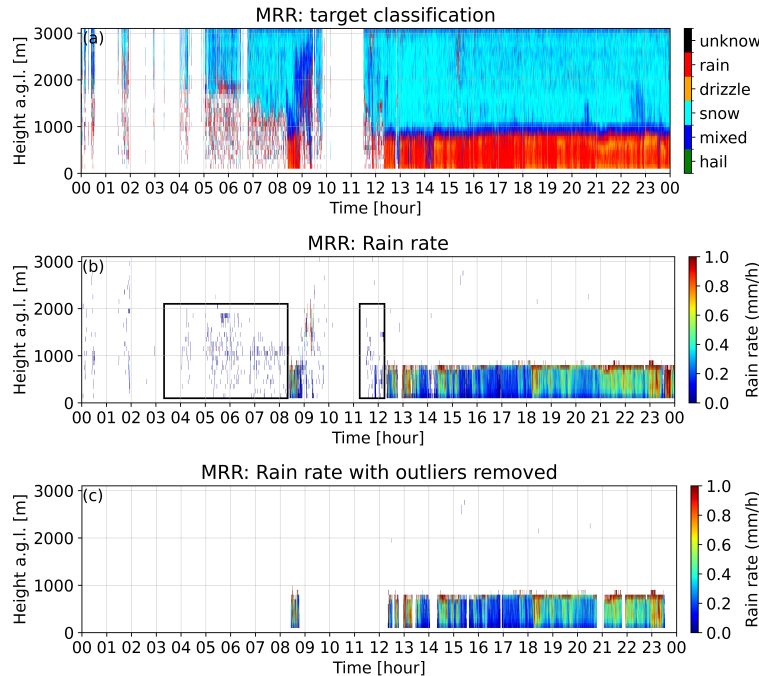
Figure 1: Outliers in Micro Rain Radar (MRR) data on January 5, 2008. (a) Raw MRR target classification. (b) Raw MRR rain rate. Part of the outliers is outlined in black box. (c) MRR rain rate data with outliers removed and rainfall duration exceeding 5 minutes.
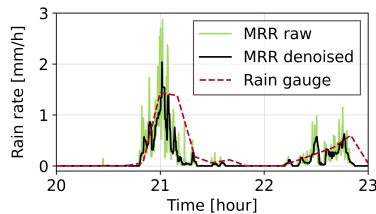

Figure 2: Denoising MRR rain rate data at 200 m height using median filtering and rain rates measured by rain gauge from 20:00 to 23:00 UTC on March 28, 2008.

3.2. Random Forest (RF)

RF is a machine learning algorithm that falls under the bagging category of ensemble learning methods, originally proposed by Breiman (2001). RF excels in regression tasks and is extensively used in studies of precipitation due to its robust performance Zhang et al. (2021); Xu, Tang, Li and Wan (2024). To construct a diverse and uncorrelated forest composed of many decision trees, RF includes two key randomness settings: sampling the original dataset using the bootstrap method, and randomly selecting a subset of features from which the best are chosen. The final model aggregates the predictions from all decision trees by taking their average.

Feature importance evaluation is a critical for RF as it helps in selecting features that enhance model performance and generalization. In RF, each tree is built by recursively selecting the best splitting features, calculating the Mean Decrease Impurity (MDI) caused by the splitting. The importance of a feature is quantified by summing the reduction in impurity it causes at each split point across all trees, and then averaging these sums over all trees to compute the importance score of the feature (Louppe, 2014; Louppe, Wehenkel, Sutera and Geurts, 2013).

3.3. Gradient Boosting Decision Trees (GBDT)

GBDT is a machine learning algorithm initially proposed by Breiman and further developed by Friedman (Breiman, 1996; Friedman, 2001, 2002). Employed for regression tasks, GBDT has demonstrated its effectiveness in various domains, especially precipitation estimation (Shen and Yong, 2021). The algorithm builds decision trees iteratively, with each subsequent tree aiming to correct the residuals left by the previous one, thus forming a robust predictive model. GBDT constructs its final model F_M by integrating multiple weak learners, which can be expressed
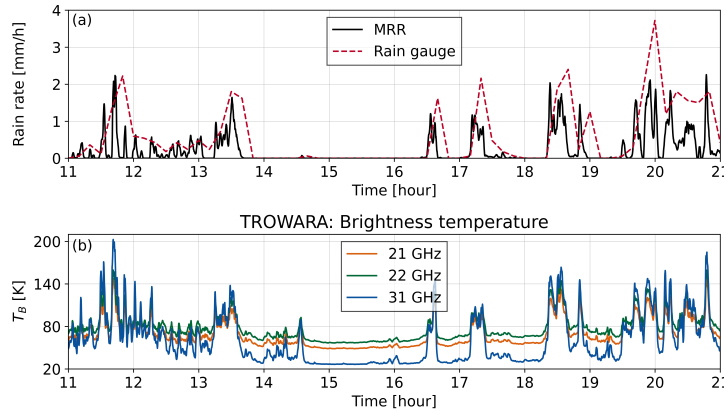
Figure 3: Effect of rain on radiation signal of microwave radiometer. (a) Denoised MRR rain rate at 200 m height (black) and rain rates (red) measured by rain gauge from 11:00 to 21:00 UTC on October 6, 2008. (b) Brightness temperature from microwave radiometer TROWARA at 21.385 (orange), 22.235 (green), and 31.5 GHz (red).

as follows (Shen and Yong, 2021):

$$F_M = \sum_{m=1}^{M} \gamma_m h(x; \theta_m) \qquad (8)$$

where M is the number of trees. $h(x; \theta_m)$ is the basic decision tree of the m-th iteration. x is the feature Variables. θ_m is the model parameter. γ_m is the weight of each decision tree.

The GBDT-based model excels in identifying the importance of various feature vectors for rainfall estimation. Friedman (2002) presented the calculation of GBDT feature importance selection. The importance of each feature in a model is determined by the frequency with which it is used to split nodes in all decision trees. This frequency is normalized into relative frequencies, and the average of these frequencies across all trees reflects the overall contribution of each feature to the model (Wu, Xia and Jin, 2021; Wang et al., 2023).

In this article, the RF and GBDT algorithms are implemented using the mature scikit-learn toolkit available in the Python module (https://scikit-learn.org/stable/).

3.4. Validation Strategy

Two strategies are employed to validate the rain rate retrieval model (Shen and Yong, 2021): ten-fold cross-validation method to assess the performance of the model itself, and applying the model to time series cases to verify rainfall estimates. The ten-fold cross-validation method partitions the samples into 10 subsets. Nine subsets are used for training the model, and one is used for testing the rainfall estimation performance. This process is repeated 10 times, with each subset being used once as the test set, and the results are averaged to ensure comprehensive evaluation across all samples. Three validation metrics are employed: the coefficient of determination (R^2), mean square error (MSE),

and mean absolute error (MAE). The formulas for these validation metrics are detailed in Table 2. The ten-fold cross-validation can only evaluate the performance of the rainfall retrieval model using these three years of rain events, but rainfall is complex and depends on various meteorological and geographical factors. Therefore, the effectiveness of the rain rate retrieval model is further estimated by estimating rainfall on time series.

The nine variables of the brightness temperature at 21.385 GHz, 22.235 GHz, and 31.5 GHz, the infrared cloud bottom brightness temperature, IWV, ILW, air temperature, air pressure, and relative humidity are used together as the feature input of the RF and GBDT learning data sets, and MRR-measured rain rates are used as labels, covering the period from January 1, 2008 to December 31, 2010. From 2008 to 2010, TROWARA's time resolution was 11 seconds. All data are normalized to a uniform 10-second temporal resolution using the sample resampling method. The dataset contains 255,550 samples.

4. Results

Figure 4 shows the validation scatter plots of rain rates from microwave radiometer (MWR) based on RF and GBDT methods, and comparison with MRR-measured rain rates. As can be seen from Figure 4(a) and (b), compared with the MRR-measured rain rates, the RF-based method for MWR rainfall estimation achieved slightly better performance than the GBDT-based method, with R^2, MSE, and MAE verified to be 0.96, 0.01 mm/h, and 0.05 mm/h, respectively. The R^2, MSE, and MAE verification of MWR rainfall estimates based on the GBDT method are 0.95, 0.02 mm/h, and 0.07 mm/h, respectively. This is not surprising since RF is less sensitive to outliers relative to GBDT. In addition, the calculation time of the RF method when retrieving rain rate is also slightly faster than that of GBDT. In general,

Table 2

Validation metrics with the range and optimum. y_i is the true label values. $\hat{y}_i$ is the predictions of methods. n is the number of samples.

Metrics	Equation	Range	Optimum
Coefficient of determination	$R^2 = 1 - \frac{\sum_{i=1}^{n}(y_i - \hat{y}_i)^2}{\sum_{i=1}^{n}(y_i - \bar{y})^2}$	$[0,1]$	1
Mean Squared Error	$MSE = \frac{1}{n}\sum_{i=1}^{n}(y_i - \hat{y}_i)^2$	$[0,\infty]$	0
Mean Absolute Error	$MAE = \frac{1}{n}\sum_{i=1}^{n}|y_i - \hat{y}_i|$	$[0,\infty]$	0

the two machine learning-based methods, RF and GBDT, demonstrate high accuracy for rain rate retrieval for MWR with a high time resolution of 10 seconds.

Another noteworthy finding in Figure 4 is that when rain rates range between 2 mm/h and 8 mm/h (moderate to heavy rain), the rain rates estimated by MWR are slightly lower than those by MRR, as indicated by the regression fit line lying below the x = y line. This discrepancy suggests that the algorithm for rain retrieval using MWR based on RF and GBDT methods tends to slightly underestimate rain, particularly in moderate to heavy rain conditions, thereby impacting the accuracy of rainfall estimation to some extent. Several factors may contribute to this underestimation of high-intensity rain:

- Inadequate Training Data: Heavy rain events often involve rapid changes in intensity over short periods of time and the spatial complexity of their rain patterns, making them challenging to accurately capture. Machine learning models trained on insufficient samples of moderate to heavy rain may fail to adequately represent high-intensity rain patterns (Table 1).

- Saturation of Higher Frequency Channels: During heavy rain, higher frequency channels, such as 31 GHz, are susceptible to brightness temperature saturation (Marzano et al., 2006; Battaglia, Saavedra, Simmer and Rose, 2009; Zhang, Xu, Xi, Ren, Wan, Zhou, Cui and Wu, 2020). This saturation phenomenon may lead to an underestimation of rain rates when using MWR for rainfall retrieval.

- Overestimation by MRR: MRR may overestimate rain rates within this range (Urgilés, Célleri, Trachte, Bendix and Orellana-Alvear, 2021), contributing further to the observed underestimation when compared with MWR.

Figure 5 shows a case study where MWR rain rate retrieval technologies are applied to time series data for verification from 18:00 to 22:00 UTC on October 6, 2011. Notably, this time period is not included in the training and testing phases of the model. This serves as an example of light to moderate stratiform rain, characterized by a melting layer situated approximately 2000 m above the ground. As can be seen from Figure 5 (b), from the beginning and end of the rain period, the rain rate retrieved by MWR based on RF and GBDT methods agrees well with the MRR-measured data, and the changing trends of these curves over

time are consistent. After the end of the rainfall detected by MRR, there is a delay of over 40 minutes observed by the rain gauge between 19:20 and 20:00 UTC. The rain rate curve recorded by the rain gauge is higher than that of both MWR and MRR, particularly around 21:40 UTC with notable differences observed. It is important to emphasize that rain gauge data provide integrated measurements of a ground point over time, and do not necessarily represent the atmospheric opacity structure of microwave radiation measurements (Marzano et al., 2006). Figure 6 shows another case study verifying MWR rain rate retrieval technologies from 13:00 to 20:00 UTC on January 6, 2011. This example features light stratiform rain, with the melting layer situated approximately 1400 m above the ground. Figure 6 is similar to Figure 5, but the rain rate observed by the rain gauge in Figure 6 exhibits better agreement with the rain rate provided by the MWR and MRR in Figure 5.

5. Discussion

We also applied the machine learning method Light Gradient-Boosting Machine (LightGBM) to retrieve rain rates in microwave radiometer data (Ke, Meng, Finley, Wang, Chen, Ma, Ye and Liu, 2017). The running speed of the model based on LightGBM is very fast, each training only takes 1 second. In comparison, for the parameters corresponding to the existing results unchanged, the RF and GBDT models require 377 seconds and 610 seconds, respectively, for training. However, it is worth noting that the accuracy of LightGBM is slightly inferior for precipitation estimation, and results show that the R^2, MSE, MAE are 0.81, 0.07 mm/h, and 0.15 mm/h, respectively. Potential reasons may be determined by the characteristics of these algorithms itself. Different from traditional tree-based algorithms, LightGBM employs a histogram optimization algorithm, which enhances training efficiency and speed but may impact the regression accuracy of the model. Compared with the robustness of RF and GBDT on small data sets, LightGBM is more suitable for large-scale data sets and more sensitive to data noise and outliers. Furthermore, this article also tried to use the Support Vector Machine (SVM) algorithm to retrieve rain rates (Cortes and Vapnik, 1995), but it took at least 10 hours to run the model for training, resulting in a high time cost. Considering that this study only encompasses 3 years of data, achieving a more stable model covering various rainfall types, patterns, and intensities in the future would necessitate participation in training with
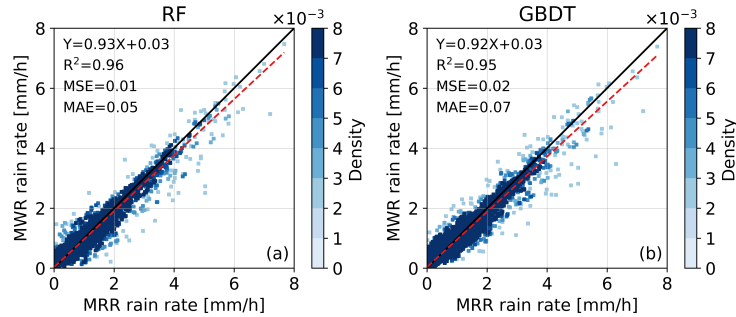
Figure 4: Scatter density plot between rain rates retrieved by machine learning methods from MWR and measured by MRR over the period 2008 to 2010. (a) Rain rate retrieved by RF from MWR. (b) Rain rate retrieved by GBDT from MWR. The black solid line is the 1:1 line, and the red dashed line is the linear regression fit line. The blue colors show the density of the data distribution calculated by Gaussian kernels.
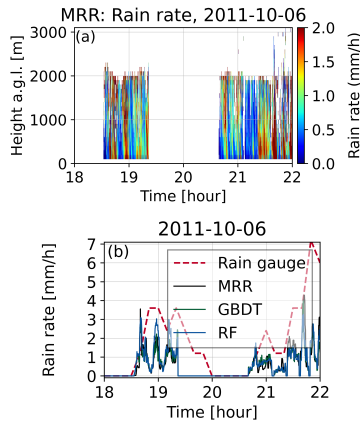

Figure 5: Example of MWR retrieved, MRR and rain gauge measured rain rates from 18:00 to 22:00 UTC on October 6, 2011. (a) MRR rain rates with the melting layer at an height of 2000 m. (b) Rain rates retrieved by GBDT and RF method from MWR, MRR rain rate at 200 m height, and rain gauge.
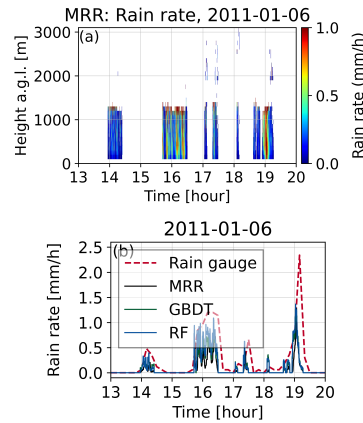
Figure 6: Same as in 5, but from 13:00 to 20:00 UTC on January 6, 2011 and the melting layer at an height of 1400 m.

data spanning a longer period. Time-consuming models may therefore not be a suitable choice, and RF and GBDT already meet the accuracy requirements (Figure 4).

A good machine learning model should not only be highly accurate in predicting rain rates but also offer strong interpretability. Figure 7 shows the importance of feature variables based on the GBDT rain rate retrieval method, offering an intuitive depiction of the model's reliance on various features. The first three important features are integrated liquid water (ILW), brightness temperature at 21.385 GHz ($T_{B,21}$), and brightness temperature at 31.4 GHz ($T_{B,31}$). The results on feature importance align with the parameter requirements of the physical algorithm for rain rate retrieval developed by Wang et al. (2021b). ILW, also known as

Liquid Water Content (LWC), refers to the vertical integration of liquid water, specifically cloud droplets, in the atmosphere. Clouds have a direct correlation with precipitation, for instance, cumulonimbus clouds are associated with thunderstorms and heavy rain. $T_{B,21}$ is more sensitive to microwaves emitted by water vapour and $T_{B,31}$ is more sensitive to microwaves emitted by atmospheric liquid water (Hocke et al., 2017). Both frequencies have been utilized in rain rate retrieval (Wang et al., 2021b; Marzano, Cimini, Ciotti and Ware, 2005a; Marzano et al., 2005b). The fourth to ninth important features are air pressure (P), air temperature (T), infrared cloud base brightness temperature ($T_{B,IR}$), brightness temperature at 22.235 GHz ($T_{B,22}$), integrated water vapor (IWV), relative humidity (RH), respectively. It can be seen in Figure 7 that $T_{B,22}$ does not contribute as significantly to rainfall estimation compared to $T_{B,21}$ and $T_{B,31}$. These variables except $T_{B,22}$ are closely related to the
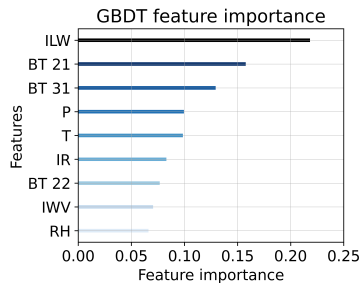
Figure 7: Variable importance of features included in GBDT method for rain rate retrieval.

evolution of rainfall (Wang and Hocke, 2022; Wang, Hocke, Nania, Cazorla, Titos, Matthey, Alados-Arboledas, Millares and Navas-Guzmán, 2024).

Rain gauges can serve as an alternative to MRR as the target variable of the methods in this article to retrieve the rain rate for ground-based microwave radiometers, but some limitations of rain gauges also need to be considered. First, rain gauges ignore rainfall that does not fall to the ground, such as virga (Beynon and Hocke, 2022; Beynon, 2022; Wang et al., 2024), so meaning that using rain gauges as tags does not fully capitalize on the potential of microwave radiometers as remote sensing instruments to study such rainfall (Wang et al., 2024). Second, rain gauges may experience decreased measurement accuracy due to wind effects. Finally, the time resolution of rain gauges is relatively low (1 to 10 minutes) compared to the high time resolution of microwave radiometers (1 to 10 seconds). Figure 3 illustrates the misalignment of time correspondences due to differences in their time resolution. MRR not only offers high time resolution but also serves as a remote sensing instrument capable of observing virga (Beynon, 2022; Beynon and Hocke, 2022).

6. Conclusions

Accurate and reliable precipitation estimation from ground-based microwave radiometers is of great significance as a complement to other precipitation measurement techniques. In this article, we present two high temporal resolution (10 seconds) rain rate retrieval models that can handle the challenge of combining microwave radiometers with micro rain radar observations to study precipitation over Swiss Plateau from 2008 to 2010. To achieve precise retrieval, the new machine learning-based models, employing algorithms RF and GBDT, first eliminate outliers and noise from the rain rate data obtained from the micro rain radar, which serves as the target variable. Then, the models' feature selection process leverage the physical characteristics of atmospheric raindrops affecting microwave radiation signals, while also incorporating meteorological variables.

The models underwent validation using the ten-fold cross-validation method and are subsequently applied to

time series data. Results show that both RF and GBDT-based models for rain rate retrieval from the ground-based microwave radiometer exhibit excellent performance, with the GBDT-based model slightly inferior the RF-based. The RF-based method achieves 0.96 R^2, 0.01 mm/h MSE, and 0.05 mm/h MAE. Using the GBDT-based method, the corresponding metrics are 0.95 R^2, 0.02 mm/h MSE, and 0.07 mm/h MAE. In the case study, reasonably good agreement is achieved between microwave radiometer precipitation estimates and micro rain radar measurements. These two methods outperform LightGBM and SVM significantly in terms of accuracy and training time efficiency, respectively. This paper also discusses the advantages of using micro rain radar as the target variable compared to rain gauges for rain rate retrieval research on ground-based microwave radiometers, and further explains the feature selection of the models based on physical principles through the feature importance of GBDT.

In future studies, the methods in this article can be applied to other regions as well as other ground-based microwave radiometers. Due to limited instrumentation, rain gauges can also be used as a substitute for micro rain radar in measuring rain rate as the target variable for model training. Another future study might be to analyze short-term characteristics of precipitation, e.g. preferred rainfall frequencies in high-resolution datasets.

CRediT authorship contribution statement

Wenyue Wang: Conceptualization of this study, Methodology, Validation, Formal analysis, Software operations, Investigation, Writing - original draft, Writing-review & editing, Visualization. **Wenzhi Fan:** Methodology, Writing-review & editing. **Klemens Hocke:** Conceptualization of this study, Supervision, Project administration, Writing-review & editing.

Declaration of Competing Interest

The authors declare that they have no known competing financial interests or personal relationships that could have appeared to influence the work reported in this paper.

Data availability

Data will be made available on request.

Acknowledgments

References

Ahrens, C.D., 2015. Meteorology today: an introduction to weather, climate, and the environment. Cengage Learning Canada Inc.

Allen, M.R., Ingram, W.J., 2002. Constraints on future changes in climate and the hydrologic cycle. Nature 419, 224–232. doi:10.1038/nature01092.

Battaglia, A., Saavedra, P., Simmer, C., Rose, T., 2009. Rain observations by a multifrequency dual-polarized radiometer. IEEE Geoscience and Remote Sensing Letters 6, 354–358. doi:10.1109/LGRS.2009.2013484.

Beynon, R., 2022. Observations of virga precipitation with a micro rain radar. Master's Thesis, Physik-Institut, Universität Zürich, Zürich, Switzerland .

Beynon, R., Hocke, K., 2022. Snow virga above the swiss plateau observed by a micro rain radar. Remote Sensing 14. doi:10.3390/rs14040890.

Brandsma, T., Buishand, T., 1997. Statistical linkage of daily precipitation in switzerland to atmospheric circulation and temperature. Journal of Hydrology 198, 98–123. doi:10.1016/S0022-1694(96)03326-4.

Breiman, L., 1996. Bagging predictors. Machine learning 24, 123–140.

Breiman, L., 2001. Random forests. Machine learning 45, 5–32.

Cimini, D., Hewison, T.J., Martin, L., Güldner, J., Gaffard, C., Marzano, F.S., 2006. Temperature and humidity profile retrievals from ground-based microwave radiometers during tuc. Meteorologische Zeitschrift 15, 45–56. doi:10.1127/0941-2948/2006/0099.

Cortes, C., Vapnik, V., 1995. Support-vector networks. Machine learning 20, 273–297.

Ellison, W., 2006. Freshwater and sea water. thermal microwave radiation: Applications for remote sensing 52, 431–455.

Friedman, J.H., 2001. Greedy function approximation: a gradient boosting machine. Annals of statistics , 1189–1232.

Friedman, J.H., 2002. Stochastic gradient boosting. Computational statistics & data analysis 38, 367–378.

Garcia-Benadi, A., Bech, J., Gonzalez, S., Udina, M., Codina, B., Georgis, J.F., 2020. Precipitation type classification of micro rain radar data using an improved doppler spectral processing methodology. Remote Sensing 12. doi:10.3390/rs12244113.

Held, I.M., Soden, B.J., 2006. Robust responses of the hydrological cycle to global warming. Journal of Climate 19, 5686 – 5699. URL: https://journals.ametsoc.org/view/journals/clim/19/21/jcli3990.1.xml, doi:10.1175/JCLI3990.1.

Hocke, K., Bernet, L., Hagen, J., Murk, A., Renker, M., Mätzler, C., 2019. Diurnal cycle of short-term fluctuations of integrated water vapour above switzerland. Atmospheric Chemistry and Physics 19, 12083–12090. doi:10.5194/acp-19-12083-2019.

Hocke, K., Navas-Guzmán, F., Moreira, L., Bernet, L., Mätzler, C., 2017. Oscillations in atmospheric water above switzerland. Atmospheric Chemistry and Physics 17, 12121–12131. doi:10.5194/acp-17-12121-2017.

Hong, Y., Adler, R.F., Negri, A., Huffman, G.J., 2007. Flood and landslide applications of near real-time satellite rainfall products. Natural Hazards 43, 285–294. doi:10.1007/s11069-006-9106-x.

Ke, G., Meng, Q., Finley, T., Wang, T., Chen, W., Ma, W., Ye, Q., Liu, T.Y., 2017. Lightgbm: A highly efficient gradient boosting decision tree. Advances in neural information processing systems 30.

Kundzewicz, Z.W., 2008. Climate change impacts on the hydrological cycle. Ecohydrology & Hydrobiology 8, 195–203. doi:10.2478/v10104-009-0015-y.

Leuenberger, A., 2009. Precipitation measurements with microwave sensors. Master's thesis. Faculty of Science, University of Bern, Bern, Switzerland.

Liu, Z., Yang, Q., Shao, J., Wang, G., Liu, H., Tang, X., Xue, Y., Bai, L., 2022. Improving daily precipitation estimation in the data scarce area by merging rain gauge and trmm data with a transfer learning framework. Journal of Hydrology 613, 128455. doi:10.1016/j.jhydrol.2022.128455.

Louppe, G., 2014. Understanding random forests: From theory to practice. arXiv preprint arXiv:1407.7502 .

Louppe, G., Wehenkel, L., Sutera, A., Geurts, P., 2013. Understanding variable importances in forests of randomized trees. Advances in neural information processing systems 26.

Maddikera, K.R., Kotamraju, S.K., Kavya, K.C.S., Gande, B.G.T., 2022. Radar reflectivity of micro rain radar (mrr2) at 16.44180 n, 80.620 e of india. International Journal of Integrated Engineering 14, 162–185.

Marzano, F., Cimini, D., Ciotti, P., Ware, R., 2005a. Modeling and measurement of rainfall by ground-based multispectral microwave radiometry. IEEE Transactions on Geoscience and Remote Sensing 43, 1000–1011. doi:10.1109/TGRS.2004.839595.

Marzano, F., Fionda, E., Ciotti, P., Martellucci, A., 2002. Ground-based multifrequency microwave radiometry for rainfall remote sensing. IEEE Transactions on Geoscience and Remote Sensing 40, 742–759. doi:10.1109/TGRS.2002.1006317.

Marzano, F.S., Cimini, D., Montopoli, M., 2010. Investigating precipitation microphysics using ground-based microwave remote sensors and disdrometer data. Atmospheric Research 97, 583–600. URL: https://www.sciencedirect.com/science/article/pii/S0169809510000682, doi:10.1016/j.atmosres.2010.03.019.

Marzano, F.S., Cimini, D., Ware, R., 2005b. Monitoring of rainfall by ground-based passive microwave systems: models, measurements and applications. Advances in Geosciences 2, 259–265. URL: https://adgeo.copernicus.org/articles/2/259/2005/, doi:10.5194/adgeo-2-259-2005.

Marzano, F.S., Fionda, E., Ciotti, P., 2006. Neural-network approach to ground-based passive microwave estimation of precipitation intensity and extinction. Journal of Hydrology 328, 121–131. URL: https://www.sciencedirect.com/science/article/pii/S0022169405006438, doi:10.1016/j.jhydrol.2005.11.042.

Mätzler, C., Morland, J., 2009. Refined physical retrieval of integrated water vapor and cloud liquid for microwave radiometer data. IEEE Transactions on Geoscience and Remote Sensing 47, 1585–1594. doi:10.1109/TGRS.2008.2006984.

Mätzler, C., Morland, J., 2014. Advances in surface-based radiometry of atmospheric water. IAP Research Report 2008-02-MW; Institute of Applied Physics, University of Bern: Bern, Switzerland .

Mätzler, C., Wegmüller, U., 1987. Dielectric properties of freshwater ice at microwave frequencies. Journal of Physics D: Applied Physics 20, 1623. doi:10.1088/0022-3727/20/12/013.

METEK, 2009. Mrr physical basics valid for mrr service version 5.2.1.0. METEK: Elmshorn, Germany .

Morland, J., 2002. Trowara-tropospheric water vapour radiometer: Radiometer review and new calibration model. IAP Research Report 2008-02-MW; Institute of Applied Physics, University of Bern: Bern, Switzerland .

Morland, J., 2007. Trowara-rain flag development and stability of instrument and calibration. IAP Research Report 2008-02-MW; Institute of Applied Physics, University of Bern: Bern, Switzerland .

Netzel, L., Heldt, S., Denecke, M., 2021. Analyzing twitter communication about heavy precipitation events to improve future risk communication and disaster reduction in germany. Urban Water Journal 18, 310–319. doi:10.1080/1573062X.2021.1878241.

Qiao, L., Li, Y., Fu, J., Tian, C., Bi, B., Zhou, Q., Committee, C.N.S.M., et al., 2012. Grade of precipitation, gb/t 28592–2012.

Rombeek, N., Leinonen, J., Hamann, U., 2024. Exploiting radar polarimetry for nowcasting thunderstorm hazards using deep learning. Natural Hazards and Earth System Sciences 24, 133–144. URL: https://nhess.copernicus.org/articles/24/133/2024/, doi:10.5194/nhess-24-133-2024.

Rose, T., Crewell, S., Löhnert, U., Simmer, C., 2005. A network suitable microwave radiometer for operational monitoring of the cloudy atmosphere. Atmospheric Research 75, 183–200. URL: https://www.sciencedirect.com/science/article/pii/S0169809505000189, doi:10.1016/j.atmosres.2004.12.005.

Sauvageat, E., Hocke, K., Maillard Barras, E., Hou, S., Errera, Q., Haefele, A., Murk, A., 2023. Microwave radiometer observations of the ozone diurnal cycle and its short-term variability over switzerland. Atmospheric Chemistry and Physics 23, 7321–7345. doi:10.5194/acp-23-7321-2023.

Shen, Z., Yong, B., 2021. Downscaling the gpm-based satellite precipitation retrievals using gradient boosting decision tree approach over mainland china. Journal of Hydrology 602, 126803. doi:10.1016/j.jhydrol.2021.126803.

Urgilés, G., Célleri, R., Trachte, K., Bendix, J., Orellana-Alvear, J., 2021. Clustering of rainfall types using micro rain radar and laser disdrometer observations in the tropical andes. Remote Sensing 13. doi:10.3390/rs13050991.

Villarini, G., Krajewski, W.F., 2010. Review of the different sources of uncertainty in single polarization radar-based estimates of rainfall. Surveys in geophysics 31, 107–129. doi:10.1007/s10712-009-9079-x.

Wang, C., Tang, G., Xiong, W., Ma, Z., Zhu, S., 2021a. Infrared precipitation estimation using convolutional neural network for fengyun satellites. Journal of Hydrology 603, 127113. doi:10.1016/j.jhydrol.2021.127113.

Wang, W., Hocke, K., 2022. Atmospheric effects and precursors of rainfall over the swiss plateau. Remote Sensing 14. doi:10.3390/rs14122938.

Wang, W., Hocke, K., Mätzler, C., 2021b. Physical retrieval of rain rate from ground-based microwave radiometry. Remote Sensing 13. doi:10.3390/rs13112217.

Wang, W., Hocke, K., Nania, L., Cazorla, A., Titos, G., Matthey, R., Alados-Arboledas, L., Millares, A., Navas-Guzmán, F., 2024. Inter-relations of precipitation, aerosols, and clouds over andalusia, southern spain, revealed by the andalusian global observatory of the atmosphere (agora). Atmospheric Chemistry and Physics 24, 1571–1585. doi:10.5194/acp-24-1571-2024.

Wang, W., Murk, A., Sauvageat, E., Fan, W., Dätwyler, C., Hervo, M., Haefele, A., Hocke, K., 2023. An indoor microwave radiometer for measurement of tropospheric water. IEEE Transactions on Geoscience and Remote Sensing 61, 1–13. doi:10.1109/TGRS.2023.3261067.

Won, H.Y., Kim, Y.H., Lee, H.S., 2009. An application of brightness temperature received from a ground-based microwave radiometer to estimation of precipitation occurrences and rainfall intensity. Asia-Pacific Journal of Atmospheric Sciences 45, 55–69.

Wu, W., Xia, Y., Jin, W., 2021. Predicting bus passenger flow and prioritizing influential factors using multi-source data: Scaled stacking gradient boosting decision trees. IEEE Transactions on Intelligent Transportation Systems 22, 2510–2523. doi:10.1109/TITS.2020.3035647.

Xu, G., Ware, R.S., Zhang, W., Feng, G., Liao, K., Liu, Y., 2014. Effect of off-zenith observations on reducing the impact of precipitation on ground-based microwave radiometer measurement accuracy. Atmospheric Research 140-141, 85–94. URL: https://www.sciencedirect.com/science/article/pii/S0169809514000234, doi:https://doi.org/10.1016/j.atmosres.2014.01.021.

Xu, Y., Tang, G., Li, L., Wan, W., 2024. Multi-source precipitation estimation using machine learning: Clarification and benchmarking. Journal of Hydrology 635, 131195. doi:10.1016/j.jhydrol.2024.131195.

Yilmaz, K.K., Hogue, T.S., lin Hsu, K., Sorooshian, S., Gupta, H.V., Wagener, T., 2005. Intercomparison of rain gauge, radar, and satellite-based precipitation estimates with emphasis on hydrologic forecasting. Journal of Hydrometeorology 6, 497 – 517. URL: https://journals.ametsoc.org/view/journals/hydr/6/4/jhm431_1.xml, doi:10.1175/JHM431.1.

Yu, W., Xu, X., Jin, S., Ma, Y., Liu, B., Gong, W., 2022. Bp neural network retrieval for remote sensing atmospheric profile of ground-based microwave radiometer. IEEE Geoscience and Remote Sensing Letters 19, 1–5. doi:10.1109/LGRS.2021.3117882.

Zhang, W., Xu, G., Xi, B., Ren, J., Wan, X., Zhou, L., Cui, C., Wu, D., 2020. Comparative study of cloud liquid water and rain liquid water obtained from microwave radiometer and micro rain radar observations over central china during the monsoon. Journal of Geophysical Research: Atmospheres 125, e2020JD032456. doi:10.1029/2020JD032456.

Zhang, Y., Wu, K., Zhang, J., Zhang, F., Xiao, H., Wang, F., Zhou, J., Song, Y., Peng, L., 2021. Estimating rainfall with multi-resource data over east asia based on machine learning. Remote Sensing 13. doi:10.3390/rs13163332.

7 INDOOR AND OUTDOOR TROPOSPHERIC MICROWAVE RADIOMETERS

7.1 SUMMARY OF THE STUDY

Exploring the measurement capabilities of K-band (21.3-31.5 GHz) ground-based microwave radiometers and analyzing biases and uncertainties in retrieving atmospheric water (water vapor, clouds, and rain) are critical for climate change research (Ji et al., 2021; Nandan et al., 2022). Comparing data from two microwave radiometers with different settings is beneficial for assessing the reliability of atmospheric water measurements because they share the same observational principle that helps account for various sources of errors (Cimini et al., 2006; Mattioli et al., 2004, 2005). Moreover, indoor observations can effectively avoid issues such as radome and antenna wetting. The water film on an outdoor radiometer radome caused by rain may affect the radiation signal, making it difficult to distinguish the signals of raindrops from other atmospheric parameters. However, previous studies have not adequately analyzed the issues radiometers face during outdoor operation.

The article presented in this chapter compared the brightness temperature measurements from the commercial outdoor microwave radiometer HATPRO with those from the indoor microwave radiometer TROWARA, assessing their performance in measuring atmospheric water. Since rain estimates are not available in the HATPRO software, the same physical retrieval method based on 31 GHz optical depth used for TROWARA was applied to retrieve rain rates for HATPRO (Wang et al., 2021). My study was the first to provide a detailed description that the innovative measurement device of indoor TROWARA avoids issues caused by water films on the radome. I employed GBDT to identify sources of brightness temperature deviations.

The study contributed to the GCOS Project. In September 2021, Swiss Federal Office of Meteorology and Climatology (MeteoSwiss) transferred the HATPRO radiometer from Payerne to Bern where it is operated in parallel with the TROWARA radiometer, and I was actively involved in the installation and the LN2 calibration of HATPRO. This campaign is unique because it provides simultaneous data from outdoor and indoor radiometers observing in the same direction (southeast) and at the same elevation angle (40°) (Hocke, 2022).

The following article was peer-reviewed and published in IEEE Transactions on Geoscience and Remote Sensing in March 2023.

7.2 PUBLICATION

FULL CITATION

Wang Wenyue, Axel Murk, Eric Sauvageat, Wenzhi Fan, Christoph Dätwyler, Maxime Hervo, Alexander Haefele, and Klemens Hocke (2023). "An indoor microwave radiometer for measurement of tropospheric water." In: *IEEE Transactions on Geoscience and Remote Sensing* 61, pp. 1-13. https://doi.org/10.1109/TGRS.2023.3261067.

An Indoor Microwave Radiometer for Measurement of Tropospheric Water

Wenyue Wang, Axel Murk, Eric Sauvageat, Wenzhi Fan, Christoph Dätwyler, Maxime Hervo, Alexander Haefele, and Klemens Hocke

Abstract— This article presents the first detailed description of the innovative measurement setup of an indoor tropospheric microwave radiometer [TROpospheric WAter RAdiometer (TROWARA)] that avoids water films on radome. We discuss the performance of a commercial outdoor microwave radiometer [Humidity And Temperature PROfiler radiometer (HATPRO)] for measuring tropospheric water parameters in Bern, Switzerland. The HATPRO is less than 20 m from the TROWARA and has different instrument characteristics. Brightness temperatures measured by HATPRO are analyzed by comparing them with coincident measurements from TROWARA and Radiative Transfer Simulations based on the [European Centre for Medium-Range Weather Forecasts (ECMWF)] operational analysis data (denoted as RTSE). To find the source of brightness temperature bias, a gradient boosting decision tree is used to analyze the sensitivity of eight feature factors to bias. Data processing routines of the two radiometers use different algorithms to retrieve integrated water vapor (IWV) and integrated cloud liquid water (ILW), whereas the same physical algorithms based on the radiative transfer equation are applied to obtain the opacity and rain rate. Using 62 days of data with varied weather conditions, it was found that TROWARA brightness temperatures are in good agreement with RTSE. HATPRO brightness temperatures are significantly overestimated by about 5 K at 22 GHz, compared to TROWARA and RTSE. HATPRO brightness temperatures at 31 GHz agree well with TROWARA and RTSE (within about ±1 K). The overestimated brightness temperatures in the K-band and the HATPRO retrieval algorithm lead to an overestimation of IWV and ILW by HATPRO. The opacities at 31 GHz match very well for TROWARA and HATPRO during no rain with a verified R^2 of 0.96. However, liquid water floating or remaining water films on the radome of the outdoor HATPRO radiometer induce an overestimation of the rain rate. The physical reason for the overestimated 22-GHz brightness temperatures of the HATPRO is mainly the result of the combined effect of instrument calibration, the surrounding environment of the instrument, and the Sun elevation angle. This can be a problem with the Generation 2 HATPRO radiometer and this problem was resolved in the Generation 5 HATPRO radiometer.

Index Terms— Atmospheric Radiative Transfer Simulator (ARTS), brightness temperature, European Centre for Medium-Range Weather Forecasts (ECMWF), gradient boosting decision tree (GBDT), Humidity And Temperature PROfiler radiometer (HATPRO), K-band, microwave radiometer, radiometer technology, rain rate, remote sensing, water films, water vapor.

I. INTRODUCTION

ACCURATE measurements of tropospheric water (e.g., water vapor, cloud, and rain) are required for studies of climate change. Water vapor is the most abundant greenhouse gas [1]. Clouds affect the Earth's radiation budget, and any subtle change in cloud properties can alter climate responses to anthropogenic aerosols or other factors associated with global change [2]. Heavy rainfall often causes flooding [3]. The advantages of ground-based microwave radiometers in the K-band (21.3–31.5 GHz) for measuring atmospheric water are well known: continuous, automatic operation with high time resolution in almost all weather conditions, day and night [4], [5]. Bernet et al. [6] showed that ground-based microwave radiometry is adequate to monitor long-term trends of integrated water vapor (IWV). Ground-based microwave radiometers are further important for cross validation of satellite measurements of IWV [7], [8]. Compared to ground-based global navigation satellite system (GNSS) receivers, a radiometer can provide IWV with a higher temporal and horizontal resolution (e.g., 10 s and 100 m). Thus, a ground-based radiometer can achieve a high coincidence with an overhead satellite observation of IWV, which is of interest for the study of the small-scale variability of IWV [9]. Exploring measurement capabilities of ground-based microwave radiometers and analyzing biases and uncertainties in atmospheric water retrievals are therefore necessary.

Microwave radiometers measure brightness temperatures (Tb) to derive atmospheric water parameters, including IWV, integrated cloud liquid water (ILW), and rain rate. To evaluate the reliability of the derived IWV, it is often compared to water vapor derived from other techniques such as radiosonde, GNSS, Fourier transform infrared spectrometer (FTIR), and Raman lidar [6], [10], [11]. Radiosondes cannot directly observe the characteristics of the cloud liquid [2]. In situ measurements of ILW can provide the most accurate microphysical information on clouds [12], but it requires aircraft to traverse

Wenyue Wang, Axel Murk, Eric Sauvageat, Christoph Dätwyler, and Klemens Hocke are with the Institute of Applied Physics and the Oeschger Centre for Climate Change Research, University of Bern, 3012 Bern, Switzerland (e-mail: wenyue.wang@unibe.ch; axel.murk@unibe.ch; eric.sauvageat@unibe.ch; christoph.daetwyler@unibe.ch; klemens.hocke@unibe.ch).

Wenzhi Fan is with the School of Earth and Space Sciences, Peking University, Beijing 100084, China (e-mail: wenzhi.fan@pku.edu.cn).

Maxime Hervo and Alexander Haefele are with the Federal Office of Meteorology and Climatology, MeteoSwiss, 1530 Payerne, Switzerland (e-mail: maxime.hervo@meteoswiss.ch; alexander.haefele@meteoswiss.ch).

rapidly evolving clouds and cannot represent radiometer sampling [13]. The vertical reflectivity of expensive and sparsely distributed cloud radar is more suitable for obtaining ILW with small droplets [14]. Rain rates are primarily verified by the accumulated rain measured by rain gauges with a coarser time resolution compared to radiometers. The inter-comparison of two microwave radiometers with a different setup is undoubtedly a good choice because they have the same observation principle, which helps to account for various sources of error. The Humidity And Temperature PROfiler (HATPRO) radiometer manufactured by Radiometer Physics GmbH (RPG) is widely used for meteorological monitoring and forecasting networks worldwide [15]. The TROpospheric WAter RAdiometer (TROWARA) built and operated by the Institute of Applied Physics (IAP) at the University of Bern, Bern, Switzerland, has been operational for 28 years. Many studies have compared it to global positioning system (GPS), in situ instruments, and reanalysis data and demonstrated TROWARA's superior ability to retrieve atmospheric water, especially IWV [16], [17], [18], [19].

Cimini et al. [20] evaluated the agreement of Tb measured by two ground-based microwave radiometers during the Temperature, hUmidity, and Cloud (TUC) profiling campaign. Mattioli et al. [21] explored the scanning capabilities of three microwave radiometers and their monitoring of IWV and ILW during the 2003 Cloudiness Inter-Comparison Experiment. Mattioli et al. [22] compared Tb calculated by radiosonde with those measured by three microwave radiometers at 23.8 and 31.4 GHz as well as the IWV from the radiometers and a GPS station. However, these studies lack an analysis of the problems of radiometers due to outdoor operation. Microwave radiation strongly emitted and scattered by rainwater on the radome affects the radiometric signal, making it difficult to identify the signal of raindrops in the air and other atmospheric parameters. This leads to a decrease in the accuracy of the atmospheric Tb measurements and parameter retrievals from ground-based microwave radiometers [23], [24]. Instrument hardware upgrades can reduce the water film bias [25], but even with blowers and hydrophobic materials, rainwater is still likely to float or remain on the radome during and after rain [26]. Indoor observations can effectively avoid radome and antenna wetting, so a comparison of indoor and outdoor radiometers can reveal possible differences in Tb, opacity, IWV, rain rate, and other atmospheric parameters, which are caused by undesired water films on the outdoor radiometer radome. TROWARA is the only indoor microwave radiometer to our knowledge for the measurement of tropospheric water parameters during rain and no rain, which is mentioned in the literature (e.g., [6]). Thus, this present article includes the details of the measurement setup of TROWARA, which are useful for the installation of indoor radiometers at other locations in the world.

This article is organized as follows. Section II describes the study site and instrumentation. Section III outlines the principle and feature selection of the gradient boosting decision tree (GBDT) and methodologies for IWV, ILW, and rain rate retrievals. Section IV presents brightness temperature, opacity,

and atmospheric water parameters comparisons in the K-band for the 62 days of coincident measurements. The brightness temperature bias for the two radiometers and the effect of liquid water on the radome of an outdoor radiometer are also discussed in this section. Conclusions are given in Section V.

II. INSTRUMENTATION

The HATPRO (HATPRO-G2) microwave radiometer was operated in Payerne (46.82°N, 6.95°E; 491 m asl) from 2009 to 2021 by the Swiss Federal Institute of Meteorology and Climatology (MeteoSwiss). The instrument was moved in November 2021 from Payerne to the roof of the ExWi building (46.95°N, 7.44°E; Alt. 575 m asl) at the University of Bern for an intercomparison between the outdoor radiometer HATPRO and the indoor radiometer TROWARA. This study assesses the brightness temperature (Tb), opacity, and the retrieval products IWV, ILW, and rain rates from December 1, 2021 to January 31, 2022. In addition, the Tb of the two instruments is also compared with the Tb simulations (RTSE Tb) based on calculations of the Atmospheric Radiative Transfer Simulator (ARTS) using the daily operational analysis data of the European Centre for Medium-Range Weather Forecasts (ECMWF). The temporal and spatial resolutions of ECMWF are 6 h and 1.125°, respectively. By using the data of the ExWi weather station, the ECMWF profiles from about 1.1 to 70 km asl are linearly extrapolated to the surface at 0.575 km asl. ARTS is a radiative transfer model focused on the microwave frequency range [27]. Inputs to the model include pressure, height, temperature, and water vapor density. H_2O, O_2, and N_2 concentrations are used to calculate the absorption coefficients over a range of microwave frequencies and simulate the emission spectrum at the location of the instruments. We do not consider hydrometeors or other aerosols in the simulation so that the modeled brightness temperature is only accurate during clear-sky periods. The outdoor HATPRO and the indoor TROWARA radiometer conduct parallel observations from locations less than 20 m apart at the same azimuth and elevation angle, 130° (southeast) and 40°, respectively.

A. Indoor Radiometer TROWARA

The TROWARA radiometer has been operated by the IAP since 1994 on the roof of the University of Bern. This instrument measures the brightness temperatures at three microwave frequency channels with a time resolution of 7 s. Two microwave channels are at frequencies of 21.385 GHz (bandwidth = 100 MHz) and 31.5 GHz (bandwidth = 200 MHz), and the third channel built in November 2007 is 22.235 GHz (bandwidth = 400 MHz). The 22.235-GHz channel is located in the center of the water vapor line and is more sensitive to microwave emission from atmospheric water vapor than the 21.385-GHz channel. The 31.5-GHz channel is more sensitive to microwave emission from atmospheric liquid water than the other two channels. The half-power beamwidth of TROWARA antenna beams is 4° for all frequencies. TROWARA also includes an additional thermal infrared channel at 9.5–11.5 μm. TROWARA can provide accurate

IWV, ILW, and high-quality rain rate values using opacity-based physical retrieval algorithms [19], [28]. A standard weather station called ExWi Weather Station is also operated on the ExWi building, a few meters away from TROWARA, to provide weather information and auxiliary data for the retrieval models.

TROWARA was on the roof outdoors from 1994 to April 2002. The disadvantages of its outdoor operation are twofold: 1) the temperature of the radiometer body was unstable due to solar heating and 2) rain collected on the radiometer radome caused unreliable measurements for up to several hours after rainfall. TROWARA was moved from outdoor to indoor constant temperature laboratory and was reinstalled in November 2002 [29] [Fig. 1(a)]. The antenna receives atmospheric radiation through a microwave transparent window that is well protected against rain by a wall overhang [Fig. 1(b)]. The window only can get wet in case of strong southeasterly winds that are very rare during rain events in Bern. This indoor operation avoids contamination of measurements caused by antenna wetness and allows TROWARA to measure even on rainy days. Generally, the stability and accuracy of TROWARA's measurements of IWV and ILW strongly increased after TROWARA became an indoor radiometer in 2002, and the rain rate retrieval is not biased by water films on the radome.

The original design and construction of TROWARA are described by Peter and Kämpfer [30]. Scientists and engineers from the IAP at the University of Bern improved TROWARA and enabled TROWARA to measure continuously without break points in the IWV time series since 2002. The amount of data gaps after 2002 is less than 2%. The latest block diagram of TROWARA is shown in Fig. 2. The developed radiometer model provides a good estimate of the antenna temperature by measuring the reflection and transmission coefficients of all radiometer components and enables automatic internal calibration at fairly small time intervals [29]. The active cold loads (ACLs) replaced cooled cold loads in 2004, and two ferrite switches for each frequency switch between the antenna, the ACL, and a matched waveguide termination, which is used as hot load [31]. TROWARA is calibrated with the ACL and hot load. The ACL temperature is determined by the manual tipping calibration using clear-sky brightness temperatures at different antenna elevation angles between 20° and 45°. Because of the high stability of TROWARA, only two tipping curve calibrations are required per year.

B. Outdoor Radiometer HATPRO

The HATPRO Generation 2 (G2) is a ground-based dual-polarization radiometer (R-DPR-09/016) manufactured in 2009 with a time resolution of 1–2 s. This instrument measures microwave radiances (brightness temperatures) at 14 frequencies. Seven microwave channels in the water vapor band (K-band) 22.24, 23.04, 23.84, 25.44, 26.24, 27.84, and 31.4 GHz provide atmospheric humidity and cloud liquid water content in the troposphere, and their bandwidth is between 0.1 and 2 GHz. Another seven channels in the oxygen band (V-band) from 51 to 58 GHz are used to deter-

(a)

(b)
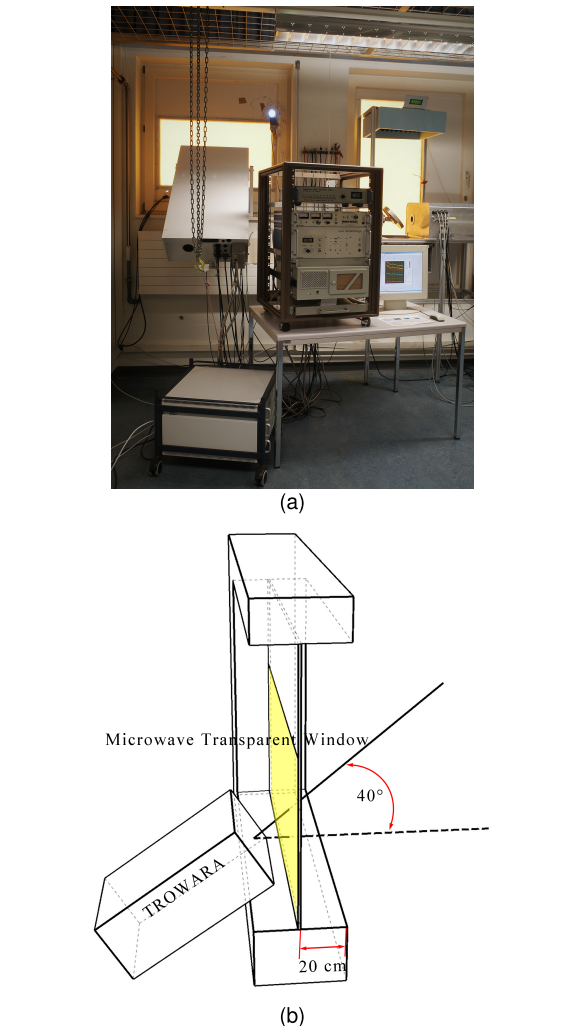
Fig. 1. (a) TROWARA in an indoor laboratory on the ExWi roof. (b) Measurement geometry of TROWARA observing the sky through a yellow microwave transparent window.

mine atmospheric temperature properties [32]. The half-power beamwidth of HATPRO antenna beams is 3.5° for K-band frequencies. HATPRO also includes a GPS for instrument location and observation time. HATPRO can retrieve IWV and ILW using quadratic regression (QR) with software provided by the HATPRO instrument manufacturer. The radiometer has additional surface sensors to observe weather parameters such as temperature, pressure, and relative humidity. These sensors also provide input data for retrieval models. The complete HATPRO instrument and software descriptions can be found on the RPG website [33].

Generation 2 HATPRO (HATPRO G2) achieves thermal stabilization through a dual-stage thermal control system consisting of a main cooler followed by a Peltier stage for the receivers [26]. The operating environment of its receiver is in the temperature range of −30 °C to 40 °C. The antenna of the
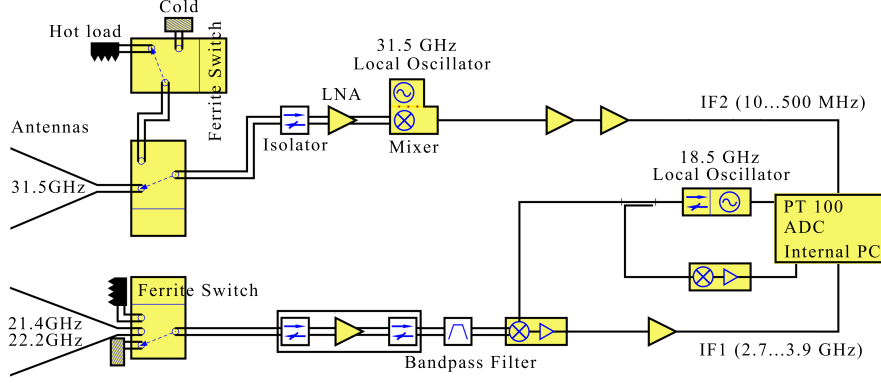
Fig. 2. Block diagram of TROWARA operating at 21.4, 22.2, and 31.5 GHz. The instrument is calibrated using two ferrite circulator switches to switch between the lens antennas, an ambient temperature load, and an ACL with an effective temperature in the order of 120 K.

outdoor HATPRO receives atmospheric radiation through the microwave transparent foil (radome). Hydrophobic material radome and radial blower prevent or reduce the water film on the radome during rain. The rain detector of the HATPRO and software-defined humidity threshold automatically control the speed of the blower.

HATPRO performs absolute calibration using a liquid nitrogen-cooled load mounted externally to the radiometer box and an internal blackbody load at ambient temperature as targets [34]. During calibration, an internal scanning mirror keeps the antenna pointed at each target, and the HATPRO software automatically corrects for calibration errors due to microwave reflections from the liquid nitrogen-air interface. One built-in diode noise source for each receiver replaces the liquid nitrogen-cooled load, enabling automatic internal calibration of the HATPRO [26]. For low atmospheric opacity (high transparency) channels, HATPRO G2 also has an option of tipping curve calibration [35], which is not enabled for the radiometer on site.

III. METHODOLOGY

A. Gradient Boosting Decision Tree

It is considered to be one of the best performing ensemble learning methods in machine learning. GBDT uses the negative gradient of the loss function to fit the residual of the previous round of base learners so that the residual estimate of each round gradually decreases close to the actual value [36]. GBDT improves the generalization ability and robustness of a single model and has an interpretable regression procedure.

An advantage of GBDT is that the relative importance of the features used by the model can be output after model training, which is often used for feature selection to understand which factors have a key impact on prediction [37]. Friedman [38] proposed the computation of GBDT feature selection. The basic idea is that the average selection frequency J_j of the feature j serves as a statistic to measure its importance. The more times an input feature is selected as a branch feature during branching in a regression tree, the more important the feature is. The number of times is normalized to the relative frequency,

and then, the selected frequencies of the input features in all regression trees are averaged

$$\hat{J}_j^2 = \frac{1}{M} \sum_{m=1}^{M} \hat{J}_j^2(T_m) \qquad (1)$$

where M is the number of trees and $m = 1, 2, \ldots, M$. The importance of feature j for a decision tree T is given as follows:

$$\hat{J}_j^2(T) = \sum_{t=1}^{L-1} \hat{i}_t^2 1(v_t = j). \qquad (2)$$

Here, it is assumed that every tree is binary tree, so L is the number of terminal nodes and $L-1$ is the number of nonterminal nodes. v_t is the splitting variable associated with node t, and i_t^2 is the square of loss reduction after node t splits.

B. IWV and ILW Retrieval

TROWARA uses the two microwave frequencies 21.385 and 31.5 GHz to retrieve IWV and integrated liquid water (ILW). The following is a brief explanation of the retrieval technique. It is assumed that there is a plane-parallel atmosphere, so the radiative transfer equation for nonscattering atmospheres is

$$\text{Tb}_f = \text{Tb}_c \cdot e^{-\tau_f/\mu} + \text{Tm}_f \cdot \left(1 - e^{-\tau_f/\mu}\right) \qquad (3)$$

where τ_f is the zenith opacity of the atmosphere. μ is the cosine of the zenith angle θ, i.e., $\mu = \cos\theta$. Tb_f is the brightness temperature observed by TROWARA, and Tb_c is the brightness temperature of the cosmic microwave background. Tm_f is the effective mean temperature of the troposphere calculated by the linear equation of surface temperature, pressure, and relative humidity. It is also frequency (and site) dependent.

Equation (3) derives the zenith opacity as

$$\tau_f = -\mu \cdot \ln\left(\frac{\text{Tm}_f - \text{Tb}_f}{\text{Tm}_f - \text{Tb}_c}\right). \qquad (4)$$

Equation (4) can also be expressed as a linear combination of IWV, ILW, and integrated rain liquid (IRL), where ILW

is the integrated liquid water of the cloud droplets along the zenith direction. Ice and dry snow contribute negligibly to radiation because of their small dielectric losses

$$\tau_f = (a_f + b_f \cdot \text{IWV} + c_f \cdot \text{ILW}) + \tau_{\text{rf}} \qquad (5)$$

$$\tau_{\text{rf}} = c_f \cdot G_{M,f} \cdot \text{IRL} \qquad (6)$$

where the coefficients a_f and b_f depend on air pressure. They can be statistically obtained from simultaneous measurements of radiosondes and fine-tuned during periods of a clear sky. The coefficient c_f depends on air temperature and frequency. It is the Rayleigh mass absorption coefficient of cloud water, which can be obtained from a dielectric model of water. τ_{rf} is the rain zenith opacity. $G_{M,f}$ is the rain Mie gain.

The retrieval of IWV and ILW uses a physical algorithm for microwave radiometer data during no rainfall ($G_{M,f} = 0$)

$$\text{IWV} = \frac{\tau_{21} - a_{21} - \gamma(\tau_{31} - a_{31})}{b_{21}(1 - \beta\gamma)} \qquad (7)$$

$$\text{ILW} = \frac{\tau_{31} - a_{31} - \beta(\tau_{21} - a_{21})}{c_{31}(1 - \beta\gamma)} \qquad (8)$$

where subscripts 21 and 31 represent the microwave frequencies of TROWARA at 21.385 and 31.5 GHz, respectively. $\beta = b_{31}/b_{21} < 0.5$, and $\gamma = c_{21}/c_{31} \cong 0.5$. Details of TROWARA's IWV and ILW retrieval algorithms are described by Mätzler and Morland [28].

HATPRO G2 uses the seven K-band microwave frequencies to retrieve IWV and ILW based on the QR method. The QR retrieval technique can be described as

$$\text{Out}_n = \text{Os}_n + \sum_{\text{sensors}} \text{ML}_{ns} \cdot \text{Mr}_s + \sum_{\text{sensors}} \text{MQ}_{ns} \cdot \text{Mr}_s^2$$
$$+ \sum_{\text{freq}} \text{TL}_{nf} \cdot \text{Tb}_f + \sum_{\text{freq}} \text{TQ}_{nf} \cdot \text{Tb}_f^2 \qquad (9)$$

where n is the number of retrieval parameters and Out_n is the output parameter (IWV or ILW). Os_n is the retrieval offset for Out_n. s is the number of times to check the surface sensor, and Mr_s is the meteorological parameters temperature, pressure, and relative humidity read by the sensor. ML_{ns} and MQ_{ns} are the linear coefficient and quadratic coefficient of Mr_s, respectively. The subscript f denotes the microwave frequency. Tb_f is the brightness temperature observed by HATPRO. TL_{nf} and TQ_{nf} are the linear coefficient and quadratic coefficient of Tb_f, respectively. These coefficients are derived by RPG based on long-term radiosonde datasets. The limitation is that the retrieval algorithms can only be applied to the range of atmospheric conditions included in their training datasets. More details for the HATPRO retrieval are described in the RPG operation and software guide [26], [39].

C. Rain Rate Retrieval

Because the rain rate retrieval is not included in the standard HATPRO software, in this study, we use the same opacity-based physical method as for TROWARA to retrieve rain rates for HATPRO. During rain, τ_{rf} is determined iteratively. The

iterative equation can be expressed as

$$\tau_{\text{rf}}^{(k+1)} = -\mu \cdot \ln\left(\frac{\text{Tm}_{\text{rf}}\left(\tau_{\text{rf}}^{(k)}\right) - \text{Tb}_{\text{rf}}}{\text{Tm}_{\text{rf}}\left(\tau_{\text{rf}}^{(k)}\right) - \text{Tb}_f}\right) \qquad (10)$$

where $\tau_{\text{rf}}^{(k+1)}$ is the rain zenith opacity at the kth iteration. Tm_{rf} is the effective mean temperature during rain. Tb_{rf} is the brightness temperature during rain, and Tb_f is the brightness temperature without rain. Equation (10) basically converges after two iterations.

Rain rate R_f can be calculated from rain zenith opacity

$$R_f = \frac{\tau_{\text{rf}}}{g_{\text{rf}} \cdot \text{Hr}} \qquad (11)$$

where g_{rf} is the effective rain absorption coefficient calculated with Mie theory. Hr is the vertical distance from the melting layer to the surface when it rains. The details of the rain rate retrieval algorithm for HATPRO and TROWARA are described by Wang et al. [19].

IV. RESULTS AND DISCUSSION

A. Brightness Temperature Comparison

The HATPRO G2 radiometer was transferred from Payerne to Bern in November 2021, and it was calibrated on November 11, 2021. Our study considers the HATPRO observations after December 1, 2021. Fig. 3 shows a two-month Tb time series of the same microwave channels 22 and 31 GHz from HATPRO, TROWARA, and RTSE. The rain flag marks the time of rain. RTSE Tb is missing during rainfall when Tb observed by HATPRO and TROWARA increases remarkably. As shown in Fig. 3(a), RTSE Tb agrees better with TROWARA Tb than HATPRO Tb. The mean value of TROWARA Tb at 22 GHz is around 22 K during no rainfall, and HATPRO Tb is significantly overestimated by more than 5 K. This overestimation can be clearly seen from January 22 to 26 (shaded area). As shown in Fig. 3(b), there is comparatively good agreement between TROWARA Tb, HATPRO Tb, and RTSE Tb. The mean value of TROWARA Tb at 31 GHz is around 17 K during no rainfall, with HATPRO overestimating Tb by around 1 K on average. During rainfall, HATPRO Tb values are significantly higher than TROWARA Tb at both 22 and 31 GHz due to the influence of a water film on the radome, which is described in detail next.

Fig. 4 shows the mean value and standard deviation of Tb of HATPRO and TROWARA in the K-band for three days of dry clear-sky conditions on January 1, 14, and 22, 2022, and RTSE Tb as a function of frequency over the same time period. The mean value of IWV and ILW is about 8.5 and 0 mm, respectively. As shown in Fig. 4(a), TROWARA Tb at microwave frequencies 22 and 31 GHz agrees very well with RTSE Tb, while there is a deviation of 2.5 K between TROWARA and RTSE at 21 GHz. Since TROWARA retrieval coefficients are corrected to match GPS and radiosonde data, the intercomparison of IWV from TROWARA and ERA5 reanalysis only resulted in a small mean difference of 0.38 mm for no rain conditions [40]. Note that the maximum value of the RTSE curve appears to be at 22.5 GHz, while the line
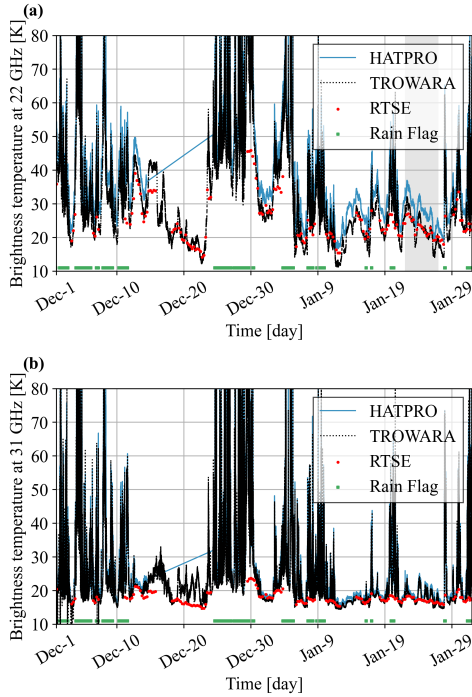
Fig. 3. Time series of the brightness temperature (Tb) observed by HATPRO and TROWARA, as well as radiative transfer simulations based on the operational analysis data ECMWF (RTSE) Tb at (a) 22 and (b) 31 GHz from December 1, 2021 to January 31, 2022. The rain flag data observed by the HATPRO rain detector are used to identify rain. The shaded area is from January 22 to 26, 2022.

Fig. 4. (a) Mean and (b) standard deviation of Tb observed by HATPRO, TROWARA, as well as RTSE Tb, only for clear conditions (three days).

center of the water vapor line should be at 22.235 GHz. The reason is the high pressure in the troposphere [41]. HATPRO Tb is significantly enhanced at all microwave frequencies. Compared to RTSE Tb, HATPRO Tb has a maximum deviation of 5.3 K at 22 GHz and a minimum deviation of 1.0 K at 31 GHz. As shown in Fig. 4(b), the standard deviations of HATPRO and TROWARA are almost the same at 22 and 31 GHz. This further suggests that the changes of Tb they observed are similar when HATPRO had no water film on the radome under dry conditions.

The effect of common instrument characteristics on brightness temperature is unlikely to be the main reason for the overestimation of HATPRO Tb, such as antenna beamwidth and individual filter bandwidth. The beamwidths of HATPRO and TROWARA are relatively narrow, with half-power beamwidths of 3.5° and 4°, respectively. At an observation elevation angle of 40°, the bias caused by these beamwidths can be negligible in the K-band. Bandwidth errors of microwave channels are less important for K-band. At these frequencies, it is acceptable to use a wider bandwidth to improve detection under low signal-to-noise ratio conditions [42]. It is worth noting that a frequency offset of the channels can lead to a considerable bias.

The HATPRO calibration bias is more likely a cause of the overestimation of HATPRO Tb, including nonlinearities in the calibration transfer characteristics and nonlinear corrections.

Rose et al. [26] stated that the HATPRO-G2 is calibrated by noise injection and based on a four-point method to correct the nonlinearities. One possible explanation for the bias is that the coefficients for this correction are incorrect. TROWARA assumes a linear transfer characteristic. It should be less prone to linearity errors since the calibration is done with the ACL and ambient, whereas HATPRO has to extrapolate from ambient and ambient plus noise diode ($\gg$ 300 K) to a sky temperature of 30 K. From 13:00 to 17:00 on September 22, 2022, we performed liquid nitrogen calibration during clear sky for HATPRO. Fig. 5 shows the change in Tb from before to after HATPRO calibration. Before the HATPRO calibration at 22 GHz, the Tb bias between HATPRO and TROWARA is 7.7 K, much higher than the one in January 2022 in Fig. 4. HATPRO calibration reduces the Tb bias, correcting 1.6 K (21%) to 6.1 K. In addition, the small-scale variations of Tb from TROWARA and HATPRO are perfectly correlated. Thus, the variations are real atmospheric variations and not instrument noise. We also checked the pointing accuracy of the two radiometers by scanning the Sun to determine whether there is any bias on the elevation angle that could explain the Tb bias between the two instruments [43] and found that HATPRO has a slightly higher elevation angle than TROWARA. The actual elevation angles of TROWARA and HATPRO determined by the solar drift scans were 40.05° and 41.53°, respectively. The effect of this difference in elevation angle on the Tb bias is
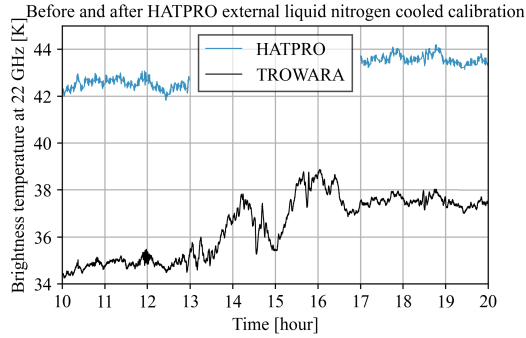
Fig. 5. Time series of Tb observed by HATPRO and TROWARA on September 22, 2022. HATPRO was calibrated with external liquid nitrogen from 13:00 to 17:00, while TROWARA continued to observe.

about −0.68 K during a clear sky in January 2022. Given that it would result in an underestimation of Tb, the pointing bias might compensate partly for HATPRO's other biases (e.g., nonlinearity of calibration).

Before the HATPRO moved to Bern, Hervo et al. [44] in Payerne studied the difference between Tb measured by this HATPRO G2 and a new Generation 5 HATPRO (HATPRO G5) and radiative transfer simulations based on radiosonde data (denoted as RTSR) from March 25 to August 25, 2021. Fig. 6 is taken from their research report. As shown in Fig. 6(a), the Tb bias between HATPRO G5 and RTSR is significantly smaller than the HATPRO G2. HATPRO G2 Tb at 22 GHz in Payerne is overestimated by about 2.19 K at zenith compared to RTSR [Fig. 6(b)]. The overestimation of HATPRO Tb occurs in a different manner in Payerne and Bern due to instrument elevation of 90° in Payerne. An observation elevation angle of 90° produces a lower overestimation than measurements at much lower elevation angles. It may also be due to different weather conditions in these two places.

The feature importance calculation of GBDT can further quantify the sensitivity of multiple factors to the contribution of Tb bias and thus infer the source of the bias [36]. The bias may be caused by a combination of factors, including voltages, channel gain (slope of the linear response), and temperature of ambient blackbody target, which are related to instrument calibration; environmental temperature and environmental relative humidity, which are related to the instrument surrounding environment; receiver temperature and receiver stability, which are related to receiver performance; and Sun elevation angle, which is related to the position of the Sun relative to the instrument and diurnal distribution. These eight factors provided by HATPRO are the input learning datasets for GBDT here. Because TROWARA fits well with RTSE and the lower temporal resolution of RTSE cannot meet machine learning data volume requirements, the difference between the Tb of HATPRO and TROWARA at 22 GHz is marked as the actual value of the bias. More than 280 000 quality control samples in 23 clear-sky days are collected to improve model generalization and prevent overfitting. The training samples and test samples are randomly selected to account for 90% and 10% of the total samples, respectively. The GBDT model parameters set in this study are given as
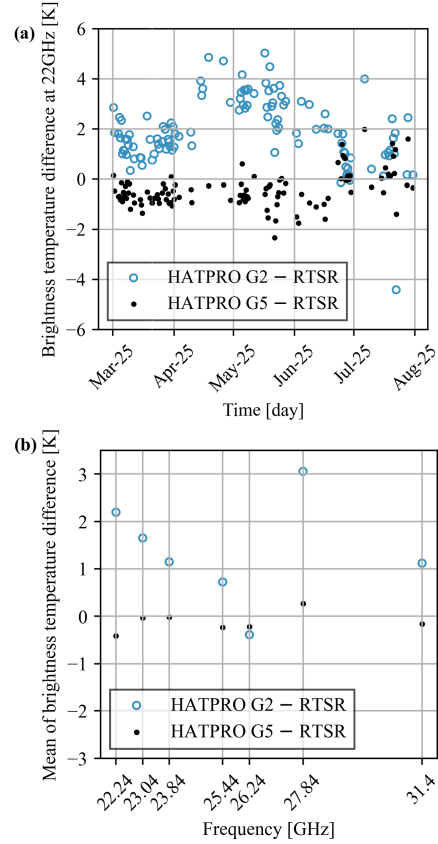
Fig. 6. (a) Difference between brightness temperatures measured by HATPRO G2 and HATPRO G5 and radiative transfer simulations based on radiosonde data (RTSR) at 22 GHz in Payerne. (b) Mean value of the difference in brightness temperature between measurements and simulations at seven K-band frequencies.

follows: the learning rate is 0.07, the subsampling rate is 0.85, the maximum depth of decision tree is 26, the minimum number of samples for leaf nodes is 22, the minimum number of samples for internal nodes is 60, the number of features for optimal segmentation is 2, the number of boosting stages to perform is 1000, and the random state is 10. After training, the GBDT model obtained a coefficient of determination (R^2) of 0.99 and a root-mean-square error (RMSE) of 0.004 K, which means that one or more of these input factors are responsible for the Tb bias. Fig. 7 shows the bias-contribution scores. The top two with high bias-contribution scores are instrument calibration, consisting of temperature of blackbody target, channel gain, and voltages; and instrument surrounding environment, consisting of relative humidity and temperature. The sums of their associated factors are all above 0.37. The Sun elevation angle also has a large bias contribution with a score of 0.21, while the HATPRO receiver performance contributes very little to the Tb bias.

B. Intercomparison of IWV, ILW, Opacity, and Rain Rate

Fig. 8 shows a two-month time series and a scatter plot of HATPRO IWV and TROWARA IWV retrieved by (7) and (9),
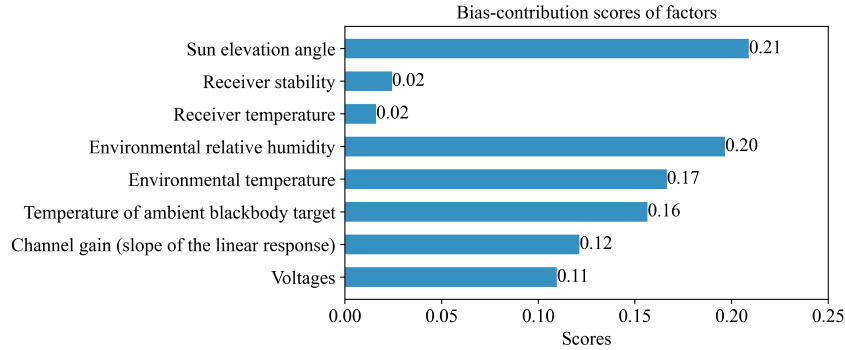
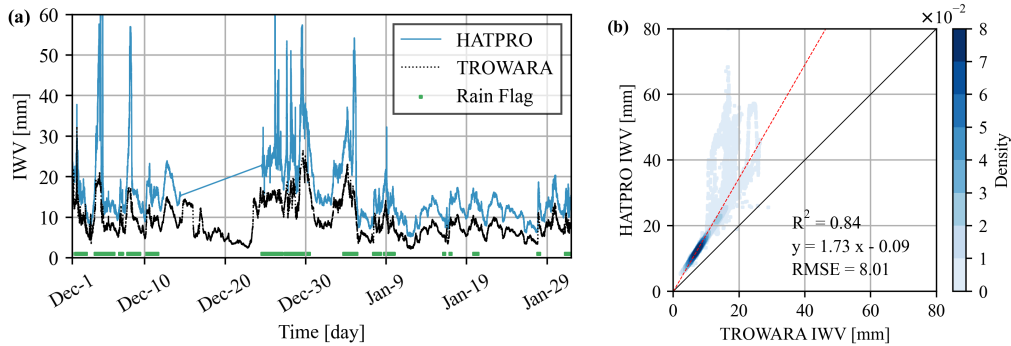Fig. 7. Contribution of factors to the Tb bias at 22 GHz using the GBDT method.

Fig. 8. (a) Time series of the IWV provided by HATPRO and TROWARA from December 1, 2021 to January 31, 2022. The rain flag data observed by the HATPRO rain detector are used to identify rain. (b) Scatter plot of IWV provided by HATPRO and TROWARA from December 1, 2021 to January 31, 2022. The black solid line is the 1:1 line, and the red dashed line is the linear regression fit line. The blue gradient represents the density of the scatter distribution calculated by the Gaussian kernel.

respectively. Note that the IWV during rain is not provided by TROWARA, but obtained by interpolating the opacity before and after rain. This interpolation of the TROWARA retrieval is useful to study the variation of IWV during rain [3], [40]. As shown in Fig. 8(a), during no rainfall, the mean value of TROWARA IWV is around 7 mm. TROWARA IWV values are higher during rainfall than during no rainfall. Hocke et al. [40] showed that TROWARA IWV agrees with GNSS IWV and ERA5 IWV even during rain conditions. During no rainfall, the mean value of HATPRO IWV is around 11 mm. HATPRO IWV increases dramatically during rainfall. As shown in Fig. 8(b), HATPRO IWV is significantly overestimated compared to TROWARA IWV. The slope and intercept of the linear fit are 1.73 and -0.09 mm, respectively. The area with the minimum distribution density (light blue area) corresponds to large values of HATPRO IWV, and the linear regression fit line is located above the 1:1 line. The overestimation of IWV by this HATPRO also occurred in the measurements in Payerne. Hocke et al. [40] intended to present a comparison between IWV obtained by radiosonde, GNSS, ERA5, and HATPRO at Payerne. However, they excluded the HATPRO G2 from this intercomparison because of its too strong positive deviations compared to the other three sources. TROWARA IWV and HATPRO IWV also present similar variations. The R^2 and RMSE between TROWARA and HATPRO IWV are 0.84 and 8.01 mm, respectively.

Fig. 9 shows a two-month time series and a scatter plot of TROWARA ILW and HATPRO ILW retrieved by (8) and (9), respectively. As shown in Fig. 9(a), during no rainfall, the mean value of TROWARA ILW and HATPRO ILW is around 0.08 and 0.2 mm, respectively. TROWARA ILW is close to zero in cloudless conditions, while it is around 0.1 mm for HATPRO. This confirms the fact that HATPRO retrievals overestimate ILW. During rainfall, TROWARA ILW and HATPRO ILW increase dramatically. As shown in Fig. 9(b), HATPRO ILW is significantly overestimated compared to TROWARA ILW. The slope and intercept of the linear fit are 1.63 and -0.1 mm, respectively. The area with the minimum distribution density (light blue area) corresponds to large values of HATPRO ILW, and the linear regression fit line is located above the 1:1 line. TROWARA ILW and HATPRO ILW also present similar variations. The R^2 and RMSE between TROWARA and HATPRO ILW are 0.81 and 0.27 mm, respectively.

The overestimation of HATPRO IWV and ILW could be due to the fact that Tb in the K-band observed by the HATPRO radiometer is overestimated, e.g., in the 22-GHz channel. We simply adjusted the brightness temperature of HATPRO by a constant difference from RTSE and reretrieved the IWV. Although the bias in IWV was slightly reduced, the overestimation persisted. Therefore, the retrieval method itself may be the main contributing factor to the overestimation of
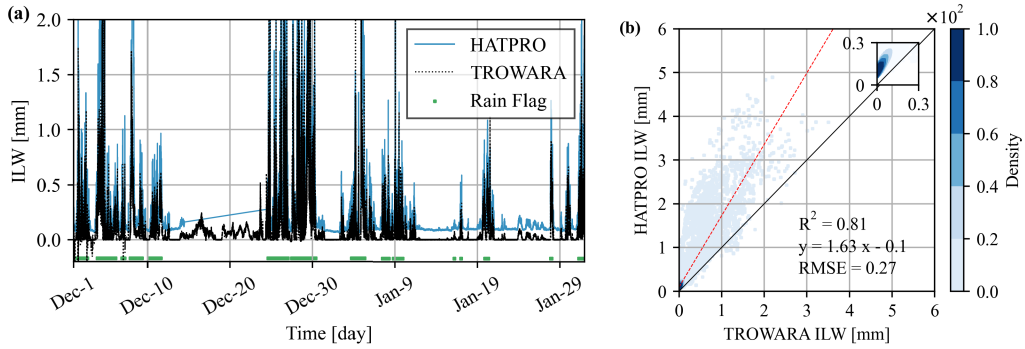
Fig. 9. (a) Time series of the ILW provided by HATPRO and TROWARA from December 1, 2021 to January 31, 2022. The rain flag data observed by the HATPRO rain detector are used to identify rain. (b) Scatter plot of ILW provided by HATPRO and TROWARA from December 1, 2021 to January 31, 2022. The black solid line is the 1:1 line, and the red dashed line is the linear regression fit line. The blue gradient represents the density of the scatter distribution calculated by the Gaussian kernel. The subplot is the ILW scatter plot from 0 to 0.3 mm.
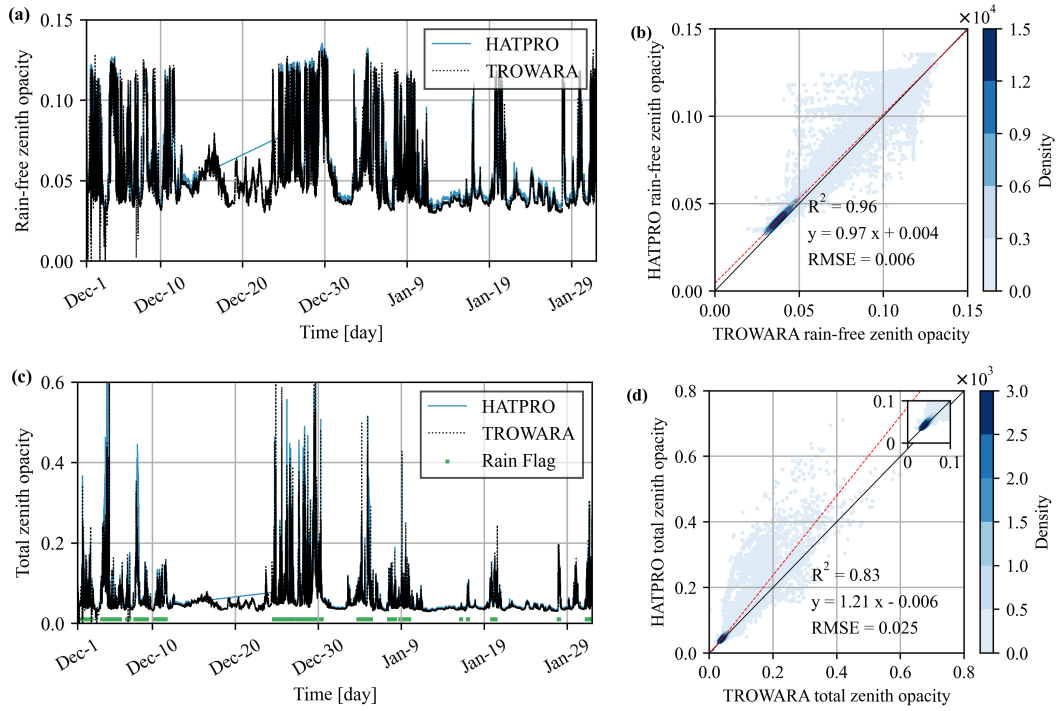
Fig. 10. (a) Time series of the rain-free zenith opacity provided by HATPRO and TROWARA from December 1, 2021 to January 31, 2022. (b) Scatter plot of the rain-free zenith opacity provided by HATPRO and TROWARA from December 1, 2021 to January 31, 2022. The black solid line is the 1:1 line, and the red dashed line is the linear regression fit line. The blue gradient represents the density of the scatter distribution calculated by the Gaussian kernel. (c) Time series of the total zenith opacity provided by HATPRO and TROWARA from December 1, 2021 to January 31, 2022. The rain flag data observed by the HATPRO rain detector are used to identify rain. (d) Scatter plot of the total zenith opacity provided by HATPRO and TROWARA from December 1, 2021 to January 31, 2022. The black solid line is the 1:1 line, and the red dashed line is the linear regression fit line. The blue gradient represents the density of the scatter distribution calculated by the Gaussian kernel. The subplot is the ILW scatter plot from 0 to 0.1.

IWV. Rose et al. [26] indicated limitations of the HATPRO G2 retrieval methods. The relationship between atmospheric water and brightness temperature varies by region and season, and statistical algorithms are problematic in a wide range of applications. This weakness of the HATPRO QR affects the retrieval accuracy of IWV and ILW. As we show in the following, another cause leading to the overestimation of IWV and ILW by HATPRO is the water film on the radome during and shortly after rain events.

Opacities are used for rain rate retrieval at 31 GHz and to study the effect of water on the radome. Fig. 10 shows a two-month time series and scatter plot of the rain-free zenith opacity and total zenith opacity (both rain-free zenith opacity and rain zenith opacity). HATPRO opacity is not calculated using the attenuation retrieved from the HATPRO QR, but by (4) and (10) in the same way as TROWARA. Note that the rain-free zenith opacity during rainfall is not provided by radiometers but is obtained by interpolating before and after
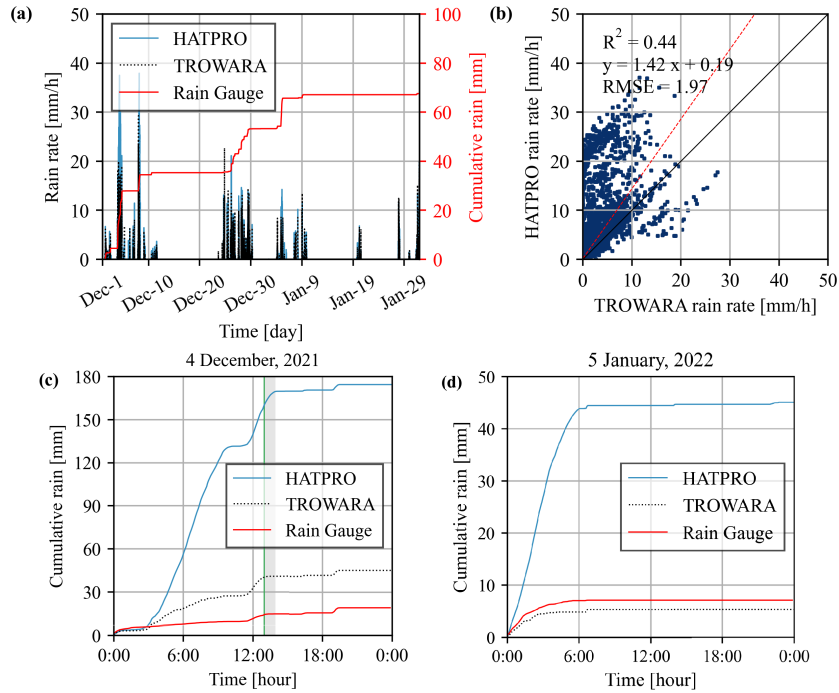
Fig. 11. (a) Time series of rain rates provided by HATPRO, TROWARA, and rain gauge from December 1, 2021 to January 31, 2022. (b) Scatter plot of rain rates provided by HATPRO and TROWARA from December 1, 2021 to January 31, 2022. The solid black line is the 1:1 line, and the red dashed line is the linear regression fit line. (c) Cumulative rain lines provided by HATPRO, TROWARA, and rain gauge on December 4, 2021. The time for the green line is 12:58 UT. The shaded area is from 12:58 UT to 13:55 UT. (d) Cumulative rain provided lines by HATPRO, TROWARA, and rain gauge on January 5, 2022.

rain. There is a high possibility of raindrops in the atmosphere if the ILW value is greater than or equal to 0.4 mm [18], [45], so ILW = 0.4 mm is used as the rainfall threshold for TROWARA. The ILW threshold for rainfall is usually between 0.1 and 0.6 mm. In fact, even if the threshold is not as accurate, the detection of rain occurrence is sufficient. This is because the enhanced emission due to the Mie effect leads to a very strong increase in ILW when the droplet size (diameter) increases to 0.3 mm. Since HATPRO retrieved a higher ILW as previously described, the threshold for rainfall is set to 0.6 mm. As shown in Fig. 10(a) and (b), during no rainfall, the HATPRO zenith opacity agrees well with TROWARA zenith opacity. The slope and intercept of the linear fit are 0.97 and 0.004, respectively. The zenith opacity of TROWARA and HATPRO also presents the same variations. The R^2 and RMSE between TROWARA and HATPRO zenith opacity are 0.96 and 0.006, respectively. As shown in Fig. 10(c) and (d), during rainfall, HATPRO zenith opacity is overestimated compared to TROWARA zenith opacity. The slope and intercept of the linear fit are 1.21 and −0.006, respectively. The linear regression fit line is located above the 1:1 line. On the other hand, the zenith opacity of TROWARA and HATPRO presents similar variations. The R^2 and RMSE between TROWARA and HATPRO zenith opacity are 0.83 and 0.025, respectively.

Fig. 11(a) and (b) shows a two-month time series and scatter plot of rain rates retrieved by (11) at 31 GHz. The rain gauge data are from the ExWi weather station with a

time resolution of 10 min. As shown in Fig. 11(a), HATPRO and TROWARA are very consistent in determining the occurrence/duration of rainfall. The more rain is measured by the rain gauge, the higher the estimated rain rate for HATPRO and TROWARA are. Note that HATPRO and TROWARA detect rain, but the rain gauge does not measure any rain, such as December 5 and 6 and January 19 and 20. This may be due to two reasons. First, the time resolution of HATPRO and TROWARA is high so that rain detected for a particularly short time contributes very little to the cumulative rain. Second, virga rainfall evaporates or sublimates before reaching the ground [46]. As shown in Fig. 11(b), HATPRO rain rates are significantly overestimated compared to TROWARA rain rates. Some smaller values (less than 10 mm/h) of TROWARA rain rates correspond to larger values (15–40 mm/h) of HATPRO rain rates. The slope and intercept of the linear fit are 1.42 and 0.19 mm/h, respectively. The linear regression fit line is located above the 1:1 line, and HATPRO rain rates agree poorly with TROWARA rain rates. The R^2 and RMSE between TROWARA and HATPRO rain rates are 0.44 and 1.97 mm/h, respectively. Fig. 11(c) and (d) shows the cumulative rain versus time for the heavy and moderate rain cases, respectively. Cumulative rain of TROWARA presents similar variations to rain gauge cumulative rain, but HATPRO continues to increase after TROWARA and rain gauge stop increasing, such as from 12:58 UT to 13:55 UT. As shown in Fig. 11(c), during heavy rain, both HATPRO and TROWARA cumulative rain
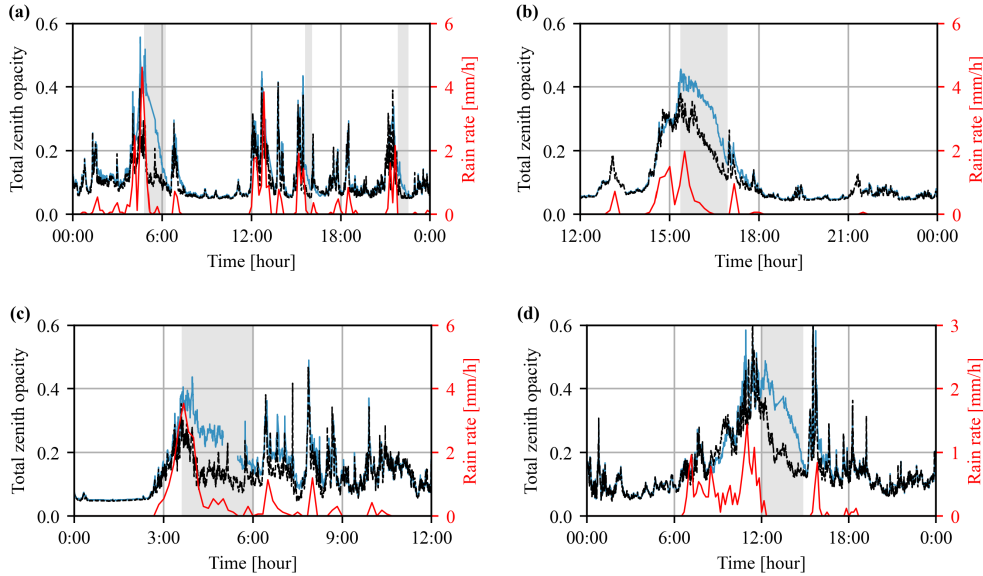
Fig. 12.   Time series of total zenith opacity provided by HATPRO (blue solid line) and TROWARA (black dashed line), as well as rain rates measured by rain gauge in (a) December 26, 2021; (b) December 27, 2021; (c) December 28, 2021; and (d) December 29, 2021. The shaded area marks when the zenith opacity of HATPRO is much stronger than that of TROWARA.

are overestimated compared to rain gauge cumulative rain. HATPRO is heavily overestimated to about nine times the rain gauge values. As shown in Fig. 11(d), during moderate rain, the TROWARA cumulative rain agrees relatively well with rain gauge cumulative rain, as described by Wang et al. [19], but HATPRO is heavily overestimated to about six times the rain gauge values.

We used the same rain zenith opacity algorithm for HATPRO and TROWARA at 31 GHz, but HATPRO shows a significant rainfall overestimation. One of the reasons is that the radome of the HATPRO radiometer placed outdoors is contaminated with liquid water left on it by rainfall. This situation can exist during and after rain. Fig. 12 shows the examples of total zenith opacity for HATPRO and TROWARA with rain. The rain rate decreases or stops, while the total zenith opacity of HATPRO remains very strong, such as on December 26 from 4:32 UT to 6:34 UT, December 27 from 15:22 UT to 16:57 UT, December 28 from 3:34 UT to 5:42 UT, and December 29 from 11:52 UT to 15:08 UT. The HATPRO zenith opacity is significantly higher than TROWARA by a maximum of 0.2. There are also some cases with less impact on HATPRO zenith opacity, such as on December 26 from 15:31 UT to 16:01 UT and 21:45 UT to 22:47 UT. When the removal of the water film is effective, the HATPRO zenith opacity agrees very well with TROWARA. This shows that for outdoor radiometers, the blower and hydrophobic coating play a role too.

V. CONCLUSION

The commercial radiometer HATPRO G2 is widely used as a source of information on atmospheric water parameters important to climate change research. To explore the bias of measurements and the uncertainty of atmospheric water

retrievals of HATPRO, we compared it with a radiometer TROWARA with the same observation principle but different instrument characteristics for indoor and outdoor parallel observations. The dataset contains more than 981 000 observations over a 62-day period from December 1, 2021 to January 31, 2022, during various weather conditions. TROWARA brightness temperatures agree well with RTSE, but there is a significant difference between brightness temperature measurements from HATPRO and TROWARA. HATPRO has the largest overestimation at 22.24 GHz, about 5 K, and the minimum overestimation at 31.4 GHz, about 1 K. Their retrieved IWV and ILW present similar changes, with R^2 of 0.84 and 0.81, respectively. IWV and ILW retrieved from HATPRO are significantly overestimated using the QR retrieval method compared to TROWARA, with slopes of 1.73 and 1.63, respectively. Since the outdoor operation of HATPRO has liquid water on the radome during and after rain, its retrieval of rain rates is less than satisfactory. Nevertheless, rain-free opacity calculated by HATPRO at 31.4 GHz using the radiative transfer equation is in good agreement with TROWARA. The R^2 and slope are 0.96 and 0.97, respectively.

To explore the causes of the brightness temperature bias in HATPRO and TROWARA at 22 GHz, we use the GBDT to compare the importance of factors to the bias. The results show that the instrument calibration, instrument surrounding environment, and Sun elevation angle have major contributions to the bias. The determination of the main contributing factors can help to further establish correction models and optimize the instrument.

TROWARA is possibly the sole indoor radiometer in the world that can measure tropospheric water parameters during rainfall. Our study showed that an indoor radiometer has many advantages since it does not affect the microwave radiation

due to the water film on the radome. It would be desirable to install more indoor radiometers for weather observations in the future so that rainfall events can be better accessed and mobile outdoor radiometers can be cross-validated.

ACKNOWLEDGMENT

REFERENCES

[1] D. Ji, J. Shi, H. Letu, W. Li, H. Zhang, and H. Shang, "A total precipitable water product and its trend analysis in recent years based on passive microwave radiometers," *IEEE J. Sel. Topics Appl. Earth Observ. Remote Sens.*, vol. 14, pp. 7324–7335, 2021.

[2] R. Nandan, M. V. Ratnam, V. R. Kiran, and D. N. Naik, "Retrieval of cloud liquid water path using radiosonde measurements: Comparison with MODIS and ERA5," *J. Atmos. Solar-Terr. Phys.*, vol. 227, Jan. 2022, Art. no. 105799.

[3] W. Wang and K. Hocke, "Atmospheric effects and precursors of rainfall over the Swiss Plateau," *Remote Sens.*, vol. 14, no. 12, p. 2938, Jun. 2022.

[4] K. Hocke, L. Bernet, J. Hagen, A. Murk, M. Renker, and C. Mätzler, "Diurnal cycle of short-term fluctuations of integrated water vapour above Switzerland," *Atmos. Chem. Phys.*, vol. 19, no. 19, pp. 12083–12090, Sep. 2019.

[5] E. Sauvageat et al., "Comparison of three high resolution real-time spectrometers for microwave ozone profiling instruments," *IEEE J. Sel. Topics Appl. Earth Observ. Remote Sens.*, vol. 14, pp. 10045–10056, 2021.

[6] L. Bernet et al., "Trends of atmospheric water vapour in Switzerland from ground-based radiometry, FTIR and GNSS data," *Atmos. Chem. Phys.*, vol. 20, no. 19, pp. 11223–11244, Oct. 2020.

[7] J. Judge, J. F. Galantowicz, and A. W. England, "A comparison of ground-based and satellite-borne microwave radiometric observations in the Great Plains," *IEEE Trans. Geosci. Remote Sens.*, vol. 39, no. 8, pp. 1686–1696, Aug. 2001.

[8] J. B. Snider, F. O. Guiraud, and D. C. Hogg, "Comparison of cloud liquid content measured by two independent ground-based systems," *J. Appl. Meteorol.*, vol. 19, no. 5, pp. 577–579, May 1980.

[9] S. Steinke et al., "Assessment of small-scale integrated water vapour variability during HOPE," *Atmos. Chem. Phys.*, vol. 15, no. 5, pp. 2675–2692, Mar. 2015.

[10] D. Cimini, E. R. Westwater, Y. Han, and S. J. Keihm, "Accuracy of ground-based microwave radiometer and balloon-borne measurements during the WVIOP 2000 field experiment," *IEEE Trans. Geosci. Remote Sens.*, vol. 41, no. 11, pp. 2605–2615, Nov. 2003.

[11] A. Foth, H. Baars, P. Di Girolamo, and B. Pospichal, "Water vapour profiles from Raman LiDAR automatically calibrated by microwave radiometer data during HOPE," *Atmos. Chem. Phys.*, vol. 15, no. 14, pp. 7753–7763, Jul. 2015.

[12] M. J. Tauc, D. W. Riesland, L. M. Eshelman, W. Nakagawa, and J. A. Shaw, "Simulations and experimental results of cloud thermodynamic phase classification with three SWIR spectral bands," *J. Appl. Remote Sens.*, vol. 13, no. 3, p. 034526, 2019.

[13] S. Crewell and U. Löhnert, "Accuracy of cloud liquid water path from ground-based microwave radiometry 2. Sensor accuracy and synergy," *Radio Sci.*, vol. 38, no. 3, pp. 1–7, 2003.

[14] A. Bell et al., "W-band radar observations for fog forecast improvement: An analysis of model and forward operator errors," *Atmos. Meas. Techn.*, vol. 14, no. 7, pp. 4929–4946, Jul. 2021.

[15] *High-Precision Microwave Radiometers for Continuous Atmospheric Profiling.* Accessed: Jul. 19, 2022. [Online]. Available: https://www.radiometer-physics.de/download/PDF/Radiometers/HATPRO/

[16] J. Morland, M. C. Coen, K. Hocke, P. Jeannet, and C. Mätzler, "Tropospheric water vapour above Switzerland over the last 12 years," *Atmos. Chem. Phys.*, vol. 9, no. 16, pp. 5975–5988, Aug. 2009.

[17] K. Hocke, N. Kämpfer, C. Gerber, and C. Mätzler, "A complete long-term series of integrated water vapour from ground-based microwave radiometers," *Int. J. Remote Sens.*, vol. 32, no. 3, pp. 751–765, Feb. 2011.

[18] F. Cossu, K. Hocke, A. Martynov, O. Martius, and C. Mätzler, "Atmospheric water parameters measured by a ground-based microwave radiometer and compared with the WRF model," *Atmos. Sci. Lett.*, vol. 16, no. 4, pp. 465–472, Oct. 2015.

[19] W. Wang, K. Hocke, and C. Mätzler, "Physical retrieval of rain rate from ground-based microwave radiometry," *Remote Sens.*, vol. 13, no. 11, p. 2217, Jun. 2021.

[20] D. Cimini, T. J. Hewison, and L. Martin, "Comparison of brightness temperatures observed from ground-based microwave radiometers during TUC," *Meteorologische Zeitschrift*, vol. 15, no. 1, pp. 19–26, 2006.

[21] V. Mattioli, E. Westwater, and V. Morris, "Monitoring of precipitable water vapor and cloud liquid path from scanning microwave radiometers during the 2003 cloudiness inter-comparison experiment," in *Proc. 14th ARM Sci. Team Meeting*, Mar. 2004, pp. 1–10.

[22] V. Mattioli, E. R. Westwater, S. I. Gutman, and V. R. Morris, "Forward model studies of water vapor using scanning microwave radiometers, global positioning system, and radiosondes during the cloudiness inter-comparison experiment," *IEEE Trans. Geosci. Remote Sens.*, vol. 43, no. 5, pp. 1012–1021, May 2005.

[23] F. S. Marzano, D. Cimini, and R. Ware, "Monitoring of rainfall by ground-based passive microwave systems: Models, measurements and applications," *Adv. Geosci.*, vol. 2, pp. 259–265, Jul. 2005.

[24] F. S. Marzano, D. Cimini, P. Ciotti, and R. Ware, "Modeling and measurement of rainfall by ground-based multispectral microwave radiometry," *IEEE Trans. Geosci. Remote Sens.*, vol. 43, no. 5, pp. 1000–1011, May 2005.

[25] R. Ware, D. Cimini, P. Herzegh, F. Marzano, J. Vivekanandan, and E. Westwater, "Ground-based microwave radiometer measurements during precipitation," in *Proc. 8th Spec. Meeting Microw. Radiometry*, 2004, pp. 24–27.

[26] T. Rose, S. Crewell, U. Löhnert, and C. Simmer, "A network suitable microwave radiometer for operational monitoring of the cloudy atmosphere," *Atmos. Res.*, vol. 75, no. 3, pp. 183–200, May 2005.

[27] S. A. Buehler, J. Mendrok, P. Eriksson, A. Perrin, R. Larsson, and O. Lemke, "ARTS, the atmospheric radiative transfer simulator—Version 2.2, the planetary toolbox edition," *Geosci. Model Develop.*, vol. 11, no. 4, pp. 1537–1556, 2018.

[28] C. Mätzler and J. Morland, "Refined physical retrieval of integrated water vapor and cloud liquid for microwave radiometer data," *IEEE Trans. Geosci. Remote Sens.*, vol. 47, no. 6, pp. 1585–1594, Jun. 2009.

[29] J. Morland, "TROWARA-tropospheric water vapour radiometer: Radiometer review and new calibration model," Institut für Angew. Physik, Universität Bern, Bern, Switzerland, IAP Res. Rep., 2002-15-MW 2002.

[30] R. Peter and N. Kämpfer, "Radiometric determination of water vapor and liquid water and its validation with other techniques," *J. Geophys. Res.*, *Atmos.*, vol. 97, no. D16, pp. 18173–18183, 1992.

[31] J. Morland, "TROWARA-Rain flag development and stability of instrument and calibration," Institut für Angew. Physik, Universität Bern, Bern, Switzerland, IAP Res. Rep. 2007-13-MW, 2007.

[32] F. Navas-Guzmán, N. Kämpfer, and A. Haefele, "Validation of brightness and physical temperature from two scanning microwave radiometers in the 60 GHz O_2 band using radiosonde measurements," *Atmos. Meas. Techn.*, vol. 9, no. 9, pp. 4587–4600, 2016.

[33] *Radiometer Physics GmbH.* Accessed: Jul. 19, 2022. [Online]. Available: http://www.radiometer-physics.de

[34] S. Kazama, T. Rose, R. Zimmermann, and R. Zimmermann, "A precision autocalibrating 7 channel radiometer for environmental research applications," *J. Remote Sens. Soc. Jpn.*, vol. 19, no. 3, pp. 265–273, 1999.

[35] Y. Han and E. R. Westwater, "Analysis and improvement of tipping calibration for ground-based microwave radiometers," *IEEE Trans. Geosci. Remote Sens.*, vol. 38, no. 3, pp. 1260–1276, May 2000.

[36] J. Hu et al., "Characterization of brightness temperature biases at channels 13 and 14 for FY-3C MWHS-2," *IEEE Trans. Geosci. Remote Sens.*, vol. 60, pp. 1–14, 2021.

[37] N. Zhang et al., "Forest height mapping using feature selection and machine learning by integrating multi-source satellite data in Baoding city, North China," *Remote Sens.*, vol. 14, no. 18, p. 4434, Sep. 2022.

[38] J. H. Friedman, "Greedy function approximation: A gradient boosting machine," *Ann. Statist.*, vol. 29, no. 5, pp. 1189–1232, Oct. 2001.

[39] *Operation Principles and Software Description for Rpg Standard Single Polarization Radiometers*. Accessed: Jul. 19, 2022. [Online]. Available: https://www.radiometer-physics.de/download/PDF/Radiometers/HATPRO/

[40] K. Hocke, L. Bernet, W. Wang, C. Mätzler, M. Hervo, and A. Haefele, "Integrated water vapor during rain and rain-free conditions above the Swiss Plateau," *Climate*, vol. 9, no. 7, p. 105, Jun. 2021.

[41] H. J. Liebe, M. C. Thompson, and T. A. Dillon, "Dispersion studies of the 22 GHz water vapor line shape," *J. Quant. Spectrosc. Radiat. Transf.*, vol. 9, no. 1, pp. 31–47, Jan. 1969.

[42] V. Meunier, U. Löhnert, P. Kollias, and S. Crewell, "Biases caused by the instrument bandwidth and beam width on simulated brightness temperature measurements from scanning microwave radiometers," *Atmos. Meas. Techn.*, vol. 6, no. 5, pp. 1171–1187, May 2013.

[43] C. Straub, A. Murk, and N. Kämpfer, "MIAWARA-C, a new ground based water vapor radiometer for measurement campaigns," *Atmos. Meas. Techn.*, vol. 3, no. 5, pp. 1271–1285, Sep. 2010.

[44] M. Hervo, P. Bättig, and A. Haefele, "Evaluation of the new microwave radiometer HATPRO-G5," Eidgenössisches Departement des Innern EDI, Bundesamt für Meteorologie und Klimatologie MeteoSchweiz, Payerne, Switzerland, Res. Rep., 2021.

[45] U. Löhnert and S. Crewell, "Accuracy of cloud liquid water path from ground-based microwave radiometry 1. Dependency on cloud model statistics," *Radio Sci.*, vol. 38, no. 3, p. 8041, 2003.

[46] R. Beynon and K. Hocke, "Snow virga above the Swiss Plateau observed by a micro rain radar," *Remote Sens.*, vol. 14, no. 4, p. 890, Feb. 2022.

Wenzhi Fan received the M.Sc.(Eng.) degree in photogrammetry and remote sensing from the China University of Mining and Technology, Xuzhou, China, in 2019. He is currently pursuing the Ph.D. degree in geophysics with Peking University, Beijing, China.

His main research interests include research in large-scale synthetic aperture radar (SAR) interferometry and applications to surface loading.

Christoph Dätwyler received the M.Sc. degree in mathematics from the Eidgenössische Technische Hochschule Zürich, Zürich, Switzerland, in 2014, and the Ph.D. degree in climate sciences from the University of Bern, Bern, Switzerland, in 2019.

His research interests include atmospheric physics.
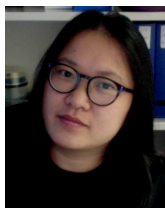
Wenyue Wang received the M.Sc.(Eng.) degree in cartography and geographical information engineering from the China University of Mining and Technology, Xuzhou, China, in 2019. She is currently pursuing the Ph.D. degree in climate sciences with the University of Bern, Bern, Switzerland.

Her research interests include microwave remote sensing, atmospheric water detected from ground-based microwave radiometer, estimation of rain rate, and the study of rainfall precursors and nowcasting.

Maxime Hervo currently works at the Federal Office of Meteorology and Climatology, MeteoSwiss, Payerne, Switzerland. His research interests include atmospheric physics.

Axel Murk received the M.Sc. degree in physics from the Technical University of Munich, Munich, Germany, in 1995, and the Ph.D. degree in physics from the University of Bern, Bern, Switzerland, in 1999.

He is currently the Leader of the Microwave Physics Division, Institute of Applied Physics, University of Bern. He has been involved in the development and characterization of millimeter- and submillimeter-wave instrumentation for different ground-based and space-borne projects. His research interests include digital real-time spectrometers and the radiometric calibration of remote sensing instruments.

Alexander Haefele received the M.S. and Ph.D. degrees from the University of Bern, Bern, Switzerland, in 2005 and 2009, respectively.

He currently works at the Federal Office of Meteorology and Climatology, MeteoSwiss, Payerne, Switzerland.

Eric Sauvageat received the M.S.(Eng.) degree in energy management and sustainability from the École Polytechnique Fédérale de Lausanne, Lausanne, Switzerland, in 2018. He is currently pursuing the Ph.D. degree in applied physics with the University of Bern, Bern, Switzerland.

His main research interests include microwave remote sensing and data analysis of atmospheric processes, with a focus on middle-atmospheric ozone.

Klemens Hocke received the Venia Legendi in atmospheric physics from the University of Bern, Bern, Switzerland, in 2011.

He is currently the Leader of the Atmospheric Processes Group, Institute of Applied Physics, University of Bern. His research interests include atmospheric dynamics, remote sensing, and data analysis of atmospheric water and stratospheric ozone.

8 | ATMOSPHERIC EFFECTS AND PRECURSORS OF RAINFALL

8.1 SUMMARY OF THE STUDY

Numerical weather models offer rainfall forecasts by solving physical equations several days in advance, but often struggle with near-future predictions due to insufficiently accurate information on the distribution of temperature and humidity, or cloud status. Nowcasting bridges the gap in this time interval limitation, typically spanning 0 to 6 hours, by utilizing available weather parameters to extrapolate the evolution of the air mass. The MeteoSwiss employs a comprehensive approach to nowcasting, integrating weather radar, satellite imagery, lightning detection, and model data. While weather radar effectively detects precipitation particles (such as rain, snow, or hail), it lacks the ability to directly observe water vapor, unlike microwave radiometers. In less developed and remote areas without radar coverage, further analysis of weather station network data for nowcasting may prove beneficial. Moreover, enhancing nowcasting accuracy requires a deep understanding of atmospheric effects and the identification of rainfall precursors.

The article presented in this chapter derived the temporal evolution of eight atmospheric parameters measured by the ground-based microwave radiometer TROWARA and weather station during rain events using a SEA method. I analyzed a total of 1199 rain events detected by TROWARA to identify the favorable conditions that trigger rainfall over a 10-year period over the Swiss Plateau and to examine their relationship with observed changes in water vapor. My study revealed the typical behavior of rainfall and its inter-relations with atmospheric parameters, while also delving into the rainfall precursors.

The following article was peer-reviewed and published in Remote Sensing in June 2022.

8.2 PUBLICATION

FULL CITATION

Wang Wenyue and Klemens Hocke (2022). "Atmospheric effects and precursors of rainfall over the Swiss Plateau." In: *Remote Sensing* 14.12, p. 2938. https://doi.org/10.3390/rs14122938.

remote sensing

MDPI

Article

Atmospheric Effects and Precursors of Rainfall over the Swiss Plateau

Wenyue Wang [1,2,*] and **Klemens Hocke [1,2]**

1   Institute of Applied Physics, University of Bern, 3012 Bern, Switzerland; klemens.hocke@unibe.ch
2   Oeschger Centre for Climate Change Research, University of Bern, 3012 Bern, Switzerland
*   Correspondence: wenyue.wang@unibe.ch

Abstract: In this study, we investigate the characteristics of atmospheric parameters before, during, and after rain events in Bern, Switzerland. Ground-based microwave radiometer data of the TROpospheric WAter RAdiometer (TROWARA) with a time resolution of 7 s, observations of a weather station, and the composite analysis method are used to derive the temporal evolution of rain events and to identify possible rainfall precursors during a 10-year period (1199 available rain events). A rainfall climatology is developed using parameters integrated water vapor (IWV), integrated liquid water (ILW), rain rate, infrared brightness temperature (T_{IR}), temperature, pressure, relative humidity, wind speed, and air density. It was found that the IWV is reduced by about 2.2 mm at the end of rain compared to the beginning. IWV and T_{IR} rapidly increase to a peak at the onset of the rainfall. Precursors of rainfall are that the temperature reaches its maximum around 30 to 60 min before rain, while the pressure and relative humidity are minimal. IWV fluctuates the most before rain (obtained with a 10 min bandpass). In 60% of rain events, the air density decreases 2 to 6 h before the onset of rain. The seasonality and the duration of rain events as well as the diurnal cycle of atmospheric parameters are also considered. Thus, a prediction of rainfall is possible with a true detection rate of 60% by using the air density as a precursor. Further improvements in the nowcasting of rainfall are possible by using a combination of various atmospheric parameters which are monitored by a weather station and a ground-based microwave radiometer.

Keywords: rainfall precursors; rainfall nowcasting; ground-based microwave radiometer; weather station; precipitation; atmospheric parameters; composite analysis

check for updates

1. Introduction

Continuous and heavy rainfall in Switzerland often triggers floods [1,2]. The Swiss Plateau is the most densely populated place with frequent floods not only causing huge economic losses but even endangering the safety of human life [3,4]. For example, flood events in August 2005, October 2011, July 2014, June 2015, June 2018, and July 2021 occurred on the Swiss Plateau, where villages and several major cities were severely affected. Due to the geographical location of the Swiss Plateau between the Jura Mountains and the Swiss Alps, rainfall is inherently complex [5,6]. Furthermore, local-scale detection of heavy rainfall trends may be masked or amplified by natural variability [7], and numerical weather prediction (NWP) models have difficulty in predicting them accurately [8]. A complete and organized description of the occurrence and development of rainfall on the Swiss Plateau, understanding of its effects with the evolution of atmospheric parameters, and seeking atmospheric precursors of rainfall for the nowcasting or prediction therefore become an urgent need.

Rainfall can be acquired by different techniques. Rain gauges and Doppler weather radars both collect rainfall data in minutes, but the former may be degraded by wind effects and the latter has a high operating cost. Satellite microwave radiometers have low temporal sampling at a certain place and are limited in the inversion of rainfall over

land [9]. To overcome these drawbacks, the ground-based microwave radiometer is now extensively being used for rainfall retrieval, nowcasting convective activity, and meteorological analysis [10–13]. The TROpospheric WAter RAdiometer (TROWARA), as a ground-based microwave radiometer, can reliably retrieve rain rate, IWV, and ILW values since 2004 in Bern [14]. The enhanced microwave emission from rain droplets due to the Mie effect leads to a rapid rise in the ILW when rain starts [15]. TROWARA rainfall retrieval takes advantage of this physical property and uses the ILW acquired by the TROWARA radiometer as an indicator to determine the onset of rain (ILW > 0.4 mm) [16]. Accurately identifying the onset of rain is important for the nowcasting of rainfall, which can clearly distinguish between the variables needed to cause rainfall and their subsequent behavior [17]. Furthermore, TROWARA's data products are available nearly continuously and in all weather with a high time resolution of 7 s [18]. Because of the intermittent nature and spatial complexity of rainfall, high-temporal-resolution observations are necessary to accurately capture rainfall [19]. High time resolution can also offer details of the microphysical, dynamic, and thermodynamic characteristics of mesoscale rainfall phenomena [20].

The convection and transportation of water vapor are closely linked to rainfall [21]. Van Baelen et al. [22] found that water vapor plays an essential role in studying the life cycle of rainfall and inducing convection. Rainfall and humidity are positively related, and tracking water vapor advection and understanding the shallow-to-deep transition of convection on the mesoscale can be enabled by integrated water vapor (IWV) [23,24]. Convergence of water vapor, anomalies in IWV, and increased tropospheric instability before the onset of heavy rain are employed as nowcasting tools [13,25]. The warm conveyor belt consists of coherent ascending airstreams along the cold front originated in extratropical cyclones' warm sector, delivering a steady stream of water vapor [26]. Heavy rainfall events on the Swiss Plateau are typically associated with warm conveyor belts and water vapor convectively enhanced lifting [21,27]. Analyses of changes in water vapor and the relationship with rainfall are thus necessary.

Composite analysis is an excellent method to explore observations and to learn about the temporal evolution of rainfall and atmospheric parameters. Adams et al. [28] conducted the composite analysis of 320 convective rain events using 3.5 years of tropical GNSS-IWV. The shallow-to-deep transition of mesoscale convection can be determined by a water vapor convergence timescale. Zhang et al. [29] investigated 10 rain events with the composite analysis using ground-based microwave radiometer and micro rain radar measurements in central China. They found IWV increases by 5 mm before monsoon light rain events. Sapucci et al. [30] studied the composite average of GNSS-IWV of 1 h before and after 18 heavy rain events. IWV increases sharply before heavy rain events, and there are oscillations in the IWV time series. The composite analysis method is also commonly applied to develop the precursors. Allan et al. [31] demonstrated atmospheric precursors of 25 heaviest rainfall events and 200 most intense 3-hourly events on regional scales through the composite analysis of rain gauge records and ERA-Interim reanalysis data over the United Kingdom. However, most related studies analyzed only a limited number of rain events or lacked long-term observations. This is likely to have a weak robustness [32], and composite results may rely on individual rain events and are not representative [33].

Air density is an important atmospheric parameter that interacts with and predicts rainfall. When rainfall increases, the air density also increases [34], and the falling velocity of raindrops is affected by the air density [35]. The air density is used as an input for many rainfall prediction models [36–38]. For example, a computer-aided rule-based rainfall prediction model is proposed by Ji et al. [39], and they found that the air density occurs at the highest level of this rule, which means the air density is most important for predicting hourly rainfall intensity.

Knowledge about atmospheric effects and precursors of rainfall contributes to a better nowcasting. Nowcasting is the use of weather parameters already obtained by technologies to extrapolate the likely future 0 to 6 h temporal evolution of the air mass. Numerical weather models such as NWP can provide rainfall forecasts by solving physical

equations a few days earlier. However, because the models do not have sufficiently accurate temperature and humidity distribution or cloud state information at startup, they tend to provide poor predictions in the short term. Nowcasting fills the limitations for this important time interval and is typically applied to weather on the local scale and mesoscale. Advances in communication technology, weather observations, and data assimilation/numerical modeling and their combined synergy can offer better possibilities for nowcasting, and the climate change adaptation requires progress in nowcasting [40]. The Federal Office of Meteorology and Climatology (MeteoSwiss) of Switzerland uses weather radar combined with satellite, lightning measurements, and model data for nowcasting. However, the weather radars miss predictions because they can only locate precipitation particles (rain, snow, or hail) and cannot observe water vapor as microwave radiometers do. In the case of high-altitude and low-temperature mountainous areas, a large amount of water vapor moves there, forming heavy rainfall rapidly, which may trigger flash floods. In addition, due to the lack of radar systems for nowcasting in less developed and remote areas, further analysis of data from the network of weather stations can be useful.

In this study, we investigate the potential of eight atmospheric parameters from a ground-based microwave radiometer and a weather station for the nowcasting of rainfall. We use 1199 rain events provided by TROWARA on the Swiss Plateau to identify conditions favorable for the triggering rainfall over 10 years and to analyze how they are related to observed changes in water vapor. The composite analysis is carried out in a long time interval of 8 h before and 16 h after rain, with the onset of rain serving as the time marker for this method. The aim of our study is to show the typical behavior of rainfall, to reveal the interaction of rainfall with atmospheric parameters, and to explore the precursors of rainfall. Section 2 outlines the derivation of the atmospheric parameters, the study area, data, and methodology. Section 3 presents the temporal evolution of atmospheric parameters, provides the analysis results, as well as analyzes rainfall mechanisms, the ILW threshold, and diurnal cycles. Section 4 discusses multiple parameters and studies by others. Conclusions are given in Section 5.

2. Study Area, Derivation, Data, and Methodology

2.1. Study Area

The Swiss Plateau lies north of the Alps and extends west–east from Lake Geneva on the French border to Lake Constance on the German–Austrian border. To the northwest of the plateau are the Jura Mountains. The entire plateau is covered with rolling hills, lakes, and rivers, with an average elevation of 580 m. The Swiss Plateau covers about one-third of Switzerland, but two-thirds of the population lives there. According to the Köppen climate classification, the Swiss Plateau is in the transition zone between a marine climate (Cfb) and a continental climate (Dfb). The weather is changeable and often overcast. It is cool in summer due to the cover of clouds, while the climate is relatively milder in winter. Freezing weather usually occurs from December to early March. The annual precipitation in Switzerland is between 1000–2000 mm, and the average annual precipitation in three-quarters of the region exceeds 1000 mm, and its precipitation is also greatly affected by the terrain.

TROWARA is operated in a room on the roof of the Exakte Wissenschaften (ExWi) (46.95°N, 7.44°E, 575 m a.s.l.) of the University of Bern. Bern is located on the Swiss Plateau. The mean annual precipitation sum and temperature in Bern are about 1059 mm and 8.8 °C, respectively [41]. Brandsma and Buishand [42] worked out that this area in summer is dominated by pre-frontal or post-frontal showers or thunderstorms, and rainfall totals are maximal during summer. The mean rain-day rainfall is about 10 mm from June to August. In winter, it is mainly frontal rainfall because of uphill or leeward effects and is an obvious dry season, nearly 6 mm rain per day.

2.2. Derivation

TROWARA's antenna receives the atmospheric radiation signal through the microwave transparent window in a temperature control room at an elevation angle of 40° pointing to the southeast. The indoor operation avoids a water film caused by raindrops falling on the antenna. TROWARA retrieves integrated water vapor (IWV) and integrated liquid water (ILW) of cloud droplets during no rain (ILW ≤ 0.4 mm) and retrieves the rain rate during rain (ILW > 0.4 mm). Mätzler and Morland [43] and Wang et al. [16] described the TROWARA measurement principles and retrieval methods in detail, which are briefly described in the following. The radiative transfer equation of the non-scattering atmosphere is

$$T_{B,i} = T_C \cdot e^{-\tau_i/\mu} + T_{mean,i} \cdot (1 - e^{-\tau_i/\mu}) \tag{1}$$

where i is the frequency of the microwave channel (21 or 31 GHz). τ_i is the zenith opacity. μ is the cosine of the zenith angle θ. $T_{B,i}$ is the brightness temperature observed by TROWARA. T_C is the brightness temperature of the cosmic background. $T_{mean,i}$ is the effective mean temperature calculated by linear combinations of the surface air temperature, pressure, and relative humidity [43].

Equation (1) can be deduced to the zenith opacity as

$$\tau_i = -\mu \cdot \ln\left(\frac{T_{mean,i} - T_{B,i}}{T_{mean,i} - T_C}\right) \tag{2}$$

The zenith opacity derived from TROWARA can be expressed as a function of IWV, ILW, and integrated rain liquid (IRL). The contributions of ice and dry snow are neglected because of their small dielectric loss.

$$\tau_i = (a_i + b_i \cdot \text{IWV} + c_i \cdot \text{ILW}) + c_i \cdot G_{M,i} \cdot \text{IRL} \tag{3}$$

where the coefficients a_i and b_i rely on the air pressure, and they can be obtained statistically by the coincident measurement of radiosondes and fine-tuned at clear sky [43]. The coefficient c_i is the Rayleigh mass absorption coefficient of cloud water and depends on temperature (and frequency) rather than pressure. It is derived from the dielectric model of water [44]. $G_{M,i}$ is the Mie gain of raindrops, up to 10 at 21 GHz and 7 at 31 GHz. When there is no rain, i.e., $G_{M,i} = 0$, IWV and ILW are calculated from the opacity measurement values of 21 and 31 GHz channels in Equation (3), whereas IRL can be obtained when there is rain. IWV during the rain period is filled by the IWV calculated by linear interpolation of opacity before and after the rain [19]. The IRL provides the rain rate using a physical retrieval method [16].

Air density (kg/m^3) depends on temperature, pressure, and water vapor content in the air [45]. The water vapor pressure p_w is calculated by the saturation water vapor pressure p_{sw} and the relative humidity RH [46]:

$$\ln p_{sw} = \sum_{i=0}^{6} g_i T^{i-2} + g_7 \ln T \tag{4}$$

$$p_w = RH \cdot p_{sw} \tag{5}$$

where the coefficients $g_i = [-0.29912729 \times 10^4, -0.60170128 \times 10^4, 0.1887643854 \times 10^2, -0.28354721 \times 10^{-1}, 0.17838301 \times 10^{-4}, -0.84150417 \times 10^{-9}, 0.44412543 \times 10^{-12}, 0.2858487 \times 10^1], i = 0, 1, 2, \ldots, 7$. T is the air temperature. The units of p_{sw} and T are Pa and K, respectively. The air density ρ is related to p_w [45] by

$$q = \frac{0.622 \cdot p_w}{P - 0.378 \cdot p_w} \tag{6}$$

$$T_V = T \cdot (1 + 0.61q) \tag{7}$$

$$\rho = \frac{P}{R \cdot T_V} \tag{8}$$

where q is the specific humidity and T_V is the virtual temperature. P is the air pressure and $R = 287.047$ (J/K·kg) is the specific gas constant of dry air. Here, we only consider the atmospheric parameters which are monitored by a Vaisala weather station at ground with a time resolution of 10 min.

2.3. Data and Methodology

To investigate the evolution of rainfall characteristics over time, the present study uses eight atmospheric parameters and rain rate to develop rainfall "climatology". The eight atmospheric parameters are IWV, ILW, T_{IR}, temperature, pressure, relative humidity, wind speed, and air density. TROWARA, as a dual-channel microwave radiometer (21.4 and 31.5 GHz), retrieves IWV, ILW, and rain rate with a time resolution of 7 s. It also has a 9.5–11.5 μm infrared radiometer channel to measure sky temperature. A standard weather station (ExWi weather station) similar to TROWARA on the roof of the ExWi building of the University of Bern acquires surface meteorological data with a time resolution of 10 min.

The composite analysis method (superposed epoch method) consists of two independent datasets. The first is discrete events in time, such as rain events. The second is the long, continuous, uniformly sampled time series, such as observations of atmospheric parameters [33]. The method assumes that these events lead to the characteristics of the continuous time series, and intercepts time series before, during, and after the event through time windows to construct a two-dimensional matrix. One row of the matrix represents a data segment for a single event. The number of rows is the sample size of these events (e.g., 1199 rain events). The columns are the epoch time. The number of columns depends on the time resolution of the data. The arithmetic mean values of these columns yield the composite of all events. The fundamental characteristic is to highlight the influence of parameters at the critical moment while weakening the influence from other phenomena and atmospheric noise [47]. It allows any fluctuations in the key time column to remain in the average value, and the time fluctuations of the row-by-row movement are averaged out [48]. To form the composite of rain events, the criteria are the following:

- The timing mark of a rain event is set as 0 epoch time (onset time of rainfall). The occurrence/duration time of rainfall is set as t; 1 h before rainfall is set as −1, 1 h during rainfall is set as +1, and 1 h after rainfall is set as $t + 1$.
- ILW = 0.4 mm is to identify the beginning and end time of rainfall [15,43,49].
- If no rainfall occurs during 8 h before the time 0 and during 16 h after the time t, then this rain event is selected.

From 1 January 2011 to 31 December 2020, all compliant rainfall events detected by TROWARA in Bern are considered. The number of rain events is denoted by N. There are, in total, 1199 rain events, including $N = 345$ in summer (June, July, August), $N = 273$ in winter (December, January, February), $N = 428$ long-duration rainfall ($t > 16$ h), and $N = 497$ short-duration rainfall ($t < 8$ h). The 8 h before rain is used because water vapor convection can be observed on this time scale [28]. The use of 16 h during and after rain is to observe the effect of rain on atmospheric parameters for as long as possible while maintaining a certain amount of available rain events.

To investigate 10 min fluctuations of IWV, its time series are filtered by a digital non-recursive, finite-impulse response (FIR), and fast-response bandpass filter. More details about the selected bandpass filter are given by Studer et al. [50].

3. Results

3.1. Atmospheric Effects of Rainfall

Figure 1a,b show the composites of IWV and ILW of all 1199 rain events before and after rain in Bern. Note that IWV during the rainfall is skipped since TROWARA cannot acquire IWV and ILW (of cloud droplets) during rain. The time before and after rain is expressed as a negative number and t + number, respectively. During the 6 to 8 h before rain, a slow increase is observed, and the mean IWV is around 17 mm. During the 0 to 6 h before rain, a rapid increase is observed, and IWV reaches the maximum value of 20.6 mm from 17 mm; it especially increases sharply by 0.6 mm within 5 min before the onset of rain. Convective processes likely play a greater role in the increase of IWV before rain. At low pressure or along the front, with the upward movement of water vapor, its convergence in highly hygroscopic condensation nuclei leads to an increase in IWV [51,52]. IWV at the end of rain is about 2.2 mm lower than at the beginning. The IWV decrease could be due to the direct removal of atmospheric water vapor by rainfall or to horizontal transport effects of water vapor. After rain, IWV decreases and remains at a stable level of 16 mm during the 4 to 16 h. ILW variations slightly vary from that of IWV. The ILW threshold for rainfall is approximately 0.4 mm [15,49]. During the 1 to 8 h before and after rain, ILW levels off about 0.03 mm but increases to 0.4 mm dramatically when rain starts. This is due to the opacity gain when the droplet diameter increases. During the 8 to 16 h after rain, ILW increases to about 0.1 mm and fluctuates. This might be due to cloud (fog) formation as a consequence of re-evaporation of surface water after rainfall.
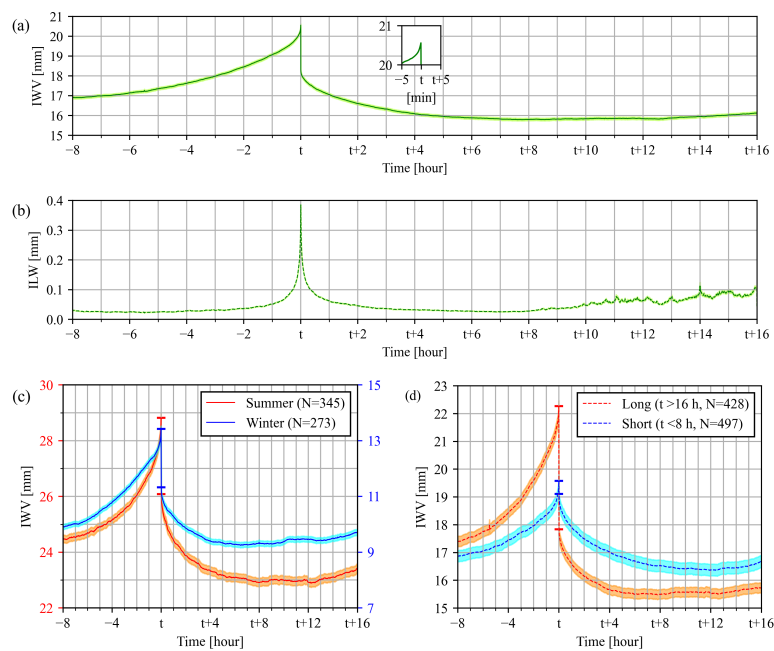
Figure 1. Composites of (**a**) integrated water vapor (IWV, green solid line) and (**b**) integrated liquid water (ILW, green dashed line) 8 h before and 16 h after rain, (**c**) the IWV composites in summer (N = 345) and winter (N = 273), as well as (**d**) the IWV composites for long (N = 428)- and short (N = 497)-duration rain events. The subplot is from 5 min before rain to 5 min after rain. IWV and ILW acquired by the TROpospheric WAter RAdiometer (TROWARA) in Bern. The shaded area shows the standard deviation of the mean (error of the mean $\sigma/\sqrt{n}$). Time t is the duration of rainfall. Short horizontal lines mark the beginning and end of rainfall.

Figure 1c,d show the composites of IWV for summer and winter as well as for short- and long-duration rain events. IWV in summer is more than twice that in winter and shows a larger peak. During the 8 h before rain, IWV in summer reaches a maximum value of 28.8 mm from 24.5 mm, and in winter it rises to 13.4 mm from 9.9 mm. IWV in summer at the end of rain is about 2.7 mm lower than at the beginning, and in winter it is 2.1 mm. As shown in Figure 1d, different duration of rainfall have different effects on IWV. The longer the rainfall, the greater the reduction in IWV from the beginning to the end of rain. The horizontal advection of water vapor plays a crucial role in cumulative rainfall. After long-duration rainfall ($t > 16$ h), IWV decreases by 4.4 mm, but the average cumulative rainfall of longer duration events is much larger than this value, about 11.8 mm. This may be due to the convergence of a small area of precipitation from the horizontal advection of a larger area of moist air. Statistics show that about 65% of all 1199 rain events have more cumulative rainfall than the difference of IWV acquired by the microwave radiometer from the onset to the end of rain. This finding may provide an indication of rainfall intensity in rainfall predictions. The impact of short-duration rainfall on IWV changes is limited. After short-duration rainfall ($t < 8$ h), IWV decreases by only 0.5 mm. IWV values of long-duration rainfall and short-duration rainfall 8 h before rain are close: both are around 17 mm. However, the IWV for long-duration rainfall reaches a peak of 22.3 mm at the beginning of rain, whereas for the short-duration rainfall, it is only 19.6 mm.

Figure 2a shows the composites of IWV, T_{IR}, and rain rate of all 1199 rain events before and during rain. Note that IWV during rain is not acquired but is interpolated from TROWARA's opacity measurements before and after rain [19]. The time before and during rain is expressed as a negative and positive number, respectively. Rain starts when time is 0, and the rain rate gradually decreases over time. From 0 to 8 h before rain, IWV is the same as in Figure 1, with an increase of 3.6 mm. It can be clearly seen that IWV reaches its peak when rain starts, and then it shows a slow downward trend. T_{IR} also reaches a peak at the beginning of rain. The reason IWV and rain rate vary with T_{IR} is that the water-holding capacity of the atmosphere increases with temperature, i.e., the warmer the air, the more water it can hold. At a given temperature, air reaches its maximum water-holding capacity (also known as the dew point) and becomes saturated. When the atmospheric temperature drops below the dew point and above 0°, the water vapor in the air condenses on the dust to form rain. As raindrops fall, they make the atmosphere cooler by evaporation. Figure 2b,c show the composites of IWV, T_{IR}, and rain rate for summer and winter as well as for short- and long-duration rain events. These three parameters in summer are higher than in winter, and the T_{IR} peak in summer is stronger and steeper than in winter. As shown in Figure 2c, after the onset of rain, the slope of IWV, T_{IR}, and rain rate are similar. For long-duration rainfall, the rain rate continues to be high and maintains an average of about 0.75 mm/h. IWV stays at about 22 mm for 6 h, and then drops slightly to 20.4 mm. T_{IR} remains at around 273 K. For short-duration rainfall, the rain rate gradually decreases to 0 from time 0 to +8. IWV and T_{IR} decrease for 8 h and continue to fall to about 16.4 mm and 250 K after 8 h, respectively.
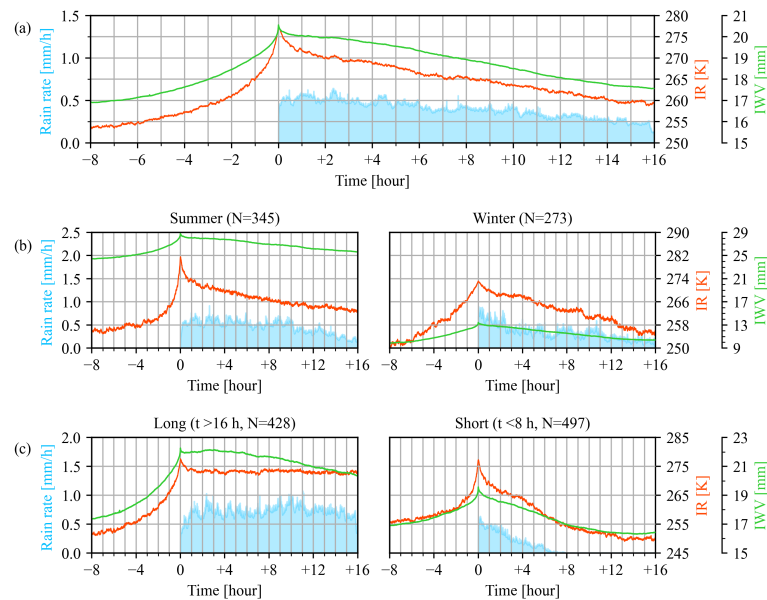
Figure 2. Composites of (**a**) IWV (green solid line), T_{IR} (red solid line), rain rate (blue area) 8 h before and 16 h during rain, considering the rain events (**b**) in summer and winter, as well as (**c**) with long and short duration.

3.2. Precursors of Rainfall

Figure 3a shows the composites of temperature, pressure, relative humidity, and wind speed before and during rain. Before rain starts, the temperature rises steadily and reaches its maximum of about 12.8 °C at 30 to 60 min before rain onset. The main reason for this increase in temperature may be that (1) thicker clouds make ground radiation blocked between the clouds and the ground, or (2) the increase of atmospheric water vapor affects the surface and atmospheric longwave radiation, and its absorption of solar radiation causes the surface temperature to increase [53]. On the other hand, at 30 to 60 min before rain onset, the pressure and relative humidity reach their minima of 947.6 hPa and 68.2%, respectively. The low density of moist air is the reason for the low pressure. The higher surface temperature before rain determines the low relative humidity. After rain starts, the temperature drops rapidly for 2 h, and then falls slowly until it remains stable. The pressure rises slowly, while the relative humidity rises rapidly for 2 h and drops slightly after reaching a maximum. These changes are because droplets begin to evaporate on the surface and energy is absorbed in the form of heat (latent heat). The wind speed increases rapidly before rain and reaches its maximum at the rain onset or a bit later. The main reason for this increase in wind may be that (1) at the front, one air mass is lifted above another, creating a low-pressure zone. The wind blows towards the low-pressure zone. The greater the temperature difference between the two air masses, the stronger the wind. (2) The falling rain creates downdrafts that spread air to the ground, creating gust fronts.
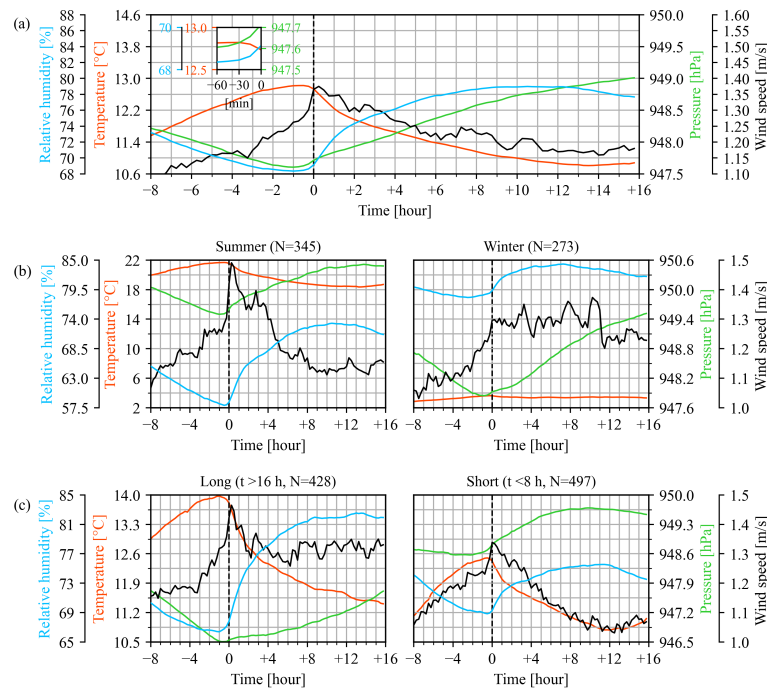
Figure 3. Composites of (**a**) temperature (red solid line), pressure (green solid line), relative humidity (blue solid line), and wind speed (black solid line) 8 h before and 16 h during rain, considering the rain events (**b**) in summer and winter, as well as (**c**) with long and short duration. Subplot (**a**) is from 60 min before rain to the onset of rain.

Figure 3b,c show the composites of temperature, pressure, relative humidity, and wind speed for summer and winter as well as for short- and long-duration rain events. The temperature and pressure in summer are higher than those in winter, whereas the relative humidity in summer is lower and shows a larger variation than in winter. In winter, the temperature variation caused by rainfall is very small, only rising by nearly 1 °C, but the pressure variation is relatively large. The wind speed in winter remains fluctuating at 1.3 m/s after rain starts. As shown in Figure 3c, long-duration rainfall has more obvious effects on temperature, pressure, relative humidity, and wind speed. Compared with short-duration rainfall, these four parameters show a larger variety and reach higher or lower extreme values before rain onset.

Fluctuations in the IWV field are closely related to the approaching frontal rainfall [54]. Figure 4a shows an individual example for the magnitude of the 10 min IWV fluctuations. To compare the difference before and after rain, the time is unified as 16 h. This rain event happened in Bern from 02:11 UT to 07:05 UT on 8 January 2011, and it is marked by the vertical blue line. The time series was obtained with a 10 min bandpass filter, and the amplitude (or magnitude) was computed as a function of time [50]. It is evident that the IWV fluctuation before rain is stronger than after rain. The maximum fluctuation is 2 to 4 h before rain and reaches a peak of 0.15 mm. During the 4 to 13 h before rain, the fluctuation remains at 0.05 to 0.1 mm. During the 13 to 16 h before rain and the 1 to 14 h after rain, it is relatively stable, with a mean value of about 0.025 mm. Figure 4b shows the composite of the IWV fluctuation amplitude 16 h before and during rain. IWV fluctuates the most around the time when rain starts, up to 0.085 mm. Ten hours before rain, the fluctuation increases from about 0.025 mm to 0.04 mm.
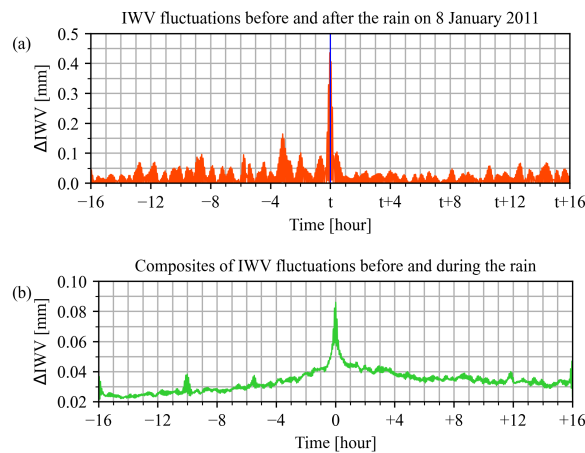
Figure 4. (**a**) IWV fluctuation series 16 h before and after a rain event between 02:11 UT and 07:05 UT on 8 January 2011 (red). The blue vertical line represent the occurrence/duration time of rain. (**b**) Composite of IWV fluctuation series of 759 rain events 16 h before and during rain (green).

Figure 5 shows the composite of air density 16 h before and during rain. The air density also reaches its minimum during the 30 to 60 min before rain. Calculating the slope in a time window is used to analyze the time derivative of the air density before rain. It was found that in about 60% of 784 rain events ($467 \div 784 = 59.57\%$), the air density decreases 2 to 6 h before rain from 1.15412 kg/m^3 to 1.15034 kg/m^3. This decrease in air density may be due to two reasons: first, extratropical cyclones cause changes in air density. Before the cold front rain passes through Bern, there is a warm front rain. Because the cold front moves faster than the warm front, the cold air mass behind the cold front moves over time into the area occupied by the warm air mass behind the warm front. The warm air has a lower density, and the cold and cool air has a higher density. The warm air mass ahead reduces the air density, and then the cold air mass replaces the warm air mass to increase the air density. Second, the density of moist air is lower than that of dry air, as was first proposed by Newton [55]. The molecular weight of water molecules is 18, which is lighter than both nitrogen and oxygen. Water vapor, instead of nitrogen and oxygen, will reduce the mass of air per cubic meter and reduce air density [56]. Before rain starts, water vapor is abundant and the air density decreases accordingly. We have the impression that air density is the best precursor because it changes earlier than the other parameters before the rain onset.
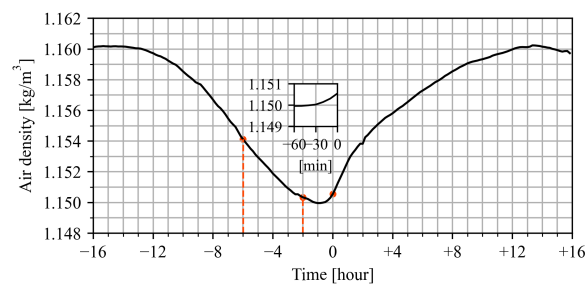
Figure 5. Composite of air density 16 h before and during rain. Red dots represent the 6 h, 2 h before rain, and the onset of the rain. The subplot is from 60 min before rain to the onset of rain. A total of 784 rain events is shown.

Figure 6 shows an example of a rain event that started at 03:14:03 UT on 2 January 2016. There is no rainfall within 8 h before the rain starts. The ILW increases rapidly, and the precipitation measured by rain gauge indicates the onset of rain when the ILW exceeds 0.4 mm in Figure 6a. As shown in Figure 6, before the onset of light rain, the IWV and temperature increase, while the pressure, relative humidity, and air density decrease. When the moderate rain starts, all these atmosphere parameters reach their extreme point. The changes in the atmosphere parameters exhibited by this example are consistent with the results of this study.
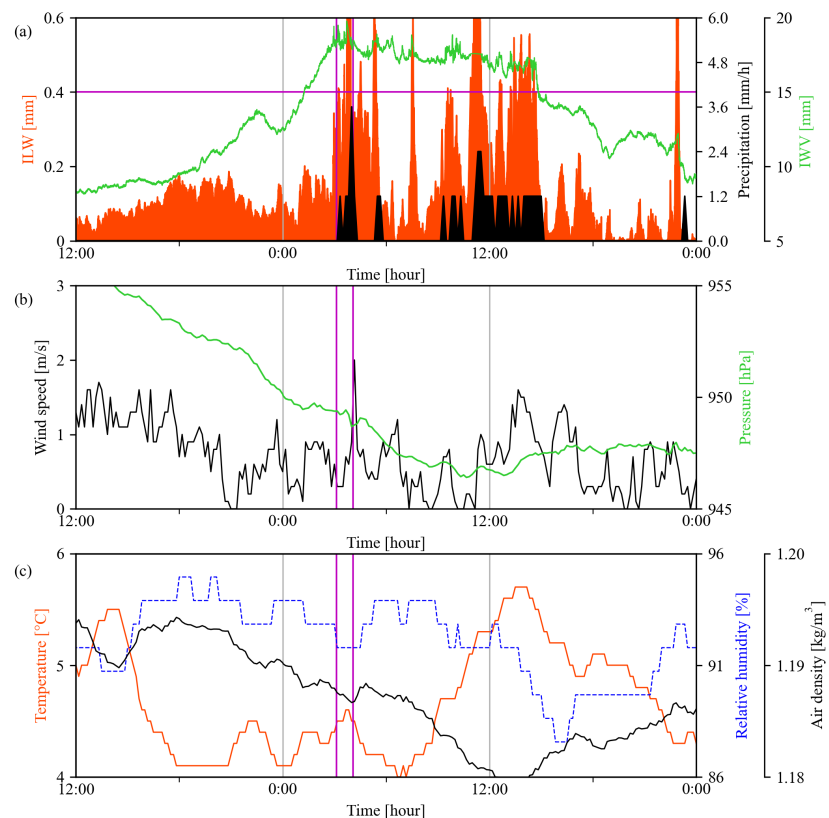
Figure 6. Time series of TROWARA and meteorological data from 1 January at 12:00 UT to 2 January at 24:00 UT, 2016. (**a**) Time series of IWV (green solid line) and ILW (red area) provided by TROWARA, and the precipitation (black area) observed by the rain gauge at the ExWi weather station. The two purple vertical lines represent the onset of light rain and moderate rain, respectively. The purple horizontal line is ILW = 0.4 mm. (**b**) Time series of surface pressure (green solid line) and wind speed (black solid line) observed by the ExWi weather station. (**c**) Time series of surface temperature (red solid line) and relative humidity (blue dashed line) observed by the ExWi weather station, as well as air density (black solid line).

3.3. ILW Threshold and Diurnal Variations

Since the IWV and ILW retrieved by TROWARA coincide in space and time, the ILW threshold is undoubtedly a good choice for identifying whether there is rain [19]. Furthermore, the physical retrieval algorithm used in this study estimates rainfall from below the melting layer, avoiding the detection of rain events that are raindrops in clouds [16].

Figure 7a shows the time series of IWV, ILW, and the rain gauge precipitation for an interesting time interval of different weather situations in January 2016. The ILW is at a high value when the rain gauge detects rain. The reason is that convergence and condensation of water vapor cause the droplet size (diameter) to increase rapidly to above 0.3 mm, resulting in a very strong rise in the ILW value. The ILW threshold is usually between 0.1 and 0.6 mm, but even an inaccurate threshold is sufficient to identify the rain period as shown in Figure 7a. Mätzler [57] found that the ILW values of non-rain clouds do not exceed 0.4 mm. Raindrops are likely to appear when the ILW value exceeds 0.4 mm [43,49], so TROWARA uses ILW = 0.4 mm as the threshold of rainfall in the present study. This threshold was also selected by Cossu et al. [15] for summer 2012. They analyzed that non-precipitating clouds are typically associated with ILW values between 0.01 and 0.4 mm. According to Cossu et al. [15], clear sky occurs if ILW is smaller than 0.01 mm, and rain occurs if ILW is greater equal 0.4 mm. Furthermore, there is a certain difference between the ILW threshold and the rain gauge in determining the start and end time of a rain event. For example, for a rain event from 8–9 January in Figure 7a, the rainfall start time to end time recorded by TROWARA and rain gauge are 10:22:35 UT on 8 January to 13:51:18 UT on 9 January and 12:20:00 UT on 8 January to 11:10:00 UT on 9 January, respectively. This time difference between TROWARA and the rain gauge might be due to the higher sensitivity of TROWARA for light rain or due to spatial variations of the rain area since the sounding volume of TROWARA is not at the place of the rain gauge (horizontal distance is about 100–500 m). TROWARA detects rain occasionally, but the rain gauge does not, such as on 24 January. It may be because of the virga that the rain evaporates or sublimates before it reaches the ground. There are also cases where only the rain gauge shows rain.

Diurnal variations of atmospheric parameters do not cause the main effect and domination during the rain period. Figure 8a shows the diurnal variation of IWV during the long clear sky period from 25–28 January. Hocke et al. [58] described that the diurnal cycle of IWV over Bern ranges from 0.5 mm below the daily average in the morning to 0.5 mm above the daily average in the evening. Because this change is less than 5%, it can be assumed that the diurnal cycle of IWV has no direct effect on its changes during the rain period. For example, there are two light rain events lasting 1 to 2 min at 22:58:01 UT on 2 January and at 5:07:11 UT on 3 January, and a rain event lasting three days from 5:20:07 UT on 10 January to 22:55:19 UT on 12 January. During these rain events, the changes in IWV are consistent with the description in the previous subsection. As shown in Figure 8b,c, the wind speed and pressure have no obvious diurnal cycle during the clear sky period (with ILW = 0 mm), but temperature, relative humidity, and air density do. The temperature is highest around 14 UT, while the relative humidity and air density are lowest. The strong diurnal cycle of temperature during the clear sky period might be due to the absence of cloud droplets and to the diurnal variation of the greenhouse gas water vapor. Because only 22.6% of all 1199 rain events in this study occur in the afternoon from 14 to 17 UT, it can be assumed that the diurnal cycle of these parameters has no strong effect on them as precursors of rainfall.
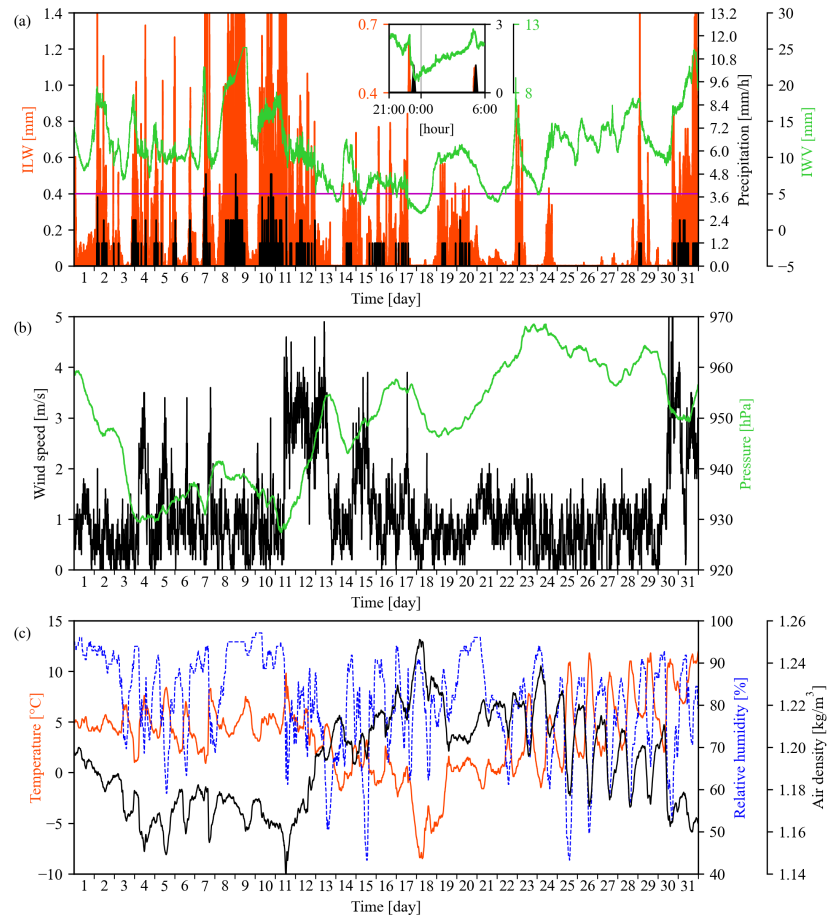
Figure 7. Time series of TROWARA and meteorological data from 1–31 January 2016. (**a**) Time series of IWV (green solid line), ILW (red area), and the precipitation (black area). The purple horizontal line is ILW = 0.4 mm. The subplot is from 21:00 UT on 2 January to 6:00 UT on 3 January. (**b**) Time series of surface pressure (green solid line) and wind speed (black solid line). (**c**) Time series of surface temperature (red solid line), relative humidity (blue dashed line), and air density (black solid line).
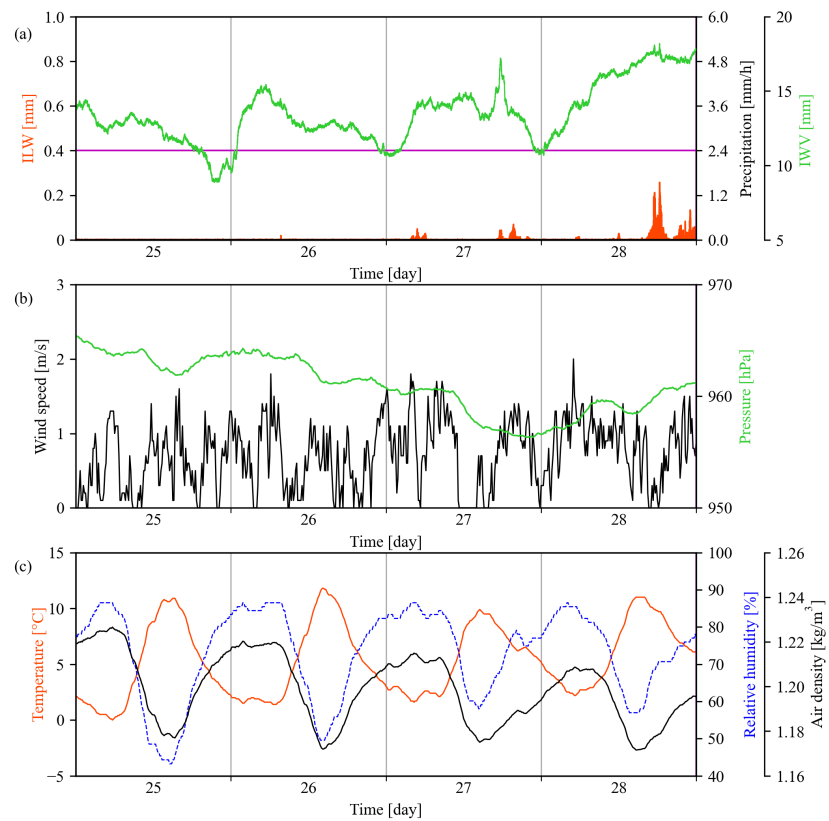
Figure 8. Time series of TROWARA and meteorological data from 24–29 January 2016. Between the two purple vertical lines is a long clear sky period that lasts from 25–28 January. (**a**) Time series of IWV (green line) and ILW (red area).The purple horizontal line is ILW = 0.4 mm. (**b**) Time series of surface pressure (green line) and wind speed (black line). (**c**) Time series of surface temperature (red line), relative humidity (blue dotted line), and air density (black line).

4. Discussion

Using only rainfall precursors obtained by a single parameter will limit the accuracy of rainfall prediction. The performance of rainfall prediction is typically evaluated with a true detection rate and a false alarm rate [29,59]. The true detection rate is the proportion of rain events detected during rain, and the false alarm rate is the proportion of rain events detected during no rain. For example, counting all 1199 rain events yields the result that the air density was significantly reduced in 60% of the cases 2 to 6 h before rain. This is the true detection rate using air density for predicting rainfall. However, because of the diurnal cycle of air density during the clear sky period or other weather, false alarms are inevitable. Therefore, considering all parameters provided by the weather station and the radiometer would lead to a higher potential for high-precision rainfall nowcasting. This is important for various meteorological and hydrological applications. During no rain, the surface temperature, relative humidity, and air density provided by the weather station have the diurnal cycle, whereas the surface pressure and wind speed have no diurnal cycle. If these weather station parameters are used together for rainfall nowcasting, the diurnal cycle problem may be avoided. IWV and ILW are directly related to rainfall processes. If

these microwave radiometer parameters are added for rainfall nowcasting, the influence of other weather may be excluded.

To the best of our knowledge, no studies in the literature have performed joint analysis of IWV and other meteorological observations in the Swiss Plateau similar to our study, which can achieve improvements to current nowcasting systems [25]. Manandhar et al. [60] proposed a simple algorithm for nowcasting of rainfall by using the composite analysis of observed changes in GNSS-IWV and its second derivative in the tropical region. The true detection rate is 87.7%, and the false alarm rate is 38.6%. However, the formation of rainfall in the tropics is simpler. It often rains in the afternoon after water vapor convection due to the sun exposure. In addition, their study only can predict rainfall events 5 min into the future. Manandhar et al. [59] applied GNSS-IWV and meteorological parameters to a data-driven method for the rainfall prediction. The false alarm rate is significantly reduced (20.3%), but they only identified characteristics of several atmospheric parameters (temperature, relative humidity, dew point, and solar radiation). For complex atmospheric states, the detailed studies of multiple atmospheric parameters inevitably enhance the predictability of rainfall [61].

5. Conclusions

The ground-based microwave radiometer TROWARA, given its high temporal resolution, is very sensitive to rain intervals. Combined with data from a weather station, we were able to derive the mean temporal evolution of eight atmospheric parameters before, during, and after rainfall from 2011 to 2020 over the Swiss Plateau. This study helps to further understand the atmospheric effects of rainfall and to achieve progress in the nowcasting of rainfall by means of a microwave radiometer and a weather station. Our study quantitatively describes the average behavior of 1199 rain events in the changes of integrated water vapor (IWV), integrated liquid water (ILW), rain rate, infrared brightness temperature (T_{IR}), temperature, pressure, relative humidity, wind speed, and air density. These parameters show noticeable variation under the influence of rainfall. For example, at the onset of the rain, IWV reaches a peak, and ILW rises rapidly in a short time. IWV at the end of rain is lower than at the beginning. Interestingly, IWV, T_{IR}, and wind speed show a sharp increase of around 3.6 mm, 25 K, and 0.27 m/s before rain. Temperature, pressure, relative humidity, and air density reach their extrema 30 to 60 min before rain. The IWV fluctuation amplitude increases slightly before rain. Air density decreases 2 to 6 h before the onset of rain. The air density seems to be the best precursor for the prediction of rainfall. We obtained a true detection rate of 60% for the nowcasting of rainfall 2 to 6 h in advance by using our time series of air density.

Further improvement of the nowcasting of rainfall might be possible if we consider a combination of different atmospheric parameters as precursors. Consideration of the influence of the seasons on rainfall might be also helpful, such as convection in summer. In terms of application, the results of this study can be used as an input factor for model training, which is of great help in building a rainfall nowcasting model with high accuracy and applicability. They can also be ingested into an expert system to provide forecasters with better forecasts.

References

1. Rössler, O.; Froidevaux, P.; Börst, U.; Rickli, R.; Martius, O.; Weingartner, R. Retrospective analysis of a nonforecasted rain-on-snow flood in the Alps—A matter of model limitations or unpredictable nature? *Hydrol. Earth Syst. Sci.* **2014**, *18*, 2265–2285. [CrossRef]

2. Barton, Y.; Giannakaki, P.; Von Waldow, H.; Chevalier, C.; Pfahl, S.; Martius, O. Clustering of regional-scale extreme precipitation events in southern Switzerland. *Mon. Weather Rev.* **2016**, *144*, 347–369. [CrossRef]

3. Beniston, M.; Stoffel, M. Rain-on-snow events, floods and climate change in the Alps: Events may increase with warming up to 4 °C and decrease thereafter. *Sci. Total Environ.* **2016**, *571*, 228–236. [CrossRef] [PubMed]

4. Schmocker-Fackel, P.; Naef, F. More frequent flooding? Changes in flood frequency in Switzerland since 1850. *J. Hydrol.* **2010**, *381*, 1–8. [CrossRef]

5. Speirs, P.; Gabella, M.; Berne, A. A comparison between the GPM dual-frequency precipitation radar and ground-based radar precipitation rate estimates in the Swiss Alps and Plateau. *J. Hydrometeorol.* **2017**, *18*, 1247–1269. [CrossRef]

6. Ragettli, S.; Tong, X.; Zhang, G.; Wang, H.; Zhang, P.; Stähli, M. Climate change impacts on summer flood frequencies in two mountainous catchments in China and Switzerland. *Hydrol. Res.* **2021**, *52*, 4–25. [CrossRef]

7. Kreienkamp, F.; Philip, S.Y.; Tradowsky, J.S.; Kew, S.F.; Lorenz, P.; Arrighi, J.; Belleflamme, A.; Bettmann, T.; Caluwaerts, S.; Chan, S.C.; et al. Rapid Attribution of Heavy Rainfall Events Leading to the Severe Flooding in Western Europe during July 2021. 2021. Available online: https://biblio.ugent.be/publication/8732135 (accessed on 15 March 2022).

8. Sun, J.; Xue, M.; Wilson, J.W.; Zawadzki, I.; Ballard, S.P.; Onvlee-Hooimeyer, J.; Joe, P.; Barker, D.M.; Li, P.W.; Golding, B.; et al. Use of NWP for nowcasting convective precipitation: Recent progress and challenges. *Bull. Am. Meteorol. Soc.* **2014**, *95*, 409–426. [CrossRef]

9. Marzano, F.S.; Fionda, E.; Ciotti, P. Neural-network approach to ground-based passive microwave estimation of precipitation intensity and extinction. *J. Hydrol.* **2006**, *328*, 121–131. [CrossRef]

10. Chakraborty, R.; Das, S.; Jana, S.; Maitra, A. Nowcasting of rain events using multi-frequency radiometric observations. *J. Hydrol.* **2014**, *513*, 467–474. [CrossRef]

11. Wei, J.; Shi, Y.; Ren, Y.; Li, Q.; Qiao, Z.; Cao, J.; Ayantobo, O.O.; Yin, J.; Wang, G. Application of ground-based microwave radiometer in retrieving meteorological characteristics of Tibet Plateau. *Remote Sens.* **2021**, *13*, 2527. [CrossRef]

12. Xu, G.; Zhang, W.; Feng, G.; Liao, K.; Liu, Y. Effect of off-zenith observations on reducing the impact of precipitation on ground-based microwave radiometer measurement accuracy. *Atmos. Res.* **2014**, *140*, 85–94. [CrossRef]

13. Chan, P.W. Performance and application of a multi-wavelength, ground-based microwave radiometer in intense convective weather. *Meteorol. Z.* **2009**, *18*, 253–265. [CrossRef]

14. Bernet, L.; Brockmann, E.; von Clarmann, T.; Kämpfer, N.; Mahieu, E.; Mätzler, C.; Stober, G.; Hocke, K. Trends of atmospheric water vapor in Switzerland from ground-based radiometry, FTIR and GNSS data. *Atmos. Chem. Phys.* **2020**, *20*, 11223–11244. [CrossRef]

15. Cossu, F.; Hocke, K.; Martynov, A.; Martius, O.; Mätzler, C. Atmospheric water parameters measured by a ground-based microwave radiometer and compared with the WRF model. *Atmos. Sci. Lett.* **2015**, *16*, 465–472. [CrossRef]

16. Wang, W.; Hocke, K.; Mätzler, C. Physical retrieval of rain rate from ground-based microwave radiometry. *Remote Sens.* **2021**, *13*, 2217. [CrossRef]

17. Sherwood, S.C. Convective precursors and predictability in the tropical western Pacific. *Mon. Weather Rev.* **1999**, *127*, 2977–2991. [CrossRef]

18. Hocke, K.; Navas-Guzmán, F.; Moreira, L.; Bernet, L.; Mätzler, C. Oscillations in atmospheric water above Switzerland. *Atmos. Chem. Phys.* **2017**, *17*, 12121–12131. [CrossRef]

19. Hocke, K.; Bernet, L.; Wang, W.; Mätzler, C.; Hervo, M.; Haefele, A. Integrated water vapor during rain and rain-free conditions above the Swiss Plateau. *Climate* **2021**, *9*, 105. [CrossRef]

20. Knupp, K.; Coleman, T.; Phillips, D.; Ware, R.; Cimini, D.; Vandenberghe, F.; Vivekanandan, J.; Westwater, E.; Coleman, T.; Phillips, D. Ground-based passive microwave profiling during dynamic weather conditions. *J. Atmos. Ocean. Techol.* **2009**, *26*, 1057–1073. [CrossRef]

21. Piaget, N.; Froidevaux, P.; Giannakaki, P.; Gierth, F.; Martius, O.; Riemer, M.; Wolf, G.; Grams, C.M. Dynamics of a local Alpine flooding event in October 2011: Moisture source and large-scale circulation. *Q. J. R. Meteorol. Soc.* **2015**, *141*, 1922–1937. [CrossRef]

22. Van Baelen, J.; Reverdy, M.; Tridon, F.; Labbouz, L.; Dick, G.; Bender, M.; Hagen, M. On the relationship between water vapor field evolution and the life cycle of precipitation systems. *Q. J. R. Meteorol. Soc.* **2011**, *137*, 204–223. [CrossRef]

23. Adams, D.K.; Fernandes, R.M.; Kursinski, E.R.; Maia, J.M.; Sapucci, L.F.; Machado, L.A.; Vitorello, I.; Monico, J.F.G.; Holub, K.L.; Gutman, S.I.; et al. A dense GNSS meteorological network for observing deep convection in the Amazon. *Atmos. Sci. Lett.* **2011**, *12*, 207–212. [CrossRef]
24. Muller, C.J.; Back, L.E.; O'Gorman, P.A.; Emanuel, K.A. A model for the relationship between tropical precipitation and column water vapor. *Geophys. Res. Lett.* **2009**, *36*, L16804. [CrossRef]
25. Benevides, P.; Catalao, J.; Miranda, P. On the inclusion of GPS precipitable water vapor in the nowcasting of rainfall. *Nat. Hazard. Earth Sys.* **2015**, *15*, 2605–2616. [CrossRef]
26. Madonna, E.; Wernli, H.; Joos, H.; Martius, O. Warm conveyor belts in the ERA-Interim dataset (1979–2010). Part I: Climatology and potential vorticity evolution. *J. Clim.* **2014**, *27*, 3–26. [CrossRef]
27. Pfahl, S.; Madonna, E.; Boettcher, M.; Joos, H.; Wernli, H. Warm conveyor belts in the ERA-Interim dataset (1979–2010). Part II: Moisture origin and relevance for precipitation. *J. Clim.* **2014**, *27*, 27–40. [CrossRef]
28. Adams, D.K.; Gutman, S.I.; Holub, K.L.; Pereira, D.S. GNSS observations of deep convective time scales in the Amazon. *Geophys. Res. Lett.* **2013**, *40*, 2818–2823. [CrossRef]
29. Zhang, W.; Xu, G.; Xi, B.; Ren, J.; Wan, X.; Zhou, L.; Cui, C.; Wu, D. Comparative study of cloud liquid water and rain liquid water obtained from microwave radiometer and micro rain radar observations over central China during the monsoon. *J. Geophys. Res. Atmos.* **2020**, *125*, e2020JD032456. [CrossRef]
30. Sapucci, L.F.; Machado, L.A.; de Souza, E.M.; Campos, T.B. Global Positioning System precipitable water vapor (GPS-PWV) jumps before intense rain events: A potential application to nowcasting. *Meteorol. Appl.* **2019**, *26*, 49–63. [CrossRef]
31. Allan, R.P.; Blenkinsop, S.; Fowler, H.J.; Champion, A.J. Atmospheric precursors for intense summer rainfall over the United Kingdom. *Int. J. Climatol.* **2020**, *40*, 3849–3867. [CrossRef]
32. Madhulatha, A.; Rajeevan, M.; Venkat Ratnam, M.; Bhate, J.; Naidu, C. Nowcasting severe convective activity over southeast India using ground-based microwave radiometer observations. *J. Geophys. Res. Atmos.* **2013**, *118*, 1–13. [CrossRef]
33. Rao, M.P.; Cook, E.R.; Cook, B.I.; Anchukaitis, K.J.; D'Arrigo, R.D.; Krusic, P.J.; LeGrande, A.N. A double bootstrap approach to Superposed Epoch Analysis to evaluate response uncertainty. *Dendrochronologia* **2019**, *55*, 119–124. [CrossRef]
34. Wan, T.; Wu, S.W. Aerodynamic analysis under influence of heavy rain. *J. Aeronaut. Astronaut. Aviat.* **2004**, *41*, 173–180.
35. Niu, S.; Jia, X.; Sang, J.; Liu, X.; Lu, C.; Liu, Y. Distributions of raindrop sizes and fall velocities in a semiarid plateau climate: Convective versus stratiform rains. *J. Appl. Meteorol. Clim.* **2010**, *49*, 632–645. [CrossRef]
36. Nakakita, E.; Ikebuchi, S.; Nakamura, T.; Kanmuri, M.; Okuda, M.; Yamaji, A.; Takasao, T. Short-term rainfall prediction method using a volume scanning radar and grid point value data from numerical weather prediction. *J. Geophys. Res. Atmos.* **1996**, *101*, 26181–26197. [CrossRef]
37. Sugimoto, S.; Nakakita, E.; Ikebuchi, S. A stochastic approach to short-term rainfall prediction using a physically based conceptual rainfall model. *J. Hydrol.* **2001**, *242*, 137–155. [CrossRef]
38. French, M.N.; Krajewski, W.F. A model for real-time quantitative rainfall forecasting using remote sensing: 1. Formulation. *Water Resour. Res.* **1994**, *30*, 1075–1083. [CrossRef]
39. Ji, S.Y.; Sharma, S.; Yu, B.; Jeong, D.H. Designing a rule-based hourly rainfall prediction model. In Proceedings of the 2012 IEEE 13th International Conference on Information Reuse and Integration (IRI), Las Vegas, NV, USA, 8–10 August 2012; pp. 303–308.
40. Mass, C. Nowcasting: The promise of new technologies of communication, modeling, and observation. *Bull. Am. Meteorol. Soc.* **2012**, *93*, 797–809. [CrossRef]
41. MeteoSwiss. *Climate Normals Bern/Zollikofen (Reference Period. 1981–2010)*; Federal Office of Meteorology and Climatology MeteoSwiss: Zurich, Switzerland, 2014. Available online: https://www.meteoswiss.admin.ch/home/climate/swiss-climate-in-detail/climate-normals/climate-diagrams-and-normals--per-station.html?station=ber (accessed on 15 March 2022).
42. Brandsma, T.; Buishand, T.A. Statistical linkage of daily precipitation in Switzerland to atmospheric circulation and temperature. *J. Hydrol.* **1997**, *198*, 98–123. [CrossRef]
43. Mätzler, C.; Morland, J. Refined physical retrieval of integrated water vapor and cloud liquid for microwave radiometer data. *IEEE Trans. Geosci. Remote Sens.* **2009**, *47*, 1585–1594. [CrossRef]
44. Ellison, W. Dielectric properties of natural media. In *Thermal Microwave Radiation: Applications for Remote Sensing*; Mätzler, C., Ed.; IET Electromagnetic Waves Series: London, UK, 2006; Volume 52, pp. 431–454. Available online: https://scholar.google.com/scholar?cluster=13553953111540458320&hl=en&as_sdt=0,5 (accessed on 16 June 2022).
Therm. Microw. Radiat. Appl. Remote Sens. **2006**, *431*, 455.
45. McIlveen, R. *Fundamentals of Weather and Climate*; Oxford University Press: New York, NY, USA, 2010.
46. Wexler, A. Vapor pressure formulation for water in range 0 to 100 C. A revision. *J. Res. Natl. Bur. Stand. A Phys. Chem.* **1976**, *80*, 775. [CrossRef] [PubMed]
47. Zheng, Z.; Xu, G.; Li, Q.; Chen, C.; Li, J. Effect of precipitation on reducing atmospheric pollutant over Beijing. *Atmos. Pollut. Res.* **2019**, *10*, 1443–1453. [CrossRef]
48. Haurwitz, M.W.; Brier, G.W. A critique of the superposed epoch analysis method: Its application to solar–weather relations. *Mon. Weather Rev.* **1981**, *109*, 2074–2079. [CrossRef]
49. Löhnert, U.; Crewell, S. Accuracy of cloud liquid water path from ground-based microwave radiometry 1. Dependency on cloud model statistics. *Radio Sci.* **2003**, *38*, 8041. [CrossRef]

50. Studer, S.; Hocke, K.; Kämpfer, N. Intraseasonal oscillations of stratospheric ozone above Switzerland. *J. Atmos. Sol. Terr. Phy.* **2012**, *74*, 189–198. [CrossRef]
51. Koffi, E.N.; Graham, C.E.; Mätzler, C. The water vapor flux above Switzerland and its role in the August 2005 extreme precipitation and flooding. *Meteorol. Z.* **2013**, *22*, 329–342. [CrossRef]
52. Graham, E.; Koffi, E.N.; Mätzler, C. An observational study of air and water vapor convergence over the Bernese Alps, Switzerland, during summertime and the development of isolated thunderstorms. *Meteorol. Z.* **2012**, *21*, 561–574. [CrossRef]
53. Wang, J.; Dai, A.; Carlson, D.J.; Ware, R.H.; Liljegren, J.C. *Diurnal Variation in Water Vapor and Liquid Water Profiles from a New Microwave Radiometer Profiler*; No. ANL/ER/CP-105344; Argonne National Lab.: Argonne, IL, USA, 2001. Available online: https://publications.anl.gov/anlpubs/2001/10/40826.pdf (accessed on 16 June 2022)
54. Priego, E.; Jones, J.; Porres, M.; Seco, A. Monitoring water vapor with GNSS during a heavy rainfall event in the Spanish Mediterranean area. *Geomat. Nat. Hazards Risk* **2017**, *8*, 282–294. [CrossRef]
55. Newton, I. *Opticks, or, a Treatise of the Reflections, Refractions, Inflections and Colours of Light*; Courier Corporation: Gloucester, MA, USA, 1952.
56. Avogadro, A. Essay on a manner of determining the relative masses of the elementary molecules of bodies, and the proportions in which they enter into these compounds. *J. Phys. (Paris)* **1811**, *73*, 58–76.
57. Mätzler, C. Ground-based observations of atmospheric radiation at 5, 10, 21, 35, and 94 GHz. *Radio Sci.* **1992**, *27*, 403–415. [CrossRef]
58. Hocke, K.; Bernet, L.; Hagen, J.; Murk, A.; Renker, M.; Mätzler, C. Diurnal cycle of short-term fluctuations of integrated water vapour above Switzerland. *Atmos. Chem. Phys.* **2019**, *19*, 12083–12090. [CrossRef]
59. Manandhar, S.; Dev, S.; Lee, Y.H.; Meng, Y.S.; Winkler, S. A data-driven approach for accurate rainfall prediction. *IEEE Trans. Geosci. Remote Sens.* **2019**, *57*, 9323–9331. [CrossRef]
60. Manandhar, S.; Lee, Y.H.; Meng, Y.S.; Yuan, F.; Ong, J.T. GPS-derived PWV for rainfall nowcasting in tropical region. *IEEE Trans. Geosci. Remote Sens.* **2018**, *56*, 4835–4844. [CrossRef]
61. Kim, D.K.; Suezawa, T.; Mega, T.; Kikuchi, H.; Yoshikawa, E.; Baron, P.; Ushio, T. Improving precipitation nowcasting using a three-dimensional convolutional neural network model from multi parameter phased array weather radar observations. *Atmos. Res.* **2021**, *262*, 105774. [CrossRef]

9 | INTER-RELATIONS OF PRECIPITATION, AEROSOLS, AND CLOUDS OVER SOUTHERN SPAIN

9.1 SUMMARY OF THE STUDY

Atmospheric aerosols serve as cloud condensation nuclei, affecting cloud cover and droplet size, which can intensify heavy rainfall and hinder weak precipitation such as drizzle (Alizadeh-Choobari and Gharaylou, 2017; Sarangi et al., 2017). Precipitation, in turn, affects aerosol concentration and size distribution through wet removal effects (Chang et al., 2016). Andalusia, located in southern Spain, has a Mediterranean climate characterized by hot, dry summers and warm, humid winters. The region suffers from intricate precipitation patterns due to Saharan dust intrusion and man-made pollution. However, studying the interrelationships of multiple factors, such as aerosols, clouds, and meteorological variables, with precipitation systems is challenging due to their complexity and high variability. This underscores the need for remote sensing and in-situ multi-instrument observations.

AGORA in Granada is a unique ACTRIS facility that includes state-of-the-art active and passive remote sensing and in-situ instruments for monitoring aerosols, clouds, and precipitation. The article presented in this chapter investigated the inter-relations of precipitation on the evolution of multiple atmospheric parameters using ground-based microwave radiometer HATPRO, ceilometer, cloud radar, nephelometer, and weather station. The HATPRO identified 684 available rain events over a 10-year period based on the physical retrieval method (Wang et al., 2021), and a SEA method was applied to develop a precipitation climatology. My study sheds light on the formation and evolution of clouds and precipitation in Andalusia by examining cloud heights. I analyzed changes in aerosol scattering and particle size before, during, and after rain to understand the mechanism of aerosol removal and its interaction with water droplets. Meteorological conditions conducive to the formation of virga were also observed.

This research is based on my two-month exchange and collaboration, supported by the IAP, as a guest researcher at the Andalusian Institute for Earth System Research (IISTA-CEAMA) at the University of Granada, Spain, from October to November 2022.

The following article was peer-reviewed and published in Atmospheric Chemistry and Physics in February 2024.

9.2 PUBLICATION

FULL CITATION

Wang Wenyue, Klemens Hocke, Leonardo Nania, Alberto Cazorla, Gloria Titos, Renaud Matthey, Lucas Alados-Arboledas, Agustín Millares, and Francisco Navas-Guzmán (2024). "Inter-relations of precipitation, aerosols, and clouds over Andalusia, southern Spain, revealed by the Andalusian Global ObseRvatory of the Atmosphere (AGORA)." In: *Atmospheric Chemistry and Physics* 24, pp. 1571–1585. https://doi.org/10.5194/acp-24-1571-2024.

Atmospheric
Chemistry
and Physics

Research article

Inter-relations of precipitation, aerosols, and clouds over Andalusia, southern Spain, revealed by the Andalusian Global ObseRvatory of the Atmosphere (AGORA)

Wenyue Wang[1,2], Klemens Hocke[1,2], Leonardo Nania[3], Alberto Cazorla[4,5], Gloria Titos[4,5],
Renaud Matthey[1,6], Lucas Alados-Arboledas[4,5], Agustín Millares[3,4], and Francisco Navas-Guzmán[4,5]

[1]Institute of Applied Physics, University of Bern, 3012 Bern, Switzerland
[2]Oeschger Centre for Climate Change Research, University of Bern, 3012 Bern, Switzerland
[3]Department of Structural Mechanics and Hydraulic Engineering, University of Granada, 18071 Granada, Spain
[4]Andalusian Institute for Earth System Research (IISTA-CEAMA), 18006 Granada, Spain
[5]Department of Applied Physics, University of Granada, 18071 Granada, Spain
[6]Federal Office of Meteorology and Climatology MeteoSwiss, 1530 Payerne, Switzerland

Correspondence: Wenyue Wang (wenyue.wang@unibe.ch)

Abstract. The south-central interior of Andalusia experiences intricate precipitation patterns as a result of its semi-arid Mediterranean climate and the impact of Saharan dust and human-made pollutants. The primary aim of this study is to monitor the inter-relations between various factors, such as aerosols, clouds, and meteorological variables, and precipitation systems in Granada using ground-based remote sensing and in situ instruments including a microwave radiometer, ceilometer, cloud radar, nephelometer, and weather station. Over an 11-year period, we detected rain events using a physical retrieval method that employed microwave radiometer measurements. A composite analysis was applied to them to construct a climatology of the temporal evolution of precipitation. It was found that convective rain is the dominant precipitation type in Granada, accounting for 68 % of the rain events. The height of the cloud base is mainly distributed at an altitude of 2 to 7 km. Integrated water vapor (IWV) and integrated cloud liquid water (ILW) increase rapidly before the onset of rain. Aerosol scattering at the surface level and hence the aerosol concentration are reduced during rain, and the predominant mean size distribution of aerosol particles before, during, and after rain is almost the same. A meteorological environment favorable for virga formation is observed in Granada. The surface weather station detected rainfall later than the microwave radiometer, indicating virga according to ceilometer and cloud radar data. We used 889 rain-day events identified by weather station data to determine precipitation intensity classes and found that light rain is the main precipitation intensity class in Granada, accounting for 72 % of the rain-day events. This can be a result of the high tropospheric temperature induced by the Andalusian climate and the reduction of cloud droplet size by the high availability of aerosol particles in the urban atmosphere. This study provides evidence that aerosols, clouds, and meteorological variables have a combined impact on precipitation which can be considered for water resource management and improving rain forecasting accuracy.

1 Introduction

Precipitation is vital for human survival and development as it affects the storage and distribution of water resources (Wilheit et al., 1977). Continuous and heavy rainfall is often a trigger for natural disasters such as floods (Hong et al., 2007). Precipitation as a driver of the hydrological cycle has great significance for climate change responses and feedbacks (Kundzewicz, 2008). Aerosols in atmosphere can act as cloud condensation nuclei. The presence of a high concentration of aerosols might increase cloud cover and decrease the size of cloud droplets (Sarangi et al., 2017; Kant et al., 2021). For heavy precipitation events such as torrential rain, aerosols promote the merging of cloud droplets and the growth of raindrops, increasing the intensity and distribution of precipitation (Hazra et al., 2017). However, for weak precipitation events such as drizzle, aerosols hinder precipitation formation (Alizadeh-Choobari and Gharaylou, 2017). Chemical reactions and turbulence within clouds as well as the washing effect of precipitation in turn might affect the concentration and size distribution of aerosols (Hobbs, 1993; Chang et al., 2016; Zheng et al., 2019). The interaction among precipitation, aerosols, and clouds is highly complex and still contains many uncertainties, requiring further research and exploration (Fan et al., 2016).

The inland regions of south-central Andalusia, such as Granada, are semi-arid with average annual precipitation of less than 500 mm and are highly vulnerable to extreme hydrological events due to climate change (AEMET, 2012; Sumner et al., 2003). A decreasing trend in precipitation for the period 1960–2006 has been observed in the Andalusia area of the Spanish Mediterranean (Ruiz Sinoga et al., 2011). Moreover, this region, like the rest of the Mediterranean region, is also prone to flooding from heavy rains, causing property damage and even casualties (Barriendos et al., 2019; Flores et al., 2022; Belmonte and Beltrán, 2001). On the other hand, the region of Granada experiences numerous Saharan dust outbreaks every year, which have a significant impact on its environment and air quality (Guerrero-Rascado et al., 2009; Navas-Guzmán et al., 2013; Cazorla et al., 2017; López-Cayuela et al., 2023; Fernández et al., 2019). Rosenfeld et al. (2008) indicated that aerosols affect precipitation and prompt droughts and floods. Understanding the temporal evolution of atmospheric variables during rain events under these conditions is significant for weather forecasting and assessing measures of artificially increased rainfall.

Deep convection contributes to the occurrence of heavy rainfall events (Luu et al., 2022), and aerosols (Saharan dust) can promote the formation of convective clouds and convective rain (Jiang et al., 2018; Gibbons et al., 2018; Khain et al., 2005; Zhao et al., 2022; Xiao et al., 2023; Chen et al., 2020). Jiang et al. (2018) discovered that various types and concentrations of aerosols have distinct impacts on deep convective clouds. Continentally polluted aerosols tend to enhance convection, while the effect of dust particles varies depending

on the region. Employing a spectral bin microphysics model, Gibbons et al. (2018) observed that an increase in Saharan dust particles leads to competition for available water vapor during diffusive growth, resulting in the formation of numerous and smaller crystals and/or droplets. This leads to the release of more latent heat and promotes convective updrafts and heterogeneous nucleation mechanisms at higher altitudes. As the concentration of ice nuclei increases, there is a proportional decrease in total surface precipitation. Khain et al. (2005) indicated that aerosols reduce precipitation efficiency of individual cumulus clouds, resulting in the formation of convective clouds and thunderstorms with higher rain rates. Chen et al. (2020) found that aerosols prompt the formation of stronger updrafts to form mesoscale convective systems that enhance vertical mass fluxes and precipitation. As the concentration of aerosols rises, the frequency of deep convective clouds increases, while the frequency of shallow warm clouds decreases.

The inter-relations between precipitation, aerosols, and clouds are highly dependent on meteorological conditions (Zhu et al., 2023). The overall impact of aerosols on precipitation is contingent upon environmental conditions, such as air humidity and wind shear, which determine whether the increase in aerosols leads to an elevation in condensation production or loss (Khain, 2009). In addition, the formation of virga is influenced by meteorological factors, including cloud height, temperature, humidity, air pressure, wind speed, and air stability. Karle et al. (2023) used ceilometer profiles, soundings, surface rain gauges, and radar data to identify the seasonal patterns of virga events and assess the influence of surface meteorological measurements. Virga formation is more likely to occur when the cloud base is high, air temperature is elevated, humidity is low, air pressure is low, wind speed is high, and air instability is present, with small raindrops also playing a role (Jullien et al., 2020; Beynon and Hocke, 2022; Airey et al., 2021). Virga is linked not only to severe climatic events like drought, but also to aerosol loads. The average cloud-base temperature of virga is below $0\,°C$, which results in effective loss of sublimation and reduced surface precipitation (Evans et al., 2011). Water vapor that is produced during evaporation or sublimation of virga can be scavenged by aerosol particles (Tost et al., 2006). The virga, which does not reach the ground, is missed in in situ precipitation observations on the surface.

Observational studies of the inter-relations of multiple factors with precipitation systems are challenging due to their complexity and high variability. Aircraft observations have proven effective in studying aerosol and cloud microphysics near cloud bases and their impact on precipitation (Wehbe et al., 2021), but the technique is expensive, and the number of measurements of this type is very limited, leading to poor representativeness. Ground-based remote sensing and in situ techniques are suitable alternatives with promising results. Various instruments, such as microwave radiometers, ceilometers, Doppler cloud radars, integrating nephelome-

ters, and weather stations, are widely utilized to measure and characterize precipitation, aerosols, and clouds with high temporal resolution. Ground-based microwave radiometers have the advantage of being able to measure vertically integrated atmospheric column (integrated water vapor and integrated liquid water) and rain rate all day and in all weather (Rose et al., 2005; Wang et al., 2021; Hocke et al., 2019). Vertical profiles from ceilometers and Doppler cloud radars make it possible to study atmospheric dynamics, the formation and evolution of clouds at different altitudes, precipitation types, and the impact of dust aerosols in detail (Airey et al., 2021). Sarna and Russchenberg (2016) showed that the interaction between aerosols and clouds can be efficiently and continuously monitored by leveraging the synergy of lidar, radar, and radiometers.

The following are the contributions and benefits of this study, which fill the gaps of previous studies.

- *The Andalusian region with a semi-arid Mediterranean climate as the study area*. The region is influenced by Saharan dust and is highly vulnerable to climate change, resulting in complex precipitation patterns. Nevertheless, there is a shortage of research on the relationship between precipitation and atmospheric variables in regions with similar conditions, such as the Mediterranean.

- *Synergy of cloud radar and other remote sensing instruments*. While lidar remote sensing has limitations in the observation of clouds, cloud radar can penetrate clouds to observe the internal structure of clouds and precipitation with exceptional time and vertical resolution. Cloud radar combined with aerosol lidar can significantly enhance the precision and accuracy of precipitation studies.

- *Cloud evolution during rain events*. Presenting the evolution and height changes of clouds before, during, and after rain can determine the mechanism and type of precipitation.

- *Detection and observation of virga*. Virga can cause inaccuracies in weather forecasts in Andalusia.

The goal of this paper is to explore the inter-relations of multiple atmospheric variables with the precipitation system using multisource ground-based observations in the Andalusian region. This paper is organized as follows. Section 2 describes the study area, remote sensing, and in situ instruments. Section 3 presents the methods used for rain rate retrieval and data analysis. Section 4 discusses the temporal evolution of precipitation, the impact of multiple factors (including aerosols, clouds, water vapor, and meteorological variables) on precipitation systems, and the phenomenon of virga rain. Conclusions are given in Sect. 5.

2 Study site description and instrumentation

2.1 Study area

Granada is located in Andalusia in southern Spain. It is surrounded by mountain ranges, including the Sierra Nevada to the southeast, Sierra de Huétor to the northeast, and Sierra de Almijara to the southwest. Differences exist between the climate inside and around the metropolitan area due to the blocking of mountains (Esteban-Parra et al., 2022). Granada is close to the Mediterranean Sea, and the region exhibits a Mediterranean climate with hot and dry summers. Winters are mild and humid, and snow is rare. The hottest month is July, with an average maximum temperature of 34.2 °C, while the coldest month is January, with an average daily temperature of 12.6 °C (AEMET, 2012). Rainfall mainly occurs from October to May. Granada is a non-industrial city with fewer than 230 000 inhabitants and sits in a depression as a plain. The city is affected by local and European human-made pollution, as well as natural dust from the Sahara in northern Africa (Valenzuela et al., 2012; Navas-Guzmán et al., 2013; Cazorla et al., 2017). These factors contribute to the complex meteorological characteristics of Granada, particularly with regards to precipitation.

Measurements presented in this study were performed at the University of Granada urban station (UGR), which is part of the Andalusian Global ObseRvatory of the Atmosphere (AGORA, https://atmosphere.ugr.es/en/about/presentation/agora, last access: 13 December 2022). The station is located in the Andalusian Institute of Earth System Research (IISTA-CEAMA) in the southern part of the city of Granada (37.16, 3.61° N; 680 m a.s.l.). AGORA combines state-of-the-art active and passive remote sensing and in situ measurements (Benavent-Oltra et al., 2021; Titos et al., 2012). Most of its instruments are part of the Aerosols, Clouds, and Trace gases Research Infrastructure of the European Research Infrastructure Consortium (ACTRIS-ERIC, https://www.actris.eu/, last access: 13 December 2022).

2.2 Remote sensing measurements

Tropospheric microwave observations were performed using a generation-2 Humidity And Temperature PROfiler (HATPRO-G2) radiometer from Radiometer Physics GmbH (RPG). This instrument performs continuous and automated measurements of the brightness temperature of the sky, with a radiometric resolution between 0.3 and 0.4 K in terms of root mean square error at 1.0 s integration time (Navas-Guzmán et al., 2014). The radiometer employs direct detection receivers in two bands: the water vapor band (K-band) from 22 to 31 GHz and the oxygen band (V-band) from 51 to 58 GHz, with bandwidths between 0.1 and 2 GHz. The half-power beamwidth for the K-band is 3.5° (Rose et al., 2005). A quadratic regression is used to retrieve integrated water vapor (IWV) and integrated cloud liquid water (ILW), among

other products. Weather sensors on the HATPRO provide some of the inputs to the retrieval process, such as environmental temperature, relative humidity, and pressure (RPG, 2014). The instrument has an additional infrared radiometer for obtaining cloud-base brightness temperature. It is part of the MWRnet (International Network of Ground-based Microwave Radiometers, http://cetemps.aquila.infn.it/mwrnet/, last access: 13 December 2022), and several studies have shown its capability to retrieve IWV, temperature profiles, and relative humidity profiles by comparing with radiosondes (Navas-Guzmán et al., 2014; Bedoya-Velásquez et al., 2019; Vaquero-Martínez et al., 2023).

The Jenoptik CHM15k ceilometer has measured atmospheric backscatter profiles with a time resolution of 15 s since November 2012. It is part of E-PROFILE (European networks of wind and aerosols profiles, https://e-profile.eu/, last access: 13 December 2022). The system uses an Nd:YAG narrow-beam microchip laser that operates at 1064 nm and generates pulses of 8.4 μJ at a repetition rate between 5 and 7 kHz. The receiver field of view is 0.45 mrad, and the laser beam has a divergence of less than 0.3 mrad. The system can measure vertically over ranges from 15 to 15 000 m with a resolution of 15 m. Full overlap of the laser beam and the telescope is realized at 1500 m above the ceilometer, while 90 % overlap can be achieved between 555 and 885 m a.g.l. using the manufacturer's overlap function calibration. Cazorla et al. (2017) described the calculation of the range-corrected signal (RCS) for the CHM15k.

The 94 GHz Doppler cloud radar used in this study was manufactured by RPG based on the frequency modulation continuous-wave technique. It measures the vertical profile of reflectivity with a time resolution of 3–4 s, and ACTRIS-Cloudnet (Illingworth et al., 2007, https://cloudnet.fmi.fi/, last access: 13 December 2022) provides its target classification (Hogan and O'Connor, 2004). The cloud radar operates at a wavelength of 3.19 mm, allowing high-sensitivity detection of clouds and raindrops. It points to zenith, covering a range between 50 and 12 000 m at a resolution 30 m. It includes accurate absolute calibration and a robust rain protection system. Use of low transmitter power (1.5 W) enables reliable operation and low maintenance. Myagkov and Rose (2016) described the instrument in more detail.

2.3   In situ measurements

The UGR weather station has measured air temperature, relative humidity, wind speed, pressure, and precipitation with a time resolution of 1 min since 2005. A Vaisala HMP60 probe gathers temperature and relative humidity, and a Campbell Scientific model 05103 anemometer monitors wind speed (de Arruda Moreira et al., 2022). The UGR weather station barometer has low accuracy (1 hPa), so the pressure in this study is only utilized for air density calculations and not for composite analysis. A rain sensor at the weather station can provide precipitation data for 2020 to 2022 with an accuracy

of 0.1 mm. Another rain sensor on the roof of the building covers the entire analysis period of 2010–2022 with an accuracy of 0.2 mm. The two rain sensors show good agreement during the overlap from 2020 to 2022. Air density was derived from weather station data following Wang and Hocke (2022).

Aerosol in situ measurements are registered in AGORA, which in addition to its contribution to ACTRIS also operates in the framework of the NOAA/ESRL federated aerosol network (Andrews et al., 2019) and has participated in global analysis of climate-relevant aerosol properties (Laj et al., 2020). The TSI model 3563 integrating nephelometer measures the light-scattering coefficient of particles at three wavelengths (450, 550, and 700 nm) at dry conditions with relative humidity less than 40 %. The data have been recorded at a time resolution of 1 min since January 2006 (Titos et al., 2012). The scattering coefficient obtained from the nephelometer could be used as a proxy for aerosol mass or volume concentration, while the Ångström exponent (AE) provides an estimation of the predominant aerosol mean size at dry conditions. Values of AE > 2 indicate a predominance of fine particles, while values of AE < 1 indicate the predominance of coarse particles. The total wide angular integration is from 7 to 170°, and the backscattering has an angular range of 90 to 170°. Temperature and pressure are measured to calculate the scattering of air molecules. This value is subtracted from the total scattering to isolate the scattering attributed to aerosol particles (Lyamani et al., 2010). Routine maintenance and calibration of the nephelometer are carried out periodically using CO_2 and filtered air. Non-idealities due to truncation errors and non-Lambertian illumination were corrected following the procedure described in Anderson and Ogren (1998). The uncertainty in the scattering coefficient is about 7 % (Heintzenberg et al., 2006). A complete description of the procedures applied in data preprocessing and processing is included in Pandolfi et al. (2018).

3   Methodology

3.1   Rain rate retrieval

The HATPRO software does not cover the retrieval of rain rates, so this study uses an opacity-based physical retrieval method to calculate rain rates. Wang et al. (2021) presented the principle of this retrieval method in detail, and a brief description is given below. The radiative transfer equation for the Rayleigh–Jeans law is

$$T_{b_f} = T_{bC} \cdot e^{-\tau_f/\mu} + T_{m_f} \cdot (1 - e^{-\tau_f/\mu}), \tag{1}$$

where f is the microwave channel of HATPRO. The 31 GHz channel is used to estimate rain rates in this study due to its sensitivity to liquid water. T_{b_f} is the non-rainfall brightness temperature, τ_f is the non-rainfall opacity along the zenith, μ is the cosine of the zenith angle, T_{bC} is the cosmic background brightness temperature, and T_{m_f} is the effective mean

temperature calculated by the linear equation of temperature, pressure, and relative humidity measured by HATPRO's weather sensors (Mätzler and Morland, 2009).

Equation (1) yields the zenith opacity as

$$\tau_f = -\mu \cdot \ln\left(\frac{T_{m_f} - T_{b_f}}{T_{m_f} - T_{bC}}\right). \tag{2}$$

During rain, the zenith opacity τ_{rf} can be computed iteratively:

$$\tau_{rf}^{(k+1)} = -\mu \cdot \ln\left(\frac{T_{m_{rf}}(\tau_{rf}^{(k)}) - T_{b_{rf}}}{T_{m_{rf}}(\tau_{rf}^{(k)}) - T_{b_f}}\right), \tag{3}$$

where $\tau_{rf}^{(k+1)}$ is the rain zenith opacity obtained after the kth iteration. $T_{m_{rf}}$ is the rain effective mean temperature. $T_{b_{rf}}$ is the rain brightness temperature observed by HATPRO. Note that T_{b_f} cannot be observed during rain. It has to be estimated by temporal interpolation of the opacity obtained during periods of no rain.

The relationship between rain rate R_f and rain zenith opacity τ_{rf} is expressed as

$$R_f = \frac{\tau_{rf}}{g_{rf} \cdot H_r}, \tag{4}$$

where g_{rf} is the specific and effective rain-absorption coefficient. It is calculated by Mie theory with droplet distributions and parameterized fall velocities. H_r is the vertical distance between the melting layer and the ground, which is calculated by the temperature gradient. Note that determination of rain stop time may be delayed by the outdoor HATPRO due to the water film on the radome (Wang et al., 2023).

3.2 Composite analysis

The composite analysis method (superposed epoch method) is a useful technique for characterizing meteorological or climatic phenomena that are difficult to observe as a whole, such as exploring and understanding the inter-relations between rainfall and atmospheric variables over time (Adams et al., 2013; Zhang et al., 2020; Sapucci et al., 2019; Allan et al., 2020). Composite analysis consists of two separate datasets of discrete events (e.g., rain events) and continuous time series. A two-dimensional matrix is constructed by intercepting part of the time series that may be affected by the event. The columns of the matrix are time epochs, the rows are events, and the arithmetic mean is computed over the columns. All selected events are expressed as a function of their epoch time so that the averaging process yields the mean evolution of a parameter before, during, and after rain. This method can highlight the impact of events on various atmospheric variables at critical moments and weaken the impact of atmospheric noise (Zheng et al., 2019). The following criteria are used for composite analysis of rain events.

- The timing mark of the onset and duration of rainfall is when ILW (measured by the HATPRO) exceeds 0.6 mm. The threshold for detecting rainfall using ILW typically ranges between 0.1 and 0.6 mm. When raindrops larger than 0.3 mm in diameter are present in the atmosphere, the emissivity increases significantly, making the accuracy of the threshold less critical (Wang and Hocke, 2022). Wang et al. (2023) showed that an ILW of 0.6 mm is suitable for the outdoor HATPRO G2 to identify rain, which obtains non-rainfall opacities that agree well with an indoor microwave radiometer. In addition, HATPRO in Granada detects rain event start and end times using ILW $= 0.6$ mm (a rain period has ILW $>= 0.6$ mm), which aligns with ceilometer attenuated backscatter.

- The epoch time 0 represents the onset of rain, and t represents the duration of rain. -1, $+1$, and $t+1$ represent 1 h before, during, and after rain, respectively.

- All compliant rain events were filtered using the HATPRO ILW threshold of no rainfall within 8 h before the onset of rain and 8 h after the end of rain for the period October 2010 to November 2021. A total of 22 % of data are missing during this time interval for reasons such as unexpected shutdown of HATPRO. There are, in total, 694 rain events, including 502 rain events for studying 8 h before and 16 h after rain, 615 rain events for studying 8 h before and 16 h during rain, and 390 rain events (from November 2012 to November 2021) for the composite analysis of ceilometer data before and after rain. The 8 h before rain can detect the water vapor convection (Adams et al., 2013), and the 16 h after rain is to have enough time to detect the effect on the atmosphere and ensure a certain number of rain events. Note that the 16 h during rain ($+16$) indicates only one rain event included within 16 h after the onset of rain and not the duration of the rain event itself.

4 Results and discussion

4.1 Inter-relations of precipitation with cloud, water vapor, and aerosols

March 2022 was one of wettest months in 61 years in Spain, with heavy rainfall causing flooding in parts of Andalusian. Because of this, March 2022 is used here as an example of the potential of the instrumentation to detect and characterize rain events and their impact on aerosols. Figure 1 provides an example of the vertical distribution of aerosols, clouds, and rainfall, as obtained from ceilometer and cloud radar measurements over 3 consecutive days from 12 to 14 March 2022. The ceilometer determines cloud bases and thin clouds as shown in Fig. 1a, while the cloud radar can give a full view of clouds as shown in Fig. 1b. Two cumulonimbus clouds with an anvil-shaped top can be seen up to 11 km

height, which is often accompanied by severe weather such as heavy torrential rain and hail. Cloud bases are from 2 to 7 km. The thickness of the clouds reaches about 9 km, indicating deep convection. The clouds at a height of 3 to 5 km are stratocumulus clouds from about 07:30 to 12:00 UT on 14 March 2022, while the ceilometer signal is mostly fully attenuated above 1 km. Figure 1c shows the cloud radar target classification from ACTRIS-Cloudnet. It can be seen from Fig. 1a that the high attenuated backscatter values (more than $4 \times 10^{-6} \, \mathrm{m^{-1} \, sr^{-1}}$) from clouds measured by the ceilometer correspond to rainfall according to Cloudnet target classification (Fig. 1c). The height of the melting layer ($0\,°\mathrm{C}$ level) here is between 2 and 3 km. A layer of attenuated backscatter (less than $1 \times 10^{-6} \, \mathrm{m^{-1} \, sr^{-1}}$) from 1 to 2 km before and after rain is due to aerosols. Solar background light affects the ceilometer signal during daytime (i.e., 06:00 to 18:00 UT).

Due to limited data from the cloud radar, which only cover a small number of rain events since March 2019, this study relies on the composite analysis of the ceilometer. Figure 2 shows the composite analysis of ceilometer attenuated backscatter before and after 390 rain events. To show the cloud-base distribution more clearly, the height and time resolutions are reduced from 15 m and 15 s to 60 m and 900 s, respectively, by computing the average value. Cloud-base height is mainly distributed from 2 to 7 km during the 8 h before rain and around 2 to 3 km during the 6 h after rain. This result closely resembles that of Fig. 1. Statistics from ceilometer data reveal that the predominant precipitation type in Granada is convective rain, comprising 68 % of the 390 recorded rain events.

The likely reason for this pattern of mostly convective rain in Granada is firstly due to the topography and climate of Granada. Granada is surrounded by mountains, so humid air from the Atlantic via the north-northwest is forced to rise to higher altitudes to form convection. The high temperature in Granada also contributes to the upward lifting of the air. Secondly, aerosols have the ability to enhance the creation of convective rain (Jiang et al., 2018). Aerosols increase the quantity of cloud droplets or ice crystals and slow down their growth rate. This causes the deposition process to release more latent heat and triggers heterogeneous nucleation mechanisms at higher altitudes, which as a result promotes convection and has an impact on its development (Gibbons et al., 2018). Figure 2 also indicates that the intensity of the attenuated backscatter, which is proportional to the aerosol concentration, is lower in the lower troposphere (below 1.8 km a.g.l.) after rain compared to before rain (black box). This is because rainfall is effective in removing aerosols, as explained in more detail below.

Figure 3 shows the composites of IWV and ILW from the HATPRO radiometer in Granada. As shown in Fig. 3a, IWV remains around 17.5 mm during the 6 to 8 h before rain but increases rapidly to a maximum value of 23 mm during the 0 to 6 h before rain. Water vapor convection may be responsible for the increase in IWV before rain. Water vapor mov-

ing up at low pressure or along a front, collecting around highly hygroscopic condensation nuclei, causes increased IWV (Koffi et al., 2013). IWV drops sharply and remains at around 16 mm during the 8 to 16 h after rain. The changes in IWV in Granada are slightly different from those observed in Bern, Switzerland (Wang et al., 2021). There is more water vapor in the atmosphere to form rain in Granada than in Bern. The composite maximum of IWV at the onset of rain in Bern was 21.5 mm, about 1.5 mm lower than in Granada. This provides plenty of vertically rising moist air for convection in Granada. In addition, IWV in Bern is significantly reduced at the end of rain compared to the beginning, which is not the case for Granada. This may be due to the different precipitation types in Granada, whereas Bern has mainly stratiform rain (Wang and Hocke, 2022). Rain events in Bern are more likely to directly remove water vapor from the atmosphere. Figure 3b shows the IWV and the infrared brightness temperature before and during rain. We can see that IWV remains 28 mm during the 4 h after the onset of rain and then decreases. This may suggest that horizontal transport effects play a major role for water vapor in Granada. It may also be that short-duration rainfall accounts for a relatively large proportion of all rain events, with short-duration rainfall of less than 8 h accounting for 57 % in Granada but only 41 % in Bern. The infrared brightness temperature (TIR) reaches its maximum before the onset of rain and then decreases. As shown in Fig. 3c, ILW is from 0.04 to 0.54 mm during the 2 h before rain with a decrease to 0.03 mm during the 2 h after rain. The sharp increase in ILW is because of the opacity gain as the droplet size (diameter) increases (Wang and Hocke, 2022). The ILW composite peaks at 0.54 mm instead of the ILW threshold of 0.6 mm due to the high temporal resolution of HATPRO. The value is 0.6 mm when calculating the composite median.

Figure 4 shows the composites of scattering coefficient at 550 nm and AE of aerosol particles from the integrating nephelometer in Granada. As shown in Fig. 4a, the scattering coefficient before rain increases by $2 \, \mathrm{mm^{-1}}$ from about $51 \, \mathrm{mm^{-1}}$ and then decreases. In Granada, the scattering coefficient at 550 nm peaks between 08:00 and 12:00 UT in the morning as well as between 18:00 and 22:00 UT in the evening due to intense urban emissions (Lyamani et al., 2010). As shown in Fig. 5, rain events mainly start to occur from 12:00 to 18:00 UT in the afternoon. Because of insolation, there is convection of moist air during daytime. In the afternoon hours, the moist air has reached a high altitude so that formation of cloud droplets and raindrops occurs in the adiabatically cooled air parcel. It also illustrates that the diurnal variation pattern of aerosols is not the main cause of the significant increase in scattering coefficient 4 h prior to the onset of rain. The scattering coefficient increases gradually after rain. Due to the removal of aerosols by rain, the scattering coefficient at the end of rain is about $10 \, \mathrm{mm^{-1}}$ lower than at the beginning. To the same effect, the scattering coefficient experiences a rapid decrease of $6 \, \mathrm{mm^{-1}}$ from approx-
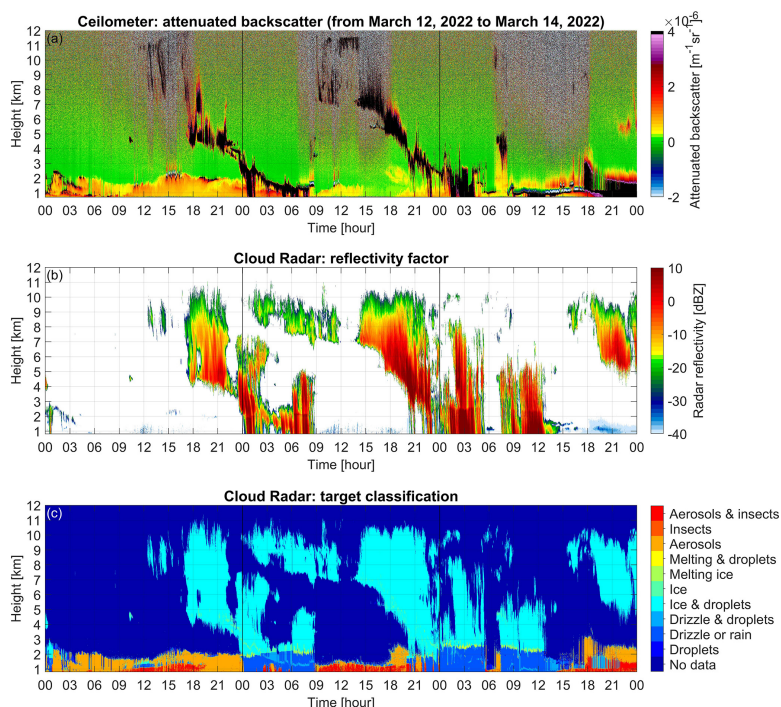
Figure 1. (a) Attenuated backscatter measured by a CHM15k ceilometer, **(b)** reflectivity measured by an RPG Doppler cloud radar, and **(c)** the radar target classification in Granada for 12–14 March 2022. Height is above sea level.
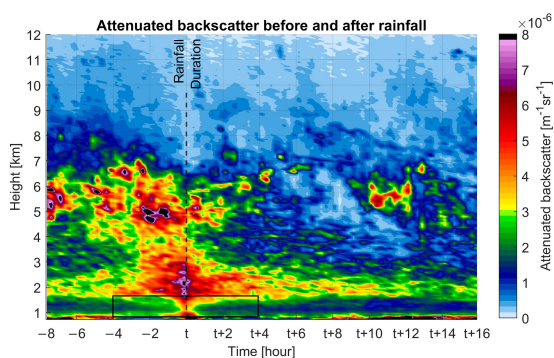

Figure 2. Composite of attenuated backscatter measured by a CHM15k ceilometer 8 h before and 16 h after rain. t is the duration of rain. -1 and $t+1$ represent 1 h before and after rain, respectively. The range of the black box is below 1.8 km, 4 h before and after rain. Altitude and time resolutions are 60 m and 900 s, respectively.

imately $48\,\mathrm{mm}^{-1}$ during the 4 h rain, followed by a slower decline, and stabilizes at 38 to $42\,\mathrm{mm}^{-1}$ (Fig. 4b). As shown in Fig. 4c and d, the AE first decreases by about 0.03 from 1.5 before rain, then increases during the 4 h rain period, and remains at about 1.51. It increases gradually to 1.58 after rain.

Figure 6 shows a schematic representation of the temporal evolution of aerosol scattering and particle size before, during, and after rain, which makes the variation of scattering coefficient and AE in Fig. 4 easy to understand. Before rain, the aerosol concentration first increases and then decreases. This is because the lower relative humidity in the atmosphere before rain increases the surface tension of aerosol particles and makes them easier to suspend in the air. Figure 7 shows the change in relative humidity. Air movement may also bring aerosols from other regions, leading to their increase. Water vapor may condense on certain aerosol particles prior to rainfall, gradually accumulating on their surfaces. After the onset of rain, most aerosol particles are trapped in raindrops and the larger ones settle. Very few larger-sized aerosol particles without a water film are also removed from the atmosphere. Smaller particles, due to their low mass, remain suspended in the air and are not easily removed by rain. As time progresses, larger particles account for a smaller proportion of the remaining particles. After rain, pollution can
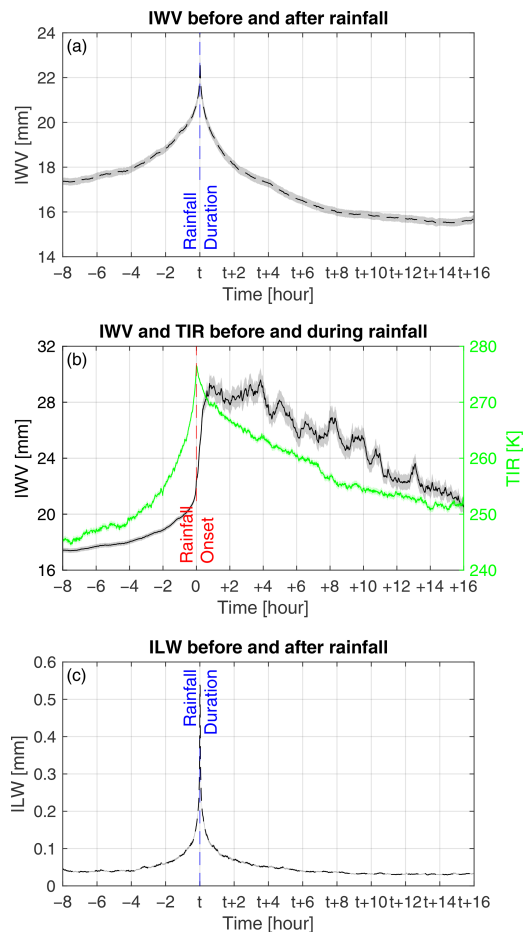
Figure 3. Composites of **(a)** IWV 8 h before and 16 h after rain, **(b)** IWV and TIR (green line) 8 h before and 16 h during rain, and **(c)** ILW 8 h before and 16 h after rain provide by HATPRO in Granada. The shaded areas show standard errors (errors of the mean $\sigma/\sqrt{n}$).

cause an increase in aerosol concentration. Since AE hardly changes during rain events as shown in Fig. 4c and d, the predominant mean size distribution of aerosol particles before, during, and after rain is almost the same. Note that the lack of change in AE from the nephelometer data does not necessarily indicate that the particle size remains constant. In ambient conditions, particles can undergo hygroscopic growth by absorbing water, which would increase their size but may not be detectable by the instrument. Conversely, the data from the nephelometer indicate that the size of "dry" particles does change, which may suggest that they have the same particle type.
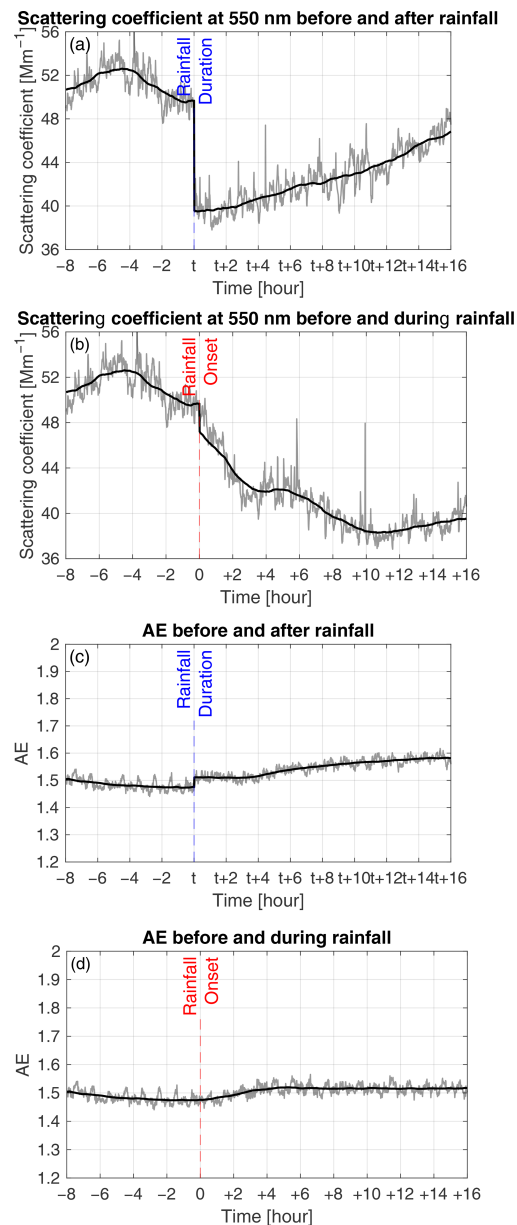
Figure 4. Composites of **(a)** scattering coefficient (grey) 8 h before and 16 h after rain, **(b)** scattering coefficient (grey) 8 h before and 16 h during rain, **(c)** AE (grey) 8 h before and 16 h after rain, and **(d)** AE (grey) 8 h before and 16 h during rain provided by an integrating nephelometer in Granada. t is the duration of rain. 0 is the onset of rain. -1, $+1$, and $t+1$ represent 1 h before, during, and after rain, respectively. The black lines are the mean value calculated over a sliding window of 3 h.
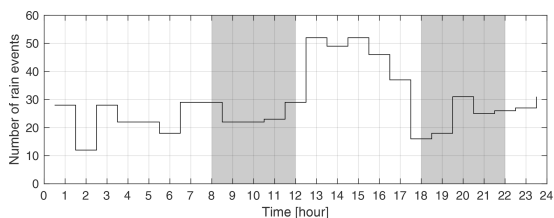
Figure 5. Stairs plot of the distribution of the number of rain events (694 in total). The grey areas represent the peak time period of the scattering coefficient at 550 nm between 08:00 and 12:00 UT and between 18:00 and 22:00 UT.

4.2 Meteorological effects and virga

Figure 7 shows the composites of surface meteorological variables before and during 615 rain events in Granada. As shown in Fig. 7a, from 4 to 8 h before rain, the ground heating from the sun causes the temperature to rise, and air thus warms and expands, reducing the relative humidity. From 0 to 4 h before rain, as convective clouds form and rise, the air cools and the surface temperature decreases, increasing relative humidity. Evaporation of surface water increases water vapor content without reaching saturation, which also increases relative humidity. When rain starts, rain droplets falling to the ground in Granada increase the water vapor content, leading to a sudden 1.6 % increase in relative humidity and a slight decrease in surface temperature. After the onset of rain, rain absorbs a large amount of latent heat, resulting in a continuous drop in temperature by 1.3 °C during the 12 h of rain and then an increase in temperature. Rainfall carries away some of the water vapor and slows down the evaporation rate of water, resulting in a decrease of about 2.4 % in relative humidity during the 2 h of rain. There is a slight increase in relative humidity over the next 10 h and then a large decrease in relative humidity. As shown in Fig. 7b, before rain, the pressure decreases by 0.9 hPa due to the lifting of air. When it rains, the sudden pressure increase of 0.4 hPa can be due to the water vapor pressure generated by the evaporation of rain droplets. This value is maintained for a duration of 4 h. From 4 to 9 h after the onset of rain, the pressure continues to rise by 0.3 hPa and subsequently decreases. Before rain, the wind speed increases by about 0.3 m s^{-1}. The pressure gradient between the updraft of the convective system and the stronger downdraft around it produces stronger wind speeds. During the 5 h of rain, the wind speed is reduced by the drag force of raindrops on the air and subsequently remains around 1.4 m s^{-1}. As shown in Fig. 7c, when rain starts, the rain rate increases rapidly. It peaks at 0.6 mm s^{-1} 4 h after the onset of rain and then slowly decreases to 0.2 mm s^{-1}.

Figure 7d shows composite of air density before and during 615 rain events in Granada. Before rain, air density first decreases and then increases. At 4 h prior to the onset of rain,
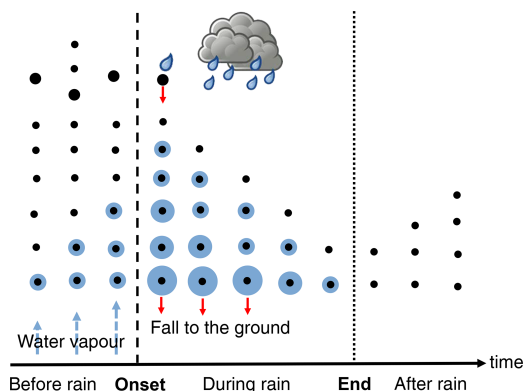
Figure 6. Schematic diagram of the temporal evolution of aerosols before, during, and after rain. The dashed line indicates the onset of rainfall, while the dotted line marks its end. The black dots represents aerosol particles, and the blue area represents the water film. The dashed blue arrow represents water vapor, and the red arrow represents particles falling to the ground.

the air density reaches its minimum value of 1.124 kg m^{-3}. During 12 h after the onset of rain, the air density continues to rise from 1.126 to 1.134 kg m^{-3} and subsequently decreases. Changes in air density before rain can be a rainfall precursor and has the potential for nowcasting (Wang and Hocke, 2022). More water vapor in the air leads to a decrease in air density due to the lower molecular weight of water vapor compared to the average molecular weight of other gases in the air. Unlike in Bern, the air density in Granada is more dependent on surface temperature (Fig. 7a). The changes in these two variables are exactly opposite to each other. Thus, at Granada, the increased surface temperature before rainfall can be taken as a precursor of rainfall too. Overall, this meteorological environment before rain is conducive to the formation of virga.

Although the number of rain events in Granada detected by HATPRO is not small, the amount of rain received by the surface is small. Virga could be the cause. HATPRO, the ceilometer, and cloud radar can detect raindrops in the atmosphere, while the rain sensor at the weather station measures the rain falling on the ground. Figure 8 shows ceilometer attenuated backscatter and cloud radar target classification for 19 April 2020 and 19 June 2021, which can reveal cloud and rain information. The time of rain event onset is marked with HATPRO and the weather station. As shown in Fig. 8a and b, stratocumulus clouds between 2 and 5 km produce stratiform rain. The onset of the rain detected by HATPRO is 07:24 UT. This time is consistent with the cloud radar target classification. The surface weather station measured the start of rain at 17:12 UT. There is a 10 h time discrepancy between these instruments in detecting the onset of rain, which could be attributed to the rapid absorption of
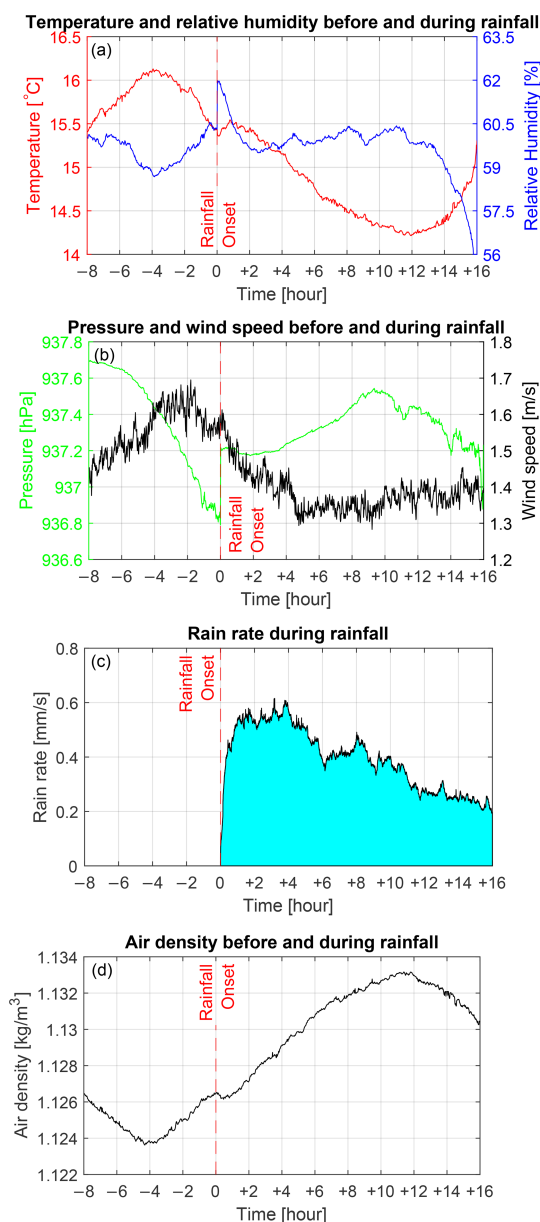
Figure 7. Composites of **(a)** temperature (red line) measured by the weather station, relative humidity (blue line) measured by the weather station, **(b)** pressure (green line) measured by the HATPRO weather sensor, wind speed (black line) measured by the weather station, and **(c)** rain rate (black line) retrieved from HATPRO 8 h before and 16 h during rain in Granada. 0 is the onset of rain. -1 and $+1$ represent 1 h before and during rain, respectively.

moisture by the dry air in Granada. Raindrops falling through the dry air may evaporate before reaching the ground, leading to the formation of virga. Unlike cloud radar, almost no rain can be seen from ceilometer attenuated backscatter at 07:00 and 09:00 UT. Cloud radar is more sensitive in detecting rain as it can detect smaller raindrops that gradually evaporate and lose water. These smaller raindrops may not be accurately captured by the ceilometer. As shown in Fig. 8c and d, cumulonimbus clouds between 3 and 11 km produce convective rain. The onset of the rain detected by HATPRO is 02:40 UT. This time is consistent with the ceilometer attenuated backscatter and cloud radar target classification. The weather station indicated that it began to rain at 17:15 UT, and the rain lasted only 10 min on the ground.

Figure 8e and f show ceilometer attenuated backscatter and cloud radar reflectivity factor on 31 May 2020. Cumulonimbus clouds between 3 and 11.5 km produce convective rain. The onset of the rain detected by HATPRO is 13:47 UT. This time is consistent with the ceilometer attenuated backscatter and cloud radar target classification. The surface weather station measured the start of rain at 16:29 UT. As shown in Fig. 8e, the virga only lasted a brief period during both 14:00 and 15:00 UT, while the virga starting around 15:30 UT continued for approximately 1 h. As shown in Fig. 8f, some places in the cloud at about 8 km have larger values of reflectivity factors. Water droplets or ice crystals from virga can be lifted by convective updrafts into cumulonimbus clouds and continuously grow and coalesce to form rain, such as from 16:29 to 17:29 UT. For this rain event, the cumulative rain is not large, only 1.1 mm. This could be due to the decay of deep convective clouds, with weakened updrafts and decreased cloud height. Another possibility is that the concentration of water vapor around the cloud base is higher due to virga, and the warmer temperature and higher cloud height promote continuous collision and merging of raindrops, resulting in drizzle. Rain-day events are commonly used to evaluate precipitation intensity classes, which represent the total cumulative amount of rainfall in a day (Wang et al., 2021). The weather station provided 889 rain-day events due to its ability to measure the amount of rainfall reaching the ground. Statistics indicate that light rain is the main precipitation intensity class in Granada (accumulation of daily rain less than 5 mm), accounting for 72 % of these recorded rain-day events. Aerosols may be partly responsible for it. Abundant aerosol particles in Granada acted as cloud condensation nuclei, increasing the number of cloud droplets. This intensified the competition among cloud droplets for water vapor molecules, leading to smaller cloud droplet sizes. Consequently, rain is finer and more disperse, becoming drizzle or light rain.
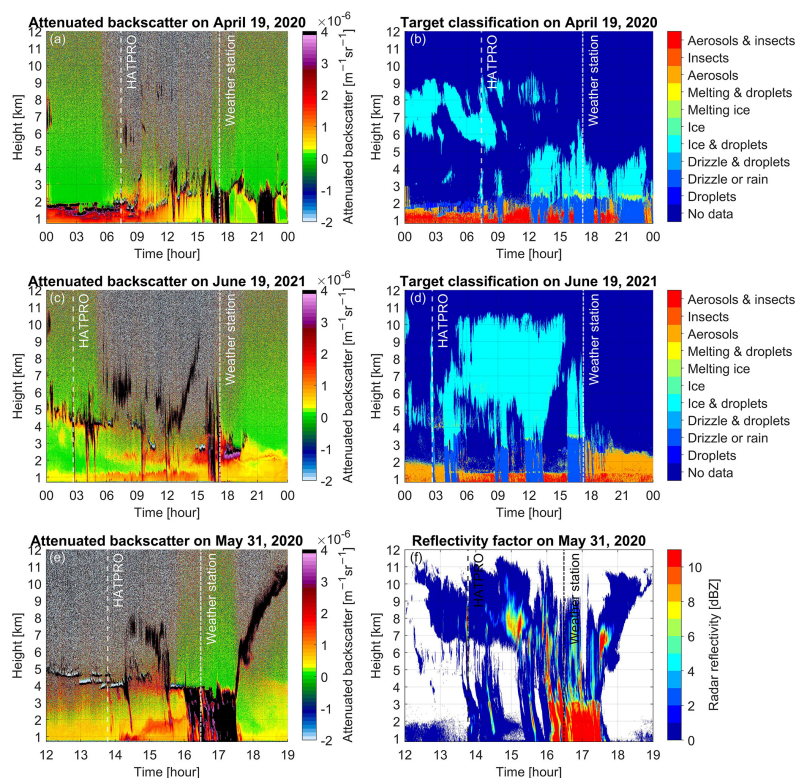
Figure 8. Ceilometer attenuated backscatter and cloud radar target classification for **(a, b)** 19 April 2020 and **(c, d)** 19 June 2021. **(e)** Ceilometer attenuated backscatter and **(f)** cloud radar reflectivity factor on 31 May 2020. Dashed and dash-dotted lines are the onset of rain identified by HATPRO and the weather station, respectively.

5 Conclusions

In this study, Andalusia, with a semi-arid Mediterranean climate region in southern Spain, is chosen as the study area due to its persistent exposure to Saharan dust and vulnerability to climate change. The precipitation patterns in the region are intricate, as evidenced by instances of severe rainfall causing flooding, as well as inaccurate weather forecasts of precipitation over land. To comprehensively understand the precipitation system in Andalusia, we utilize a combination of ground-based remote sensing and in situ instruments to investigate the inter-relations of precipitation in the evolution of various atmospheric variables. The instruments used in this investigation include the microwave radiometer, ceilometer, cloud radar, integrating nephelometer, and weather station. Rain events and rain-day events were detected by the microwave radiometer HATPRO and weather station for 11 years from October 2010 to November 2021, respectively. The time series of variables obtained from all these instruments is subjected to composite analysis.

First, it was found that convective rain is the main type of precipitation in Granada. Convective rainfall accounts for 68 % of the rain events. The vertical distribution of cloud, rain, and aerosol observed by the ceilometer is well interpreted with the assistance of cloud radar. The cloud-base height is primarily distributed in the 2–7 km range 8 h before rain and around 2–3 km during the 6 h after rain. Integrated water vapor (IWV) provided by the microwave radiometer increases rapidly from 0 to 6 h before rain and remains above 28 mm within 4 h after the onset of rain. IWV is not significantly reduced at the end of rain compared to the beginning.

Observations from both the ceilometer and the integrating nephelometer show that aerosols are removed after rain, but the latter instrument gives more detail. The integrating nephelometer data show that aerosol scattering increases slightly before rain, followed by a decline with the removal by rainfall, with gradual recovery after rain. There is no significant variation in the predominant mean size distribution of aerosol particles before, during, and after rain.

Before rain, the temperature shows an initial increase followed by a decrease; the relative humidity decreases and then increases, the pressure decreases by 0.9 hPa, and the wind speed increases by $0.3 \, \mathrm{m \, s^{-1}}$. At the onset of rain, the raindrops fall onto the warmer surface and evaporate, causing a sudden increase in relative humidity of 1.6 % and a pressure increase of 0.4 hPa. The meteorological environment before rain is conducive to the formation of virga. Virga is identified by measuring the time delay between rainfall in the atmosphere and its arrival at the surface using the microwave radiometer and weather station. The vertical distribution of virga is well observed and shown by the ceilometer and cloud radar. Furthermore, light rain is the main precipitation intensity class in Granada. Light rain accounts for 72 % of the rain-day events.

The results of this work on cloud heights before and after rain lead to a better understanding of the formation and evolution of clouds and precipitation in Andalusia. The changes in aerosol scattering and particle size before, during, and after rain reveal the mechanism of aerosol removal and the interaction between aerosol particles and water droplets. Observations and detections of virga can provide the knowledge required for improvement of local precipitation forecasts, which is crucial for managing droughts, floods, soil erosion, and water resources. Future research could explore the impact of topographic settings and the proximity of the Mediterranean Sea on meteorological changes and spatial pattern assessment.

Code availability. The code is not publicly accessible, but readers can contact Wenyue Wang (wenyue.wang@unibe.ch) for more information.

Data availability. The CHM15k ceilometer data can be downloaded from the European networks of radar wind profilers and automatic lidars and ceilometers for the monitoring of vertical profiles of wind and aerosols (E-PROFILE) in the Centre for Environmental Data Analysis (CEDA) archives (EUMETNET E-PROFILE, 2018). The 94 GHz Doppler cloud radar data in Granada are available from ACTRIS-Cloudnet (Granados Muñoz and Alados-Arboledas, 2023; Cazorla et al., 2023).

Author contributions. WW, KH, and FN conceptualized the study. WW performed methods, formal analysis, and software operations, as well as preparing the original draft. LN, AC, GT, LAA, AM, and FNG provided support with respect to data curation. RM contributed to the interpretation of the ceilometer results. All co-authors contributed to the interpretation of the results and participated in the paper editing and discussion.

Competing interests. The contact author has declared that none of the authors has any competing interests.

Disclaimer. Publisher's note: Copernicus Publications remains neutral with regard to jurisdictional claims made in the text, published maps, institutional affiliations, or any other geographical representation in this paper. While Copernicus Publications makes every effort to include appropriate place names, the final responsibility lies with the authors.

References

Adams, D. K., Gutman, S. I., Holub, K. L., and Pereira, D. S.: GNSS observations of deep convective time scales in the Amazon, Geophys. Res. Lett., 40, 2818–2823, 2013.

AEMET: Valores climatológicos normales y estadísticos de estaciones principales (1981–2010), http://hdl.handle.net/20.500.11765/407 (last access: 18 January 2024), 2012.

Airey, M. W., Nicoll, K. A., Harrison, R. G., and Marlton, G. J.: Characteristics of desert precipitation in the UAE derived from a ceilometer dataset, Atmosphere, 12, 1245, https://doi.org/10.3390/atmos12101245, 2021.

Alizadeh-Choobari, O. and Gharaylou, M.: Aerosol impacts on radiative and microphysical properties of clouds and precipitation formation, Atmos. Res., 185, 53–64, 2017.

Allan, R. P., Blenkinsop, S., Fowler, H. J., and Champion, A. J.: Atmospheric precursors for intense summer rainfall over the United Kingdom, Int. J. Climatol., 40, 3849–3867, 2020.

Anderson, T. L. and Ogren, J. A.: Determining aerosol radiative properties using the TSI 3563 integrating nephelometer, Aerosol Sci. Technol., 29, 57–69, 1998.

Andrews, E., Sheridan, P. J., Ogren, J. A., Hageman, D., Jefferson, A., Wendell, J., Alástuey, A., Alados-Arboledas, L., Bergin, M., Ealo, M., et al.: Overview of the NOAA/ESRL federated aerosol network, B. Am. Meteorol. Soc., 100, 123–135, 2019.

Barriendos, M., Gil-Guirado, S., Pino, D., Tuset, J., Pérez-Morales, A., Alberola, A., Costa, J., Balasch, J. C., Castelltort, X., Mazón, J., et al.: Climatic and social factors behind the Spanish Mediterranean flood event chronologies from documentary sources (14th–20th centuries), Global Planet. Change, 182, 102997, https://doi.org/10.1016/j.gloplacha.2019.102997, 2019.

Bedoya-Velásquez, A. E., Navas-Guzmán, F., de Arruda Moreira, G., Román, R., Cazorla, A., Ortiz-Amezcua, P., Benavent-Oltra, J. A., Alados-Arboledas, L., Olmo-Reyes, F. J., Foyo-Moreno, I., et al.: Seasonal analysis of the atmosphere during five years by using microwave radiometry over a mid-latitude site, Atmos. Res., 218, 78–89, 2019.

Belmonte, A. M. C. and Beltrán, F. S.: Flood events in Mediterranean ephemeral streams (ramblas) in Valencia region, Spain, Catena, 45, 229–249, 2001.

Benavent-Oltra, J. A., Casquero-Vera, J. A., Román, R., Lyamani, H., Pérez-Ramírez, D., Granados-Muñoz, M. J., Herrera, M., Cazorla, A., Titos, G., Ortiz-Amezcua, P., Bedoya-Velásquez, A. E., de Arruda Moreira, G., Pérez, N., Alastuey, A., Dubovik, O., Guerrero-Rascado, J. L., Olmo-Reyes, F. J., and Alados-Arboledas, L.: Overview of the SLOPE I and II campaigns: aerosol properties retrieved with lidar and sun–sky photometer measurements, Atmos. Chem. Phys., 21, 9269–9287, https://doi.org/10.5194/acp-21-9269-2021, 2021.

Beynon, R. and Hocke, K.: Snow Virga above the Swiss Plateau Observed by a Micro Rain Radar, Remote Sens., 14, 890, https://doi.org/10.3390/rs14040890, 2022.

Cazorla, A., Casquero-Vera, J. A., Román, R., Guerrero-Rascado, J. L., Toledano, C., Cachorro, V. E., Orza, J. A. G., Cancillo, M. L., Serrano, A., Titos, G., Pandolfi, M., Alastuey, A., Hanrieder, N., and Alados-Arboledas, L.: Near-real-time processing of a ceilometer network assisted with sun-photometer data: monitoring a dust outbreak over the Iberian Peninsula, Atmos. Chem. Phys., 17, 11861–11876, https://doi.org/10.5194/acp-17-11861-2017, 2017.

Cazorla Cabrera, A., Granados Muñoz, M. J., Navas Guzmán, F., O'Connor, E., and Alados-Arboledas, L.: Classification data from Granada on 13 March 2022. ACTRIS Cloud remote sensing data centre unit (CLU), [data set], https://cloudnet.fmi.fi/file/d847a5ae-5de9-453b-b803-22f3744cc1df (last access: 23 January 2024), 2023.

Chang, K., Bench, J., Brege, M., Cantrell, W., Chandrakar, K., Ciochetto, D., Mazzoleni, C., Mazzoleni, L., Niedermeier, D., and Shaw, R.: A laboratory facility to study gas–aerosol–cloud interactions in a turbulent environment: The Π chamber, B. Am. Meteorol. Soc., 97, 2343–2358, 2016.

Chen, Q., Fan, J., Yin, Y., and Han, B.: Aerosol impacts on mesoscale convective systems forming under different vertical wind shear conditions, J. Geophys. Res.-Atmos., 125, e2018JD030027, https://doi.org/10.1029/2018JD030027, 2020.

de Arruda Moreira, G., Sánchez-Hernández, G., Guerrero-Rascado, J. L., Cazorla, A., and Alados-Arboledas, L.: Estimating the ur-

ban atmospheric boundary layer height from remote sensing applying machine learning techniques, Atmos. Res., 266, 105962, https://doi.org/10.1016/j.atmosres.2021.105962, 2022.

Esteban-Parra, M. J., García-Valdecasas Ojeda, M., Peinó-Calero, E., Romero-Jiménez, E., Yeste, P., Rosa-Cánovas, J. J., Rodríguez-Brito, A., Gámiz-Fortis, S. R., and Castro-Díez, Y.: Climate Variability and Trends, in: The Landscape of the Sierra Nevada: A Unique Laboratory of Global Processes in Spain, edited by: Zamora, R. and Oliva, M., Springer, 129–148, 2022.

EUMETNET E-PROFILE: ceilometer cloud base height and aerosol profile data from a network covering most of Europe with additional sites worldwide, NERC EDS Centre for Environmental Data Analysis, [data set], http://catalogue.ceda.ac.uk/uuid/345c47d378b64c75b7957aef0c09c81f (last access: 23 January 2024), 2018.

Evans, E., Stewart, R., Henson, W., and Saunders, K.: On precipitation and virga over three locations during the 1999–2004 Canadian Prairie drought, Atmos. Ocean, 49, 366–379, 2011.

Fan, J., Wang, Y., Rosenfeld, D., and Liu, X.: Review of aerosol–cloud interactions: Mechanisms, significance, and challenges, J. Atmos. Sci., 73, 4221–4252, 2016.

Fernández, A. J., Sicard, M., Costa, M. J., Guerrero-Rascado, J. L., Gómez-Amo, J. L., Molero, F., Barragán, R., Basart, S., Bortoli, D., Bedoya-Velásquez, A. E., et al.: Extreme, wintertime Saharan dust intrusion in the Iberian Peninsula: Lidar monitoring and evaluation of dust forecast models during the February 2017 event, Atmos. Res., 228, 223–241, 2019.

Flores, M. J., Ropero, R. F., and Rumí, R.: Flood Risk: Evolution and Analysis in a Mediterranean area, PREPRINT (Version 1) available at Research Square, https://doi.org/10.21203/rs.3.rs-1533031/v1, 2022.

Gibbons, M., Min, Q., and Fan, J.: Investigating the impacts of Saharan dust on tropical deep convection using spectral bin microphysics, Atmos. Chem. Phys., 18, 12161–12184, https://doi.org/10.5194/acp-18-12161-2018, 2018.

Granados Muñoz, M. J. and Alados-Arboledas, L.: Radar data from Granada on 13 March 2022. ACTRIS Cloud remote sensing data centre unit (CLU), [data set], https://cloudnet.fmi.fi/file/56fa3908-f274-41ce-bb5c-a950a4a57be7 (last access: 23 January 2024), 2023.

Guerrero-Rascado, J. L., Olmo, F. J., Avilés-Rodríguez, I., Navas-Guzmán, F., Pérez-Ramírez, D., Lyamani, H., and Alados Arboledas, L.: Extreme Saharan dust event over the southern Iberian Peninsula in september 2007: active and passive remote sensing from surface and satellite, Atmos. Chem. Phys., 9, 8453–8469, https://doi.org/10.5194/acp-9-8453-2009, 2009.

Hazra, A., Chaudhari, H. S., Ranalkar, M., and Chen, J.-P.: Role of interactions between cloud microphysics, dynamics and aerosol in the heavy rainfall event of June 2013 over Uttarakhand, India, Q. J. Roy. Meteor. Soc., 143, 986–998, 2017.

Heintzenberg, J., Wiedensohler, A., Tuch, T., Covert, D., Sheridan, P., Ogren, J., Gras, J., Nessler, R., Kleefeld, C., Kalivitis, N., et al.: Intercomparisons and aerosol calibrations of 12 commercial integrating nephelometers of three manufacturers, J. Atmos. Ocean. Tech., 23, 902–914, 2006.

Hobbs, P. V.: Aerosol-cloud interactions, in: International Geophysics, edited by: Houze, R. A., Vol. 54, Elsevier, 33–73, 1993.

Hocke, K., Bernet, L., Hagen, J., Murk, A., Renker, M., and Mätzler, C.: Diurnal cycle of short-term fluctuations of integrated wa-

ter vapour above Switzerland, Atmos. Chem. Phys., 19, 12083–12090, https://doi.org/10.5194/acp-19-12083-2019, 2019.

Hogan, R. J. and O'Connor, E. J.: Facilitating cloud radar and lidar algorithms: the Cloudnet Instrument Synergy/Target Categorization product, 2004.

Hong, Y., Adler, R. F., Negri, A., and Huffman, G. J.: Flood and landslide applications of near real-time satellite rainfall products, Nat. Hazards, 43, 285–294, 2007.

Illingworth, A., Hogan, R., O'connor, E., Bouniol, D., Brooks, M., Delanoë, J., Donovan, D., Eastment, J., Gaussiat, N., Goddard, J., et al.: Cloudnet: Continuous evaluation of cloud profiles in seven operational models using ground-based observations, B. Am. Meteorol. Soc., 88, 883–898, 2007.

Jiang, J. H., Su, H., Huang, L., Wang, Y., Massie, S., Zhao, B., Omar, A., and Wang, Z.: Contrasting effects on deep convective clouds by different types of aerosols, Nat. Commun., 9, 3874, https://doi.org/10.1038/s41467-018-06280-4, 2018.

Jullien, N., Vignon, É., Sprenger, M., Aemisegger, F., and Berne, A.: Synoptic conditions and atmospheric moisture pathways associated with virga and precipitation over coastal Adélie Land in Antarctica, The Cryosphere, 14, 1685–1702, https://doi.org/10.5194/tc-14-1685-2020, 2020.

Kant, S., Panda, J., Rao, P., Sarangi, C., and Ghude, S. D.: Study of aerosol-cloud-precipitation-meteorology interaction during a distinct weather event over the Indian region using WRF-Chem, Atmos. Res., 247, 105144, https://doi.org/10.1016/j.atmosres.2020.105144, 2021.

Karle, N. N., Sakai, R. K., Fitzgerald, R. M., Ichoku, C., Mercado, F., and Stockwell, W. R.: Systematic analysis of virga and its impact on surface particulate matter observations, Atmos. Meas. Tech., 16, 1073–1085, https://doi.org/10.5194/amt-16-1073-2023, 2023.

Khain, A.: Notes on state-of-the-art investigations of aerosol effects on precipitation: a critical review, Environ. Res. Lett., 4, 015004, https://doi.org/10.1088/1748-9326/4/1/015004, 2009.

Khain, A., Rosenfeld, D., and Pokrovsky, A.: Aerosol impact on the dynamics and microphysics of deep convective clouds, Quarterly Journal of the Royal Meteorological Society: A journal of the atmospheric sciences, Appl. Meteorol. Phys. Ocean., 131, 2639–2663, 2005.

Koffi, E. N., Graham, C. E., and Mätzler, C.: The water vapour flux above Switzerland and its role in the August 2005 extreme precipitation and flooding, Meteorol. Z., 22, 329–342, 2013.

Kundzewicz, Z. W.: Climate change impacts on the hydrological cycle, Ecohydrol. Hydrobiol., 8, 195–203, 2008.

Laj, P., Bigi, A., Rose, C., Andrews, E., Lund Myhre, C., Collaud Coen, M., Lin, Y., Wiedensohler, A., Schulz, M., Ogren, J. A., Fiebig, M., Gliß, J., Mortier, A., Pandolfi, M., Petäjä, T., Kim, S.-W., Aas, W., Putaud, J.-P., Mayol-Bracero, O., Keywood, M., Labrador, L., Aalto, P., Ahlberg, E., Alados Arboledas, L., Alastuey, A., Andrade, M., Artíñano, B., Ausmeel, S., Arsov, T., Asmi, E., Backman, J., Baltensperger, U., Bastian, S., Bath, O., Beukes, J. P., Brem, B. T., Bukowiecki, N., Conil, S., Couret, C., Day, D., Dayantolis, W., Degorska, A., Eleftheriadis, K., Fetfatzis, P., Favez, O., Flentje, H., Gini, M. I., Gregorič, A., Gysel-Beer, M., Hallar, A. G., Hand, J., Hoffer, A., Hueglin, C., Hooda, R. K., Hyvärinen, A., Kalapov, I., Kalivitis, N., Kasper-Giebl, A., Kim, J. E., Kouvarakis, G., Kranjc, I., Krejci, R., Kulmala, M., Labuschagne, C., Lee, H.-J., Lihavainen, H., Lin, N.-H.,

Löschau, G., Luoma, K., Marinoni, A., Martins Dos Santos, S., Meinhardt, F., Merkel, M., Metzger, J.-M., Mihalopoulos, N., Nguyen, N. A., Ondracek, J., Pérez, N., Perrone, M. R., Petit, J.-E., Picard, D., Pichon, J.-M., Pont, V., Prats, N., Prenni, A., Reisen, F., Romano, S., Sellegri, K., Sharma, S., Schauer, G., Sheridan, P., Sherman, J. P., Schütze, M., Schwerin, A., Sohmer, R., Sorribas, M., Steinbacher, M., Sun, J., Titos, G., Toczko, B., Tuch, T., Tulet, P., Tunved, P., Vakkari, V., Velarde, F., Velasquez, P., Villani, P., Vratolis, S., Wang, S.-H., Weinhold, K., Weller, R., Yela, M., Yus-Diez, J., Zdimal, V., Zieger, P., and Zikova, N.: A global analysis of climate-relevant aerosol properties retrieved from the network of Global Atmosphere Watch (GAW) near-surface observatories, Atmos. Meas. Tech., 13, 4353–4392, https://doi.org/10.5194/amt-13-4353-2020, 2020.

López-Cayuela, M. Á., Córdoba-Jabonero, C., Bermejo-Pantaleón, D., Sicard, M., Salgueiro, V., Molero, F., Carvajal-Pérez, C. V., Granados-Muñoz, M. J., Comerón, A., Couto, F. T., Barragán, R., Zorzano, M.-P., Bravo-Aranda, J. A., Muñoz-Porcar, C., Costa, M. J., Artíñano, B., Rodríguez-Gómez, A., Bortoli, D., Pujadas, M., Abril-Gago, J., Alados-Arboledas, L., and Guerrero-Rascado, J. L.: Vertical characterization of fine and coarse dust particles during an intense Saharan dust outbreak over the Iberian Peninsula in springtime 2021, Atmos. Chem. Phys., 23, 143–161, https://doi.org/10.5194/acp-23-143-2023, 2023.

Luu, L. N., Vautard, R., Yiou, P., and Soubeyroux, J.-M.: Evaluation of convection-permitting extreme precipitation simulations for the south of France, Earth Syst. Dynam., 13, 687–702, https://doi.org/10.5194/esd-13-687-2022, 2022.

Lyamani, H., Olmo, F. J., and Alados-Arboledas, L.: Physical and optical properties of aerosols over an urban location in Spain: seasonal and diurnal variability, Atmos. Chem. Phys., 10, 239–254, https://doi.org/10.5194/acp-10-239-2010, 2010.

Mätzler, C. and Morland, J.: Refined physical retrieval of integrated water vapor and cloud liquid for microwave radiometer data, IEEE T. Geosci. Remote, 47, 1585–1594, https://doi.org/10.1109/TGRS.2008.2006984, 2009.

Myagkov, A. and Rose, T.: RPG Dual Polarization Dual Frequency Scanning Cloud Radar Systems: Configurations and Applications, https://www.radiometer-physics.de/downloadftp/pub/PDF/CloudRadar/ (last access: 19 July 2022), 2016.

Navas-Guzmán, F., Antonio Bravo-Aranda, J., Luis Guerrero-Rascado, J., Jose Granados-Munoz, M., and Alados-Arboledas, L.: Statistical analysis of aerosol optical properties retrieved by Raman lidar over Southeastern Spain, Tellus B, 65, 21234, https://doi.org/10.3402/tellusb.v65i0.21234, 2013.

Navas-Guzmán, F., Fernández-Gálvez, J., Granados-Muñoz, M. J., Guerrero-Rascado, J. L., Bravo-Aranda, J. A., and Alados-Arboledas, L.: Tropospheric water vapour and relative humidity profiles from lidar and microwave radiometry, Atmos. Meas. Tech., 7, 1201–1211, https://doi.org/10.5194/amt-7-1201-2014, 2014.

Pandolfi, M., Alados-Arboledas, L., Alastuey, A., Andrade, M., Angelov, C., Artiñano, B., Backman, J., Baltensperger, U., Bonasoni, P., Bukowiecki, N., Collaud Coen, M., Conil, S., Coz, E., Crenn, V., Dudoitis, V., Ealo, M., Eleftheriadis, K., Favez, O., Fetfatzis, P., Fiebig, M., Flentje, H., Ginot, P., Gysel, M., Henzing, B., Hoffer, A., Holubova Smejkalova, A., Kalapov, I., Kalivitis, N., Kouvarakis, G., Kristensson, A., Kulmala, M., Lihavainen, H., Lunder, C., Luoma, K., Lyamani, H., Marinoni,

A., Mihalopoulos, N., Moerman, M., Nicolas, J., O'Dowd, C., Petäjä, T., Petit, J.-E., Pichon, J. M., Prokopciuk, N., Putaud, J.-P., Rodríguez, S., Sciare, J., Sellegri, K., Swietlicki, E., Titos, G., Tuch, T., Tunved, P., Ulevicius, V., Vaishya, A., Vana, M., Virkkula, A., Vratolis, S., Weingartner, E., Wiedensohler, A., and Laj, P.: A European aerosol phenomenology – 6: scattering properties of atmospheric aerosol particles from 28 ACTRIS sites, Atmos. Chem. Phys., 18, 7877–7911, https://doi.org/10.5194/acp-18-7877-2018, 2018.

Rose, T., Crewell, S., Löhnert, U., and Simmer, C.: A network suitable microwave radiometer for operational monitoring of the cloudy atmosphere, Atmos. Res., 75, 183–200, 2005.

Rosenfeld, D., Lohmann, U., Raga, G. B., O'Dowd, C. D., Kulmala, M., Fuzzi, S., Reissell, A., and Andreae, M. O.: Flood or drought: how do aerosols affect precipitation?, Science, 321, 1309–1313, 2008.

RPG: Operation Principles and Software Description for RPG standard single polarization radiometers, https://www.radiometer-physics.de/download/PDF/Radiometers/HATPRO/ (last access: 19 July 2022), 2014.

Ruiz Sinoga, J. D., Garcia Marin, R., Martinez Murillo, J. F., and Gabarron Galeote, M. A.: Precipitation dynamics in southern Spain: trends and cycles, Int. J. Climatol., 31, 2281–2289, 2011.

Sapucci, L. F., Machado, L. A., de Souza, E. M., and Campos, T. B.: Global Positioning System precipitable water vapour (GPS-PWV) jumps before intense rain events: A potential application to nowcasting, Meteorol. Appl., 26, 49–63, 2019.

Sarangi, C., Tripathi, S. N., Kanawade, V. P., Koren, I., and Pai, D. S.: Investigation of the aerosol–cloud–rainfall association over the Indian summer monsoon region, Atmos. Chem. Phys., 17, 5185–5204, https://doi.org/10.5194/acp-17-5185-2017, 2017.

Sarna, K. and Russchenberg, H. W. J.: Ground-based remote sensing scheme for monitoring aerosol–cloud interactions, Atmos. Meas. Tech., 9, 1039–1050, https://doi.org/10.5194/amt-9-1039-2016, 2016.

Sumner, G., Romero, R., Homar, V., Ramis, C., Alonso, S., and Zorita, E.: An estimate of the effects of climate change on the rainfall of Mediterranean Spain by the late twenty first century, Clim. Dynam., 20, 789–805, 2003.

Titos, G., Foyo-Moreno, I., Lyamani, H., Querol, X., Alastuey, A., and Alados-Arboledas, L.: Optical properties and chemical composition of aerosol particles at an urban location: An estimation of the aerosol mass scattering and absorption efficiencies, J. Geophys. Res.-Atmos., 117, D04206, https://doi.org/10.1029/2011JD016671, 2012.

Tost, H., Jöckel, P., Kerkweg, A., Sander, R., and Lelieveld, J.: Technical note: A new comprehensive SCAVenging submodel for global atmospheric chemistry modelling, Atmos. Chem. Phys., 6, 565–574, https://doi.org/10.5194/acp-6-565-2006, 2006.

Valenzuela, A., Olmo, F., Lyamani, H., Antón, M., Quirantes, A., and Alados-Arboledas, L.: Analysis of the desert dust radiative properties over Granada using principal plane sky radiances and spheroids retrieval procedure, Atmos. Res., 104, 292–301, 2012.

Vaquero-Martínez, J., Antón, M., Costa, M. J., Bortoli, D., Navas-Guzmán, F., and Alados-Arboledas, L.: Microwave radiometer, sun-photometer and GNSS multi-comparison of integrated water vapor in Southwestern Europe, Atmos. Res., 287, 106698, https://doi.org/10.1016/j.atmosres.2023.106698, 2023.

Wang, W. and Hocke, K.: Atmospheric effects and precursors of rainfall over the Swiss Plateau, Remote Sens., 14, 2938, https://doi.org/10.3390/rs14122938, 2022.

Wang, W., Hocke, K., and Mätzler, C.: Physical retrieval of rain rate from ground-based microwave radiometry, Remote Sens., 13, 2217, https://doi.org/10.3390/rs13112217, 2021.

Wang, W., Murk, A., Sauvageat, E., Fan, W., Dätwyler, C., Hervo, M., Haefele, A., and Hocke, K.: An Indoor Microwave Radiometer for Measurement of Tropospheric Water, IEEE T. Geosci. Remote, 61, 1–13, https://doi.org/10.1109/TGRS.2023.3261067, 2023.

Wehbe, Y., Tessendorf, S. A., Weeks, C., Bruintjes, R., Xue, L., Rasmussen, R., Lawson, P., Woods, S., and Temimi, M.: Analysis of aerosol–cloud interactions and their implications for precipitation formation using aircraft observations over the United Arab Emirates, Atmos. Chem. Phys., 21, 12543–12560, https://doi.org/10.5194/acp-21-12543-2021, 2021.

Wilheit, T. T., Chang, A., V. Rao, M., Rodgers, E., and Theon, J.: A satellite technique for quantitatively mapping rainfall rates over the oceans, J. Appl. Meteorol. Clim., 16, 551–560, 1977.

Xiao, Z., Yu, Y., Miao, Y., Zhu, S., He, H., Wang, Y., and Che, H.: Impact of aerosols on convective system over the North China Plain: a numerical case study in autumn, J. Geophys. Res.-Atmos., 128, https://doi.org/10.1029/2022JD037465, e2022JD037465, 2023.

Zhang, W., Xu, G., Xi, B., Ren, J., Wan, X., Zhou, L., Cui, C., and Wu, D.: Comparative study of cloud liquid water and rain liquid water obtained from microwave radiometer and micro rain radar observations over central China during the monsoon, J. Geophys. Res.-Atmos., 125, e2020JD032456, https://doi.org/10.1029/2022JD037465, 2020.

Zhao, X., Zhao, C., Yang, Y., Sun, Y., Xia, Y., Yang, X., and Fan, T.: Distinct changes of cloud microphysical properties and height development by dust aerosols from a case study over Inner-Mongolia region, Atmos. Res., 273, 106175, https://doi.org/10.1016/j.atmosres.2022.106175, 2022.

Zheng, Z., Xu, G., Li, Q., Chen, C., and Li, J.: Effect of precipitation on reducing atmospheric pollutant over Beijing, Atmos. Pollut. Res., 10, 1443–1453, 2019.

Zhu, H., Li, R., Yang, S., Zhao, C., Jiang, Z., and Huang, C.: The impacts of dust aerosol and convective available potential energy on precipitation vertical structure in southeastern China as seen from multisource observations, Atmos. Chem. Phys., 23, 2421–2437, https://doi.org/10.5194/acp-23-2421-2023, 2023.

10 | CONCLUSIONS AND OUTLOOK

10.1 CONCLUSIONS

In this thesis, I present the work done to achieve optimal rain rate estimates from ground-based microwave radiometers and the application of the retrieval method. This involves the synergy of multiple instruments (e.g. radiometers, radars, and rain gauges).

The thesis contains six of my studies on precipitation in the troposphere. The first study in Chapter 4 aims to achieve accurate rain detection. Detecting rain is not only a prerequisite for the rain rate retrieval algorithms, but also can effectively eliminate rain-contaminated data from microwave radiometers due to raindrops in the atmosphere, thereby enhancing the credibility of other atmospheric water parameter studies. In the first study, I detected precipitation (rain, drizzle, and mixed) from rain-contaminated TROWARA data combined with the target variable MRR precipitation type classification data. The approach is based on the machine learning method GBDT, accounting for various seasons and rain types, and is compared with the ILW threshold method. This study detects precipitation from the time series of microwave radiometer measurements with a high temporal resolution of 10 s and a high accuracy of 98.4%.

The second and third studies in Chapter 5 and Chapter 6 aim to achieve precise rain rate retrievals. Exploiting of the high temporal resolution and sensitivity to rain of ground-based microwave radiometers for rain rate retrieval is of great value for precipitation research. This will also complement the shortcomings of other precipitation monitoring technologies. In the second study, I retrieved rain rates using an physical method for TROWARA. The method is to obtain the physical relationship between the zenith rain optical depth and the rain rate by establishing the radiation transfer equation during rain. The 14-year cumulative rain over time (day, month, and year) was compared with the two rain gauges and ERA5 reanalysis data. The comparison results show that the method performs well in rain estimation at 31 GHz. I also applied this physical rainfall rate retrieval algorithm to commercial radiometers (HATPROs) in Payerne, Schaffhausen, Grenchen, Bern in Switzerland and Granada in Spain. After understanding of the physical mechanism of rain estimation from microwave radiometers in the second study, I developed two machine learning (RF and GBDT) based rain rate retrieval methods in the third

study. The methods use TROWARA measurements as input variables and the rain rate measured by MRR as the target variable, and the resulting estimated rainfall has a temporal resolution of up to 10 s and and an R^2 greater than 0.95.

The fourth study in Chapter 7 aims at the performance assessment of indoor and outdoor microwave radiometers. In the fourth study, I compared the brightness temperatures measured by indoor and outdoor coincident microwave radiometers (TROWARA and HATPRO) and the tropospheric water they retrieved. Using the GBDT method, I identified the contribution of eight factors related to both instruments to the deviation, with the goal of locating the sources of bias. Results indicate that the indoor installation design of TROWARA effectively avoids the influence of water film on the radome on the accuracy of precipitation and other tropospheric water measurements. On the other hand, data deviations can reflect instrumental or observational uncertainties in microwave radiometers. The overestimation in the brightness temperature of HATPRO at 22 GHz is due to the instrument calibration, the surrounding environment, and elevation angle of the Sun.

The fifth study in Chapter 8 aims at the identification of rainfall precursors. By analyzing the time series of atmospheric parameters before and after the onset of rain, a "climatology" can be built to provide a comprehensive description of rain occurrence and development, and enables seeking rainfall precursors that can improve nowcasting. In the fifth study, I characterized the temporal evolution of rain events over a 10-year period to identify potential rainfall precursors. The approach uses a SEA method that takes into account the variations of eight atmospheric parameters provided by TROWARA and ExWi weather station. This study reveals that IWV rapidly increases to a peak value when rainfall begins, and changes in air density 2 to 6 hours prior to rainfall can serve as a precursor, with a true detection rate of 60%.

The sixth study in Chapter 9 aims at interrelationships of precipitation, aerosols, and clouds. Studying multiple atmospheric parameters during rain, especially aerosols and clouds, helps to explain the complexities of precipitation systems. Multi-instrument coordinated observations, both remote sensing and in situ, can achieve this purpose. In the sixth study, I monitored the interrelationships between various factors (such as aerosols, clouds and meteorological variables) and precipitation systems over southern Spain using ground-based remote sensing and in situ instruments at the AGORA Observatory, including a microwave radiometer, a nephelometer, a cloud radar, a ceilometer and a weather station. The approach is to conduct a SEA method of these factors and construct a climatology of the temporal evolution of precipitation. The analysis suggests that Andalusia is affected by Saharan dust and has a Mediterranean climate, which potentially leads to a dominant convective rain type with high cloud base, light rain as the main precipitation intensity class, and meteorological conditions for virga formation.

10.2 OUTLOOK

The findings of my fourth study in Chapter 7 indicated that even though HATPRO uses a blower and hydrophobic materials, the water film will remain on its radome for a while after rain stops. The microwave radiation signal will be affected by the strong emission and scattering of rain on the radome and mistakenly regarded as raindrops in the atmosphere. This leads to a decrease in the accuracy of brightness temperature measurements and parameter retrievals of ground-based microwave radiometers before the water film evaporates. Therefore, the detection method of rain-contaminated microwave radiometer data in my first study in Chapter 4 can be extended to the study of eliminating the influence of water film on the radome after rain, and compared with the rain detected by the rain sensor equipped with HATPRO.

Rainfall estimation algorithms (physical and machine learning methods) for ground-based microwave radiometers can still be improved. For the physical rain rate retrieval algorithm, my GBDT-based rain detection model can replace the ILW threshold method to detect the onset and end of rain. This is crucial for the studies of the temporal evolution of complex precipitation systems and rainfall precursors using microwave radiometers. The stratiform melting layer heights (rain layer heights) in the physical algorithm were calculated by the ratio of the temperature difference from the ground to the melting layer and an assumed temperature gradient. Using the actual heights of the melt layer observed by MRR is expected to improve the accuracy of the retrieval algorithm. For the machine learning rain rate retrieval algorithms, it is necessary to provide data from more locations or longer interval time series to the training set. The reason is that rain patterns are highly sensitive to geographical location and climate, and adding a large number of samples under different conditions can improve the generalization ability of the retrieval model.

Spaceborne radiometry has been successfully applied for global-scale precipitation retrieval and has proven to be a fairly accurate tool (Lazri et al., 2020), although its main drawbacks include poor spatial resolution and low temporal sampling. Cross-validation between the precipitation products from ground-based microwave radiometers, using physical and machine learning retrievals of this thesis, and those from space-based radiometers is interesting and holds promise for improving precipitation estimation models. For example, ground-based data can provide correction factors for satellite measurements by comparing precipitation estimates.

Noise in microwave radiometer data arises from both the instrument itself and atmospheric effects. The coincident measurements by TROWARA and

HATPRO in Bern have the potential to detect noise from atmospheric effects, such as that caused by atmospheric turbulence. The study of atmospheric effects noise would enhance our understanding about tropospheric small-scale inhomogeneities.

ACKNOWLEDGMENTS

going. I thank myself for my persistence and courage in accepting challenges, taking good care of myself after two ankle surgeries.

BIBLIOGRAPHY

AEMET (2012). *Valores climatológicos normales y estadísticos de estaciones principales (1981-2010)*. URL: http://hdl.handle.net/20.500.11765/407.

AMS (2015). In: *American Meteorological Society. Glossary of Meteorology: Virga. Electronic Version*. URL: https://glossary.ametsoc.org/wiki/Virga.

Ahrens, C. D. and R. Henson (2019a). "Air masses and fronts." In: *Meteorology today: an introduction to weather, climate, and the environment*. Ed. by C. D. Ahrens and R. Henson. Cengage Learning Canada Inc. Chap. 7, pp. 293–319.

— (2019b). "Precipitation." In: *Meteorology today: an introduction to weather, climate, and the environment*. Ed. by C. D. Ahrens and R. Henson. Cengage Learning Canada Inc. Chap. 7, pp. 167–195.

Alexander, S. P. and A. Protat (2018). "Cloud properties observed from the surface and by satellite at the northern edge of the Southern Ocean." In: *Journal of Geophysical Research: Atmospheres* 123.1, pp. 443–456. DOI: 10.1002/2017JD026552.

Alizadeh-Choobari, O. and M. Gharaylou (2017). "Aerosol impacts on radiative and microphysical properties of clouds and precipitation formation." In: *Atmospheric Research* 185, pp. 53–64. DOI: 10.1016/j.atmosres.2016.10.021.

Anderson, T. L. and J. A. Ogren (1998). "Determining aerosol radiative properties using the TSI 3563 integrating nephelometer." In: *Aerosol Science and Technology* 29.1, pp. 57–69. DOI: 10.1080/02786829808965551.

Arruda Moreira, G. de, G. Sánchez-Hernández, J. L. Guerrero-Rascado, A. Cazorla, and L. Alados-Arboledas (2022). "Estimating the urban atmospheric boundary layer height from remote sensing applying machine learning techniques." In: *Atmospheric Research* 266, p. 105962. DOI: 10.1016/j.atmosres.2021.105962.

Bengtsson, L. (2010). "The global atmospheric water cycle." In: *Environmental Research Letters* 5.2, p. 025202. DOI: 10.1088/1748-9326/5/2/025202.

Beynon, R. (2022). "Observations of virga precipitation with a micro rain radar." MA thesis. Physics Institute, University of Zurich. URL: https://www.physik.uzh.ch/dam/jcr:294d1794-7adb-45d0-8015-06ba7eaf619f/Beynon%20Ruben_MA_2022.pdf.

Beynon, R. and K. Hocke (2022). "Snow virga above the Swiss Plateau observed by a micro rain radar." In: *Remote Sensing* 14.4. DOI: 10.3390/rs14040890.

Bohren, C. F. and D. R. Huffman (1998). "Absorption and Scattering by a Sphere." In: *Absorption and Scattering of Light by Small Particles*. Ed. by C. F.

Bohren and D. R. Huffman. John Wiley & Sons, Ltd. Chap. 4, pp. 82–129. DOI: 10.1002/9783527618156.ch4.

Boltzmann, L. (1884). "Ableitung des Stefan'schen Gesetzes, betreffend die Abhängigkeit der Wärmestrahlung von der Temperatur aus der electromagnetischen Lichttheorie." In: *Annalen der Physik* 258.6, pp. 291–294. DOI: 10.1002/andp.18842580616.

Brandsma, T. and T. Buishand (1997). "Statistical linkage of daily precipitation in Switzerland to atmospheric circulation and temperature." In: *Journal of Hydrology* 198.1, pp. 98–123. DOI: 10.1016/S0022-1694(96)03326-4.

Breiman, L., J. Friedman, R. Olshen, and C. Stone (1984). "Regression Trees." In: *Classification and regression trees*. Ed. by L. Breiman, J. Friedman, R. Olshen, and C. Stone. Taylor & Francis. Chap. 8. DOI: 10.1201/9781315139470.

Breiman, L. (2001). "Random forests." In: *Machine learning* 45, pp. 5–32. DOI: 10.1023/A:1010933404324.

Cazorla, A., J. A. Casquero-Vera, R. Román, J. L. Guerrero-Rascado, C. Toledano, V. E. Cachorro, J. A. G. Orza, M. L. Cancillo, A. Serrano, G. Titos, et al. (2017). "Near-real-time processing of a ceilometer network assisted with sun-photometer data: monitoring a dust outbreak over the Iberian Peninsula." In: *Atmospheric Chemistry and Physics* 17.19, pp. 11861–11876. DOI: 10.5194/acp-17-11861-2017.

Ceccaldi, M., J. Delanoë, R. J. Hogan, N. L. Pounder, A. Protat, and J. Pelon (2013). "From CloudSat-CALIPSO to EarthCare: Evolution of the DARDAR cloud classification and its comparison to airborne radar-lidar observations." In: *Journal of Geophysical Research: Atmospheres* 118.14, pp. 7962–7981. DOI: 10.1002/jgrd.50579.

Chang, K., J. Bench, M. Brege, W. Cantrell, K. Chandrakar, D. Ciochetto, C. Mazzoleni, L. R. Mazzoleni, D. Niedermeier, and R. A. Shaw (2016). "A laboratory facility to study gas-aerosol-cloud interactions in a turbulent environment: the Π chamber." In: *Bulletin of the American Meteorological Society* 97.12, pp. 2343–2358. DOI: 10.1175/BAMS-D-15-00203.1.

Cho, D., H. Chen, J. Shin, and S. Jeon (2021). "Mechanoresponsive scatterers for high-contrast optical modulation." In: *Nanophotonics* 11.11, pp. 2737–2762. DOI: 10.1515/nanoph-2021-0642.

Chree, C. (1913). "III. Some phenomena of sunspots and of terrestrial magnetism at Kew Observatory." In: *Philosophical Transactions of the Royal Society of London. Series A, Containing Papers of a Mathematical or Physical Character* 212.484-496, pp. 75–116. DOI: 10.1098/rsta.1913.0003.

Cimini, D., M. Nelson, J. Güldner, and R. Ware (2015). "Forecast indices from a ground-based microwave radiometer for operational meteorology." In: *Atmospheric Measurement Techniques* 8.1, pp. 315–333. DOI: 10.5194/amt-8-315-2015.

Cimini, D., T. J. Hewison, and L. Martin (2006). "Comparison of brightness temperatures observed from ground-based microwave radiometers dur-

ing TUC." In: *Meteorologische Zeitschrift* 15.1, pp. 19–26. DOI: 10.1127/0941-2948/2006/0096.

Cimini, D., F. Nasir, E. R. Westwater, V. H. Payne, D. D. Turner, E. J. Mlawer, M. L. Exner, and M. P. Cadeddu (2009). "Comparison of ground-based millimeter-wave observations and simulations in the Arctic winter." In: *IEEE Transactions on Geoscience and Remote Sensing* 47.9, pp. 3098–3106. DOI: 10.1109/TGRS.2009.2020743.

Cossu, F., K. Hocke, A. Martynov, O. Martius, and C. Mätzler (2015). "Atmospheric water parameters measured by a ground-based microwave radiometer and compared with the WRF model." In: *Atmospheric Science Letters* 16.4, pp. 465–472. DOI: 10.1002/asl.583.

Cugerone, K., C. De Michele, A. Ghezzi, and V. Gianelle (2018). "Aerosol removal due to precipitation and wind forcings in Milan urban area." In: *Journal of Hydrology* 556, pp. 1256–1262. DOI: 10.1016/j.jhydrol.2017.06.033.

Dave, P., M. Bhushan, and C. Venkataraman (2017). "Aerosols cause intraseasonal short-term suppression of Indian monsoon rainfall." In: *Scientific Reports* 7.1, p. 17347. DOI: 10.1038/s41598-017-17599-1.

Deuber, B., N. Kampfer, and D. Feist (2004). "A new 22-GHz radiometer for middle atmospheric water vapor profile measurements." In: *IEEE Transactions on Geoscience and Remote Sensing* 42.5, pp. 974–984. DOI: 10.1109/TGRS.2004.825581.

Dicke, R. H., R. Beringer, R. L. Kyhl, and A. B. Vane (1946). "Atmospheric Absorption Measurements with a Microwave Radiometer." In: *Physical Review* 70 (5-6), pp. 340–348. DOI: 10.1103/PhysRev.70.340.

Ellison, W. (2007). "Permittivity of pure water, at standard atmospheric pressure, over the frequency range–25THz and the temperature Range–100° C." In: *Journal of physical and chemical reference data* 36.1, pp. 1–18. DOI: 10.1063/1.2360986.

Emery, W. and A. Camps (2017). "Microwave radiometry." In: *Introduction to Satellite Remote Sensing*. Ed. by W. Emery and A. Camps. Elsevier, pp. 131–290. DOI: 10.1016/B978-0-12-809254-5.00004-X.

Friedman, J. H. (2001). "Greedy function approximation: A gradient boosting machine." In: *The Annals of Statistics* 29.5, pp. 1189–1232. DOI: 10.1214/aos/1013203451.

Garcia-Benadi, A., J. Bech, S. Gonzalez, M. Udina, B. Codina, and J.-F. Georgis (2020). "Precipitation type classification of micro rain radar data using an improved Doppler spectral processing methodology." In: *Remote Sensing* 12.24. DOI: 10.3390/rs12244113.

Grody, N. (1976). "Remote sensing of atmospheric water content from satellites using microwave radiometry." In: *IEEE Transactions on Antennas and Propagation* 24.2, pp. 155–162. DOI: 10.1109/TAP.1976.1141324.

Guernsey, J. L. (1987). "Orographic precipitation." In: *Climatology*. Boston, MA: Springer US, pp. 643–643. DOI: 10.1007/0-387-30749-4_128.

Guyot, A., A. Protat, S. P. Alexander, A. R. Klekociuk, P. Kuma, and A. Mc-Donald (2022). "Detection of supercooled liquid water containing clouds with ceilometers: development and evaluation of deterministic and data-driven retrievals." In: *Atmospheric Measurement Techniques* 15.12, pp. 3663–3681. DOI: 10.5194/amt-15-3663-2022.

Han, G., F. Liu, T. Zhang, W. Xu, Y. Zhang, N. Wu, and S. Ouyang (2023). "Study of microwave non-thermal effects on hydrogen bonding in water by Raman spectroscopy." In: *Spectrochimica Acta Part A: Molecular and Biomolecular Spectroscopy* 285, p. 121877. DOI: 10.1016/j.saa.2022.121877.

Han, Y. and E. R. Westwater (2000). "Analysis and improvement of tipping calibration for ground-based microwave radiometers." In: *IEEE transactions on geoscience and remote sensing* 38.3, pp. 1260–1276. DOI: 10.1109/36.843018.

Hastie, T., R. Tibshirani, and J. Friedman (2009). "Random forests." In: *The Elements of Statistical Learning: Data Mining, Inference, and Prediction*. New York, NY: Springer New York, pp. 587–604. DOI: 10.1007/978-0-387-84858-7_15.

Heintzenberg, J, A Wiedensohler, T. Tuch, D. Covert, P Sheridan, J. Ogren, J Gras, R Nessler, C Kleefeld, N Kalivitis, et al. (2006). "Intercomparisons and aerosol calibrations of 12 commercial integrating nephelometers of three manufacturers." In: *Journal of Atmospheric and Oceanic Technology* 23.7, pp. 902–914. DOI: 10.1175/JTECH1892.1.

Hersbach, H., P. de Rosnay, B. Bell, D. Schepers, A. Simmons, C. Soci, S. Abdalla, M. Alonso-Balmaseda, G. Balsamo, P. Bechtold, et al. (2018). *Operational global reanalysis: progress, future directions and synergies with NWP*. Report. Reading, UK: ECMWF. DOI: 10.21957/tkic6g3wm.

Hocke, K. (2022). *Operational monitoring of the rain rate by ground-based microwave radiometry in Switzerland*. Report. Payerne, Switzerland: MeteoSwiss. URL: https://www.meteoswiss.admin.ch/dam/jcr:aab3d00d-b9ea-4bdf-abc2-8722f6661616/Final-report-Hocke-Klemens.pdf.

Hocke, K., L. Bernet, J. Hagen, A. Murk, M. Renker, and C. Mätzler (2019). "Diurnal cycle of short-term fluctuations of integrated water vapour above Switzerland." In: *Atmospheric Chemistry and Physics* 19.19, pp. 12083–12090. DOI: 10.5194/acp-19-12083-2019.

Hocke, K., N. Kämpfer, C Gerber, and C. Mätzler (2011). "A complete long-term series of integrated water vapour from ground-based microwave radiometers." In: *International Journal of Remote Sensing* 32.3, pp. 751–765. DOI: 10.1080/01431161.2010.517792.

Hocke, K., F. Navas-Guzmán, L. Moreira, L. Bernet, and C. Mätzler (2017). "Oscillations in atmospheric water above Switzerland." In: *Atmospheric chemistry and physics* 17.19, pp. 12121–12131. DOI: 10.5194/acp-17-12121-2017.

Hogan, R. J. and E. J. O'Connor (2004). *Facilitating cloud radar and lidar algorithms: the Cloudnet Instrument Synergy/Target Categorization product*. Cloudnet documentation. Reading, UK: University of Reading. URL: http://www.met.rdg.ac.uk/~swrhgnrj/publications/categorization.pdf.

Houze Jr., R. A. (2014). "Nimbostratus and the separation of convective and stratiform precipitation." In: *International Geophysics*. Vol. 104. Elsevier, pp. 141–163. DOI: 10.1016/B978-0-12-374266-7.00006-8.

Hu, J., Q. Lu, X. Dong, C. Wu, F. Sun, Y. Guo, S. Gu, D. An, S. Wu, and F. Dou (2021). "Characterization of brightness temperature biases at channels 13 and 14 for FY-3C MWHS-2." In: *IEEE Transactions on Geoscience and Remote Sensing* 60, pp. 1–14. DOI: 10.1029/98RS01182.

Illingworth, A., R. Hogan, E. O'connor, D. Bouniol, M. Brooks, J. Delanoë, D. Donovan, J. Eastment, N Gaussiat, J. Goddard, et al. (2007). "Cloudnet: Continuous evaluation of cloud profiles in seven operational models using ground-based observations." In: *Bulletin of the American Meteorological Society* 88.6, pp. 883–898. DOI: 10.1175/BAMS-88-6-883.

Ji, D., J. Shi, H. Letu, W. Li, H. Zhang, and H. Shang (2021). "A total precipitable water product and its trend analysis in recent years based on passive microwave radiometers." In: *IEEE Journal of Selected Topics in Applied Earth Observations and Remote Sensing* 14, pp. 7324–7335. DOI: 10.1109/JSTARS.2021.3096535.

Jullien, N., E. Vignon, M. Sprenger, F. Aemisegger, and A. Berne (2020). "Synoptic conditions and atmospheric moisture pathways associated with virga and precipitation over coastal Adélie Land in Antarctica." In: *The Cryosphere* 14.5, pp. 1685–1702. DOI: 10.5194/tc-14-1685-2020.

Kirchhoff, G. (1978). "Über das Verhältnis zwischen dem Emissionsvermögen und dem Absorptionsvermögen der Körper für Wärme und Licht." In: *Von Kirchhoff bis Planck: Theorie der Wärmestrahlung in historisch-kritischer Darstellung*. Ed. by H.-G. Schöpf. Wiesbaden: Vieweg+Teubner Verlag, pp. 131–151. DOI: 10.1007/978-3-663-13885-3_10.

Klein, M. and A. J. Gasiewski (2000). "Nadir sensitivity of passive millimeter and submillimeter wave channels to clear air temperature and water vapor variations." In: *Journal of Geophysical Research: Atmospheres* 105.D13, pp. 17481–17511. DOI: 10.1029/2000JD900089.

Küchler, N, D. Turner, U Löhnert, and S Crewell (2016). "Calibrating ground-based microwave radiometers: Uncertainty and drifts." In: *Radio Science* 51.4, pp. 311–327. DOI: 10.1002/2015RS005826.

Kummerow, C. D. (2020). "Introduction to passive microwave retrieval methods." In: *Satellite Precipitation Measurement: Volume 1*. Ed. by C. D. Kummerow. Cham: Springer International Publishing, pp. 123–140. DOI: 10.1007/978-3-030-24568-9_7.

Lazri, M., K. Labadi, J. M. Brucker, and S. Ameur (2020). "Improving satellite rainfall estimation from MSG data in Northern Algeria by using a multi-

classifier model based on machine learning." In: *Journal of Hydrology* 584, p. 124705. DOI: https://doi.org/10.1016/j.jhydrol.2020.124705.

Leuenberger, A. (2009). "Precipitation measurements with microwave sensors." MA thesis. Faculty of Science, University of Bern.

Li, N. (2019). "Study on global precipitation retrieval and typhoon simulation based on the Microwave Humidity and Temperature Sounder (MWHTS) onboard FY-3C satellite." PhD thesis. The University of Chinese Academy of Sciences.

Liaw, A., M. Wiener, et al. (2002). "Classification and regression by random-Forest." In: *R news* 2.3, pp. 18–22. URL: https://journal.r-project.org/articles/RN-2002-022/RN-2002-022.pdf.

Löhnert, U. and S. Crewell (2003). "Accuracy of cloud liquid water path from ground-based microwave radiometry 1. Dependency on cloud model statistics." In: *Radio Science* 38.3, p. 8041. DOI: 10.1029/2002RS002654.

Louppe, G., L. Wehenkel, A. Sutera, and P. Geurts (2013). "Understanding variable importances in forests of randomized trees." In: *NIPS'13: Proceedings of the 26th International Conference on Neural Information Processing Systems–Volume 1*. Red Hook, NY, USA: Curran Associates Inc., pp. 431–439.

METEK (2009). *MRR physical basics valid for MRR Service Version 5.2.1.0*. Report. Elmshorn, Germany: METEK. URL: https://ghrc.nsstc.nasa.gov/pub/doc/gpmgv/mrr_NASA/MRR-Manual_20110324.pdf.

Ma, L., J. Nie, and J. Yang (2009). "Two forms of Wien's displacement law." In: *Latin-American Journal of Physics Education* 3.3, p. 12. URL: http://www.lajpe.org/sep09/12_LAJPE_303_Lianxi.pdf.

Marshall, J. and F. Schott (1999). "Open-ocean convection: Observations, theory, and models." In: *Reviews of geophysics* 37.1, pp. 1–64. DOI: 10.1029/98RG02739.

Marzano, F. S., D. Cimini, and R. Ware (2005a). "Monitoring of rainfall by ground-based passive microwave systems: models, measurements and applications." In: *Advances in Geosciences* 2, pp. 259–265. DOI: 10.5194/adgeo-2-259-2005.

Marzano, F., D. Cimini, P. Ciotti, and R. Ware (2005b). "Modeling and measurement of rainfall by ground-based multispectral microwave radiometry." In: *IEEE Transactions on Geoscience and Remote Sensing* 43.5, pp. 1000–1011. DOI: 10.1109/TGRS.2004.839595.

Marzano, F., E. Fionda, P. Ciotti, and A. Martellucci (2002). "Ground-based multifrequency microwave radiometry for rainfall remote sensing." In: *IEEE Transactions on Geoscience and Remote Sensing* 40.4, pp. 742–759. DOI: 10.1109/TGRS.2002.1006317.

Marzano, F. S., D. Cimini, and M. Montopoli (2010). "Investigating precipitation microphysics using ground-based microwave remote sensors and disdrometer data." In: *Atmospheric Research* 97.4, pp. 583–600. DOI: 10.1016/j.atmosres.2010.03.019.

Marzano, F. S., E. Fionda, and P. Ciotti (2006). "Neural-network approach to ground-based passive microwave estimation of precipitation intensity and extinction." In: *Journal of Hydrology* 328.1, pp. 121–131. DOI: 10.1016/j.jhydrol.2005.11.042.

Maschwitz, G, U Löhnert, S Crewell, T Rose, and D. Turner (2013). "Investigation of ground-based microwave radiometer calibration techniques at 530 hPa." In: *Atmospheric Measurement Techniques* 6.10, pp. 2641–2658. DOI: 10.5194/amt-6-2641-2013.

Mattioli, V., E. Westwater, and V. Morris (2004). "Monitoring of precipitable water vapor and cloud liquid path from scanning microwave radiometers during the 2003 cloudiness inter-comparison experiment." In: *Fourteenth ARM Science Team Meeting Proceedings, Albuquerque, New Mexico*, pp. 1–10. URL: https://api.semanticscholar.org/CorpusID:129122467.

Mattioli, V., E. R. Westwater, S. I. Gutman, and V. R. Morris (2005). "Forward model studies of water vapor using scanning microwave radiometers, global positioning system, and radiosondes during the cloudiness inter-comparison experiment." In: *IEEE Transactions on Geoscience and Remote Sensing* 43.5, pp. 1012–1021. DOI: 10.1109/TGRS.2004.839926.

Mätzler, C. and C. Melsheime (2006). "Radiative transfer and microwave radiometry." In: *Thermal microwave radiation: applications for remote sensing*. Ed. by C. Mätzler. The Institution of Engineering and Technology. Chap. 1, pp. 1–23.

Mätzler, C. and J. Morland (2009). "Refined physical retrieval of integrated water vapor and cloud liquid for microwave radiometer data." In: *IEEE Transactions on Geoscience and Remote Sensing* 47.6, pp. 1585–1594. DOI: 10.1109/TGRS.2008.2006984.

— (2014). *Advances in surface-based radiometry of atmospheric water*. IAP Research Report 2008-02-MW. Bern, Switzerland: Institute of Applied Physics, University of Bern.

MeteoSwiss (2014). *Climate normals Bern/Zollikofen (reference period: 1981-2010)*. URL: https://web.archive.org/web/20220114033933/https://www.meteoswiss.admin.ch/product/output/climate-data/climate-diagrams-normal-values-station-processing/BER/climsheet_BER_np9120_e.pdf.

Miacci, M. A., C. F. Angelis, A. J. Calheiros, and L. A. Machado (2015). "Some considerations on the cryogenic calibration technique for microwave and millimeter wave ground-based radiometry." In: *Revista de Gestão & Tecnologia* 3.3, pp. 47–52. URL: https://radiometrics.com/wp-content/uploads/2021/10/Miacci_REGET_2015.pdf.

Moosmüller, H. and W. P. Arnott (2009). "Particle optics in the Rayleigh regime." In: *Journal of the Air & Waste Management Association* 59.9, pp. 1028–1031. DOI: 10.3155/1047-3289.59.9.1028.

Morland, J. (2002). *TROWARA-Tropospheric water vapour radiometer: Radiometer review and new calibration model*. IAP Research Report 2002-15-MW. Bern, Switzerland: Institute of Applied Physics, University of Bern.

— (2007). *TROWARA—Rain flag development and stability of instrument and calibration*. IAP Research Report 2007-13-MW. Bern, Switzerland: Institute of Applied Physics, University of Bern.

Muinonen, K., J. Tyynelä, E. Zubko, H. Lindqvist, A. Penttilä, and G. Videen (2011). "Polarization of light backscattered by small particles." In: *Journal of Quantitative Spectroscopy and Radiative Transfer* 112.13, pp. 2193–2212. DOI: 10.1016/j.jqsrt.2011.06.009.

Myagkov, A. and T. Rose (2016). "Dual polarization dual frequency scanning cloud radar systems: configurations and applications." In: *Radiometer Physics GmbH*. URL: https://www.radiometer-physics.de/downloadftp/pub/PDF/CloudRadar/.

Nandan, R., M. V. Ratnam, V. R. Kiran, and D. N. Naik (2022). "Retrieval of cloud liquid water path using radiosonde measurements: Comparison with MODIS and ERA5." In: *Journal of Atmospheric and Solar-Terrestrial Physics* 227, p. 105799. DOI: 10.1016/j.jastp.2021.105799.

Ohata, S., N. Moteki, T. Mori, M. Koike, and Y. Kondo (2016). "A key process controlling the wet removal of aerosols: new observational evidence." In: *Scientific reports* 6.1, p. 34113. DOI: 10.1038/srep34113.

Pandolfi, M., L. Alados-Arboledas, A. Alastuey, M. Andrade, C. Angelov, B. Artiñano, J. Backman, U. Baltensperger, P. Bonasoni, N. Bukowiecki, et al. (2018). "A European aerosol phenomenology–6: scattering properties of atmospheric aerosol particles from 28 ACTRIS sites." In: *Atmospheric Chemistry and Physics* 18.11, pp. 7877–7911. DOI: 10.5194/acp-18-7877-2018.

Peter, R and N Kämpfer (1992). "Radiometric determination of water vapor and liquid water and its validation with other techniques." In: *Journal of Geophysical Research: Atmospheres* 97.D16, pp. 18173–18183. DOI: 10.1029/92JD01717.

Planck, M. (1914). "The Law of the Normal Distribution Of Energy. Elementary Quanta Of Matter and Electricity." In: *The theory of heat radiation*. Ed. by M. Planck. Philadelphia: P. Blakistons Son & Co., pp. 197–220. URL: https://www.gutenberg.org/files/40030/40030-pdf.pdf.

RPG (2014). *Operation principles and software description for RPG standard single polarization radiometers*. URL: https://www.radiometer-physics.de/download/PDF/Radiometers/HATPRO/.

Rao, M. P., E. R. Cook, B. I. Cook, K. J. Anchukaitis, R. D. D'Arrigo, P. J. Krusic, and A. N. LeGrande (2019). "A double bootstrap approach to Superposed Epoch Analysis to evaluate response uncertainty." In: *Dendrochronologia* 55, pp. 119–124. DOI: 10.1016/j.dendro.2019.05.001.

Rayleigh, L. (1871). "On the light from the sky, its polarization and colour." In: *Philosophical Magazine* 41, pp. 107–120.

Redmond, H. E., K. D. Dial, and J. E. Thompson (2010). "Light scattering and absorption by wind blown dust: Theory, measurement, and recent data." In: *Aeolian research* 2.1, pp. 5–26. DOI: 10.1016/j.aeolia.2009.09.002.

Ritter, M. E. (2017). "Atmospheric moisture." In: *The physical environment*. Ed. by M. E. Ritter. University of Wisconsin-Stevens Point. Chap. 7. URL: https://geo.libretexts.org/Bookshelves/Geography_(Physical)/The_Physical_Environment_(Ritter).

Rong, P., C. von Savigny, C. Zhang, C. G. Hoffmann, and M. J. Schwartz (2020). "Response of middle atmospheric temperature to the 27 d solar cycle: an analysis of 13 years of microwave limb sounder data." In: *Atmospheric Chemistry and Physics* 20.3, pp. 1737–1755. DOI: 10.5194/acp-20-1737-2020.

Rose, T., S. Crewell, U. Löhnert, and C. Simmer (2005). "A network suitable microwave radiometer for operational monitoring of the cloudy atmosphere." In: *Atmospheric Research* 75.3, pp. 183–200. DOI: 10.1016/j.atmosres.2004.12.005.

Rosenfeld, D. (2006). "Aerosols, clouds, and climate." In: *Science* 312.5778, pp. 1323–1324. DOI: 10.1126/science.1128972.

Rosenfeld, D., U. Lohmann, G. B. Raga, C. D. O'Dowd, M. Kulmala, S. Fuzzi, A. Reissell, and M. O. Andreae (2008). "Flood or drought: how do aerosols affect precipitation?" In: *Science* 321.5894, pp. 1309–1313. DOI: 10.1126/science.1160606.

Rosenkranz, P. W. (1998). "Water vapor microwave continuum absorption: A comparison of measurements and models." In: *Radio Science* 33.4, pp. 919–928. DOI: 10.1029/98RS01182.

Sarangi, C., S. N. Tripathi, V. P. Kanawade, I. Koren, and D. S. Pai (2017). "Investigation of the aerosol–cloud–rainfall association over the Indian summer monsoon region." In: *Atmospheric Chemistry and Physics* 17.8, pp. 5185–5204. DOI: 10.5194/acp-17-5185-2017.

Srivastava, R. (1987). "A model of intense downdrafts driven by the melting and evaporation of precipitation." In: *Journal of Atmospheric Sciences* 44.13, pp. 1752–1774. DOI: 10.1175/1520-0469(1987)044<1752:AMOIDD>2.0.CO;2.

Stefan, J (1879). "Über die Beziehung zwischen der Wärmestrahlung und der Temperatur, sitzungsberichte der mathematisch-naturwi-ssenschaftlichen classe der kaiserlichen." In: *Akademie der Wissenschaften* 79. Ed. by J Stefan, S–391. URL: https://www.bio-physics.at/wiki/images/Stefan1879.pdf.

Tien, K.-J. C., R. D. De Roo, J. Judge, and H. Pham (2007). "Comparison of calibration techniques for ground-based C-band radiometers." In: *IEEE Geoscience and Remote Sensing Letters* 4.1, pp. 83–87. DOI: 10.1109/LGRS.2006.886420.

Titos, G, I Foyo-Moreno, H Lyamani, X Querol, A Alastuey, and L Alados-Arboledas (2012). "Optical properties and chemical composition of aerosol

particles at an urban location: An estimation of the aerosol mass scattering and absorption efficiencies." In: *Journal of Geophysical Research: Atmospheres* 117.D04206. DOI: 10.1029/2011JD016671.

Trenberth, K. E., J. T. Fasullo, and J. Kiehl (2009). "Earth's global energy budget." In: *Bulletin of the American Meteorological Society* 90.3, pp. 311–324. DOI: 10.1175/2008BAMS2634.1.

Villarini, G. and W. F. Krajewski (2010). "Review of the different sources of uncertainty in single polarization radar-based estimates of rainfall." In: *Surveys in geophysics* 31, pp. 107–129. DOI: 10.1007/s10712-009-9079-x.

Walton, S. D. and K. R. Murphy (2022). "Superposed epoch analysis using time-normalization: A Python tool for statistical event analysis." In: *Frontiers in Astronomy and Space Sciences* 9, p. 1000145. DOI: 10.3389/fspas.2022.1000145.

Wang, W., K. Hocke, L. Nania, A. Cazorla, G. Titos, R. Matthey, L. Alados-Arboledas, A. Millares, and F. Navas-Guzmán (2024). "Inter-relations of precipitation, aerosols, and clouds over Andalusia, southern Spain, revealed by the Andalusian Global ObseRvatory of the Atmosphere (AGORA)." In: *Atmospheric Chemistry and Physics* 24.2, pp. 1571–1585. DOI: 10.5194/acp-24-1571-2024.

Wang, W. and K. Hocke (2022). "Atmospheric effects and precursors of rainfall over the Swiss Plateau." In: *Remote Sensing* 14.12. DOI: 10.3390/rs14122938.

Wang, W., K. Hocke, and C. Mätzler (2021). "Physical retrieval of rain rate from ground-based microwave radiometry." In: *Remote Sensing* 13.11. DOI: 10.3390/rs13112217.

Wang, W., A. Murk, E. Sauvageat, W. Fan, C. Dätwyler, M. Hervo, A. Haefele, and K. Hocke (2023). "An indoor microwave radiometer for measurement of tropospheric water." In: *IEEE Transactions on Geoscience and Remote Sensing* 61, pp. 1–13. DOI: 10.1109/TGRS.2023.3261067.

Wien, W. (1894). "Temperatur und entropie der strahlung." In: *Annalen der physik* 288.5, pp. 132–165. DOI: 10.1002/andp.18942880511.

Wu, L., S. Peng, Z. Xiao, T. Hu, and J. Xu (2010). "Calibration of a W band radiometer using tipping curve." In: *2010 International Symposium on Signals, Systems and Electronics*. Vol. 2. IEEE, pp. 1–3. DOI: 10.1109/ISSSE.2010.5606983.

Zhang, N., M. Chen, F. Yang, C. Yang, P. Yang, Y. Gao, Y. Shang, and D. Peng (2022). "Forest height mapping using feature selection and machine learning by integrating multi-source satellite data in Baoding City, North China." In: *Remote Sensing* 14.18, p. 4434. DOI: 10.3390/rs14184434.

Zhang, R. (2019). "Study on the tropical cyclone rain retrieval from FY-3B Microwave Imager (MWRI) brightness temperature." PhD thesis. The University of Chinese Academy of Sciences.

Zhang, Y., K. Wu, J. Zhang, F. Zhang, H. Xiao, F. Wang, J. Zhou, Y. Song, and L. Peng (2021). "Estimating rainfall with multi-resource data over East

Asia based on machine learning." In: *Remote Sensing* 13.16. DOI: `10.3390/rs13163332`.

Zhu, H., R. Li, S. Yang, C. Zhao, Z. Jiang, and C. Huang (2023). "The impacts of dust aerosol and convective available potential energy on precipitation vertical structure in southeastern China as seen from multisource observations." In: *Atmospheric Chemistry and Physics* 23.4, pp. 2421–2437. DOI: `10.5194/acp-23-2421-2023`.

LIST OF PUBLICATIONS

ARTICLES

Wang, W.*[1], W. Fan, and K. Hocke (2024). "Rain detection for rain-contaminated ground-based microwave radiometer data using physics-informed machine learning method." submitted to *Journal of Hydrology*.

Wang, W.*, W. Fan, and K. Hocke (2024). "Precipitation retrievals for ground-based microwave radiometer using physics-informed machine learning methods." submitted to *Journal of Hydrology*.

Wang, W.*, K. Hocke, L. Nania, A. Cazorla, G. Titos, R. Matthey, L. Alados-Arboledas, A. Millares, and F. Navas-Guzmán (2024). "Inter-relations of precipitation, aerosols, and clouds over Andalusia, southern Spain, revealed by the Andalusian Global ObseRvatory of the Atmosphere (AGORA)." In: *Atmospheric Chemistry and Physics* 24, pp. 1571–1585. `https://doi.org/10.5194/acp-24-1571-2024`.

Wang, W.*, A. Murk, E. Sauvageat, W. Fan, C. Dätwyler, M. Hervo, A. Haefele, and K. Hocke (2023). "An indoor microwave radiometer for measurement of tropospheric water." In: *IEEE Transactions on Geoscience and Remote Sensing* 61, pp. 1-13. `https://doi.org/10.1109/TGRS.2023.3261067`.

Wang, W.*, K. Hocke (2022). "Atmospheric effects and precursors of rainfall over the Swiss Plateau." In: *Remote Sensing* 14.12, p. 2938. `https://doi.org/10.3390/rs14122938`.

Wang, W.*, K. Hocke, and C. Mätzler (2021). "Physical retrieval of rain rate from ground-based microwave radiometry." In: *Remote Sensing* 13.11, p. 2217. `https://doi.org/10.3390/rs13112217`.

Wang, W., J. Yu*, Y. Wang, C. Jia, L. Wu, and S. Zhang (2020). "Ionospheric tomography method by reducing grid resolution locally". In: *Acta Geodaetica et Cartographica Sinica* 49.7, pp. 843-853. `http://xb.chinasmp.com/EN/Y2020/V49/I7/843`.

Yu, J.*, **W. Wang***, L. Holden, Z. Liu, L. Wu, S. Zhang, and K. Zhang (2020). "Enhancing the quality of tomographic image by means of image reconstruction based on hybrid grids". In: *Advances in Space Research*, 66.3, pp. 591-603. `https://doi.org/10.1016/j.asr.2020.04.026`.

Hocke, K.*, **W. Wang**, M. Cahyadi, and G. Ma (2024). "Quasi-diurnal lunar tide O_1 in ionospheric total electron content at solar minimum." submitted to *Journal of Geophysical Research - Space Physics*.

---

1 *: Corresponding author

Hocke, K.*, **W. Wang**, and G. Ma (2024). "Influences of sudden stratospheric warmings on the ionosphere above Okinawa." In: *Atmospheric Chemistry and Physics* 24.10, pp. 5837–5846. https://doi.org/10.5194/acp-24-5837-2024.

Hocke, K*. and **W. Wang** (2023). "Observation of an extremely dry atmospheric air column above Bern." In: *Climate* 11.3. https://doi.org/10.3390/cli11030063.

Hocke, K.*, L. Bernet, **W. Wang**, C. Mätzler, M. Hervo, and A. Haefele (2021). "Integrated water vapor during rain and rain-free conditions above the Swiss Plateau." In: *Climate* 9.7. https://doi.org/10.3390/cli9070105.

PRESENTATIONS

Wang, W., K. Hocke, L. Nania, A. Cazorla, G. Titos, R. Matthey, L. Alados-Arboledas, A. Millares, and F. Navas-Guzmán (2023). "Multi-instrument observations of the evolution of atmospheric parameters during rainfall events over Andalusia." In: *IUGG General Assembly 2023, Berlin, Germany*. https://doi.org/10.57757/IUGG23-1541.

Wang, W. (2023). "Evolution of rainfall parameters observed in Granada." In: *IAP seminar 2023-05-MW; Institute of Applied Physics, University of Bern: Bern, Switzerland*.

Navas-Guzmán, F., **Wang, W.**, K. Hocke, L. Nania, A. Cazorla, G. Titos, R. Matthey, L. Alados-Arboledas (2023). "Investigation of rainfall precursors using in-situ and remote sensing techniques in the southeast of the Iberian Peninsula." In: *EGU General Assembly 2023, Vienna, Austria*. https://doi.org/10.5194/egusphere-egu23-12641.

Wang, W., K. Hocke, and C. Mätzler (2022). "Atmospheric effects and precursors of rainfall over the Swiss Plateau." In: *EGU General Assembly 2022, Vienna, Austria*. https://doi.org/10.5194/egusphere-egu22-1950.

Wang, W. (2021). "TROWARA rain rate retrieval and atmospheric precursors of rainfall." In: *IAP seminar 2021-12-MW; Institute of Applied Physics, University of Bern: Bern, Switzerland*.

Wang, W. (2020). "Ionospheric tomography method via image reconstruction based on hybrid grids." In: *IAP seminar 2020-12-MW; Institute of Applied Physics, University of Bern: Bern, Switzerland*.

POSTERS

Wang, W., A. Murk, E. Sauvageat, W. Fan, C. Dätwyler, M. Hervo, A. Haefele, and K. Hocke (2023). "An indoor microwave radiometer for measurement of tropospheric water." In: *Swiss Remote Sensing Days 2023, St.Gallen, Switzerland*.

Wang, W. and K. Hocke (2022). "Atmospheric effects and precursors of rainfall over the Swiss Plateau." In: *20th Swiss Climate Summer School, Grindelwald, Switzerland*.

Wang, W., K. Hocke, and C. Mätzler (2022). "TROWARA rain rate retrieval and atmospheric precursors of rainfall." In: *Swiss Remote Sensing Days 2022, Ascona, Switzerland*.

Wang, W., K. Hocke, and C. Mätzler (2021). "Physical retrieval of rain rate from ground-based microwave radiometry." In: *19th Swiss Geoscience Meeting*.

Wang, W., K. Hocke, and C. Mätzler (2021). "Physical retrieval of rain rate from ground-based microwave radiometry." In: *Swiss National GAW/GCOS Symposium*.

ERKLÄRUNG

gemäss Art. 18 PromR Phil.-nat. 2019

Name/Vorname:	Wenyue Wang
Matrikelnummer:	20-131-710
Studiengang:	PhD in Climate Sciences
	Bachelor ☐ Master ☐ Dissertation ☒
Titel der Arbeit:	Investigation of precipitation using ground-based remote sensing and in situ techniques
Leiter der Arbeit:	PD. Dr. Klemens Hocke

Ich erkläre hiermit, dass ich diese Arbeit selbständig verfasst und keine anderen als die angegebenen Quellen benutzt habe. Alle Stellen, die wörtlich oder sinngemäss aus Quellen entnommen wurden, habe ich als solche gekennzeichnet. Mir ist bekannt, dass andernfalls der Senat gemäss Artikel 36 Absatz 1 Buchstabe r des Gesetzes über die Universität vom 5. September 1996 und Artikel 69 des Universitätsstatuts vom 7. Juni 2011 zum Entzug des Doktortitels berechtigt ist. Für die Zwecke der Begutachtung und der Überprüfung der Einhaltung der Selbständigkeitserklärung bzw. der Reglemente betreffend Plagiate erteile ich der Universität Bern das Recht, die dazu erforderlichen Personendaten zu bearbeiten und Nutzungshandlungen vorzunehmen, insbesondere die Doktorarbeit zu vervielfältigen und dauerhaft in einer Datenbank zu speichern sowie diese zur Überprüfung von Arbeiten Dritter zu verwenden oder hierzu zur Verfügung zu stellen.

Bern, September 2024

Wenyue Wang